Cancer Cell

Volume 23
Number 4

April 15, 2013

www.cellpress.com

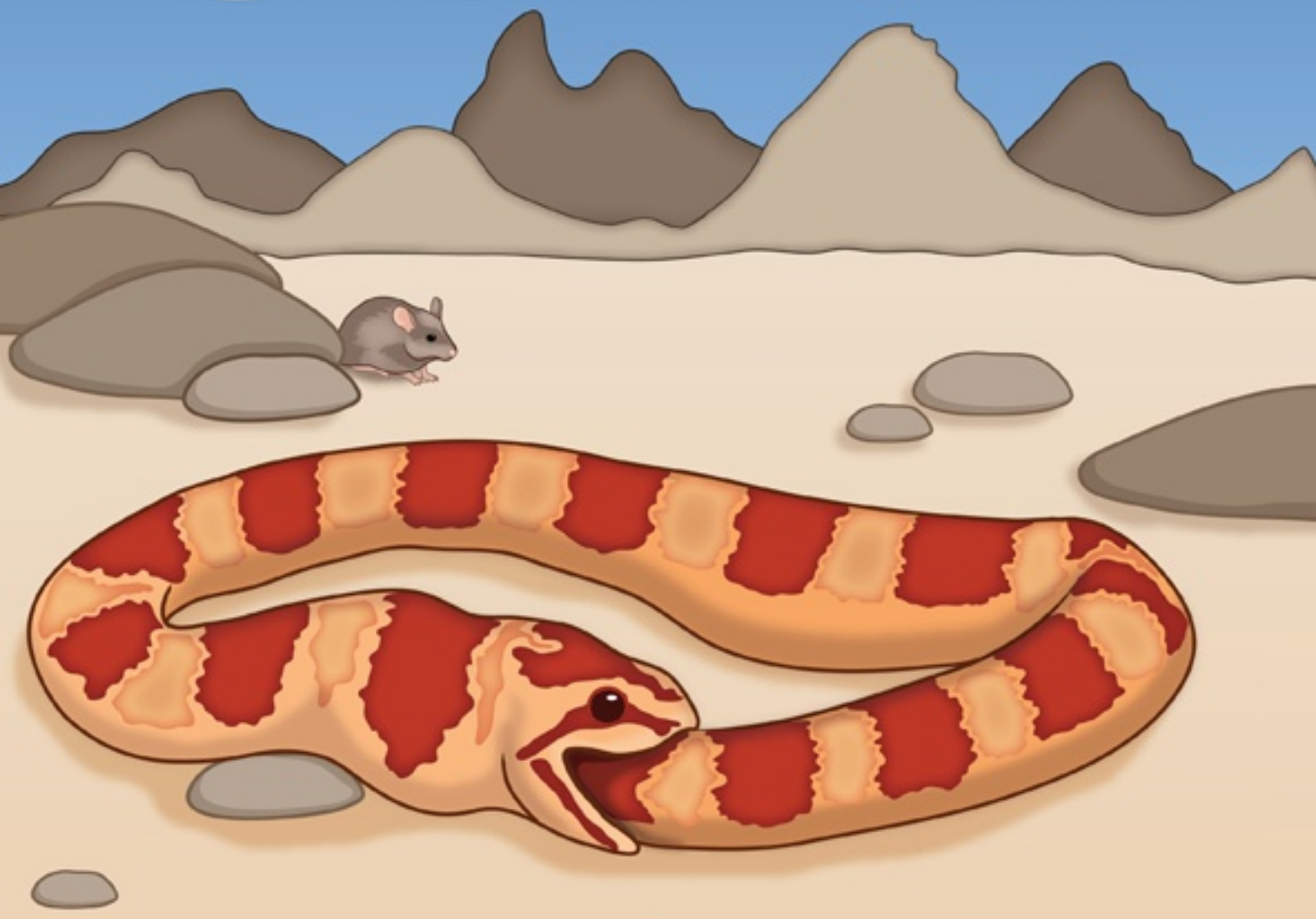

Caspase-10 Tempers Autophagy in Multiple Myeloma

Cancer Cell
Article

Lysine-5 Acetylation Negatively Regulates Lactate Dehydrogenase A and Is Decreased in Pancreatic Cancer

Di Zhao,[1,2,5,9] Shao-Wu Zou,[6,9] Ying Liu,[4] Xin Zhou,[1,2,5] Yan Mo,[1,2,3] Ping Wang,[1,5] Yan-Hui Xu,[1,5] Bo Dong,[6] Yue Xiong,[1,2,5,7,*] Qun-Ying Lei,[1,2,3,*] and Kun-Liang Guan[1,2,3,8,*]

[1]Ministry of Education Key Laboratory of Molecular Medicine, Shanghai Medical College and State Key Laboratory of Genetic Engineering, School of Life Sciences
[2]Laboratory of Molecular Cell Biology, Institute of Biomedical Science
[3]Department of Biochemistry and Molecular Biology
[4]Department of Pathology, School of Basic Medical Sciences, Shanghai Medical College
[5]School of Life Sciences
Fudan University, Shanghai 200032, China
[6]Department of Hepatopancreatobiliary Surgery, Shanghai Tenth People's Hospital, Tong Ji University, Shanghai 200072, China
[7]Department of Biochemistry and Biophysics, Lineberger Comprehensive Cancer Center, University of North Carolina at Chapel Hill, NC 27599, USA
[8]Department of Pharmacology and Moores Cancer Center, University of California San Diego, La Jolla, CA 92037-0695, USA
[9]These authors contributed equally to this work
*Correspondence: yxiong@email.unc.edu (Y.X.), qlei@fudan.edu.cn (Q.-Y.L.), kuguan@ucsd.edu (K.-L.G.)
http://dx.doi.org/10.1016/j.ccr.2013.02.005

SUMMARY

Tumor cells commonly have increased glucose uptake and lactate accumulation. Lactate is produced from pyruvate by lactate dehydrogenase A (LDH-A), which is frequently overexpressed in tumor cells and is important for cell growth. Elevated transcription by c-Myc or HIF1α may contribute to increased LDH-A in some cancer types. Here, we show that LDH-A is acetylated at lysine 5 (K5) and that this acetylation inhibits LDH-A activity. Furthermore, the K5-acetylated LDH-A is recognized by the HSC70 chaperone and delivered to lysosomes for degradation. Replacement of endogenous LDH-A with an acetylation mimetic mutant decreases cell proliferation and migration. Importantly, K5 acetylation of LDH-A is reduced in human pancreatic cancers. Our study reveals a mechanism of LDH-A upregulation in pancreatic cancers.

INTRODUCTION

Alteration in cell metabolism is a common event in tumorigenesis, as indicated by the dramatic increase of glucose utilization. However, the increased glucose uptake in tumor cells often does not lead to a corresponding increase in oxidative phosphorylation even in the presence of sufficient oxygen supply. Instead, glycolysis is highly elevated in most cancer cells. This metabolic alteration, known as the Warburg effect (Warburg, 1956), is believed to benefit tumor cells not only by conditioning the microenvironment, but also by increasing the levels of glycolytic intermediates, many of which also serve as precursors for anabolic biosynthesis, to support increased cell growth (Koppenol et al., 2011; Vander Heiden et al., 2009). The fact that tumor cells have a dramatically increased glucose uptake has provided the basis for ^{18}F-fluorodeoxyglucose-positron emission tomography technology, which is widely used for detecting tumors.

The last step of glycolysis is catalyzed by pyruvate kinase (PK), which converts phosphoenopyruvate to pyruvate. In normal nonproliferating cells, most, if not all, of pyruvate enters mitochondria, where it is converted to acetyl-CoA by the pyruvate dehydrogenase complex to fuel the tricarboxylic acid (TCA) cycle and oxidative phosphorylation for efficient energy production. In contrast, in cancer cells, and probably other highly proliferating cells, the influx of pyruvate into mitochondria and the

Significance

This study uncovers a critical role and the mechanism of acetylation in the regulation of lactate dehydrogenase A (LDH-A), which is elevated in cancer cells. Lysine-5 acetylation inhibits LDH-A by two mechanisms: decreasing enzymatic activity and increasing degradation by a chaperone-mediated autophagy. Moreover, LDH-A lysine-5 acetylation inversely correlates with pancreatic cancer initiation. Therefore, acetylation plays an important role in the regulation of cell growth and cancer metabolism.

TCA is not proportional to the increased glucose uptake; instead, more pyruvate is converted to lactate by lactate dehydrogenase (LDH). Therefore, a high conversion rate of pyruvate to lactate, hence high LDH, is commonly observed in cancer cells.

LDH is a homo- or hetero-tetrameric enzyme composed of two subunits, M and H, encoded by two highly related genes, *LDH-A* (also known as *LDHM*, *LDH1*, *GSD11*, and *PIG19*) and *LDH-B* (also known as *LDH-H, H-LDH*, and *LDH2*), resulting in five different isozymes depending on the ratio of the M and H subunits (M4, M3H1, M2H2, M1H3, and H4). LDH enzyme catalyzes the reversible conversion of pyruvate to lactate using NAD+ as a cofactor. Although the physiologic significance of lactate accumulation in tumor cells, a dead-end product in cellular metabolism, is currently a topic of debate, it has long been known that many tumor cells express a high level of LDH-A (Goldman et al., 1964), including non-small cell lung cancer (Koukourakis et al., 2003), colorectal cancer (Koukourakis et al., 2006), and breast and gynecologic cancers (Koukourakis et al., 2009). In many tumors, elevated LDH-A levels have been correlated with poor prognosis and resistance to chemotherapy and radiation therapy. Further evidence linking an LDH-A increase to tumorigenesis comes from the findings that the *LDH-A* gene is a direct target of both Myc and HIF transcription factors (Lewis et al., 1997; Semenza et al., 1996; Shim et al., 1997). Inhibition of LDH-A by either RNA interference or pharmacologic agents blocks tumor progression in vivo (Fantin et al., 2006; Le et al., 2010; Xie et al., 2009), supporting an important role of elevated LDH-A in tumorigenesis and LDH-A as a potential therapeutic target.

We and others have recently discovered that a large number of non-nuclear proteins, especially those involved in intermediate metabolism, are acetylated (Choudhary et al., 2009; Kim et al., 2006; Wang et al., 2010; Zhao et al., 2010). In this report, we investigated LDH-A acetylation and its functional significance in tumorigenesis.

RESULTS

LDH-A Is Acetylated at Lysine 5

Eight putative acetylation sites were identified in LDH-A by mass spectrometry (Figure S1A available online; Choudhary et al., 2009). Western blotting with anti-acetyllysine antibody showed that LDH-A was indeed acetylated and its acetylation was enhanced approximately 3.5-fold after treatment with trichostatin A (TSA), an inhibitor of histone deacetylase HDAC I and II (Ekwall et al., 1997; Furumai et al., 2001), and nicotinamide (NAM), an inhibitor of the SIRT family of deacetylases (Avalos et al., 2005) (Figure 1A).

We then mutated each of eight putative acetylation sites individually to glutamine (Q), and examined their acetylation. Mutation of either K5 or K318, but not other lysine residues, to glutamine resulted in a significant reduction in LDH-A acetylation (Figure S1B). Arginine substitution of K5, but not K318, dramatically decreased the LDH-A acetylation by approximately 70% (Figure 1B; data not shown), indicating that K5, which is evolutionarily conserved from *Caenorhabditis elegans* to mammals (Figure S1C), is a major acetylation site in LDH-A.

We generated an antibody specifically recognizing the K5-acetylated LDH-A. The specificity of the anti-acetyl-LDH-A (K5) antibody was verified as it recognized the K5-acetylated peptide but not the unacetylated control peptide (Figure S1D). Western blotting using this antibody detected ectopically expressed wild-type, but only weakly recognized the K5R mutant LDH-A (Figure 1C). Moreover, this antibody detected the acetylated but not the unacetylated LDH-A that was expressed and purified from bacteria (Figure 1I). These characterizations demonstrate the specificity of our anti-acetyl-LDH-A(K5) antibody in recognizing the K5-acetylated LDH-A.

We used the anti-acetyl-LDH-A (K5) antibody to determine acetylation of endogenous LDH-A. Acetylation of LDH-A could readily be detected by the antibody. This signal was diminished by LDH-A knockdown and was completely blocked by the preincubation with the antigen peptide (Figure 1D), confirming the specificity of the anti-acetyl-LDH-A(K5) antibody. Treatment of cells with deacetylase inhibitors TSA and NAM strongly increased K5 acetylation of both endogenously (Figure 1E) and the ectopically expressed LDH-A (Figure S1E). To quantify LDH-A acetylation, we employed IEF (isoelectric focusing) to separate the acetylated protein based on the loss of positive charge due to lysine acetylation. The spot with highest pI, spot 0, showed the lowest relative acetylation, while the lowest pI spot 4 had the highest acetylation, indicating that the change of LDH-A pI is at least in part due to acetylation (Figure 1F). Assuming that spot 0 represented the unacetylated LDH-A while spot 4 represented the fully acetylated LDH-A, we estimated that approximately 20% of the LDH-A is acetylated on lysine 5. Therefore, a substantial fraction of endogenous LDH-A could be acetylated.

K5 Acetylation Inhibits LDH-A Enzyme Activity

To test the effect of K5 acetylation, the activity of LDH-A^{K5R} and LDH-A^{K5Q} mutants was compared with that of wild-type LDH-A. We found that LDH-A^{K5Q} displayed only 18% of the wild-type activity, while the LDH-A^{K5R} mutation had a minor effect on the LDH-A activity (Figure 1G). Consistent with an inhibitory effect of acetylation on LDH-A activity, inhibition of deacetylases by NAM and TSA treatment significantly decreased LDH-A enzyme activity by more than 60% (Figures 1H and S1F). Moreover, treatment of NAM and TSA had little effect on the activity of either LDH-A^{K5Q} or LDH-A^{K5R} mutants (Figure 1H).

To definitively demonstrate the effect of K5 acetylation on LDH-A activity, we employed the system of genetically encoding Nε-acetyllysine to prepare recombinant proteins in *Escherichia coli* (Neumann et al., 2008, 2009). This expression system produced LDH-A proteins with 100% acetylation at K5 due to the suppression of the K5-TAG stop codon by the Nε-acetyllysine-conjugated amber suppressor tRNA. We prepared both unacetylated and K5-acetylated LDH-A and compared their enzymatic activity. As shown in Figure 1I, K5-acetylated LDH-A showed significantly lower activity when compared with the unacetylated LDH-A. Collectively, these results demonstrate that acetylation at lysine 5 inhibits LDH-A activity.

SIRT2 Decreases LDH-A Acetylation and Increases Its Enzyme Activity

To identify the deacetylase responsible for LDH-A regulation, we first determined how inhibition of either SIRT or HDAC could affect LDH-A acetylation at lysine 5. Treatment of cells with

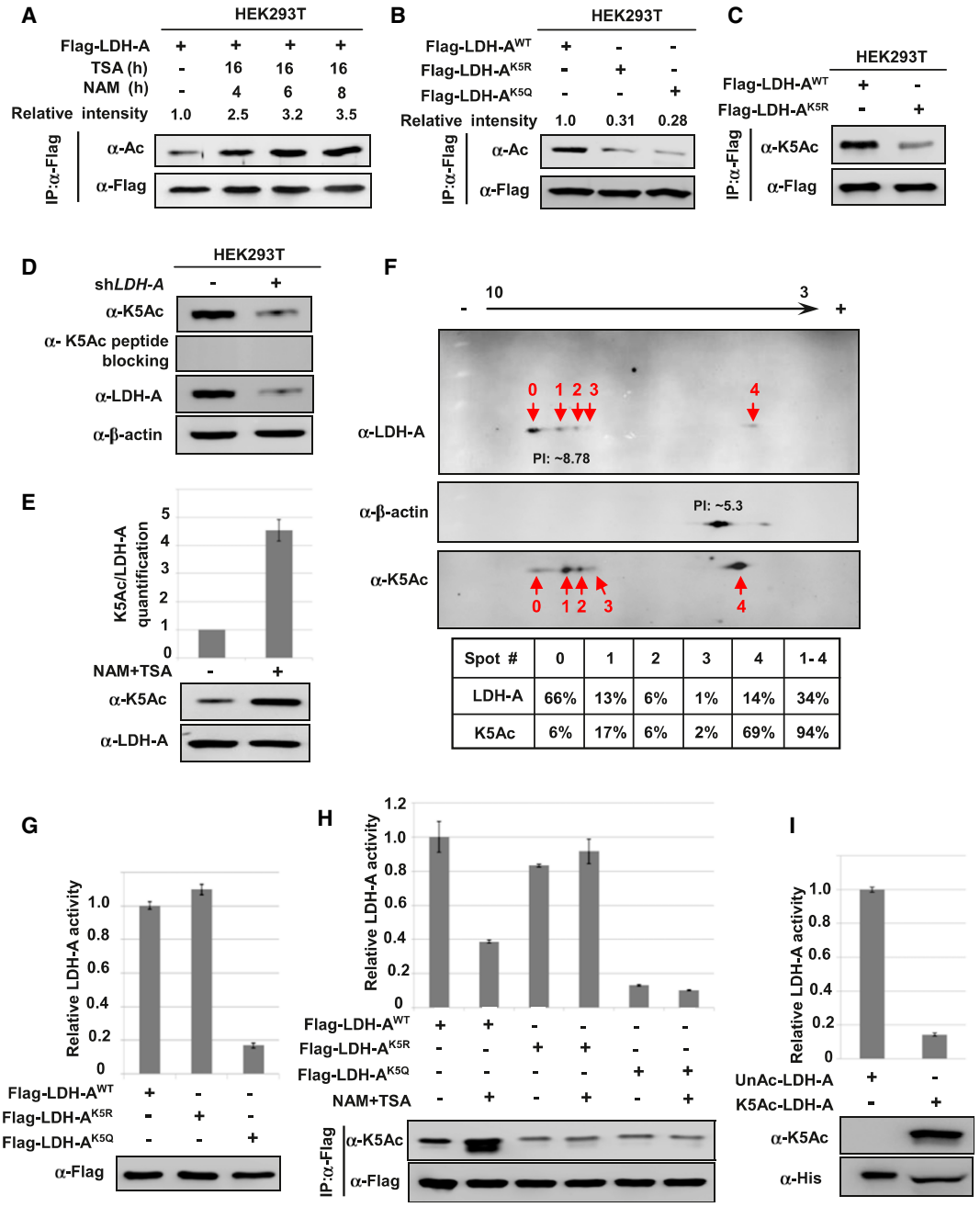

Figure 1. Acetylation at Lys-5 Decreases LDH-A Enzyme Activity

(A) LDH-A is acetylated. Flag-LDH-A was transfected into 293T cells followed by treatment with deacetylase inhibitors TSA and NAM for indicated time. LDH-A acetylation and protein levels were analyzed by western blot with indicated antibody. Relative ratios of acetylation were calculated from normalizing against Flag-LDH-A.

(B) Mutation of K5 decreases LDH-A acetylation. The indicated plasmids were transfected into 293T cells and proteins were immunoprecipitated for western blotting.

(C) Characterization of acetyl-LDH-A (K5) antibody. The indicated plasmids were transfected into 293T cells, acetylation level of immunoprecipitated Flag-LDH-A was measured by direct western bloting using the acetyl-LDH-A (K5) antibody (α-K5Ac).

(D) Endogenous LDH-A is acetylated on lysine 5. Cell lysate from scramble or LDH-A shRNA knockdown stable cells were probed with indicated antibodies.

(E) Treatment with NAM and TSA increases endogenous LDH-A acetylation; 293T cells were treated with TSA and NAM. Endogenous LDH-A protein levels and acetylation of K5 were determined by western blotting with indicated antibodies (bottom panel). Relative K5-acetylated LDH-A over total LDH-A protein was quantified (top panel). Error bars represent ± SD for triplicate experiments.

(F) Quantitative analysis of endogenous LDH-A acetylation at K5 by isoelectric focusing (IEF) analysis; 293T cells lysate were separated by IEF, followed by western blotting using indicated antibodies. Relative LDH-A K5 acetylation and LDH-A protein levels for each spot were quantified by intensity, and the relative percentage of each spot is calculated and listed below the western blot panels.

(legend continued on next page)

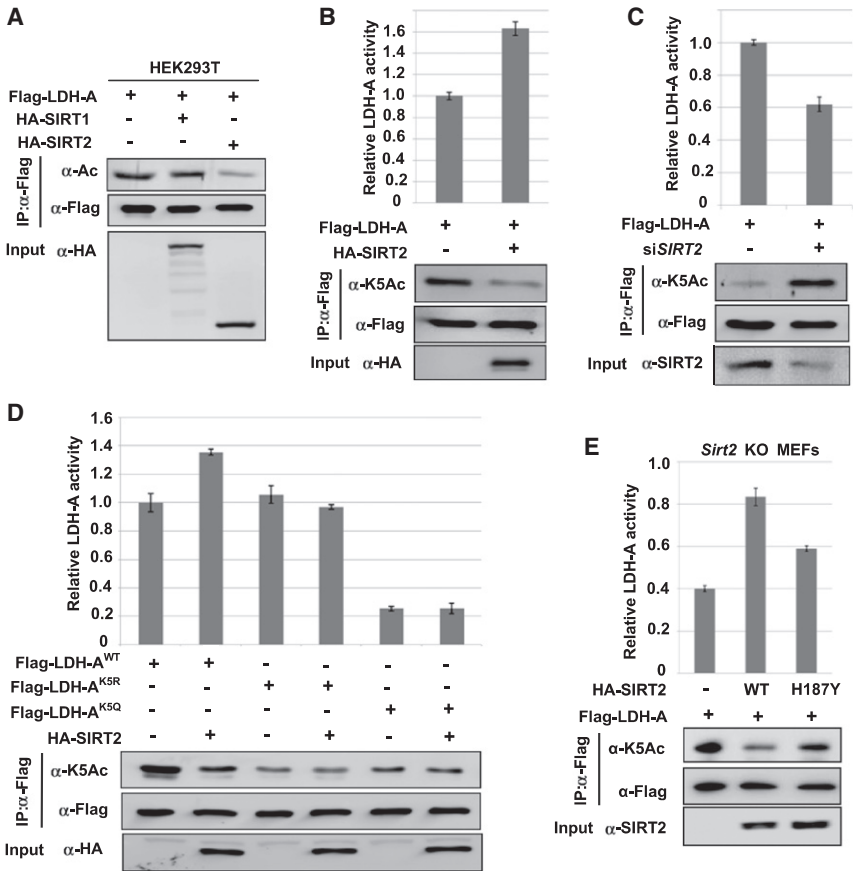

Figure 2. SIRT2 Deacetylates LDH-A at K5 and Increases LDH-A Activity

(A) SIRT2 overexpression decreases LDH-A acetylation. 293T cells were transfected with indicated plasmids and LDH-A acetylation was determined by western blotting.

(B) SIRT2 decreases K5 acetylation and increases LDH-A activity. 293T cells were transfected with indicated plasmids, Flag-LDH-A was immunoprecipitated, and LDH-A activity was assayed. LDH-A activity was normalized against protein levels. Relative enzyme activities of triplicated experiments ± SD are presented.

(C) *SIRT2* knockdown increases K5 acetylation and decreases LDH-A activity. 293T cells were transfected with indicated plasmids and *SIRT2* siRNA oligonucleotides. LDH-A was immunoprecipitated and activity was assayed. LDH-A acetylation at K5 was determined by western blotting. Relative enzyme activities of triplicate experiments ± SD are presented.

(D) SIRT2 overexpression increases the activity of wild-type, but not acetylation-deficient K5R or K5Q mutant LDH-A. 293T cells were transfected with indicated plasmids, followed by immunoprecipitation and enzyme assay. Relative enzyme activities of triplicate experiments ± SD are presented.

(E) The deacetylase activity of SIRT2 is required to increase LDH-A activity. *Sirt2* knockout MEFs were co-transfected with Flag-LDH-A and SIRT2 wild-type or the inactive mutant (H187Y). LDH-A was immunoprecipitated and enzyme activity was assayed. LDH-A activity was normalized against protein levels. Relative enzyme activities of triplicate experiments ± SD are presented.

See also Figure S2.

SIRT inhibitor NAM, but not HDAC inhibitor TSA, increased acetylation at K5 (Figure S2), indicating that a SIRT deacetylase is probably involved in K5 deacetylation. To identify the specific SIRT, we co-expressed LDH-A with the two cytosolic SIRT deacetylases, SIRT1 and SIRT2, and found that SIRT2, but not SIRT1, decreased LDH-A acetylation (Figures 2A and 2B). Supporting this observation, knocking down *SIRT2* significantly increased K5 acetylation (Figure 2C). Co-expression of SIRT2 increased the activity of the LDH-A by 63% along with the decreased lysine 5 acetylation (Figure 2B). Conversely, *SIRT2* knockdown decreased LDH-A activity by 38% (Figure 2C). Together, these observations demonstrate a specific and prominent role of SIRT2 in the deacetylation and enzyme activation of LDH-A.

We also found that SIRT2 co-expression had no significant effect on the activity of LDH-A^{K5Q} and LDH-A^{K5R} mutants (Figure 2D), indicating that SIRT2 stimulates LDH-A activity mostly via deacetylation of K5. Furthermore, re-expression of wild-type SIRT2, but not the inactive H187Y mutant, reduced LDH-A acetylation and increased LDH-A enzyme activity in *Sirt2* knockout MEFs (Figure 2E). Collectively, these data support a critical role of SIRT2 enzyme activity in LDH-A regulation by deacetylating lysine 5.

Acetylation at K5 Decreases LDH-A Protein Level

In addition to the effect on LDH-A enzyme activity, NAM and TSA treatment also led to a time-dependent reduction of LDH-A protein levels (Figures 3A and S3A). We then determined whether acetylation downregulating of LDH-A protein level occurs at or after transcription. Quantitative RT-PCR showed that NAM and TSA treatment had a minor effect on LDH-A mRNA levels (Figure S3B), indicating a posttranscriptional regulation of LDH-A

(G) K5Q mutant decreases LDH-A enzyme activity. Flag-tagged wild-type and mutant LDH-A protein were expressed in 293T cells and purified by immunoprecipitation. The enzyme activity was measured and normalized against protein level. Relative enzyme activities of triplicate experiments with ± SD are presented.

(H) NAM and TSA treatment decreases the enzyme activity of wild-type, but not mutant LDH-A. Flag-tagged wild-type and mutant LDH-A protein were expressed in 293T cells and treated with or without NAM and TSA, then purified by immunoprecipitation. The LDH-A enzyme activity was measured and normalized against protein level. Relative enzyme activities of triplicate experiments ± SD are presented.

(I) Acetylated LDH-A has lower enzyme activity. Recombinant un-acetylated and K5-acetylated LDH-A protein were prepared by the system of genetically encoding Nε-acetyllysine in *E. coli*. The enzyme activity was measured and normalized against protein level. Relative enzyme activities of triplicate experiments ± SD are presented.

See also Figure S1.

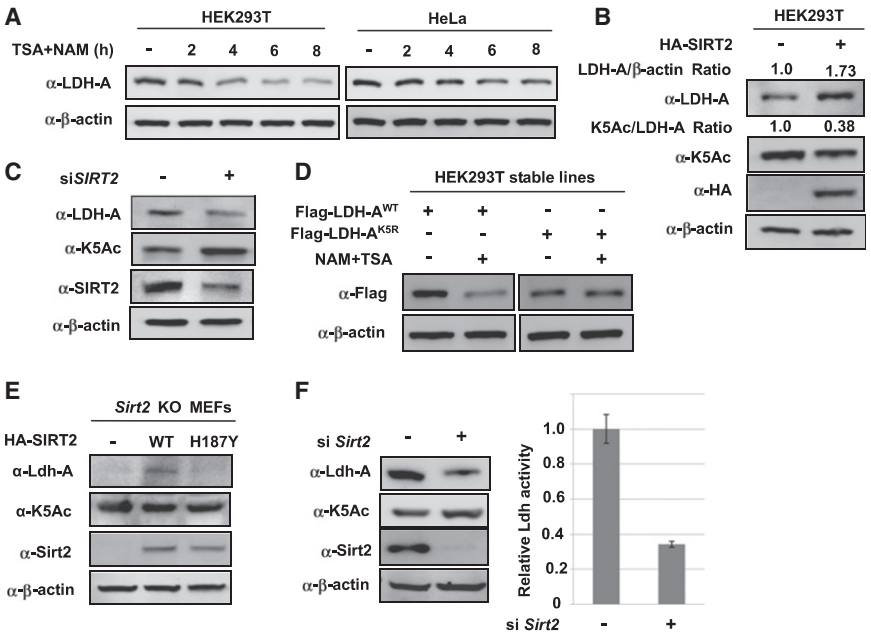

Figure 3. Acetylation at K5 Decreases LDH-A Protein Level

(A) NAM and TSA treatment decreases endogenous LDH-A protein level. 293T and HeLa cells were either untreated or treated with NAM and TSA for different lengths of time, as indicated. The steady-state levels of LDH-A protein were determined by western blotting and normalized against β-actin.

(B) SIRT2 overexpression decreases endogenous LDH-A K5 acetylation and increases LDH-A protein level. Plasmid expressing SIRT2 was transfected into 293T cells, and endogenous K5 acetylation and LDH-A expression level were determined by western blotting.

(C) *SIRT2* knockdown increases LDH-A K5 acetylation and decreases LDH-A protein level. siRNA oligo nucleotide targeting *SIRT2* was transfected into 293T cells and the levels of endogenous LDH-A K5-acetylation, total LDH-A protein, and SIRT2 protein were determined by western blotting.

(D) NAM and TSA treatment decreases the level of wild-type, but not K5R mutant LDH-A. 293T cells stably expressing wild-type and K5R mutant LDH-A were either untreated or treated with NAM and TSA. The levels of K5-acetylated and total LDH-A protein were determined by western blotting.

(E) SIRT2 deacetylase activity is required to increase LDH-A protein level. Wild-type or H187Y mutant SIRT2 was expressed in *Sirt2* knockout MEFs, and then endogenous Ldh-A protein level and acetylation at K5 were detected by WB.

(F) *SIRT2* knockdown decreases LDH-A activity and protein level in mouse liver. siRNA oligo-nucleotides targeting mouse *Sirt2* gene were injected into mouse tail vein and liver tissue was harvested to determine total LDH-A activity (left panel). SIRT2, LDH-A protein, and K5 acetylation were measured by western blotting (right panel). Error bars represent ± SD of triplicated experiments.

See also Figure S3.

protein by acetylation. To determine if acetylation could affect LDH-A protein level, we analyzed the effect of SIRT2 overexpression or knockdown on LDH-A protein. Overexpression of SIRT2 decreased LDH-A K5 acetylation and increased LDH-A protein in both 293T and pancreatic cancer cell line (Figures 3B and S3C). Conversely, *SIRT2* knockdown increased LDH-A acetylation and concomitantly decreased the steady-state level of LDH-A protein (Figure 3C). These results indicate that acetylation may decrease LDH-A protein. Furthermore, we found that inhibition of deacetylases decreased the level of wild-type, but not the K5R mutant (Figure 3D). Based on these results, we propose that acetylation of K5 destabilizes LDH-A protein.

Next, we investigated the function of SIRT2 in regulation of LDH-A protein levels. We observed that re-expression of the wild-type, but not the H187Y mutant SIRT2, increased LDH-A protein level in *Sirt2* knockout MEFs (Figure 3E). In addition, the relative K5 acetylation (the ratio of K5 acetylation over LDH-A protein level) was also reduced by expression of the wild-type, but not the H187Y mutant SIRT2. These data support the notion that the SIRT2 deacetylase activity plays a role in regulating LDH-A protein levels. To determine the function of SIRT2 in LDH-A regulation in vivo, we injected *Sirt2* siRNA into mice via the tail vein, and Sirt2 was efficiently reduced in the mouse livers by western blot analysis (Figure 3F). We found that Ldh-A protein levels and activity were significantly decreased. As expected, the relative K5 acetylation was increased in *Sirt2* knockdown livers (Figure 3F), indicating a critical function of SIRT2 in LDH-A regulation in vivo.

Acetylation Stimulates LDH-A Degradation by Chaperone-Mediated Autophagy

Inhibition of protein synthesis with cycloheximide (CHX) showed that LDH-A was a rather stable protein in HeLa cells with a half-life longer than 8 hr (Figure S4A). Treatment with the proteasome inhibitor MG132 did not increase LDH-A, but significantly increased the protein level of PEPCK (Figure 4A), a metabolic enzyme targeted by the proteasome for degradation (Jiang et al., 2011). These results indicate that the acetylation-induced decrease of LDH-A is mediated by a mechanism that is independent of proteasome.

Autophagy is a major mechanism in intracellular degradation. Macro-autophagy is believed to be a nonselective bulk degradation of intracellular components, whereas chaperone-mediated autophagy (CMA) is a selective degradation for proteins, especially those with a long half-life (Mizushima et al., 2008). We treated cells with leupeptin, an inhibitor of lysosomal proteases that can block lysosome-dependent protein degradation (Jeong et al., 2009), and found that this treatment caused a significant accumulation of LDH-A protein and K5 acetylation (Figure 4B), confirming the involvement of lysosome in acetylation-induced LDH-A degradation. Two-dimensional PAGE analysis showed that leupeptin blocked LDH-A degradation in cells treated with deacetylase inhibitors (Figure S4B). Costaining of LDH-A and lysosomal marker also indicated that a fraction of LDH-A was colocalized with the lysosomal marker LAMP1 (Figure S4C), consistent with a role of lysosome in LDH-A degradation.

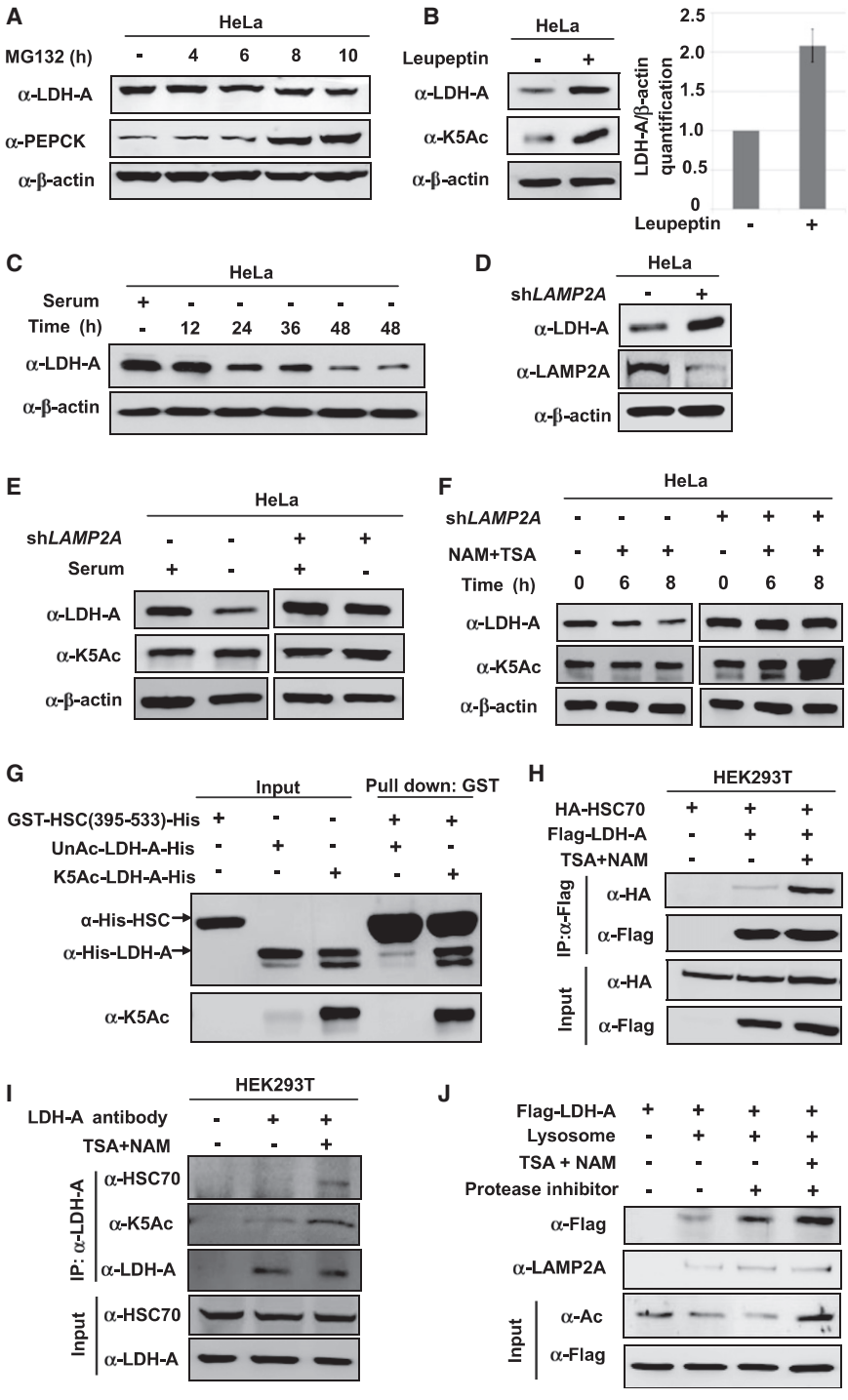

Figure 4. Acetylation Promotes LDH-A Degradation via CMA

(A) LDH-A is not degraded by the ubiquitin-proteasome system (UPS). HeLa cells were treated with a proteasome inhibitor MG132 and the LDH-A protein level was analyzed by western blotting. PEPCK, a known substrate of UPS, was included as a control.

(B) Leupeptin accumulates K5-acetylated and total LDH-A protein. HeLa cells were either untreated or treated with leupeptin for 48 hr. The levels of total and acetylated LDH-A were determined by western blotting. LDH-A level was normalized against β-actin. Error bars represent ± SD of triplicated experiments.

(C) Serum withdrawal decreases LDH-A protein. LDH-A level was determined by western blotting after serum withdrawal for different lengths of time, as indicated in HeLa cells.

(D) *LAMP2A* knockdown accumulates LDH-A. *LAMP2A* was stably knocked down in HeLa cells by shRNA. The knockdown efficiency and LDH-A protein level were determined by western blotting.

(E and F) *LAMP2A* knockdown blocks the effect of serum deprivation or NAM and TSA treatment on LDH-A protein levels. HeLa cell pools stably expressing *LAMP2A* shRNA were cultured with or without serum (E) or NAM and TSA (F). The levels of K5-acetylated and total LDH-A protein were determined by western blotting.

(G) Acetylation at K5 increases LDH-A binding to the HSC70 C-terminal domain in vitro. Recombinant unacetylated and K5-acetylated LDH-A protein were prepared by the system of genetically encoding Nε-acetyllysine in *E. coli*. GST-HCS70 C-terminal domain (from 395 to 533 amino acids) was used in an in vitro binding assay to pulldown the purified LDH-A.

(H and I) Inhibition of deacetylases increases overexpressed or endogenous LDH-A-HSC70 binding. Indicated plasmids were co-transfected into 293T cells, followed by NAM and TSA treatment. LDH-A-HSC70 binding was determined by immunoprecipitation-western analysis (H). The 293T cells were untreated or treated with NAM and TSA (I). Endogenous LDH-A-HSC70 binding was determined by immunoprecipitation and western blot analysis.

(J) Inhibition of deacetylases promotes lysosomal uptake of LDH-A. Flag-tagged LDH-A was immunopurified from 293T cells untreated or treated with deacetylase inhibitors TSA and NAM. The immunoprecipitated LDH-A was incubated with the lysosomes isolated from rat liver. Lysosomes were re-isolated and the associated LDH-A (either inside or binding to the surface) were determined by western blotting.

See also Figure S4.

Prolonged serum starvation is known to activate CMA (Cuervo et al., 1995; Wing et al., 1991). We found that serum starvation caused a decrease of the steady-state level of LDH-A (Figure 4C), providing additional evidence for a CMA-dependent degradation of LDH-A. To rule out macro-autophagy in LDH-A degradation, we compared the subcellular localization of LDH-A with GFP-LC-3, which is a marker for autophagosome in the macro-autophagy pathway. As shown in Figure S4D, GFP-LC3 and LDH-A showed different subcellular localizations. Moreover, we determined LDH-A protein level in *Atg5* knockout MEF cells, which is defective in macro-autophagy, and found that LDH-A protein levels were comparable in *Atg5* wild-type and knockout MEF cells (Figure S4E).These data indicate that CMA, but not macro-autophagy, is responsible for LDH-A degradation.

During CMA, the HSC70 chaperone carries target proteins to the lysosomal receptor LAMP2A, which then translocates the target proteins into lysosome for degradation (Cuervo, 2010). To provide additional evidence for the role of CMA in LDH-A degradation, we found that *LAMP2A* knockdown significantly increased LDH-A protein (Figure 4D). Moreover, *LAMP2A* knockdown also blocked the LDH-A protein reduction caused by either serum starvation (Figure 4E) or inhibition of deacetylases (Figure 4F). These data support a model that acetylation promotes CMA-dependent degradation of LDH-A.

To explore the role of K5 acetylation in LDH-A degradation by CMA, we examined the interaction between LDH-A and HSC70. Co-immunoprecipitation showed that the acetylation mimetic K5Q mutant displayed a much stronger interaction with HSC70 than the wild-type LDH-A (Figure S4G). Fully acetylated or unacetylated recombinant LDH-A was prepared by the system of genetically encoded Nε-acetyllysine in *E. coli*, and their interaction with HSC70 was examined. The acetylated, but not the unacetylated, LDH-A could readily pull down endogenous HSC70 (Figure S4F). The C-terminal domain (amino acid residues 395–533) is the substrate binding domain of HSC70. We prepared recombinant HSC70 C-terminal domain and found it to preferentially pull down acetylated but not unacetylated LDH-A (Figure 4G). Consistently, treatment of cells with deacetylase inhibitors TSA and NAM significantly increased the binding between either ectopically expressed (Figure 4H) or endogenous LDH-A and HSC70 (Figure 4I). Collectively, these data demonstrate that LDH-A acetylation, in particular at lysine 5, promotes its interaction with HSC70.

To determine directly if LDH-A could be taken up by lysosomes, we incubated the immunopurified LDH-A with isolated lysosomes in vitro. The results showed LDH-A binding to isolated lysosomes (Figure 4J). When lysosomal protease was inhibited, more LDH-A was found with lysosome, presumably due to the accumulation of intralysosomal LDH-A. Notably, the LDH-A isolated from TSA- and NAM-treated cells showed more lysosomal binding/up-taken than LDH-A isolated from untreated cells. These data are consistent with a model that LDH-A acetylation increases its interaction with HSC70, binding to and being taken up by the lysosomes, and leading to its eventual degradation.

K5 Acetylation Impairs the Function of LDH-A in Supporting Cell Proliferation and Migration

Elevated LDH-A protein levels are frequently seen in different types of tumors (Goldman et al., 1964). LDH-A is essential for cancer cell growth in vitro and in vivo (Fantin et al., 2006; Xie et al., 2009). We therefore investigated the effect of K5 acetylation of LDH-A on cell proliferation and migration. We knocked down endogenous *LDH-A* in the BxPC-3 pancreatic cancer cell line by shRNA and re-expressed shRNA-resistant wild-type and K5Q mutant LDH-A to a level similar to endogenous LDH-A (Figure 5A). Consistent with a previous report (Fantin et al., 2006), knocking down *LDH-A* caused a significant decrease of BxPC-3 cell proliferation that was substantially rescued by the re-expression of the wild-type LDH-A (Figure 5B). Notably, the LDH-A^{K5Q} mutant was much less effective than the wild-type LDH-A in restoring *LDH-A*—knocking down cell proliferation. Similar effects were observed in 293 cells (Figure S5A). These results demonstrate that acetylation at Lys 5, which reduces the activity of LDH-A, impairs the ability of LDH-A in supporting BxPC-3 pancreatic cancer cell proliferation.

We then investigated the effect of LDH-A^{K5Q} mutant on cell migration. Knockdown of *LDH-A* decreased cell migration in BxPC-3 (Figure 5C), 293, and 293T cells (Figures S5B and S5C), as determined by the wound-healing assay. Re-expression of wild-type, but not the K5Q mutant LDH-A restored cell migration, indicated that the acetylation at lysine-5 of LDH-A inhibits tumor cell migration.

LDH catalyzes the reversible conversion of pyruvate to lactate with LDH-A and LDH-B kinetically favoring the forward and the backward reactions, respectively (Ross et al., 2010). To confirm that the impaired ability of LDH-A K5Q mutant in supporting BxPC-3 cell proliferation and migration is due to its reduced catalytic activity, we measured pyruvate and lactate concentration in *LDH-A* knocking down cells that were re-introduced with either wild-type or K5Q mutant LDH-A. We found that the ratio of lactate to pyruvate was decreased by nearly one-half that of both intracellular (upper panel) and extracellular (low panel) levels in cells expressing K5Q mutant compared to cells expressing the wild-type LDH-A (Figure 5D). These results suggest LDH-A acetylation plays an important role in regulating the conversion of pyruvate to lactate.

It has been reported that lactate could drive cell migration (Bonuccelli et al., 2010; Végran et al., 2011). Therefore, we also determined the effect of lactate on migration in BxPC-3 cells. Consistently, we found that lactate promoted BxPC-3 cell migration (Figure S5D). These data indicate that K5 acetylation of LDH-A decreases lactate production, thereby restraining BxPC-3 pancreatic cancer cell migration.

To address the biologic significance of K5 acetylation in tumor growth, we performed xenograft experiments using the BxPC-3 stable cell lines with *LDH-A* knockdown and re-expression of shRNA-resistant wild-type or K5Q mutant LDH-A. As shown in Figures 5E and 5F, the K5Q mutant-expressing BxPC-3 cells displayed tumor growth significantly slower than the wild-type LDH-A-expressing cells. Taken together, these data indicate that LDH-A K5 acetylation impairs its function in catalyzing pyruvate to lactate conversion, and then inhibits cell proliferation and tumor growth.

K5 Acetylation of LDH-A Is Downregulated in Pancreatic Cancer

Pancreatic ductal adenocarcinoma cancer (PDAC) is the fourth leading cause of cancer death, with less than 5% 5 year survival after diagnosis. Pharmacologic inhibition of LDH-A has been reported to suppress the progression of pancreatic tumors in a xenograft model (Le et al., 2010). The finding that acetylmimetic substitution at lysine-5 impairs the ability of LDH-A to support BxPC-3 pancreatic cancer cell proliferation and tumor growth prompted us to examine both the K5 acetylation and total LDH-A protein in human cancers. We collected a total of 127 primary human pancreatic cancer samples, including 65 pairs that had surrounding normal pancreatic ducts tissues. We first carried out a direct immunoblotting analysis of a panel of 19 pairs of primary pancreatic tumors (T) and their adjacent normal tissues (N), for which we were able to obtain sufficient amounts of proteins. This analysis revealed that, when compared to normal pancreatic tissues, eight pairs showed a significant

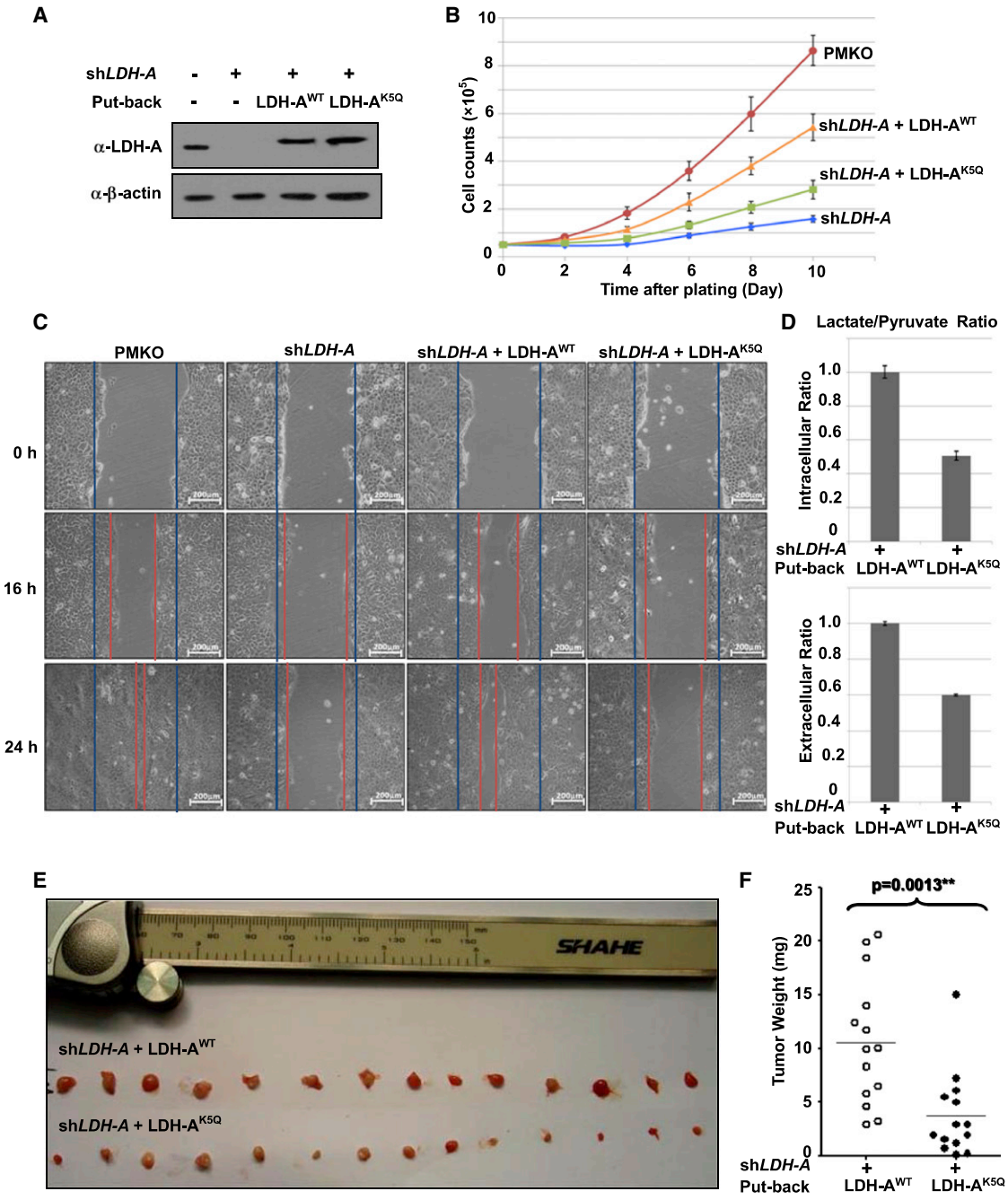

Figure 5. Acetylation Mimetic LDH-A^{K5Q} Mutant Has Reduced Ability to Support Cell Proliferation and Cell Migration

(A) Generation of LDH-A-expressing BxPC-3 stable cell lines. BxPC-3 cells stably knockdown *LDH-A* and re-express the shRNA-resistant wild-type or K5Q mutant were established. *LDH-A* knockdown efficiency and re-expression were determined by western blotting.

(B) LDH-A^{K5Q} is compromised to support cell proliferation. LDH-A^{WT} or LDH-A^{K5Q} cells were seeded in each well. Cell numbers were counted every 48 hr. Error bars represent cell numbers ± SD for triplicate experiments.

(C) LDH-A^{K5Q} mutant is compromised to support cell migration. BxPC-3 cells as described in panel A were analyzed for migration by a wound-healing assay. Scale bars are 200 μm.

(D) LDH-A^{K5Q} decreases intracellular and extracellular lactate/pyruvate ratio. LDH-A^{WT} or LDH-A^{K5Q}cells were seeded in each well. Intracellular or extracellular pyruvate and lactate production were measured according to manufacturer's protocol (BioVision). Error bars represent ± SD for triplicate experiments.

(E and F) LDH-A^{K5Q} is defective in supporting tumor growth in vivo. Xenograft was performed using the BxPC-3 stable cell lines with *LDH-A* knockdown and re-expression of shRNA-resistant wild-type or K5Q mutant LDH-A as indicated. Seven weeks later, mice were sacrificed and tumor weight was measured. The p value was calculated by paired t test.

See also Figure S5.

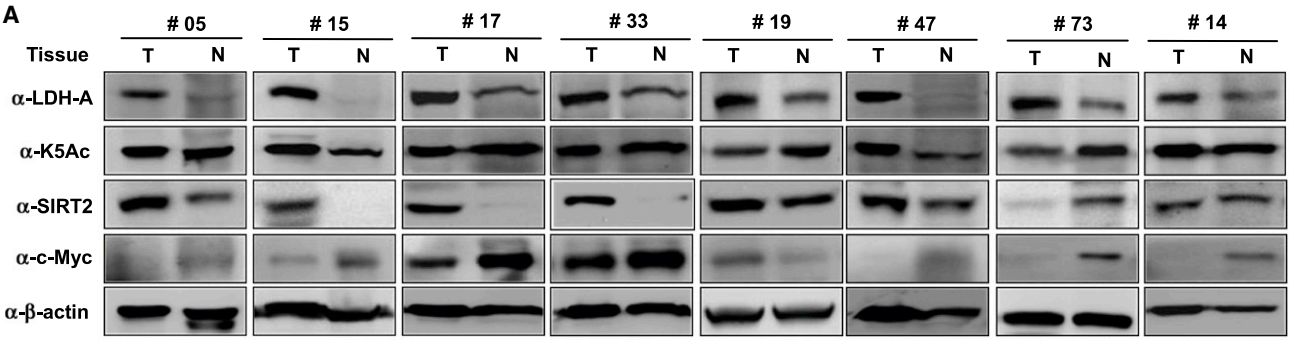

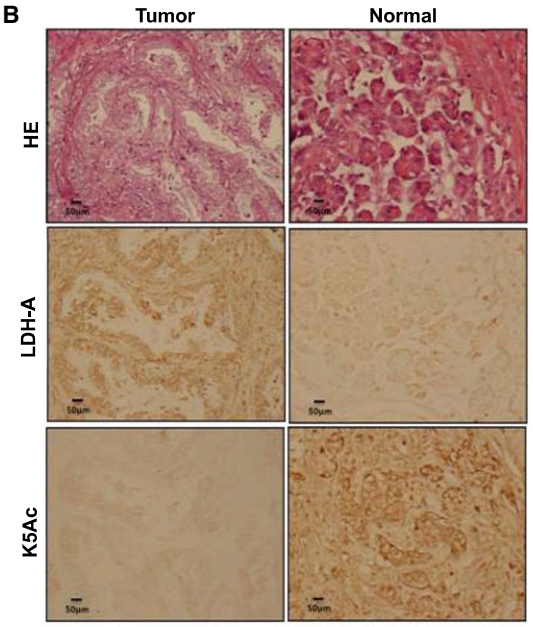

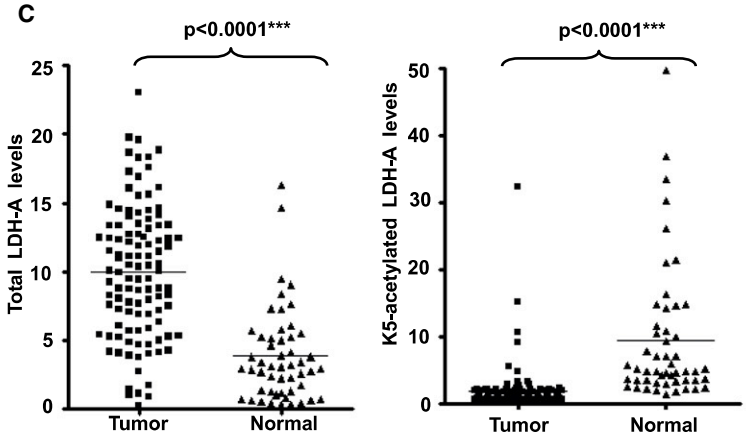

Relative Value	Total LDH-A	K5Ac LDH-A	K5Ac /total LDH-A
Tumor (n = 108)	10.00 ± 0.46	12.11 ± 0.49	1.98 ± 0.34
Normal (n = 51)	3.85 ± 0.47	16.99 ± 0.72	9.54 ± 1.43
t test	p < 0.0001	p < 0.0001	p < 0.0001

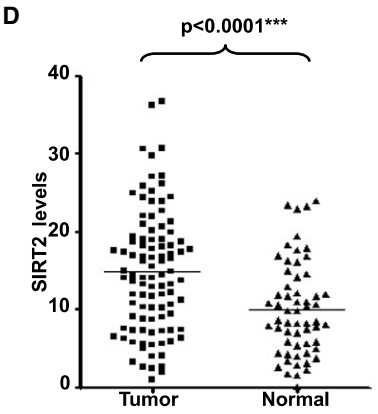

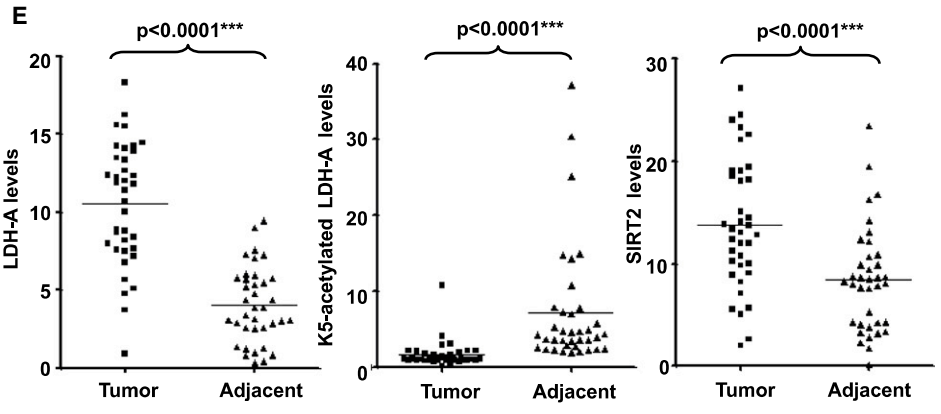

Relative Value	SIRT2
Tumor (n = 99)	14.85 ± 0.78
Normal (n = 59)	10.09 ± 0.78
t test	p < 0.0001

Relative Value	Total LDH-A	K5Ac LDH-A	K5Ac /total LDH-A	SIRT2
Tumor (n = 37)	10.52 ± 0.64	12.96 ± 0.70	1.64 ± 0.28	13.75 ± 1.04
Adjacent (n = 37)	4.09 ± 0.40	16.30 ±0.52	7.23 ±1.32	8.42 ± 0.84
Paired *t* test	p < 0.0001	p < 0.0001	p < 0.0001	p < 0.0001

(legend on next page)

increase of the steady-state levels of total LDH-A protein without a corresponding increase of K5 acetylation (Figure 6A). Therefore, these eight pairs of tumor samples had a decreased ratio of K5-acetylated versus total LDH-A proteins. Quantification of six pairs (two pairs exhibiting levels of LDH-A in the normal tissues too low to be reliably quantified) confirmed that both the increase of total LDH-A ($p < 0.0001$) and the decrease in the ratio of K5-acetylated LDH-A versus total LDH-A proteins ($p = 0.0031$) in tumor cells are statistically significant (Figure S6A). Of the remaining 11 pairs, the total LDH-A protein was increased in four pairs, unchanged in four pairs, and decreased in three pairs in tumor tissues when compared to the adjacent normal tissues (Figure S6B). The ratio of K5-acetylated versus total LDH-A was not significantly decreased in these 11 pairs.

C-Myc has been implicated in transcription regulation of many metabolic genes, including LDH-A (Shim et al., 1997). We also examined c-Myc protein levels in these 19 pairs of pancreatic tissues. However, we did not find an increase of c-Myc in pancreatic tumor tissues or a positive correlation between c-Myc and LDH-A protein levels (Figures 6A and S6B). Therefore, the reduced LDH-A K5 acetylation correlates with the increased LDH-A protein levels in the pancreatic tumors.

To substantiate the finding that K5-aetylated LDH-A is significantly decreased in some pancreatic tumors, we explored the feasibility of determining the level of both total and K5-acetylated LDH-A by immunohistochemistry in paraffin-embedded tissues to expand our study. The anti-acetyl-LDH-A(K5) antibody was characterized by its suitability for immunohistochemistry. We found that this antibody could detect strong signals that were specifically blocked by the acetyl-K5 antigen peptide in paraffin-embedded tissues (Figure S6C). Taking the advantage of this reagent, we then performed immunohistochemistry in 108 pancreatic cancer samples, including 46 samples that had the adjacent normal pancreatic ducts tissues. In most samples, we observed that the levels of total LDH-A were higher and the levels of relative K5-acetylated LDH-A were lower in the tumor tissues than in the adjacent normal tissues (Figure 6B). Statistical analyses of quantified images indicated that the differences between tumor and normal tissues in total LDH-A protein levels ($p < 0.0001$), in K5-acetylated LDH-A ($p < 0.0001$), and in the ratio of K5-acetylated LDH-A versus total LDH-A proteins ($p < 0.0001$) are all highly significant, comparing either the 108 tumor samples to the 51 normal pancreatic ducts samples (Figure 6C), or the 46 tumor samples with their adjacent normal tissues (Figure S6D). We also found that SIRT2 expression was increased in pancreatic tumor tissues compared to adjacent normal tissues (Figures 6A, 6D, and S6E).

Although more than 100 case tumors were collected, most pancreatic tumors are very small, and the number of paired paraffin sections with both tumor and adjacent on the same slide is hence limited. We determined the levels of LDH-A, K5-acetylated LDH-A, and SIRT2 in only 39 paired tissues. Among these pairs, high LDH-A protein level is found in 37 pairs of tumor compared with adjacent tissue. These tumors also exhibited increased SIRT2 and decreased acetylation at K5 as shown in Figure 6E. The tumor sample analyses demonstrate that LDH-A protein levels have a negative correlation with K5 acetylation and a positive correlation with SIRT2 levels in pancreatic tumors. These data also indicate that LDH-A and K5 acetylation may be potential biomarkers for pancreatic tumor.

The development of pancreatic cancer can be divided into five stages according to their location, size, and metastatic features: stage 0 (carcinoma in situ found in the lining of the pancreas), stage I (found only in pancreas with size smaller [IA] or larger [IB] than 2 cm), stage II (spread to nearby tissue, either including [IIB] or excluding [IIA] the lymph nodes), stage III (spread to major blood vessels near the pancreas), and stage IV (spread to distant organs). To determine whether LDH-A K5-acetylation level is related to the pancreatic tumor progression, we analyzed the levels of K5-acetylated as well as total LDH-A in the panel of 108 pancreatic tumors according to their stages. LDH-A protein level was significantly increased in all cancer stages when compared to normal tissues (Figure S6F, left panel), but no significant difference was detected between different stages (Figure S6G). The levels of K5-acetylated LDH-A were decreased significantly in all cancer stages when compared to normal tissues (Figure S6F, right panel), and there appeared to be a progressive decrease in the levels of K5-acetylated LDH-A from stage IA to stage IB ($p = 0.009$) and then to stage IIA ($p = 0.0068$ versus IA, Figure S6H). There was no significant difference in the levels of K5-acetylated LDH-A among stages IIA, IIB, III, and IV. Taken together, these data suggest a possible role of K5 acetylation contributing to pancreatic cancer initiation, but not progression to the advanced stages.

Figure 6. K5-Acetylation of LDH-A Is Downregulated in Pancreatic Cancer

(A) Total LDH-A and SIRT2 protein are increased and K5-acetylated LDH-A decreased in pancreatic cancer tissues compared to adjacent tissues. The levels of LDH-A protein, K5 acetylation, SIRT2, and c-Myc in 19 pairs of pancreatic cancer and adjacent normal tissues were analyzed by western blotting. Eight pairs that exhibited clear inverse correlation between K5-acetylated and total LDH-A and positive correlation between SIRT2 and total LDH-A are shown. See also Figure S6A for the complete western blotting of the other 11 pairs.

(B and C) Immunohistochemical stainings of K5-acetylated and total LDH-A proteins in tumor and adjacent normal tissues. One example is shown in (B) and the statistical analysis of all samples is shown in (C). Scale bars are 50 μm. The intensities of the total (left panel) and K5-acetylated (right panel) LDH-A proteins were quantified using the Motic Images Advanced software, followed by statistical analysis. A total of 108 pancreatic cancer tissues and 51 adjacent normal pancreatic tissues were analyzed. The mean value of multiple samples and standard deviation are presented.

(D) Immunohistochemical staining of SIRT2 proteins in tumor and adjacent normal pancreatic cancer tissues. The statistical analysis of 99 tumor and 59 normal samples is shown. The intensities of SIRT2 proteins were quantified using the Motic Images Advanced software, followed by statistical analysis. The mean value of multiple samples and standard deviation is presented.

(E) LDH-A protein levels show negative correlation with K5 acetylation, and positive correlation with SIRT2 protein in pancreatic tumors. Among the 39 paired pancreatic cancer tissues that had been examined for all three signals (LDH-A, K5Ac, and SIRT2), 37 cases showed high LDH-A protein levels in tumors compared with adjacent tissues. These tumors also exhibited increased SIRT2 and decreased acetylation at K5.

See also Figure S6.

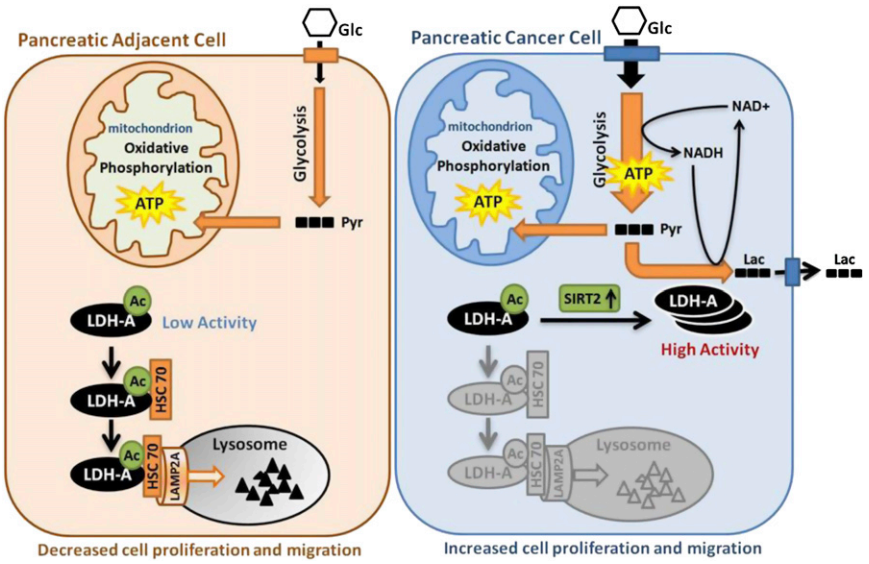

Figure 7. Working Model
Acetylation at K5 inhibits LDH-A enzyme activity and promotes its lysosomal degradation via CMA. In pancreatic cancer tissues, SIRT2 deacetylates LDH-A and increases its activity and protein level, thereby accelerating glycolysis and lactate production, leading to increased cell proliferation and migration. Glc, glucose; Pyr, pyruvate; Lac, lactate; Ac, acetylation.

DISCUSSION

Reprogramming of energy metabolism, including elevated glycolysis, is a hallmark of cancer (Hanahan and Weinberg, 2011). To support rapid cell growth, glucose uptake and metabolic intermediates for macromolecule biosynthesis are dramatically increased in cancer cells. In particular, glycolysis is highly elevated. Among the glycolytic enzymes, LDH is unique because it is essential to maintain high glycolysis rate by regenerating NAD+ required in early steps in glycolysis (Bui and Thompson, 2006). Moreover, LDH channels pyruvate to lactate instead of converting it to acetyl-CoA for oxidative phosphorylation, a commonly observed phenomenon in many tumor cells. In this study, we uncovered a mechanism of LDH-A regulation that contributes to its increased protein level and activity to meet the elevated lactate production in tumor cells (Figure 7). We demonstrate that acetylation at K5 inhibits LDH-A enzyme activity and promotes its lysosomal degradation via CMA. In pancreatic cancer tissues, SIRT2 deacetylates LDH-A and increases its activity and protein level, thereby accelerating glycolysis and lactate production, leading to increased cell proliferation and migration.

LDH-A upregulation is commonly observed in cancers. This is in part due to transcriptional activation by the increased Myc and HIF in cancers. In this study, we report another mechanism in regulation of LDH-A protein levels. Acetylation plays an important role in posttranslational regulation of LDH-A by two mechanisms. First, acetylation directly inhibits LDH-A enzymatic activity. Second, acetylation stimulates CMA-mediated degradation of LDH-A. Notably, the relative acetylation of LDH-A is reduced in pancreatic cancer. We propose that the decreased LDH-A acetylation in cancer cells may contribute to the elevated LDH-A protein levels and activity as well as tumorigenesis (Figure 7).

A key step in CMA regulation is the interaction between chaperone HSC70 and target proteins. It has been reported that posttranslation modifications can regulate this process (Cuervo, 2010). For LDH-A, acetylation enhances the interaction between LDH-A and HSC70 (Figure 7). We show that HSC70 selectively interacts with acetylated proteins and thereby preferentially promotes lysosome-dependent degradation of the acetylated LDH-A. The three-dimensional structure of LDH indicates that lysine 5 is located in the N-terminal alpha-helix region of LDH-A, which is structurally separated from the catalytic domain (Read et al., 2001). Therefore, the K5-containing helix can be available for interaction with other proteins. Chaperone normally interacts with unfolded proteins that often have an exposed hydrophobic surface. It is conceivable that lysine acetylation increases surface hydrophobicity of the K5 helix in LDH-A and therefore promotes its interaction with the HSC70 chaperone. Further structural studies will be needed to obtain a precise understanding of how HSC70 recognizes acetylated target proteins.

Fantin and colleagues reported that LDH-A knockdown could inhibit tumor cell proliferation, especially under hypoxia (Fantin et al., 2006). A unique feature of LDH-A is that it acts at the end of the glycolytic pathway and catalyzes pyruvate to produce lactate, which is often accumulated in cancer cells (Figure 7). Many studies have shown that lactate can condition the microenvironment, which promotes interaction between cancer cells and stromal cells, eventually resulting in cancer cell invasion. Indeed, the ratio of lactate to pyruvate is significantly decreased in the acetylation mimetic K5Q mutant-expressing cells. Moreover, K5Q mutant is compromised in its ability to support proliferation and migration of BxPC-3 cells, most likely due to the decreased LDH-A activity. This may potentially explain why cancer cells have reduced LDH-A acetylation and increased LDH-A protein levels.

We observed that LDH-A expression positively correlates with SIRT2 expression in pancreatic cancer tissues, suggesting that SIRT2 may have oncogenic function in pancreatic cancer. However, SIRT2 has been reported as a tumor suppressor gene in a knockout mouse model (Kim et al., 2011). Notably, SIRT1 has been also suggested to act as both tumor promoter and suppressor in a context-dependent manner. Therefore, it is possible that SIRT2 may promote tumor growth under one circumstance, such as in human pancreatic cancer, and suppress tumor growth under another circumstance, such as hepatocellular carcinoma in *Sirt2* knockout mice. A noticeable difference in these two systems is that SIRT2 expression is increased at the initial stage of pancreatic cancer while the mouse model has a complete deletion even before tumor

development. Therefore, the functions of both SIRT1 and SIRT2 in cancer development may be context-dependent.

Previous studies have indicated an important role of LDH-A in tumor initiation and progression (Koukourakis et al., 2006; Le et al., 2010). LDH-A overexpression in pancreatic β cells led to increased mitochondrial membrane potential in many carcinomas (Ainscow et al., 2000; Chen, 1988). We showed that LDH-A is significantly increased in pancreatic cancer tissues compared to adjacent normal tissues. Consistently, LDH-A K5 acetylation was significantly decreased in pancreatic cancer tissues but not further increased during late stage tumor progression, indicating that LDH-A acetylation at K5 may play a role in pancreatic cancer initiation. Our study indicates an important mechanism of LDH-A regulation by acetylation and LDH-A K5 acetylation as a potential pancreatic cancer initiation marker.

EXPERIMENTAL PROCEDURES

LDH-A Enzyme Assay

Flag-LDH-A was ectopically expressed, immunoprecipitated, and eluted using 250 μg/ml of Flag peptide. The eluent was added to a reaction buffer containing 0.2M Tris-HCl (pH 7.3), 30 mM pyruvate, and 6.6 mM NADH. The change in absorbance (340 nm) resulting from NADH oxidation was measured using a F-4600 fluorescence spectrophotometer (HITACHI).

Genetically Encoding Nε-Acetyllysine in Recombinant Proteins

To generate a homogenously K5-acetylated LDH-A construct, we used a three-plasmid system as described (Neumann et al., 2008, 2009). This system allows for the site-specific incorporation of N-acetyllysine by way of a *Methanosarcina barkeri* acetyl-lysyl-tRNA synthetase/tRNACUA pair that responds to the amber codon. We cloned wild-type LDH-A into pTEV-8 (pET-21b as backboned with TEV cleavage site) producing a C-terminal His6-tagged construct, and incorporated an amber codon at lysine 5 (AAG to TAG by site-directed mutagenesis). Cells were induced at an OD600 of 0.6 with 0.5 mM IPTG. The amber construct was overexpressed in LB with spectinomycin (50 μg/ml), kanamycin (50 μg/ml), and ampicillin (150 μg/ml), in addition to 2 mM N-acetyllysine (Sigma-Aldrich) and 20 mM nicotinamide at the time of induction. Both LDH-A and K5-acetylated LDH-A protein are purified for enzyme activity analysis.

Pancreatic Cancer Model by Xenograft

BxPC-3 stable cell lines with *LDH-A* knockdown and re-expressed shRNA resistant wild-type or K5Q mutant LDH-A were prepared; 7.5×10^6 cells in PBS were subcutaneously injected into each of 14 nude mice, purchased from SLAC. Shanghai. Every mouse was injected LDH-A^{WT} cells on left side and LDH-A^{K5Q} on right side. Seven weeks later, all mice were sacrificed and tumors were harvested, followed by photography and weighing. The animal protocols were approved by the Animal Welfare Committee of Shanghai Medical College, Fudan University.

Pancreatic Tumor Samples and Immunohistochemistry

Pancreatic tumor samples were acquired from Affiliated Shanghai Tenth People's Hospital of Tongji University. A physician obtained informed consent from the patients. The procedures related to human subjects were approved by Ethic Committee of the Institutes of Biomedical Sciences (IBS), Fudan University. Immunohistochemistry (IHC) was performed as previously described (Lei et al., 2006). To quantify the IHC result of positive staining, the tissue areas of five ducts (173 μm^2) in each sample were microscopically examined and analyzed by an experienced pathologist. Images were captured using a charge-coupled device camera and analyzed using Motic Images Advanced software (version 3.2, Motic China Group). Average of staining score was calculated by dividing the positive areas with total areas. Data obtained were expressed as mean values ± SD. Differences were considered significant if the p value was less than 0.05.

SUPPLEMENTAL INFORMATION

Supplemental Information includes six figures and Supplemental Experimental Procedures and can be found with this article online at http://dx.doi.org/10.1016/j.ccr.2013.02.005.

ACKNOWLEDGMENTS

We thank the members of the Fudan MCB laboratory for discussions throughout this study. We also thank Dr. Liming Wei for IEF assay. This work was supported by the Chinese Ministry of Sciences and Technology 973 (grant nos. 2009CB918401, 2011CB910600, and NCET-09-0315), the NSFC (grant nos. 31271454 and 81225016), NSFC-NIH (grant no. 81110313), the 100 Talents Program of Shanghai Health, the Scholar of "Dawn" Program of Shanghai Education Commission, Shanghai Outstanding Academic Leader, and the Shanghai Key basic research program (12JC1401100) to Q.Y.L.; NIH grants (to Y.X. and K.L.G.); and Fudan University Medical School Graduate Student Ming Dao Project funds (to D.Z.). This work was also supported by the Chinese Ministry of Education 985 Program. This work is dedicated to the memory of Zhen Yu, who prepared the K5 acetylation antibody. Y.-H.X. and Q.-Y.L. are members of the Chinese Hippo Consortium.

Received: May 22, 2012
Revised: December 7, 2012
Accepted: February 6, 2013
Published: March 21, 2013

REFERENCES

Ainscow, E.K., Zhao, C., and Rutter, G.A. (2000). Acute overexpression of lactate dehydrogenase-A perturbs beta-cell mitochondrial metabolism and insulin secretion. Diabetes *49*, 1149–1155.

Avalos, J.L., Bever, K.M., and Wolberger, C. (2005). Mechanism of sirtuin inhibition by nicotinamide: altering the NAD(+) cosubstrate specificity of a Sir2 enzyme. Mol. Cell *17*, 855–868.

Bonuccelli, G., Tsirigos, A., Whitaker-Menezes, D., Pavlides, S., Pestell, R.G., Chiavarina, B., Frank, P.G., Flomenberg, N., Howell, A., Martinez-Outschoorn, U.E., et al. (2010). Ketones and lactate "fuel" tumor growth and metastasis: Evidence that epithelial cancer cells use oxidative mitochondrial metabolism. Cell Cycle *9*, 3506–3514.

Bui, T., and Thompson, C.B. (2006). Cancer's sweet tooth. Cancer Cell *9*, 419–420.

Chen, L.B. (1988). Mitochondrial membrane potential in living cells. Annu. Rev. Cell Biol. *4*, 155–181.

Choudhary, C., Kumar, C., Gnad, F., Nielsen, M.L., Rehman, M., Walther, T.C., Olsen, J.V., and Mann, M. (2009). Lysine acetylation targets protein complexes and co-regulates major cellular functions. Science *325*, 834–840.

Cuervo, A.M. (2010). Chaperone-mediated autophagy: selectivity pays off. Trends Endocrinol. Metab. *21*, 142–150.

Cuervo, A.M., Knecht, E., Terlecky, S.R., and Dice, J.F. (1995). Activation of a selective pathway of lysosomal proteolysis in rat liver by prolonged starvation. Am. J. Physiol. *269*, C1200–C1208.

Ekwall, K., Olsson, T., Turner, B.M., Cranston, G., and Allshire, R.C. (1997). Transient inhibition of histone deacetylation alters the structural and functional imprint at fission yeast centromeres. Cell *91*, 1021–1032.

Fantin, V.R., St-Pierre, J., and Leder, P. (2006). Attenuation of LDH-A expression uncovers a link between glycolysis, mitochondrial physiology, and tumor maintenance. Cancer Cell *9*, 425–434.

Furumai, R., Komatsu, Y., Nishino, N., Khochbin, S., Yoshida, M., and Horinouchi, S. (2001). Potent histone deacetylase inhibitors built from trichostatin A and cyclic tetrapeptide antibiotics including trapoxin. Proc. Natl. Acad. Sci. USA *98*, 87–92.

Goldman, R.D., Kaplan, N.O., and Hall, T.C. (1964). Lactic Dehydrogenase in Human Neoplastic Tissues. Cancer Res. *24*, 389–399.

Hanahan, D., and Weinberg, R.A. (2011). Hallmarks of cancer: the next generation. Cell *144*, 646–674.

Jeong, H., Then, F., Melia, T.J., Jr., Mazzulli, J.R., Cui, L., Savas, J.N., Voisine, C., Paganetti, P., Tanese, N., Hart, A.C., et al. (2009). Acetylation targets mutant huntingtin to autophagosomes for degradation. Cell *137*, 60–72.

Jiang, W., Wang, S., Xiao, M., Lin, Y., Zhou, L., Lei, Q., Xiong, Y., Guan, K.L., and Zhao, S. (2011). Acetylation regulates gluconeogenesis by promoting PEPCK1 degradation via recruiting the UBR5 ubiquitin ligase. Mol. Cell *43*, 33–44.

Kim, S.C., Sprung, R., Chen, Y., Xu, Y., Ball, H., Pei, J., Cheng, T., Kho, Y., Xiao, H., Xiao, L., et al. (2006). Substrate and functional diversity of lysine acetylation revealed by a proteomics survey. Mol. Cell *23*, 607–618.

Kim, H.S., Vassilopoulos, A., Wang, R.H., Lahusen, T., Xiao, Z., Xu, X., Li, C., Veenstra, T.D., Li, B., Yu, H., et al. (2011). SIRT2 maintains genome integrity and suppresses tumorigenesis through regulating APC/C activity. Cancer Cell *20*, 487–499.

Koppenol, W.H., Bounds, P.L., and Dang, C.V. (2011). Otto Warburg's contributions to current concepts of cancer metabolism. Nat. Rev. Cancer *11*, 325–337.

Koukourakis, M.I., Giatromanolaki, A., Sivridis, E., Bougioukas, G., Didilis, V., Gatter, K.C., and Harris, A.L.; Tumour and Angiogenesis Research Group. (2003). Lactate dehydrogenase-5 (LDH-5) overexpression in non-small-cell lung cancer tissues is linked to tumour hypoxia, angiogenic factor production and poor prognosis. Br. J. Cancer *89*, 877–885.

Koukourakis, M.I., Giatromanolaki, A., Sivridis, E., Gatter, K.C., and Harris, A.L.; Tumour Angiogenesis Research Group. (2006). Lactate dehydrogenase 5 expression in operable colorectal cancer: strong association with survival and activated vascular endothelial growth factor pathway—a report of the Tumour Angiogenesis Research Group. J. Clin. Oncol. *24*, 4301–4308.

Koukourakis, M.I., Kontomanolis, E., Giatromanolaki, A., Sivridis, E., and Liberis, V. (2009). Serum and tissue LDH levels in patients with breast/gynaecological cancer and benign diseases. Gynecol. Obstet. Invest. *67*, 162–168.

Le, A., Cooper, C.R., Gouw, A.M., Dinavahi, R., Maitra, A., Deck, L.M., Royer, R.E., Vander Jagt, D.L., Semenza, G.L., and Dang, C.V. (2010). Inhibition of lactate dehydrogenase A induces oxidative stress and inhibits tumor progression. Proc. Natl. Acad. Sci. USA *107*, 2037–2042.

Lei, Q., Jiao, J., Xin, L., Chang, C.J., Wang, S., Gao, J., Gleave, M.E., Witte, O.N., Liu, X., and Wu, H. (2006). NKX3.1 stabilizes p53, inhibits AKT activation, and blocks prostate cancer initiation caused by PTEN loss. Cancer Cell *9*, 367–378.

Lewis, B.C., Shim, H., Li, Q., Wu, C.S., Lee, L.A., Maity, A., and Dang, C.V. (1997). Identification of putative c-Myc-responsive genes: characterization of rcl, a novel growth-related gene. Mol. Cell. Biol. *17*, 4967–4978.

Mizushima, N., Levine, B., Cuervo, A.M., and Klionsky, D.J. (2008). Autophagy fights disease through cellular self-digestion. Nature *451*, 1069–1075.

Neumann, H., Peak-Chew, S.Y., and Chin, J.W. (2008). Genetically encoding N(epsilon)-acetyllysine in recombinant proteins. Nat. Chem. Biol. *4*, 232–234.

Neumann, H., Hancock, S.M., Buning, R., Routh, A., Chapman, L., Somers, J., Owen-Hughes, T., van Noort, J., Rhodes, D., and Chin, J.W. (2009). A method for genetically installing site-specific acetylation in recombinant histones defines the effects of H3 K56 acetylation. Mol. Cell *36*, 153–163.

Read, J.A., Winter, V.J., Eszes, C.M., Sessions, R.B., and Brady, R.L. (2001). Structural basis for altered activity of M- and H-isozyme forms of human lactate dehydrogenase. Proteins *43*, 175–185.

Ross, J.M., Öberg, J., Brené, S., Coppotelli, G., Terzioglu, M., Pernold, K., Goiny, M., Sitnikov, R., Kehr, J., Trifunovic, A., et al. (2010). High brain lactate is a hallmark of aging and caused by a shift in the lactate dehydrogenase A/B ratio. Proc. Natl. Acad. Sci. USA *107*, 20087–20092.

Semenza, G.L., Jiang, B.H., Leung, S.W., Passantino, R., Concordet, J.P., Maire, P., and Giallongo, A. (1996). Hypoxia response elements in the aldolase A, enolase 1, and lactate dehydrogenase A gene promoters contain essential binding sites for hypoxia-inducible factor 1. J. Biol. Chem. *271*, 32529–32537.

Shim, H., Dolde, C., Lewis, B.C., Wu, C.S., Dang, G., Jungmann, R.A., Dalla-Favera, R., and Dang, C.V. (1997). c-Myc transactivation of LDH-A: implications for tumor metabolism and growth. Proc. Natl. Acad. Sci. USA *94*, 6658–6663.

Vander Heiden, M.G., Cantley, L.C., and Thompson, C.B. (2009). Understanding the Warburg effect: the metabolic requirements of cell proliferation. Science *324*, 1029–1033.

Végran, F., Boidot, R., Michiels, C., Sonveaux, P., and Feron, O. (2011). Lactate influx through the endothelial cell monocarboxylate transporter MCT1 supports an NF-κB/IL-8 pathway that drives tumor angiogenesis. Cancer Res. *71*, 2550–2560.

Wang, Q., Zhang, Y., Yang, C., Xiong, H., Lin, Y., Yao, J., Li, H., Xie, L., Zhao, W., Yao, Y., et al. (2010). Acetylation of metabolic enzymes coordinates carbon source utilization and metabolic flux. Science *327*, 1004–1007.

Warburg, O. (1956). On the origin of cancer cells. Science *123*, 309–314.

Wing, S.S., Chiang, H.L., Goldberg, A.L., and Dice, J.F. (1991). Proteins containing peptide sequences related to Lys-Phe-Glu-Arg-Gln are selectively depleted in liver and heart, but not skeletal muscle, of fasted rats. Biochem. J. *275*, 165–169.

Xie, H., Valera, V.A., Merino, M.J., Amato, A.M., Signoretti, S., Linehan, W.M., Sukhatme, V.P., and Seth, P. (2009). LDH-A inhibition, a therapeutic strategy for treatment of hereditary leiomyomatosis and renal cell cancer. Mol. Cancer Ther. *8*, 626–635.

Zhao, S., Xu, W., Jiang, W., Yu, W., Lin, Y., Zhang, T., Yao, J., Zhou, L., Zeng, Y., Li, H., et al. (2010). Regulation of cellular metabolism by protein lysine acetylation. Science *327*, 1000–1004.

Cancer Cell
Article

Control of Autophagic Cell Death by Caspase-10 in Multiple Myeloma

Laurence Lamy,[1] Vu N. Ngo,[1] N.C. Tolga Emre,[1] Arthur L. Shaffer III,[1] Yandan Yang,[1] Erming Tian,[3] Vinod Nair,[4] Michael J. Kruhlak,[2] Adriana Zingone,[1] Ola Landgren,[1] and Louis M. Staudt[1,*]
[1]Metabolism Branch, Center for Cancer Research
[2]Experimental Immunology Branch
National Cancer Institute, National Institutes of Health, 9000 Rockville Pike, Bethesda, MD 20892, USA
[3]University of Arkansas for Medical Sciences, 4301 W. Markham Street #776, ACRC 947, Little Rock, AR 72205, USA
[4]Research Technologies Section/RTB, Rocky Mountain Laboratories/NIAID/NIH, 903 South 4th Street, Hamilton, MT 59840, USA
*Correspondence: lstaudt@mail.nih.gov
http://dx.doi.org/10.1016/j.ccr.2013.02.017

SUMMARY

We performed a loss-of-function RNA interference screen to define therapeutic targets in multiple myeloma, a genetically diverse plasma cell malignancy. Unexpectedly, we discovered that all myeloma lines require caspase-10 for survival irrespective of their genetic abnormalities. The transcription factor IRF4 induces both caspase-10 and its associated protein $cFLIP_L$ in myeloma, generating a protease that does not induce apoptosis but rather blocks an autophagy-dependent cell death pathway. Caspase-10 inhibits autophagy by cleaving the BCL2-interacting protein BCLAF1, itself a strong inducer of autophagy that acts by displacing beclin-1 from BCL2. While myeloma cells require a basal level of autophagy for survival, caspase-10 tempers this response to avoid cell death. Drugs that disrupt this vital balance may have therapeutic potential in myeloma.

INTRODUCTION

Multiple myeloma is a malignant proliferation of plasma cells in the bone marrow. Autologous stem cell transplantation and drugs such as lenalidomide and bortezomib have improved survival, yet myeloma remains largely incurable. One of the challenges in treating myeloma is its genomic and phenotypic heterogeneity (Kuehl and Bergsagel, 2012). Hence, an optimal therapy in myeloma would be one that targets an essential regulatory pathway in all subtypes of this cancer.

RNA interference screening can systematically identify genes and pathways that are essential for cancer cell proliferation and survival (Ngo et al., 2006). In some instances, these screens identify pathways that are affected by somatic mutations, thereby revealing "oncogene addiction." In other cases, these screens identify essential genes that are not affected by structural abnormalities, a phenomenon dubbed "nononcogene addiction" (Luo et al., 2009). In myeloma, one such nononcogene addiction target is the transcription factor IRF4, which is required for the survival of all genetic subtypes of this cancer (Shaffer et al., 2008). Although the oncogene *MYC* is an important IRF4 target in myeloma, other targets must contribute to IRF4 addiction in myeloma.

Following ligand engagement of certain members of the tumor necrosis factor receptor superfamily, caspase-10 and its paralogue caspase-8 initiate a form of programmed cell death known as apoptosis (Wang et al., 2001; Wilson et al., 2009). The recruitment of these caspases to membrane-associated "DISC" complexes induces their autoproteolysis, releasing p10/p18 dimers that initiate apoptosis by activating effector caspases. However, caspase-10 and caspase-8 have functions in addition to their pro-apoptotic role. Both proteins can activate the NF-κB pathway when overexpressed (Chaudhary et al., 2000), and caspase-8 deficiency is associated with defective T cell activation and immunodeficiency in humans and mice (Chun et al., 2002; Salmena et al., 2003). During

Significance

A variety of translocations, mutations, and copy number alterations drive the malignant phenotype of multiple myeloma. Faced with this genetic diversity, it is imperative that we design therapeutics to attack vulnerabilities that are shared by all myeloma subtypes. Using an unbiased genetic screen we discovered that all multiple myeloma subtypes tested require caspase-10 for survival. This instance of "nononcogene addiction" appears to stem from a basal level of autophagy that is required to maintain myeloma cell viability. Caspase-10 modulates this autophagic response, preventing it from inducing cell death. Therapies targeting caspase-10 would exploit this regulatory pathway and could have broad efficacy across myeloma subtypes.

T cell activation, macroautophagy (hereafter referred to as autophagy) is activated to meet the increased bioenergetic requirements of cell proliferation, but this autophagy is kept in check by caspase-8 (Bell et al., 2008; Hubbard et al., 2010; Yu et al., 2004).

Autophagy is a cellular process in which portions of the cytosol or entire organelles are sequestered into double membrane vesicles termed autophagosomes and subsequently fused with the lysosome, where the content is digested and recycled (Levine and Kroemer, 2008; Rabinowitz and White, 2010). Autophagy is essential to maintain cell homeostasis, recycle damaged organelles, and overcome nutrient deprivation and metabolic stress. However, autophagy can be associated with a nonapoptotic form of cell death (Galluzzi et al., 2012), and hence this cellular reaction to stress must be tightly regulated (Bell et al., 2008; Shimizu et al., 2004; Yu et al., 2004). One level of regulation is dictated by the abundance of anti-apoptotic Bcl-2 family proteins, which sequester beclin-1, a key inducer of autophagy (Pattingre et al., 2005).

In addition to its regulation of autophagy, caspase-8 blocks a form of regulated necrosis by preventing the activation of RIP kinase 3 (RIPK3) (Green et al., 2011). This regulatory pathway appears to require two caspase-8-interacting proteins, FADD and the caspase-like protein $cFLIP_L$, forming a protease with limited activity that can block necrosis but cannot initiate apoptosis. $cFLIP_L$ pairs with caspase-8 and prevents its autocleavage while itself being a substrate of caspase-8, resulting in a caspase-8 complex containing a p43 cFLIP isoform (Budd et al., 2006).

Here, we report an RNA interference-based genetic screen to discover therapeutic targets in genetically heterogeneous multiple myeloma cells, but not in lymphoma cells.

RESULTS

Caspase-10 Is Essential for Myeloma Viability

To uncover essential pathways required for myeloma proliferation and survival, we performed a loss-of-function RNA interference screen using a retroviral library to inducibly express short hairpin RNAs (shRNAs) (Ngo et al., 2006). An shRNA-targeting caspase-10 was depleted during a 3-week culture of three myeloma cell lines, indicating its toxicity, but had no effect in four lymphoma lines (Figure 1A). To extend this finding, we cloned this shRNA and five additional caspase-10 shRNAs (Figure 1B; Figures S1A and S1B available online) into a retroviral vector that allows coexpression of green fluorescent protein (GFP). In myeloma lines transduced with these vectors, the fraction of GFP^+/$shRNA^+$ cells declined over time, but no toxicity was observed in lymphoma lines (Figures 1C, S1C, and S1D). One caspase-10 shRNA (#1) targets a sequence unique to the D splice isoform (Figure 1B), indicating its essential role in myeloma. The toxicity of this shRNA could be rescued by ectopic provision of a TAP-tagged caspase-10 isoform D that is resistant to this shRNA (TAP-Casp10*), showing that the toxicity of this shRNA for myeloma cells was not due to off-target effects (Figure 1D). Of note, caspase-10 shRNAs were toxic to all myeloma cell lines tested, regardless of their various oncogenic aberrations (Figure 1C).

Myeloma Viability Depends on Caspase-10 Catalytic Activity

To determine if the prosurvival effect of caspase-10 in myeloma requires its protease activity, we generated a protease-dead version of the caspase-10 D isoform in which the catalytic site cysteine was replaced by serine. Wild-type and protease-dead caspase-10 were cloned into a doxycycline-inducible vector that coexpresses GFP, allowing the abundance of caspase-10-transduced cells to be monitored over time (Figure 2A). After caspase-10 induction, myeloma cells expressing the protease-dead mutant were killed whereas those overexpressing wild-type caspase-10 were not, suggesting that protease-dead caspase-10 functions in a dominant negative fashion to induce cell death.

Consistent with this hypothesis, myeloma lines had readily detectable proteolytic activity for the caspase-10 substrate AEVD-*p*NA, but this was not a feature of lymphoma cell lines (Figure 2B). This proteolytic activity was inhibited by the broad-spectrum caspase inhibitor Q-VD-OPH and a more selective caspase-10 inhibitor Q-AEVD-OPH (Figure 2B). Because the selectivity of synthetic caspase inhibitors is not absolute (McStay et al., 2008; Walsh et al., 2011), we further assessed whether caspase-10 was responsible for the observed proteolytic activity. First, immunoprecipitated caspase-10 from different myeloma cell lines had proteolytic activity for AEVD-*p*NA (Figure S2A). Furthermore, this proteolytic activity was decreased when caspase-10 was knocked down by RNA interference in myeloma cells (Figure S2B). Together, these data indicate that the elevated AEVD-pNA cleavage observed in myeloma cells is largely due to caspase-10 activity.

The caspase inhibitors Q-VD-OPH and Q-AEVD-OPH killed myeloma lines in a time-dependent manner but did not kill the lymphoma line HBL1 (Figure 2C). Because stromal cells are known to protect myeloma cells from the lethal effect of certain cytotoxic agents (Hideshima and Anderson, 2002), we investigated whether the stromal line HS-5 would mitigate the effect of caspase inhibitors on myeloma viability (Figure 2D). Whereas the toxic effect of dexamethasone was blocked by coculture with HS-5 cells, the caspase-10 inhibitor Q-AEVD-OPH was still able to kill the myeloma cells while not affecting the viability of the stromal cells (data not shown). Finally, we isolated $CD138^+$ neoplastic cells from patients with newly diagnosed myeloma and cocultured the neoplastic cells with HS-5 cells for 16 hr before adding Q-AEVD-OPH, Q-VD-OPH, or DMSO. The caspase inhibitors decreased the number of viable myeloma cells in a time-dependent fashion (Figure 2E).

Because caspase-8 and caspase-10 share structural and functional similarities, we examined whether caspase-8 might also regulate myeloma viability. Two shRNAs targeting caspase-8 reduced its expression by ~50% but were not toxic in the RNA interference screen (Figures S2C and S2D). To test if caspase-10 might function redundantly with caspase-8, we knocked down caspase-10 expression in myeloma lines and then treated them with a caspase-8 inhibitor (IETD-OPH) that does not inhibit caspase-10. As expected, caspase-10 knockdown was toxic, but inhibition of caspase-8 activity did not increase this toxicity, even though this inhibitor did reduce Fas-mediated apoptosis (Figure S2E). We conclude that caspase-10, but not caspase-8, maintains the viability of myeloma cells.

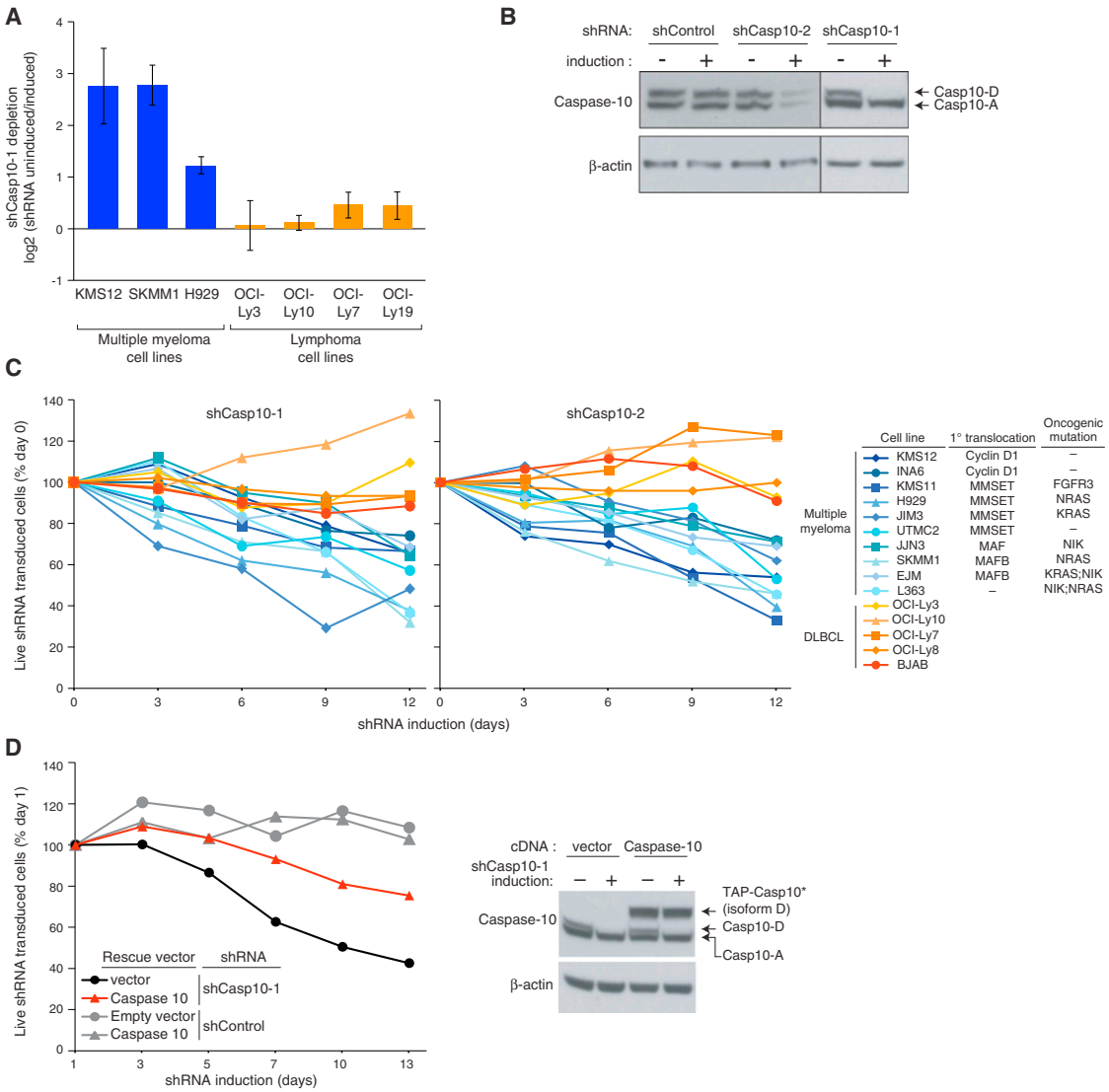

Figure 1. Caspase-10 Knockdown Is Toxic for All Myeloma Cell Lines

(A) Caspase-10 shRNA toxicity in an RNA interference screen was quantified as the ratio of shRNA abundance in shRNA-uninduced cells at time 0 versus shRNA-induced cells after 21 days. Data represent the mean ± SEM of four independent experiments.

(B) Caspase-10 protein level in the SKMM1 myeloma line 4 days after the expression of two caspase-10 shRNAs (shCasp10-1, shCasp10-2). Caspase-10 A and D isoforms are indicated.

(C) The indicated cell lines were infected with retroviruses coexpressing shCasp10-1 or shCasp10-2 and GFP. The percentage of GFP^+ cells was measured over time by flow cytometry and normalized to the percentage of GFP^+ cells before retroviral transduction.

(D) SKMM1 cells were infected with a retrovirus expressing a TAP-tagged caspase-10 isoform D carrying mutations in the shCasp10-1 target sequence (TAP-Casp10*) or with an empty vector. The toxicities of shCasp10-1 and a control shRNA were measured as in (C). The endogenous caspase-10 and the TAP-Casp10* protein levels are shown in the right panel.

See also Figure S1.

Caspase-10 Inhibition of Autophagic Cell Death in Myeloma

While the proportions of myeloma cells in the G1, S, and G2/M phases of the cell cycle were not affected by caspase-10 knockdown, the number of dead cells, as identified by sub-G1 DNA content, increased 3.5-fold (Figure 3A). Two hallmarks of apoptosis, phosphatidylserine exposure and caspase-3 activation, were not induced upon caspase-10 knockdown, but were induced following Fas crosslinking, as expected (Figure 3B). Moreover, treatment of myeloma cells with the caspase inhibitor Q-VD-OPH did not induce other apoptotic features, including cleavage of PARP, p23 (PTGES3), and caspase-7, but the apoptosis inducer etoposide did (Figure S3A). These experiments indicate that caspase-10 inhibits a nonapoptotic form of cell death in myeloma cells.

Ultrastructural analysis of UTMC2 myeloma cells treated with Q-VD-OPH or Q-AEVD-OPH revealed typical morphological features of autophagy (Figure 3C). By 12 hr after Q-VD-OPH

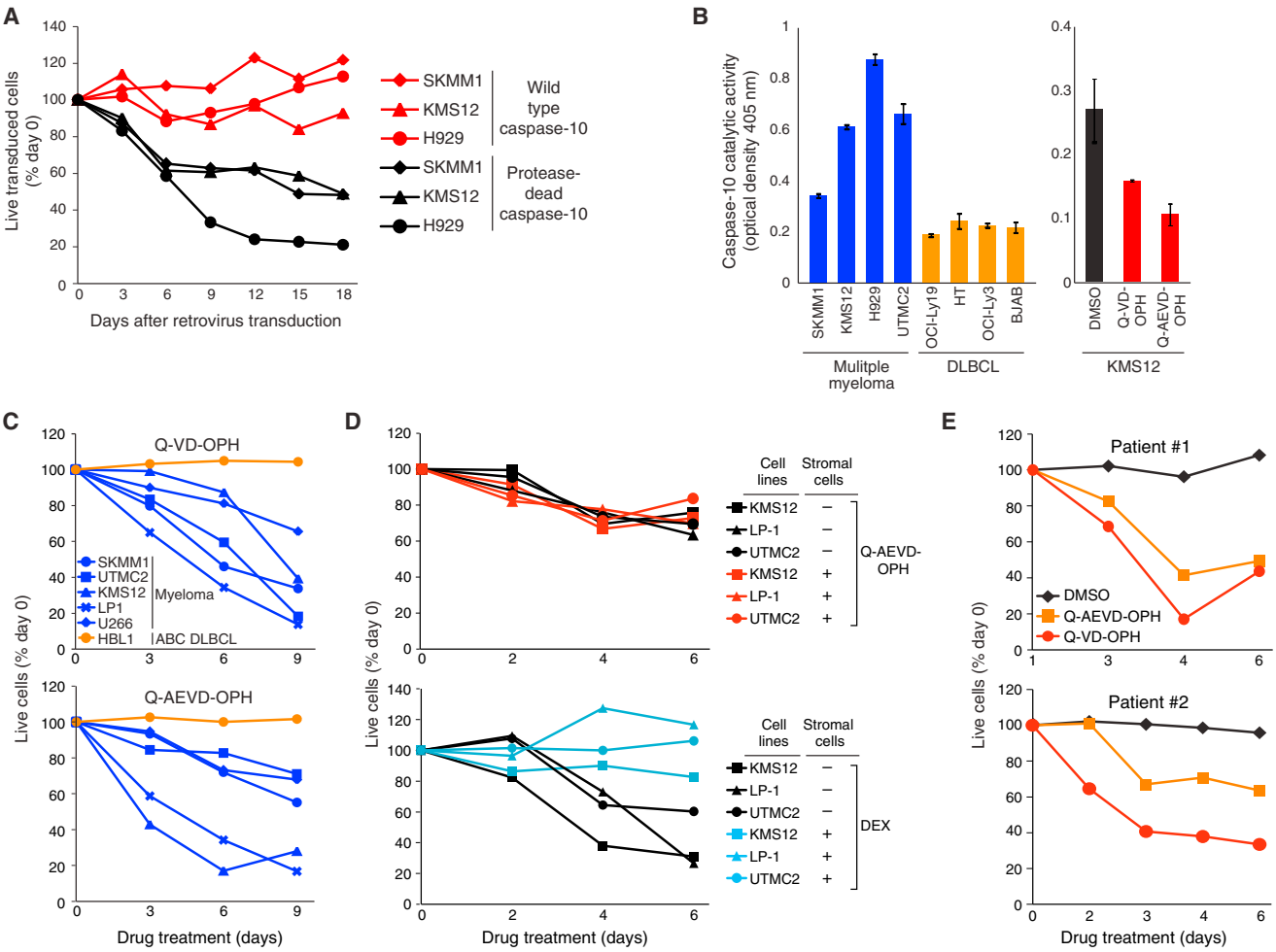

Figure 2. Caspase-10 Catalytic Activity Is Essential to Myeloma Survival

(A) The indicated myeloma lines were infected with a retrovirus coexpressing GFP with caspase-10 isoform D, either as the wild-type or protease-dead mutant. The percentage of GFP$^+$ cells was normalized to the percentage before retroviral transduction.

(B) Caspase-10 activity in the indicated lines (left panel) and in KMS12 myeloma cells treated for 3 hr as indicated (right panel) was determined using an AEVD-*p*NA colorimetric assay. Shown are mean ± SEM from triplicates.

(C) The indicated cell lines were treated with the caspase inhibitors Q-VD-OPH or Q-AEVD-OPH for the indicated times. Live cells (calcein$^+$, PI$^-$) were quantified by FACS using flow count fluorospheres (representative of three experiments).

(D) The indicated myeloma lines were cultured alone or together with GFP-expressing HS-5 stromal cells for 16 hr. Cells were then exposed to Q-AEVD-OPH (25 μM) or dexamethasone (DEX, 0.5 μM) and the relative number of live myeloma cells (GFP$^-$, PI$^-$) was monitored by FACS.

(E) CD138$^+$ primary myeloma cells were cocultured with HS-5 stromal cells for 16 hr before adding 25 μM Q-AEVD-OPH or Q-VD-OPH, or DMSO. The relative number of viable myeloma cells was quantified by FACS.

See also Figure S2.

treatment, early autophagosomes with double membranes accumulated as did a limited number of autophagic vacuoles. After 24 to 72 hr, large autophagic vacuoles containing disintegrated cellular structures appeared in the cytosol. The accumulation of autophagic vacuoles was accompanied by fewer intracellular organelles over time. By 48 hr, the endoplasmic reticulum network was barely visible and the mitochondria that remained were highly condensed. The characteristic hallmarks of apoptosis were absent (e.g., membrane blebbing, nuclear condensation), consistent with a nonapoptotic form of cell death. Similar results were obtained when caspase-10 was depleted using two different shRNAs (Figure S3B). Of note, autophagic vesicles were present at a low level in untreated myeloma cells (Figures 3C and S3B), suggesting that autophagy is active at a basal rate in myeloma (see below).

To quantify autophagy and evaluate further the effect of caspase-10 inhibition on the formation of autophagosomes, myeloma cells were infected with a retrovirus expressing the autophagosome-associated protein LC3 fused to GFP. Upon initiation of autophagy, LC3 relocates from the cytosol to autophagosome membranes, where it plays a role in autophagosome enlargement (Reggiori and Klionsky, 2002), and cytosolic LC3 (LC3-I, 18 kDa) undergoes C-terminal proteolytic processing to a 16 kDa isoform, LC3-II. Autophagy is thus characterized by

the accumulation of GFP-LC3 in punctate structures and by an increase in LC3-II levels (Kabeya et al., 2000). Treatment of two myeloma lines with Q-VD-OPH induced a time-dependent redistribution of GFP-LC3 into punctate vesicles, in association with cell death (Figure S3C). By day 5, GFP-LC3 punctate structures were present in over 60% of caspase inhibitor-treated cells but in fewer than 5% of DMSO-treated cells.

We next wished to track autophagic flux induced by caspase-10 inhibition by distinguishing between early autophagosomes and later steps when these structures fuse with lysosomes, using a tandem GFP-mCherry-tagged LC3 (Kimura et al., 2007; Pankiv et al., 2007). Within the acidic lysosome, GFP fluorescence is quenched whereas mCherry fluorescence is stable. Hence, early autophagosomes produce yellow signals (green plus red) whereas autolysosomes produce red signals. Following exposure to the caspase inhibitor Q-VD-OPH, many myeloma cells developed overlapping green and red punctate structures by 4 hr and thus were engaged in an early phase of autophagy, but by 16 hr, most cells had only red puncta, indicating autolysosome formation (Figure 3D). Similarly, knockdown of caspase-10 expression induced both yellow and red puncta, as did the autophagy inducer rapamycin (Figure S3D). In contrast, DMSO-treated myeloma cells had diffuse green and red fluorescence as well as a few yellow and red punctate structures, consistent with a low degree of basal autophagy. Q-VD-OPH had no effect on control OCI-Ly19 lymphoma cells. Of note, the cell death induced by Q-VD-OPH did not cause chromatin condensation, as was evident in etoposide-treated cells undergoing apoptosis (Figure S3D). To quantify autophagic responses in myeloma, we used flow cytometry to monitor GFP and mCherry fluorescence in live cells following treatment with the caspase inhibitor Q-VD-OPH or DMSO (Figure S3E) (Hundeshagen et al., 2011). After 36 hr of Q-VD-OPH treatment, GFP fluorescence decreased while the mCherry signal was stable, indicating that autophagy had started and that some autophagosomes had already fused with the lysosomes. By 48 hr, both green and red signals faded, consistent with full degradation of the GFP-mCherry-LC3 fusion protein in the lysosome over time. Another way to assess autophagic flux through the lysosome is to monitor GFP-LC3 by immunoblotting because initial lysosomal processing of GFP-LC3 releases an isolated GFP domain. Treatment of myeloma cells with Q-VD-OPH increased GFP cleavage, consistent with increased autophagic flux and lysosomal fusion (Figure S3F). To further evaluate LC3-II degradation in the lysosome, we used bafilomycin A1, which inhibits lysosomal acidification, as well as the lysosomal protease inhibitors pepstatin A and E64d. The LC3-II levels in myeloma cells were increased by Q-VD-OPH treatment, and these levels were further elevated by concurrent treatment with bafilomycin A1 or with lysosomal protease inhibitors (Figures 3E and S3G). Of note, both bafilomycin A1 and the lysosomal protease inhibitors increased LC3-II levels in myeloma cells even without caspase inhibition, consistent with a low level of basal autophagy. These data show that caspase-10 inhibition stimulates autophagic flux in myeloma cells by increasing the formation of autophagosomes that, over time, form autolysosomes.

We next tested whether the autophagic pathway is required for the death of myeloma cells following caspase-10 inhibition. Knockdown of the autophagy-related protein ATG5 decreased the induction of autophagy, as judged by LC3 processing (Figure 3F), and cell death induced by caspase inhibitors (Figure 3G). Similarly, knockdown of beclin-1 reduced Q-VD-OPH-induced death at an early time point (day 5), but depletion of beclin-1 was itself toxic at later time points (Figure 3G). Moreover, knockdown of caspase-10 was less toxic in myeloma cells induced to express shRNAs targeting the autophagy regulators beclin-1 or ATG5 than in cells expressing a control shRNA (Figure 3H). Hence, ATG5 and beclin-1 are important for the induction of cell death following caspase-10 inhibition, demonstrating that caspase-10 limits an autophagy-dependent death pathway in myeloma.

The fact that beclin-1 depletion was toxic for myeloma lines over time suggested that a basal level of autophagy is needed to maintain myeloma survival, as previously suggested (Hoang et al., 2009). Indeed, inhibition of autophagy using 3-methyladenine decreased the viability of all myeloma lines tested, but had no effect on lymphoma lines (Figure 3I).

IRF4 Drives Caspase-10 and cFLIP$_L$ Expression in Myeloma

We next wondered why myeloma cells are uniquely reliant upon caspase-10 activity. Caspase-10 protein is highly expressed in myeloma lines, with little if any expression in lymphoma lines (Figure 4A). Moreover, *CASP10* mRNA levels are higher in normal bone marrow-derived plasma cells than in resting peripheral blood B cells (Figure 4B). Given that IRF4 is a master transcription factor specifying the myeloma and plasma cell phenotype (Shaffer et al., 2008), we hypothesized that IRF4 might transactivate *CASP10*. Indeed, knockdown of IRF4 in a myeloma cell line substantially reduced *CASP10* mRNA and protein levels (Figures 4C and S4A). Chromatin immunoprecipitation (ChIP) followed by high-throughput DNA sequencing (ChIP-Seq) revealed that IRF4 binds to three regions of the *CASP10* locus in a myeloma line but not in a control lymphoma line that lacks IRF4 expression, which was confirmed by conventional ChIP (NCBI Geo ID SRA025850; Yang et al., 2012; Figures S4B and S4C). The IRF4 peaks were centered over repeats of an IRF4 DNA binding motif (GAAA or TTTC). We conclude IRF4 upregulates *CASP10* expression in normal and malignant plasma cells.

Another gene that is induced by IRF4 in myeloma cells is *CFLAR*, which encodes the caspase-like protein cFLIP (Shaffer et al., 2008). ChIP analyses confirmed that IRF4 binds to a promoter-proximal region in the *CFLAR* first intron (Figures S4D and S4E), coinciding with evolutionarily conserved tandem IRF4 binding motifs (TTTC). Two *CFLAR* splice variants exist that encode a 55 kDa isoform (cFLIP$_L$) and a 28 kDa isoform (cFLIP$_S$). Both variants can block death receptor-induced apoptosis by heterodimerizing with caspase-8 and caspase-10, but cFLIP$_L$ has additional signaling functions, including a positive role in antigen-induced proliferation of T cells. cFLIP$_L$ was the predominant isoform in myeloma lines whereas cFLIP$_S$ was more abundant in lymphoma lines (Figure 4D).

Function of cFLIP$_L$ in Myeloma

Because IRF4 upregulates both caspase-10 and cFLIP$_L$ in myeloma, we investigated whether their heterodimerization might play a role in caspase-10 function in these cells. An shRNA targeting both cFLIP$_L$ and cFLIP$_S$ was toxic for all myeloma lines

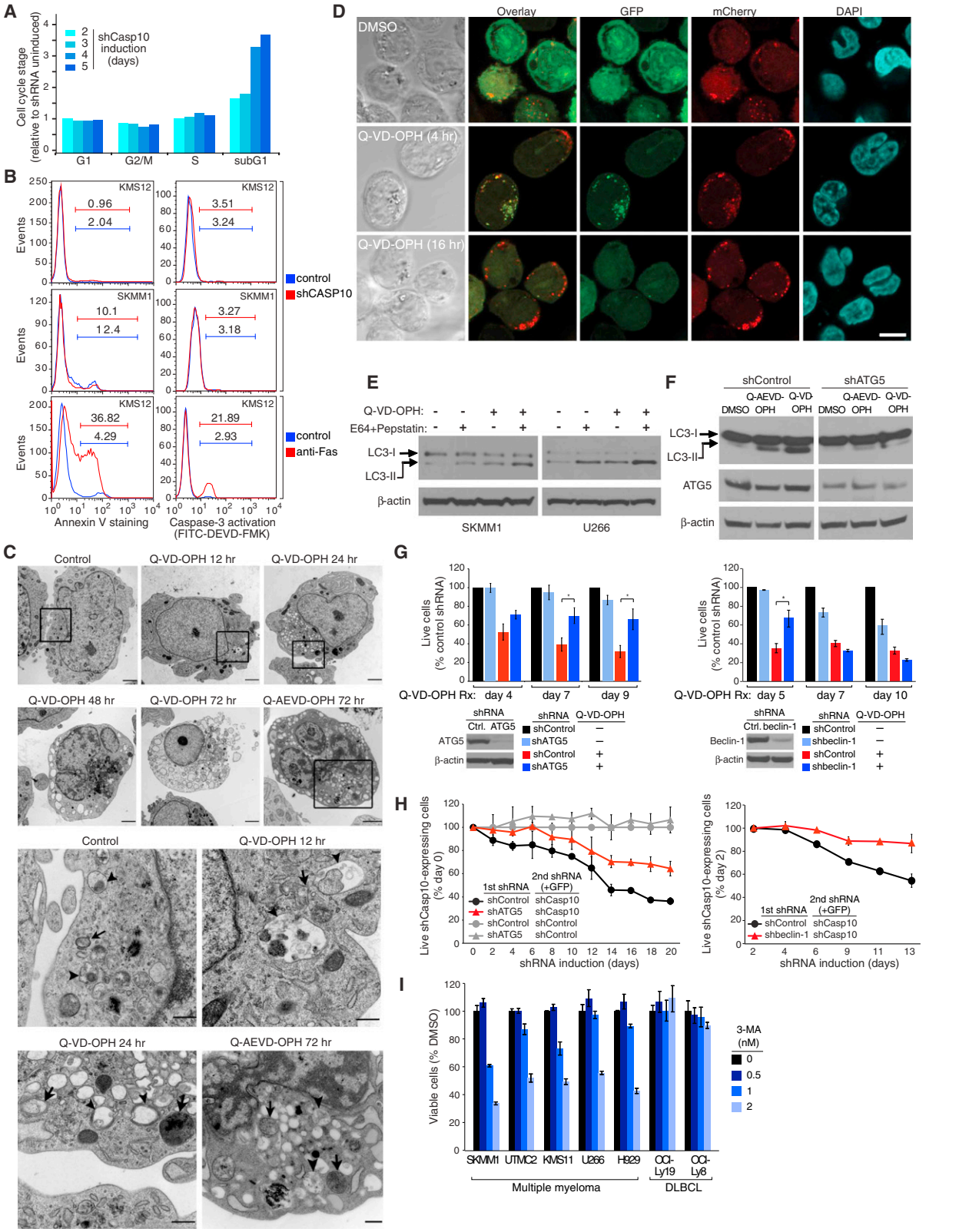

(legend on next page)

tested but not for lymphoma lines (Figures 4E and S4F). This effect on myeloma viability was due to modulation of cFLIP because ectopic expression of $cFLIP_L$ rescued the SKMM1 myeloma line from the toxicity of the cFLIP shRNA (Figure S4G). Immunoprecipitation of endogenous caspase-10 in KMS12 myeloma cells enriched for $cFLIP_L$ and immunoprecipitation of cFLIP enriched for caspase-10 (Figure 4F), confirming that these two proteins heterodimerize in myeloma.

To investigate whether binding of $cFLIP_L$ to caspase-10 promotes caspase-10 activity, we used TAP-Casp10*, enabling streptavidin precipitation. In the myeloma line SKMM1, we expressed wild-type TAP-Casp10* or a mutant version with an amino acid substitution that abrogates protease activity. Precipitation of wild-type TAP-Casp10* pulled down a 43 kDa cFLIP isoform (p43FLIP), which was barely visible in the input lysate but was detected in anti-cFLIP immunoprecipitation (Figure 4F, upper panel), suggesting that the association of $cFLIP_L$ with TAP-Casp10* may promote its processing into p43FLIP, either within the myeloma cells or during the immunoprecipitation (Figure 4G, lower panel). In contrast, protease-dead TAP-Casp10* associated with full-length $cFLIP_L$ as well as with p43FLIP. The presence of p43FLIP under these conditions suggested that protease-dead TAP-Casp10* may associate with endogenous caspase-10, allowing some $cFLIP_L$ cleavage to proceed. This hypothesis is compatible with the analysis of TAP-Casp10* in these same immunoprecipitates (Figure 4G, upper panel). Wild-type TAP-Casp10* was predominantly present as an ~47-kD fragment, presumably the product of autocatalytic cleavage occurring either in the myeloma cell or during the immunoprecipitation. Protease-dead TAP-Casp10* was mostly present as the full-length isoform, but some cleaved TAP-Casp10* was present, potentially due to the presence of endogenous caspase-10 in the immunoprecipitates.

To test whether $cFLIP_L$ might induce the partial autocatalytic cleavage of caspase-10, we purified TAP-Casp10* using streptavidin beads from transfected HEK293T cells, which do not have detectable $cFLIP_L$. Incubation of these TAP-Casp10*-coated beads with an extract from the SKMM1 myeloma line pulled down full-length $cFLIP_L$ as well as p43FLIP (Figure 4H). Incubation of TAP-Casp10* with the SKMM1 extract at 4°C yielded primarily the full-length TAP-Casp10*, but also a small amount of a cleaved ~47 kDa TAP-Casp10* fragment, which was not observed following incubation with a HEK293T extract (Figure 4H). We next tested whether the processing of $cFLIP_L$ and the cleavage of caspase-10 are temperature-dependent, as would be expected if these events are due to the enzymatic activities of caspase-10. Following overnight incubation of TAP-Casp10*-coated beads with the SKMM1 extract at 4°C, warming to 37°C for 10 min significantly increased the cleavage of caspase-10 and the processing of $cFLIP_L$ into p43FLIP (Figure 4I). Finally, knockdown of cFLIP decreased caspase-10 proteolytic activity in myeloma lines, as did caspase-10 knockdown (Figure 4J). Together, these data suggest that the interaction between $cFLIP_L$ and caspase-10 in myeloma cells promotes partial activation of caspase-10.

Caspase-10 Protects Myeloma Cells from BCLAF1-Induced Autophagy

To gain further insight into pathways regulated by caspase-10 in myeloma, we profiled gene expression following caspase-10 knockdown. *BCLAF1*, encoding BCL2-associated transcription factor 1, was the most consistently upregulated gene following caspase-10 inhibition in myeloma lines but not in lymphoma lines (Figure S5A), a finding confirmed by real-time PCR (Figure S5B). Although caspase-10 is unlikely to directly affect *BCLAF1* transcription, these data suggested that BCLAF1 and caspase-10 might participate in a common regulatory pathway in myeloma cells. We noted that the degree of BCLAF1 protein induction following caspase-10 knockdown was quantitatively greater than the degree of *BCLAF1* mRNA induction (Figures S5B and

Figure 3. Caspase-10 Inhibition in Myeloma Induces Autophagy

(A) Cell cycle distribution of KMS12 myeloma cells following shCasp10-2 induction determined by PI labeling and FACS analysis. Results were normalized to day 0 values.

(B) shCasp10-2 was induced in the indicated myeloma lines for 5 days or left untreated. Phosphatidylserine (PS) exposure was monitored by Annexin V-PE binding (left). Caspase-3 activation was evaluated by incubation with FITC-DEVD-FMK (right). Apoptosis was induced by treatment with anti-Fas antibody CH11 (0.5 mg/ml) for 4 hr.

(C) Representative electron microscopic images of UTMC2 myeloma cells treated with Q-VD-OPH (25 μM), Q-AEVD-OPH (25 μM), or vehicle for the indicated times. Lower panels show expanded view of the boxed areas in upper panel. Arrowheads indicate autophagosomes with a double membrane structure. Arrows indicate autophagolysosomes with degraded organelles. Scale bars: 1 μm.

(D) Representative confocal images of SKMM1 myeloma cells expressing GFP-mCherry-tagged LC3 showing autophagosomes (green + red) and autolysosomes (red). Scale bar: 10 μm.

(E) LC3-I and LC3-II levels in the indicated myeloma lines treated with QVD-OPH (25 μM) or with vehicle alone for 30 hr, and exposed to pepstatin A (10 μg/ml) plus E64-d (10 μg/ml) or vehicle in the last 12 hr.

(F) ATG5 or control shRNAs were induced in SKMM1 myeloma cells for 3 days before treating with Q-VD-OPH (25 μM), Q-AEVD-OPH (25 μM), or DMSO for 2 more days, followed by immunoblot analysis of LC3, ATG5, and β-actin.

(G) Left: Four myeloma lines (KMS11, KMS12, UTMC2, SKMM1) were infected with retroviruses expressing GFP with ATG5 or control shRNAs and induced for shRNA expression for 3 days before Q-AEVD-OPH (25 μM) exposure. Live GFP^+, $shRNA^+$ cells were quantified by FACS. Data from all myeloma lines were averaged. Error bars show mean ± SEM. *$p < 0.05$. ATG5 protein level in KMS12 cells 4 days after shATG5 induction was determined by immunoblot. Right panel: Beclin-1 or control shRNAs were induced in KMS12 myeloma cells for 3 days, followed by treatment with Q-VD-OPH (25 μM) for the indicated times. Live GFP^+, $shRNA^+$ cells were quantified by FACS. Shown are means from three experiments ± SEM. *$p < 0.05$. Beclin-1 protein level 4 days after beclin-1 shRNA induction was determined by immunoblot.

(H) Myeloma lines were infected with retroviruses expressing the indicated shRNAs, selected for integration for 4 days, then infected with retroviruses expressing GFP together with caspase-10 or control shRNAs. The relative abundance of GFP^+ cells was measured by FACS. Data from two myeloma lines (U266 and KMS11) were averaged. Error bars show mean ± SEM. Data are representative of three independent experiments.

(I) Myeloma and lymphoma lines were treated with 3-MA at the indicated concentrations for 72 hr, and viability was determined using MTS assay.

See also Figure S3.

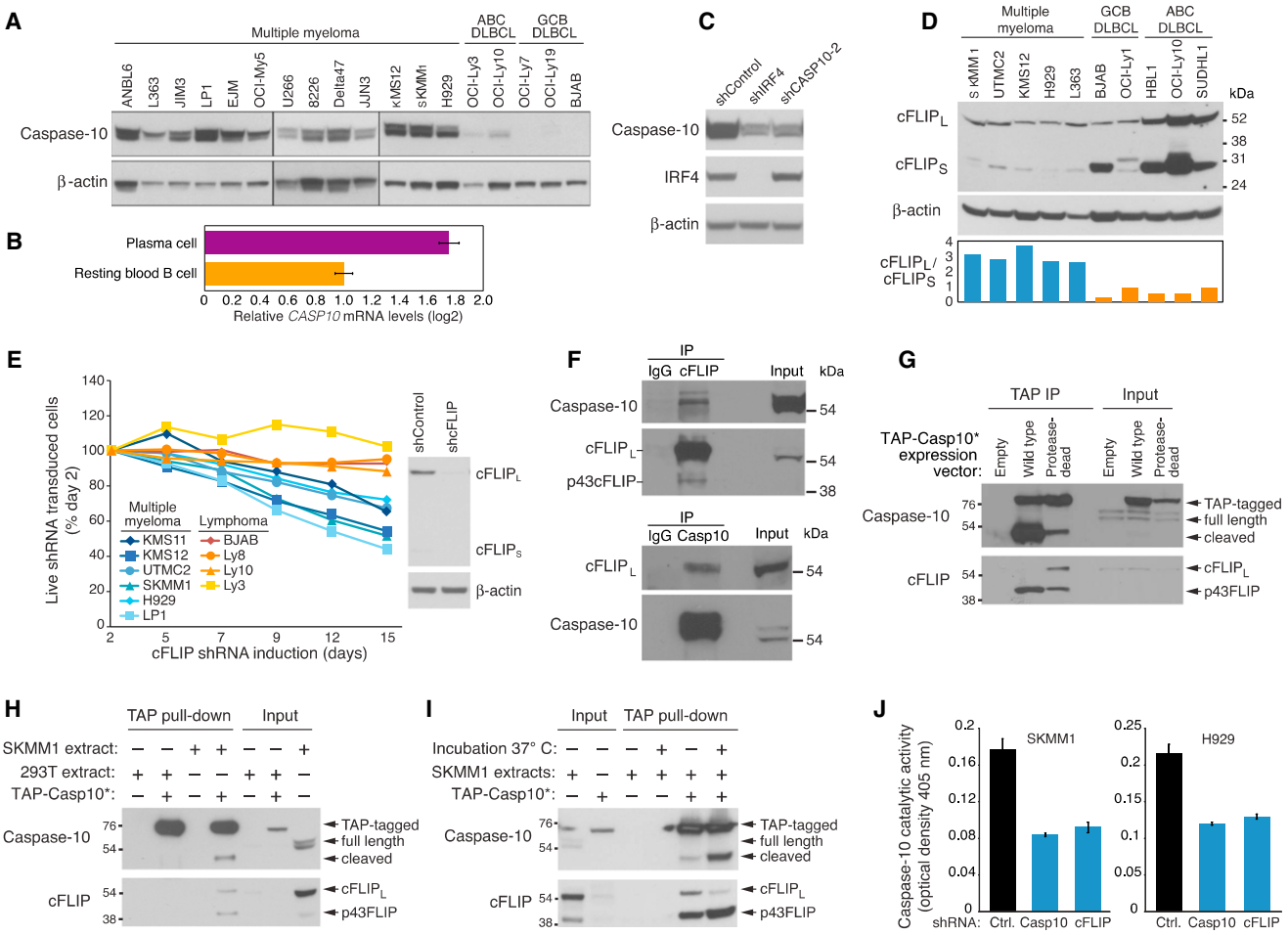

Figure 4. Myeloma Cell Viability Requires cFLIP

(A) Immunoblot analysis of caspase-10 and β-actin in the indicated lines.

(B) Relative *CASP10* mRNA expression levels in human resting blood B cells and BM plasma cells quantified by Affymetrix microarray feature 210955_at using data from Gutiérrez et al., 2007. Mean normalized log2 signal values ± SEM are shown.

(C) Immunoblot analysis of caspase-10, IRF4, and β-actin in UTMC2 myeloma cells induced for 4 days to express IRF4, caspase-10, or control shRNAs.

(D) Immunoblot analysis of cFLIP expression in the indicated lines. The ratio of $cFLIP_L$ to $cFLIP_S$ was quantified by densitometry (bottom).

(E) The indicated lines were infected with retroviruses coexpressing GFP and a cFLIP shRNA. Relative numbers of live $GFP^+/shRNA^+$ cells were monitored by FACS Right: immunoblot analysis of cFLIP in SKMM1 cells after induction of *CFLAR* or control shRNAs for 4 days.

(F) Caspase-10 or cFLIP immunoprecipitates prepared from KMS12 myeloma cells were analyzed by immunoblotting for caspase-10 and cFLIP. Mouse IgG was used as an immunoprecipitation control and a light chain specific secondary antibody was used to improve reading around 55 kDa. Input proteins were also analyzed.

(G) Wild-type or protease-dead TAP-Casp10* were affinity purified on streptavidin beads from transduced SKMM1 cells and analyzed by immunoblotting for caspase-10 and cFLIP. Input extracts were also analyzed.

(H) TAP-Casp10* purified from 293T cells on streptavidin beads was incubated overnight at 4°C with extracts from SKMM1 or 293T cells, and bound caspase-10 and cFLIP were analyzed by immunoblotting. An apparent cleavage product of caspase-10 is indicated. Input extracts were also analyzed.

(I) TAP-Casp10* on streptavidin beads was incubated overnight at 4°C with extracts from the myeloma line SKMM1, then warmed to 37°C or kept at 4°C for 10 min followed by immunoblot analysis of caspase-10 and cFLIP. Input extracts were also analyzed.

(J) Caspase-10 activity was measured using an AEVD-*p*NA colorimetric assay in whole cell extracts of SKMM1 and H929 myeloma lines after 4 days of caspase-10 or cFLIP shRNA induction (mean ± SEM, n = 3).

See also Figure S4.

S5C), suggesting that caspase-10 might control BCLAF1 post-transcriptionally. Moreover, full-length BCLAF1 protein coexisted with various smaller BCLAF1 species in myeloma lines, whereas full-length BCLAF1 was predominant in lymphoma lines, raising the possibility that BCLAF1 might be targeted by a protease in myeloma cells (Figure 5A).

Knockdown of caspase-10 in the SKMM1 myeloma line increased the abundance of full-length BCLAF1 while decreasing the abundance of several smaller species, suggesting that caspase-10 is responsible for BCLAF1 cleavage in myeloma (Figure 5B). Similarly, treatment of myeloma lines with the caspase inhibitor Q-VD-OPH eliminated the smaller

BCLAF1 isoforms, coinciding with an increase in the level of full-length BCLAF1 (Figure 5C). In contrast, knockdown of caspase-8 had no effect on BCLAF1 cleavage in myeloma cells (Figure S5D). Immunoprecipitation of endogenous caspase-10 in SKMM1 myeloma cells enriched for BCLAF1, confirming their interaction (Figure 5D). However, the amount of endogenous BCLAF1 that coprecipitated with caspase-10 was low, suggesting that the cleavage of BCLAF1 by caspase-10 may cause the proteins to disassociate. We therefore expressed the proteolytically dead form of TAP-Casp10* or, as a control, an unrelated TAP-tagged protein (MyD88) in myeloma cells (Figure S5E). Full-length BCLAF1 readily coimmunoprecipitated with this mutant TAP-Casp10* isoform but not with TAP-MyD88, supporting the notion that BCLAF1 is a substrate for caspase-10 in myeloma (Figure S5E). Of note, the abundance of BCLAF1 cleavage products decreased in cells expressing proteolytically dead TAP-Casp10*, suggesting that it acts in a dominant negative fashion, consistent with other data (Figure 2A).

In the MEROPS database of protease cleavage sites (Rawlings et al., 2004), the aspartic acid at position 452 of BCLAF1 is predicted to be a caspase-10 cleavage site. To test this, we sought to compare wild-type BCLAF1 with a mutant isoform in which this aspartate is replaced by alanine (D452A). However, initial attempts to produce retroviruses expressing full-length BCLAF1 were unsuccessful, potentially due to toxicity of BCLAF1 overexpression in the HEK293T retroviral producer cells (data not shown). To circumvent this problem, we engineered an inducible form of BCLAF1 by fusing it to an 18 kDa dihydrofolate reductase (DHFR)-derived ''destruction'' domain that targets fusion proteins for proteasomal degradation (Iwamoto et al., 2010). Proteins bearing this engineered destruction domain can be stabilized by the addition of the membrane-permeable ligand trimethoprim to the culture medium. Using this system, wild-type and D452A BCLAF1-DHFR were induced in the SKMM1 myeloma line and the levels of full-length and cleaved products were assessed by immunoblotting (Figure 5E). Expression of wild-type BCLAF1-DHFR yielded a 52 kDa fragment that was not present when the cells were treated with the caspase-10 inhibitor AEVD-OPH. This 52 kDa fragment was not detected in cells expressing D452A BCLAF1-DHFR, suggesting that D452 is a direct proteolytic target of caspase-10.

BCLAF1 was originally identified as a protein that binds to the adenoviral Bcl-2 homolog E1B19K as well as to several anti-apoptotic members of the BCL2 protein family and is toxic when overexpressed (Kasof et al., 1999; Rénert et al., 2009). Indeed, induction of the BCLAF1-DHFR fusion protein was lethal to three myeloma lines (Figure 5F). We therefore investigated whether BCLAF1 is involved in the same cell death pathway in myeloma as caspase-10. We generated two shRNAs targeting BCLAF1 that lowered its mRNA and protein levels in myeloma cells without toxicity (Figures S5F–S5H). We stably expressed these BCLAF1 shRNAs or a control shRNA in three myeloma lines. In the control lines, expression of a caspase-10 shRNA was toxic, as expected, but in BCLAF1 knockdown lines, the toxicity of the caspase-10 shRNA was mitigated (Figure 5G). BCLAF1 knockdown also blocked the myeloma cell death caused by Q-VD-OPH or Q-AEVD-OPH (Figure 5H) or cFLIP depletion (Figure S5I). We conclude that BCLAF1 is an important cleavage target of caspase-10/c-FLIP$_L$ that accumulates following caspase-10 inhibition, contributing to myeloma cell death.

We next investigated whether the toxicity of BCLAF1 was associated with induction of autophagy. Induction of BCLAF1-DHFR expression in myeloma cells did not induce apoptosis (Figure S6A) but instead increased LC3-II conversion, consistent with autophagy (Figure 6A). Moreover, in myeloma cells expressing GFP-LC3, expression of BCLAF1-DHFR increased the percentage of cells with GFP-LC3 puncta compared with uninduced cells or cells bearing a control vector (Figure S6B). Electron micrographs of BCLAF1-DHFR-expressing cells revealed many vacuolated cells, with autophagosomes and late autophagic vacuoles visible at higher magnification (Figure 6B). As observed following caspase-10 inhibition, BCLAF1-DHFR-expressing cells had mitochondrial condensation and less endoplasmic reticulum, but the nucleus remained intact without evident chromatin changes (Figure 6B). We measured autophagic flux following BCLAF1-DHFR expression using GFP-mCherry-LC3 (Figure 6C). Control cells had a small number of LC3$^+$ autophagosomes (yellow) and autolysosomes (red). Following BCLAF1-DHFR induction, the number of LC3$^+$ autophagosomes increased after 2 days and by 4 days, LC3 was localized predominantly in autolysosomes. Hence, BCLAF1 overexpression in myeloma cells induces autophagy. Knockdown of the autophagy regulators ATG5 and ATG7 rescued myeloma cells from BCLAF1-induced death, demonstrating that BCLAF1 induces autophagic cell death (Figure 6D).

The previous experiments suggested that the prevention of autophagic cell death by caspase-10 relies on its ability to cleave BCLAF1. Earlier work suggested that BCLAF1 binds to anti-apoptotic BCL2 family members (Kasof et al., 1999), as does the autophagy inducer beclin-1 (Pattingre et al., 2005). We therefore investigated whether caspase-10 activity might control the association of these two proteins with BCL-2. Beclin-1 could be co-immunoprecipitated with BCL-2 from myeloma cell extracts, but treatment of these cells with the caspase inhibitor Q-VD-OPH reduced this interaction (Figure 6E). By contrast, trace amounts of BCLAF1 could be detected in BCL-2 immunoprecipitates from myeloma cells, but caspase inhibition strongly increased the interaction of these two proteins (Figure 6F). Next, we expressed BCLAF1-DHFR in myeloma cells and observed that the amount of beclin-1 that could be coimmunoprecipitated with BCL-2 decreased (Figure 6G). These data are consistent with a model in which the increased interaction of BCLAF1 with BCL2 upon caspase-10 inhibition results in the dissociation of beclin-1 from BCL-2, thereby initiating autophagy.

DISCUSSION

The identification of caspase-10 as essential for myeloma cell viability has unveiled a molecular pathway that regulates autophagy. Autophagy is required physiologically in normal plasma cells to moderate the expansion of the endoplasmic reticulum and immunoglobulin secretion, thereby maintaining cellular energy balance (Pengo et al., 2013) (Figure 7A). In addition, various types of endoplasmic reticulum stress, including misfolded proteins, activate the unfolded protein response, which in turn initiates autophagy (Hetz and Glimcher, 2009; Ogata et al., 2006). Myeloma cells may inherit the autophagy

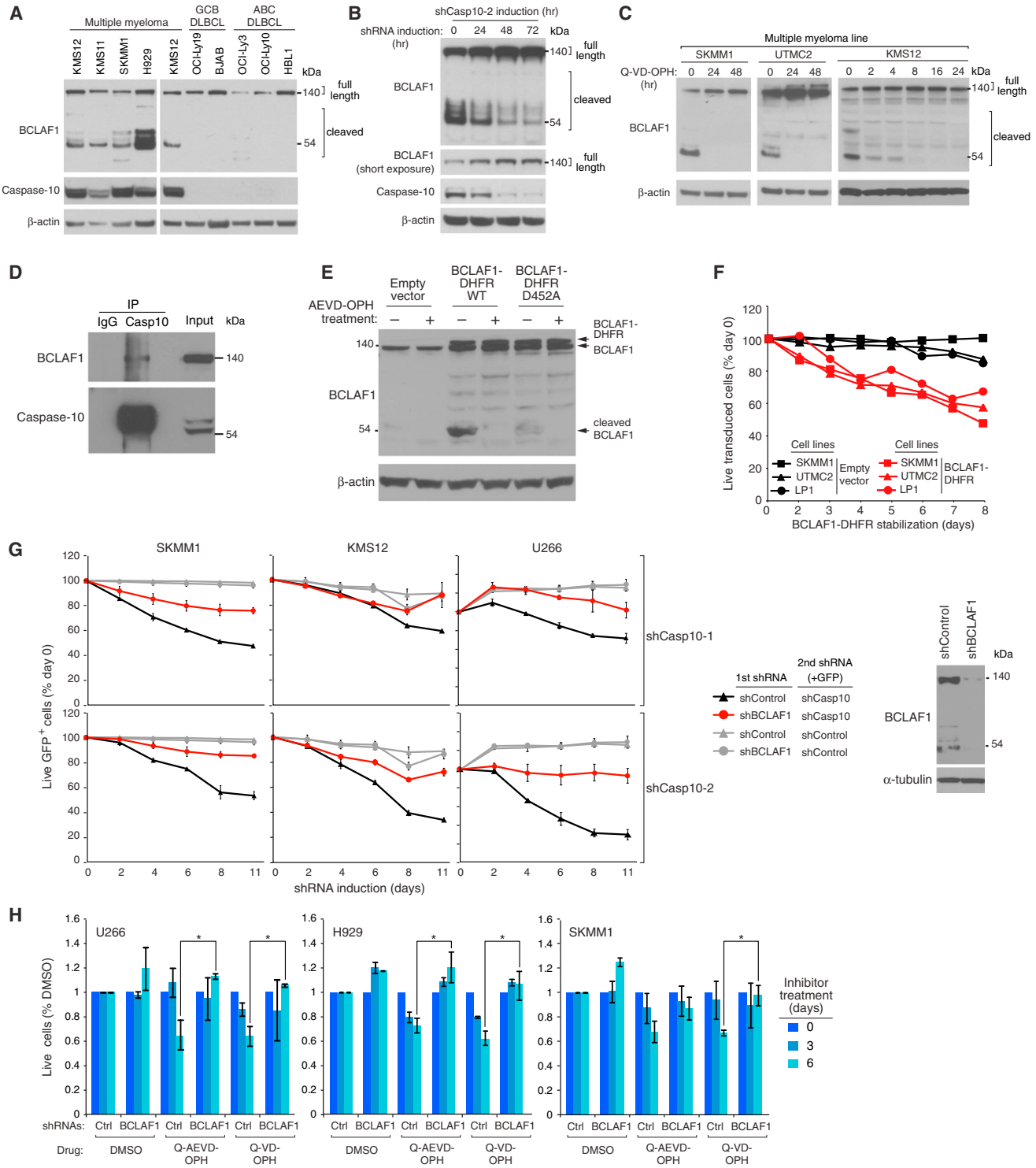

Figure 5. BCLAF1 Is a Substrate for Caspase-10

(A) Immunoblot analysis of BCLAF1 in the indicated cell lines.

(B) A caspase-10 shRNA was induced in SKMM1 myeloma cells for the indicated times, and then caspase-10, BCLAF1, and β-actin were analyzed by immunoblotting.

(C) The indicated myeloma lines were treated with Q-VD-OPH (25 μM) for the indicated times, followed by immunoblotting for caspase-10, BCLAF1, and β-actin.

(D) Caspase-10 immunoprecipitates prepared from SKMM1 myeloma cells were analyzed by immunoblotting using the indicated antibodies. Mouse IgG was used as an immunoprecipitation control. Input proteins were also analyzed.

(E) SKMM1 myeloma cells were transduced with retroviruses expressing the wild-type or the D452A mutant BCLAF1 fused to DHFR, BCLAF1, and β-actin were analyzed by immunoblotting following a 3-day induction of BCLAF1 expression. Data are representative of three experiments.

(legend continued on next page)

dependence of normal plasma cells and may also induce autophagy through the unfolded protein response. Indeed, myeloma cells had ultrastructural features consistent with low-level autophagy under basal conditions. Moreover, pharmacologic or genetic inhibition of autophagy caused myeloma cells to die, as previously described (Hoang et al., 2009). On the flip side, uncontrolled autophagy can reduce cellular viability under some circumstances, presumably when this catabolic process reduces the abundance of cellular organelles beyond a critical point (Galluzzi et al., 2012). Our studies demonstrate that a heterodimeric protease composed of caspase-10 and $cFLIP_L$ is used by myeloma cells to balance the prosurvival and prodeath effects of autophagy.

All myeloma lines tested were caspase-10 dependent, irrespective of their underlying genetic abnormality, qualifying this phenomenon as ''nononcogene addiction'' (Luo et al., 2009). The high expression of caspase-10 and $cFLIP_L$ in myeloma is due to the fact that their genes are transactivated by IRF4, a master regulator of the plasma cell phenotype (Shaffer et al., 2008). IRF4 levels in myeloma are higher than those in normal plasma cells due to a positive autoregulatory loop with c-Myc (Shaffer et al., 2008), driving IRF4 target genes to high levels in myeloma. By an unknown mechanism, myeloma cells preferentially express the $cFLIP_L$ isoform, which promotes caspase-10 activity, and not the $cFLIP_S$ isoform, which is inhibitory. These transcriptional and posttranscriptional influences promote high expression of caspase-10 and $cFLIP_L$ in myeloma, which may drive their heterodimerization and proteolytic activity. The present study implies that loss of this caspase-10 proteolytic activity is one of the many reasons that myeloma cells die upon IRF4 knockdown (Shaffer et al., 2008).

Caspase-10 inhibition in myeloma cells triggers an autophagic cell death that is reminiscent in some respects to the death invoked by caspase-8 inhibition in other cell types (Bell et al., 2008; Yu et al., 2004). In both cases, cell death can be blocked by inhibiting components of the autophagic machinery (e.g., beclin-1 and ATG5). Caspase-8 also regulates a necrotic death response, primarily by reducing RIPK3 activity. Caspase-10 does not seem to share this mechanistic feature because RIPK3 knockdown did not prevent death upon caspase-10 inhibition (data not shown). Caspase-8 itself was not required for myeloma survival, leading us to conclude that the caspase-10/$cFLIP_L$ protease performs an essential, nonredundant role in plasmacytic cells that limits the autophagic response.

BCLAF1 emerged from our studies as a potent autophagy inducer that must be cleaved and inactivated by caspase-10 to protect myeloma cells from uncontrolled autophagy. By an unknown mechanism, BCLAF1 was also transcriptionally upregulated following caspase-10 inhibition, suggesting an orchestrated transcriptional and posttranscription regulatory module that promotes the expression of full-length BCLAF1 under these circumstances. BCLAF1 function has been enigmatic. While BCLAF1 binds to anti-apoptotic BCL2 family proteins and can induce apoptosis when overexpressed in some contexts (Kasof et al., 1999), cells from BCLAF1-deficient mice do not have obvious defects in apoptosis (McPherson et al., 2009). In myeloma cells, BCLAF1 interacted with BCL2, and their association increased following caspase-10 inhibition. BCL2 residing on the endoplasmic reticulum regulates autophagy by sequestering the BH3-only protein beclin-1 (Pattingre et al., 2005). Release of beclin-1 from BCL2, and the subsequent initiation of autophagy, can be achieved by expression of BH3-only proteins that compete for binding of beclin-1 to BCL2 (Maiuri et al., 2007). Hence, it is conceivable that BCLAF1 may induce autophagy by antagonizing the interaction of beclin-1 with BCL2 (Figure 7B). Consistent with this hypothesis, caspase-10 inhibition decreased the association of BCL2 with beclin-1 while increasing its association with BCLAF1. Although plausible, a variety of other functions have been ascribed to BCLAF1, including participation in mRNA splicing and transcriptional repression (Sarras et al., 2010), which could also contribute to its function in myeloma.

The essential role of caspase-10/$cFLIP_L$ in myeloma raises the possibility that this enzyme might serve as a therapeutic target in this disease. Functional studies of caspase-10 have been limited by the fact that this caspase is not encoded in rodent genomes. Humans with inherited caspase-10 deficiency develop an autoimmune lymphoproliferative disorder, apparently due to the absence of pro-apoptotic caspase-10 signaling (Wang et al., 1999). Full autoproteolytic processing of caspase-10 involves two internal cleavage sites and releases the active dimer that initiates apoptosis (Wachmann et al., 2010). The association of $cFLIP_L$ with caspase-10 in myeloma cells appears to prevent one of these two cleavage events, yielding a heterodimer composed of a partially cleaved caspase-10 subunit and a p43FLIP subunit. Conceivably, small molecules could be identified that would inhibit this caspase-10/$cFLIP_L$ heterodimer but not the fully cleaved caspase-10 homodimer. Such inhibitors might induce autophagic cell death of myeloma cells while not blocking caspase-10-dependent physiological apoptosis.

EXPERIMENTAL PROCEDURES

Molecular Biology

The retroviral constructs for shRNA expression and the design of shRNA library sequences have been described (Ngo et al., 2006). shRNA target sequences

(F) The indicated myeloma lines were infected with a retrovirus coexpressing mouse CD8α and BCLAF1-DHFR, or with empty vector. At time 0, the DHFR ligand trimethoprim was added to stabilize the BCLAF1-DHFR fusion protein. The percentage of $LyT2^+$ cells was measured by FACS over time following induction of BCLAF1-DHFR, and normalized to day 0 values.

(G) The indicated myeloma lines were infected with retroviruses expressing a mix of two BCLAF1 shRNAs or a control shRNA. Following shRNA induction for 2 days, cells were infected with a retrovirus coexpressing GFP and a caspase-10 shRNA or a control shRNA. Following shRNA induction, the percentage of GFP^+ $shCasp10^+$ cells was measured by FACS. Shown are means ± SEM. BCLAF1 and α-tubulin were analyzed by immunoblotting in SKMM1 cells after 4 days of shRNA induction.

(H) The indicated myeloma lines were infected with retroviruses expressing a mix of two BCLAF1 shRNAs or a control shRNA, induced to express the shRNAs for 3 days, and then treated with 25 μM Q-VD-OPH or Q-AEVD-OPH, or with DMSO for the indicated times. Live $calcein^+$, PI^- cells were quantified by FACS, and normalized to DMSO values. Shown are means ± SEM. *$p < 0.05$.

See also Figure S5.

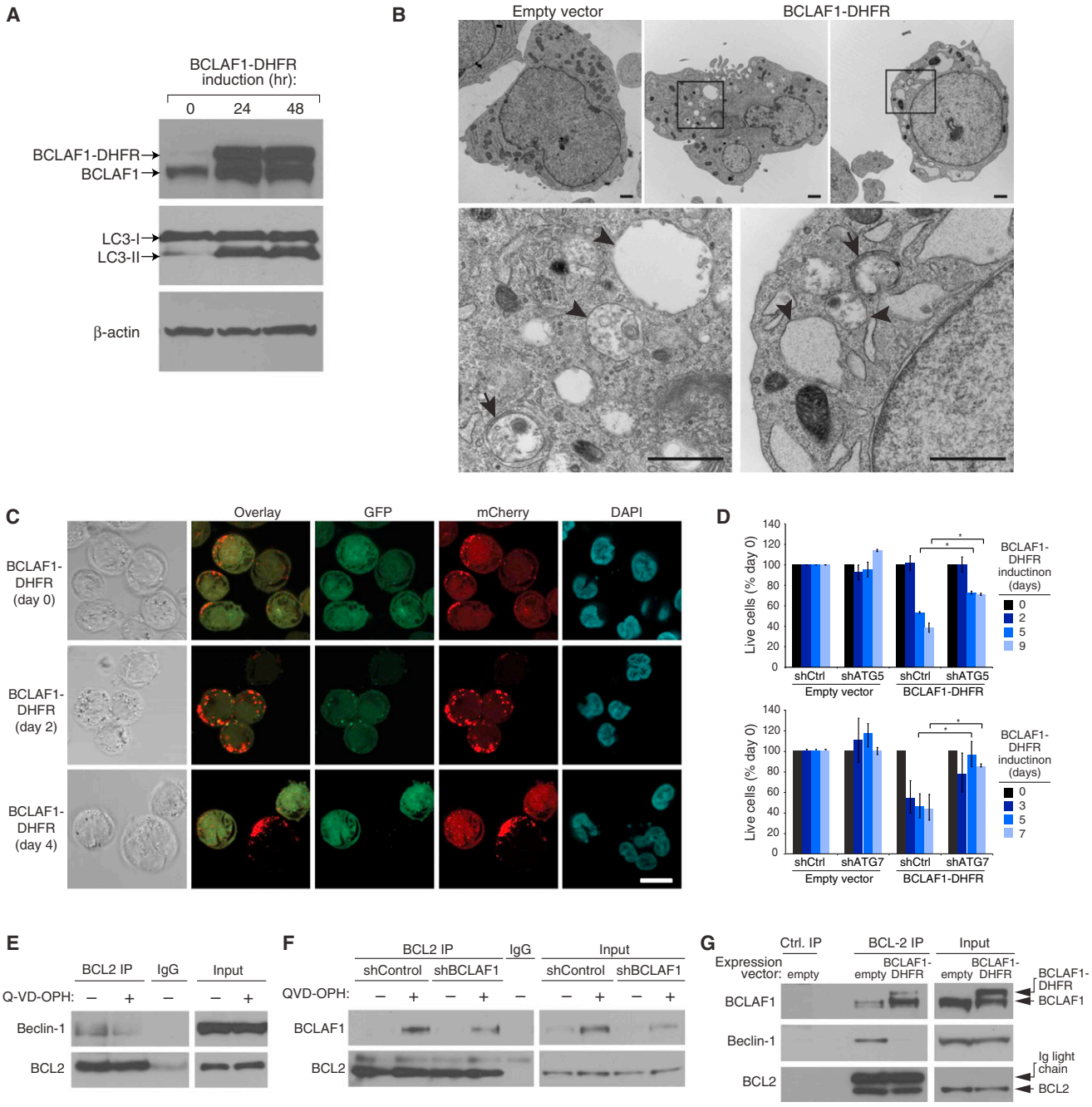

Figure 6. BCLAF1 Promotes Autophagy

(A) Immunoblot analysis of LC3, BCLAF1, and β-actin in SKMM1 myeloma cells induced to express BCLAF1-DHFR for the indicated times. The autophagy-associated LC3-II isoform is indicated.

(B) Electron micrographs of UTMC2 myeloma cells induced to express BCLAF1-DHFR for 3 days, or transduced with empty vector. Higher-power images (bottom) corresponding to boxed areas show autophagosomes with double membrane structure (arrows) and autophagolysosomes with degraded organelles (arrowheads). Scale bars: 1 μm.

(C) Representative confocal images of SKMM1 myeloma cells expressing mCherry-GFP-LC3B and induced for BCLAF1-DHFR expression for the indicated times. Scale bar: 10 μm.

(D) Two myeloma lines (SKMM1, KMS12) were first infected with retroviruses expressing BCLAF1-DHFR or with an empty vector, superinfected with retroviruses expressing an ATG5, ATG7, or control shRNAs and induced for shRNA expression for 2 days prior to BCLAF1-DHFR induction for the indicated periods of time. Live calcein^{+}, PI^{-} cells were quantified by FACS and data were normalized to DMSO values. Shown are means ± SEM. *$p < 0.05$. Data are representative of three independent experiments.

(E) KMS12 myeloma cells were treated with Q-VD-OPH (25 μM) or with vehicle for 48 hr, and then BCL2 immunoprecipitates were analyzed by immunoblotting for beclin-1 and BCL2. Mouse IgG was used as an immunoprecipitation control. Input proteins were also analyzed.

(legend continued on next page)

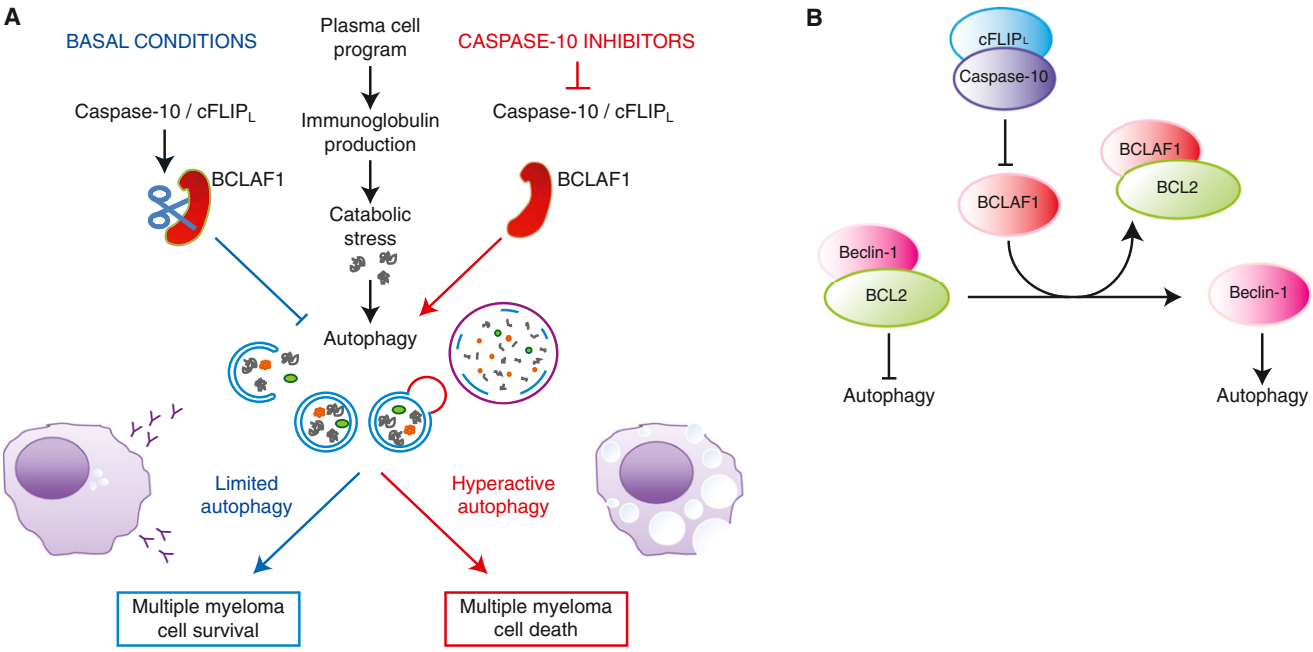

Figure 7. Model of Caspase-10 Control of Autophagic Cell Death in Multiple Myeloma

(A) Caspase-10 maintains the proper balance between prosurvival and prodeath autophagic responses.

(B) BCLAF1 upregulation following caspase-10 inhibition leads to the dissociation of beclin-1 from BCL2, thereby augmenting autophagy.

as well as plasmid constructions are described in the Supplemental Experimental Procedures.

Study Subjects

Bone marrow (BM) aspirate specimens were collected from patients with newly diagnosed multiple myeloma. After Ficoll–Hypaque gradient centrifugation, plasma cells were isolated from the mononuclear-cell fraction by immunomagnetic bead selection with the use of a monoclonal mouse antihuman CD138 antibody (Miltenyi-Biotec). Plasma cell purity (>90%) was confirmed by two-color flow cytometry using $CD138^+/CD45^-$ and $CD38^+/CD45^-$ antibodies (Becton Dickinson, San Jose, CA). All subjects provided written informed consent approving use of their samples for research purposes in accordance with the Declaration of Helsinki. All protocols were approved by the Institutional Review Board of the National Cancer Institute.

Cell Culture

Myeloma cell lines, lymphoma cell lines, and the human stromal cell line HS-5 (kindly provided by Dr. Selina Chen-Kiang, Weill Cornell Medical College, New York, NY) were maintained as described in the Supplemental Experimental Procedures. For efficient retroviral infection and transduction, cell lines were engineered to express the murine ecotropic retroviral receptor and the bacterial tetracycline repressor (TETR) (Ngo et al., 2006).

Caspase-10 Activity

One hundred microgram aliquots of cell lysate were prepared and used following the manufacturer's recommendations to assay caspase-10 activity using the AEVD-*p*NA substrat in a colorimetric assay (Biovision, Mountain View, CA).

Cell Viability and Cell Death Measurement

To assess toxicity of a shRNA, retroviruses that coexpressed GFP were used as described (Ngo et al., 2006). In brief, flow cytometry was performed 2 days after retroviral infection to determine the initial GFP-positive proportion of live cells for each shRNA, then cells were subsequently cultured with doxycycline to induce shRNA and sampled over time. The GFP^+ proportion at each time was monitored using a FACScan (Becton Dickinson) and normalized to the initial value. For enumeration of live cells after vLyt-2 retroviral transductions, measured aliquots of cultures were stained on ice for 15 min with PE-conjugated antimouse CD8a (BD PharMingen). The $LyT2^+$ proportion was monitored by flow cytometry and normalized to the initial value. To assess Q-VD-OPH and Q-AEVD-OPH toxicity, cells were incubated with green calcein and propidium iodide (PI) at 37°C for 30 min. Flow count fluorospheres (Beckman Coulter, Fullerton, CA) were used to quantify the number of living cells (calcein positive, PI negative) with flow cytometry. Under each condition, 20,000 microbeads were added just prior to the analysis, 2,000 microbeads were collected, and the number of living cells was determined using a FACScan (Becton Dickinson).

Phosphatidylserine exposure and in situ labeling of active caspase-3 were measured by flow cytometry using a FACScan (BD Biosciences) and data were processed with the CellQuest program (BD Biosciences). See Supplemental Experimental Procedures for details.

Immunoprecipitations, Pulldown Assays, and Immunblot Analysis

TAP-tag affinity purifications, immunoprecipitations, and pulldown assays were performed using standard procedures from nondenaturing cell extracts. See Supplemental Experimental Procedures for details.

(F) SKMM1 myeloma cells were induced to express shBCLAF1-1 for 3 days prior to Q-VD-OPH (25 μM) or vehicle treatment for 36 hr, and then BCL2 immunoprecipitates were analyzed by immunoblotting for BCLAF1 and BCL2.

(G) SKMM1 myeloma cells were transduced with BCLAF1-DHFR or with an empty vector and induced to express BCLAF1-DHFR for 48 hr. Immunoprecipitates prepared using anti-BCL2 antibody-conjugated agarose beads were analyzed by immunoblotting for BCLAF1, Beclin-1, or BCL2. A control precipitate prepared from SKMM1 cells transduced with an empty vector was also analyzed as were lysates.

See also Figure S6.

Electron Microscopy

Cell pellets were fixed with 2.5% glutaraldehyde in 0.1 M phosphate buffer (Electron Microscopy Sciences, Hatfield, PA). The cells were washed with 0.1 M sodium cacodylate buffer and postfixed with 1% osmium tetroxide/0.8% potassium ferricyanide in 0.1 M sodium cacodylate, followed by 1% tannic acid in distilled water, and stained en bloc with 1% aqueous uranyl acetate. The pellets were then dehydrated in graded ethanol series, infiltrated, and embedded in Spurr's resin. Thin sections were cut on a UC6 ultramicrotome (Leica Microsystems, Vienna, Austria) and stained with 4% aqueous uranyl acetate and Reynold's lead citrate prior to viewing on a Tecnai BioTwin Spirit TEM (FEI, Hillsboro, OR). Digital images were acquired with a Hamamatsu XR-100 digital camera system (AMT, Danvers, MA.).

Fluorescence Microscopy and Confocal Microscopy

Multiple myeloma cells were infected with a retrovirus expressing LC3-GFP fusion protein. After induction of autophagy, samples were examined using an epifluorescent microscope (Olympus BX61). For confocal microscopy, 1–2 × 10^5 cells were seeded on bottom glass 35-mm dishes coated with polylysine (MatTek Corp.) for 30 min at room temperature. The cells were fixed with 4% paraformaldehyde for 30 min at room temperature and washed two times in PBS. Nuclear counterstaining was performed with 0.1 μg/ml 4,6-diamidino-2-phenylindole (DAPI) in PBS for 10 min. Cells were washed two times with PBS and were examined using a Zeiss LSM510 laser scanning confocal microscope.

ACCESSION NUMBERS

Gene expression profiling data have been deposited in GEO under accession number GSE43878.

SUPPLEMENTAL INFORMATION

Supplemental Information includes six figures and Supplemental Experimental Procedures and can be found with this article online at http://dx.doi.org/10.1016/j.ccr.2013.02.017.

ACKNOWLEDGMENTS

This research was supported by the Intramural Research Program of the National Institutes of Health, National Cancer Institute, and the Center for Cancer Research. The authors thank Mike Lenardo for helpful discussions and Kathleen Meyer for her assistance with GEO submissions.

Received: March 28, 2012
Revised: January 30, 2013
Accepted: February 20, 2013
Published: March 28, 2013

REFERENCES

Bell, B.D., Leverrier, S., Weist, B.M., Newton, R.H., Arechiga, A.F., Luhrs, K.A., Morrissette, N.S., and Walsh, C.M. (2008). FADD and caspase-8 control the outcome of autophagic signaling in proliferating T cells. Proc. Natl. Acad. Sci. USA *105*, 16677–16682.

Budd, R.C., Yeh, W.C., and Tschopp, J. (2006). cFLIP regulation of lymphocyte activation and development. Nat. Rev. Immunol. *6*, 196–204.

Chaudhary, P.M., Eby, M.T., Jasmin, A., Kumar, A., Liu, L., and Hood, L. (2000). Activation of the NF-kappaB pathway by caspase 8 and its homologs. Oncogene *19*, 4451–4460.

Chun, H.J., Zheng, L., Ahmad, M., Wang, J., Speirs, C.K., Siegel, R.M., Dale, J.K., Puck, J., Davis, J., Hall, C.G., et al. (2002). Pleiotropic defects in lymphocyte activation caused by caspase-8 mutations lead to human immunodeficiency. Nature *419*, 395–399.

Galluzzi, L., Vitale, I., Abrams, J.M., Alnemri, E.S., Baehrecke, E.H., Blagosklonny, M.V., Dawson, T.M., Dawson, V.L., El-Deiry, W.S., Fulda, S., et al. (2012). Molecular definitions of cell death subroutines: recommendations of the Nomenclature Committee on Cell Death 2012. Cell Death Differ. *19*, 107–120.

Green, D.R., Oberst, A., Dillon, C.P., Weinlich, R., and Salvesen, G.S. (2011). RIPK-dependent necrosis and its regulation by caspases: a mystery in five acts. Mol. Cell *44*, 9–16.

Gutiérrez, N.C., Ocio, E.M., de Las Rivas, J., Maiso, P., Delgado, M., Fermiñán, E., Arcos, M.J., Sánchez, M.L., Hernández, J.M., and San Miguel, J.F. (2007). Gene expression profiling of B lymphocytes and plasma cells from Waldenström's macroglobulinemia: comparison with expression patterns of the same cell counterparts from chronic lymphocytic leukemia, multiple myeloma and normal individuals. Leukemia *21*, 541–549.

Hetz, C., and Glimcher, L.H. (2009). Fine-tuning of the unfolded protein response: Assembling the IRE1alpha interactome. Mol. Cell *35*, 551–561.

Hideshima, T., and Anderson, K.C. (2002). Molecular mechanisms of novel therapeutic approaches for multiple myeloma. Nat. Rev. Cancer *2*, 927–937.

Hoang, B., Benavides, A., Shi, Y., Frost, P., and Lichtenstein, A. (2009). Effect of autophagy on multiple myeloma cell viability. Mol. Cancer Ther. *8*, 1974–1984.

Hubbard, V.M., Valdor, R., Patel, B., Singh, R., Cuervo, A.M., and Macian, F. (2010). Macroautophagy regulates energy metabolism during effector T cell activation. J. Immunol. *185*, 7349–7357.

Hundeshagen, P., Hamacher-Brady, A., Eils, R., and Brady, N.R. (2011). Concurrent detection of autolysosome formation and lysosomal degradation by flow cytometry in a high-content screen for inducers of autophagy. BMC Biol. *9*, 38.

Iwamoto, M., Björklund, T., Lundberg, C., Kirik, D., and Wandless, T.J. (2010). A general chemical method to regulate protein stability in the mammalian central nervous system. Chem. Biol. *17*, 981–988.

Kabeya, Y., Mizushima, N., Ueno, T., Yamamoto, A., Kirisako, T., Noda, T., Kominami, E., Ohsumi, Y., and Yoshimori, T. (2000). LC3, a mammalian homologue of yeast Apg8p, is localized in autophagosome membranes after processing. EMBO J. *19*, 5720–5728.

Kasof, G.M., Goyal, L., and White, E. (1999). Btf, a novel death-promoting transcriptional repressor that interacts with Bcl-2-related proteins. Mol. Cell. Biol. *19*, 4390–4404.

Kimura, S., Noda, T., and Yoshimori, T. (2007). Dissection of the autophagosome maturation process by a novel reporter protein, tandem fluorescent-tagged LC3. Autophagy *3*, 452–460.

Kuehl, W.M., and Bergsagel, P.L. (2012). Molecular pathogenesis of multiple myeloma and its premalignant precursor. J. Clin. Invest. *122*, 3456–3463.

Levine, B., and Kroemer, G. (2008). Autophagy in the pathogenesis of disease. Cell *132*, 27–42.

Luo, J., Solimini, N.L., and Elledge, S.J. (2009). Principles of cancer therapy: oncogene and non-oncogene addiction. Cell *136*, 823–837.

Maiuri, M.C., Criollo, A., Tasdemir, E., Vicencio, J.M., Tajeddine, N., Hickman, J.A., Geneste, O., and Kroemer, G. (2007). BH3-only proteins and BH3 mimetics induce autophagy by competitively disrupting the interaction between Beclin 1 and Bcl-2/Bcl-X(L). Autophagy *3*, 374–376.

McPherson, J.P., Sarras, H., Lemmers, B., Tamblyn, L., Migon, E., Matysiak-Zablocki, E., Hakem, A., Azami, S.A., Cardoso, R., Fish, J., et al. (2009). Essential role for Bclaf1 in lung development and immune system function. Cell Death Differ. *16*, 331–339.

McStay, G.P., Salvesen, G.S., and Green, D.R. (2008). Overlapping cleavage motif selectivity of caspases: implications for analysis of apoptotic pathways. Cell Death Differ. *15*, 322–331.

Ngo, V.N., Davis, R.E., Lamy, L., Yu, X., Zhao, H., Lenz, G., Lam, L.T., Dave, S., Yang, L., Powell, J., and Staudt, L.M. (2006). A loss-of-function RNA interference screen for molecular targets in cancer. Nature *441*, 106–110.

Ogata, M., Hino, S., Saito, A., Morikawa, K., Kondo, S., Kanemoto, S., Murakami, T., Taniguchi, M., Tanii, I., Yoshinaga, K., et al. (2006). Autophagy is activated for cell survival after endoplasmic reticulum stress. Mol. Cell. Biol. *26*, 9220–9231.

Pankiv, S., Clausen, T.H., Lamark, T., Brech, A., Bruun, J.A., Outzen, H., Øvervatn, A., Bjørkøy, G., and Johansen, T. (2007). p62/SQSTM1 binds

directly to Atg8/LC3 to facilitate degradation of ubiquitinated protein aggregates by autophagy. J. Biol. Chem. *282*, 24131–24145.

Pattingre, S., Tassa, A., Qu, X., Garuti, R., Liang, X.H., Mizushima, N., Packer, M., Schneider, M.D., and Levine, B. (2005). Bcl-2 antiapoptotic proteins inhibit Beclin 1-dependent autophagy. Cell *122*, 927–939.

Pengo, N., Scolari, M., Oliva, L., Milan, E., Mainoldi, F., Raimondi, A., Fagioli, C., Merlini, A., Mariani, E., Pasqualetto, E., et al. (2013). Plasma cells require autophagy for sustainable immunoglobulin production. Nat. Immunol. *14*, 298–305.

Rabinowitz, J.D., and White, E. (2010). Autophagy and metabolism. Science *330*, 1344–1348.

Rawlings, N.D., Tolle, D.P., and Barrett, A.J. (2004). MEROPS: the peptidase database. Nucleic Acids Res. *32* (Database issue), D160–D164.

Reggiori, F., and Klionsky, D.J. (2002). Autophagy in the eukaryotic cell. Eukaryot. Cell *1*, 11–21.

Rénert, A.F., Leprince, P., Dieu, M., Renaut, J., Raes, M., Bours, V., Chapelle, J.P., Piette, J., Merville, M.P., and Fillet, M. (2009). The proapoptotic C16-ceramide-dependent pathway requires the death-promoting factor Btf in colon adenocarcinoma cells. J. Proteome Res. *8*, 4810–4822.

Salmena, L., Lemmers, B., Hakem, A., Matysiak-Zablocki, E., Murakami, K., Au, P.Y., Berry, D.M., Tamblyn, L., Shehabeldin, A., Migon, E., et al. (2003). Essential role for caspase 8 in T-cell homeostasis and T-cell-mediated immunity. Genes Dev. *17*, 883–895.

Sarras, H., Alizadeh Azami, S., and McPherson, J.P. (2010). In search of a function for BCLAF1. ScientificWorldJournal *10*, 1450–1461.

Shaffer, A.L., Emre, N.C., Lamy, L., Ngo, V.N., Wright, G., Xiao, W., Powell, J., Dave, S., Yu, X., Zhao, H., et al. (2008). IRF4 addiction in multiple myeloma. Nature *454*, 226–231.

Shimizu, S., Kanaseki, T., Mizushima, N., Mizuta, T., Arakawa-Kobayashi, S., Thompson, C.B., and Tsujimoto, Y. (2004). Role of Bcl-2 family proteins in a non-apoptotic programmed cell death dependent on autophagy genes. Nat. Cell Biol. *6*, 1221–1228.

Wachmann, K., Pop, C., van Raam, B.J., Drag, M., Mace, P.D., Snipas, S.J., Zmasek, C., Schwarzenbacher, R., Salvesen, G.S., and Riedl, S.J. (2010). Activation and specificity of human caspase-10. Biochemistry *49*, 8307–8315.

Walsh, J.G., Logue, S.E., Lüthi, A.U., and Martin, S.J. (2011). Caspase-1 promiscuity is counterbalanced by rapid inactivation of processed enzyme. J. Biol. Chem. *286*, 32513–32524.

Wang, J., Zheng, L., Lobito, A., Chan, F.K., Dale, J., Sneller, M., Yao, X., Puck, J.M., Straus, S.E., and Lenardo, M.J. (1999). Inherited human Caspase 10 mutations underlie defective lymphocyte and dendritic cell apoptosis in autoimmune lymphoproliferative syndrome type II. Cell *98*, 47–58.

Wang, J., Chun, H.J., Wong, W., Spencer, D.M., and Lenardo, M.J. (2001). Caspase-10 is an initiator caspase in death receptor signaling. Proc. Natl. Acad. Sci. USA *98*, 13884–13888.

Wilson, N.S., Dixit, V., and Ashkenazi, A. (2009). Death receptor signal transducers: nodes of coordination in immune signaling networks. Nat. Immunol. *10*, 348–355.

Yang, Y., Shaffer, A.L., Emre, N.C., Ceribelli, M., Zhang, M., Wright, G., Xiao, W., Powell, J., Platig, J., Kohlhammer, H., et al. (2012). Exploiting synthetic lethality for the therapy of ABC diffuse large B cell lymphoma. Cancer Cell. *21*, 723–737.

Yu, L., Alva, A., Su, H., Dutt, P., Freundt, E., Welsh, S., Baehrecke, E.H., and Lenardo, M.J. (2004). Regulation of an ATG7-beclin 1 program of autophagic cell death by caspase-8. Science *304*, 1500–1502.

Cancer Cell
Article

Molecular Mechanism of SSR128129E, an Extracellularly Acting, Small-Molecule, Allosteric Inhibitor of FGF Receptor Signaling

Corentin Herbert,[1,11] Ulrich Schieborr,[2,11] Krishna Saxena,[2,11] Jarek Juraszek,[3,11] Frederik De Smet,[4,5,11] Chantal Alcouffe,[1] Marc Bianciotto,[1] Giorgio Saladino,[3] David Sibrac,[1] Denis Kudlinzki,[2] Sridhar Sreeramulu,[2] Alan Brown,[7] Patrice Rigon,[1] Jean-Pascal Herault,[1] Gilbert Lassalle,[1] Tom L. Blundell,[7] Frederic Rousseau,[8] Ann Gils,[6] Joost Schymkowitz,[8] Peter Tompa,[9,10] Jean-Marc Herbert,[1] Peter Carmeliet,[4,5,11] Francesco Luigi Gervasio,[3,11,*] Harald Schwalbe,[2,11,*] and Françoise Bono[1,11,*]

[1]E2C and LGCR-SDI Department, Sanofi Research and Development, 31100 Toulouse, France
[2]Institute for Organic Chemistry and Chemical Biology, Center for Biomolecular Magnetic Resonance (BMRZ), University of Frankfurt, D-60438 Frankfurt, Germany
[3]Computational Biophysics Group, Spanish National Cancer Research Center (CNIO), E-28029 Madrid, Spain
[4]Laboratory of Angiogenesis and Neurovascular Link, Vesalius Research Center (VRC), VIB, 3000 Leuven, Belgium
[5]Laboratory of Angiogenesis and Neurovascular Link, Vesalius Research Center (VRC)
[6]Laboratory for Pharmaceutical Biology, Pharmaceutical Sciences
KU Leuven, 3000 Leuven, Belgium
[7]Department of Biochemistry, University of Cambridge, CB2 1GA Cambridge, UK
[8]VIB Switch Laboratory, Department of Cellular and Molecular Medicine, VIB-KU Leuven, 3000 Leuven, Belgium
[9]VIB Department of Structural Biology, Vrije Universiteit Brussel, 1050 Brussels, Belgium
[10]Institute of Enzymology, Research Center for Natural Sciences, Hungarian Academy of Sciences, H-1113 Budapest, Hungary
[11]These authors contributed equally to this work
*Correspondence: flgervasio@cnio.es (F.L.G.), schwalbe@nmr.uni-frankfurt.de (H.S.), francoise.bono@sanofi-aventis.com (F.B.)
http://dx.doi.org/10.1016/j.ccr.2013.02.018

SUMMARY

The fibroblast growth factor (FGF)/fibroblast growth factor receptor (FGFR) signaling network plays an important role in cell growth, survival, differentiation, and angiogenesis. Deregulation of FGFR signaling can lead to cancer development. Here, we report an FGFR inhibitor, SSR128129E (SSR), that binds to the extracellular part of the receptor. SSR does not compete with FGF for binding to FGFR but inhibits FGF-induced signaling linked to FGFR internalization in an allosteric manner, as shown by crystallography studies, nuclear magnetic resonance, Fourier transform infrared spectroscopy, molecular dynamics simulations, free energy calculations, structure-activity relationship analysis, and FGFR mutagenesis. Overall, SSR is a small molecule allosteric inhibitor of FGF/FGFR signaling, acting via binding to the extracellular part of the FGFR.

INTRODUCTION

Receptor tyrosine kinases (RTKs) constitute a major class of drug targets (Overington et al., 2006). Most efforts have been invested in developing agents that orthosterically compete for binding between RTKs with their endogenous ligands, such as antibodies recognizing growth factors or their receptors or small molecules that inhibit their tyrosine kinase (TK) activity (Gasparini et al., 2005; Zhang et al., 2009). Only a few drugs that interact with allosteric sites have been developed for ion channels and G protein-coupled receptors (Christopoulos, 2002; Conn et al., 2009) and kinases (Zhang et al., 2009). In contrast to orthosteric inhibitors, advantages of allosteric drugs include specificity and safety (Christopoulos, 2002).

Significance

FGF receptors (FGFRs) belong to the receptor tyrosine kinase (RTK) superfamily, which is of immense importance for numerous (patho-)physiological processes and a key target for drug development. Most drugs targeting the extracellular domains of RTKs are traditionally antibodies, but small chemical compounds, acting extracellularly, which are capable of inhibiting RTK signaling, have not been described yet. This study identified an extracellularly binding allosteric inhibitor of FGFRs and investigated its allosteric mechanisms. Besides therapeutic advantages of allosteric drugs, our data warrant further development of additional small, extracellularly acting, allosteric molecules for targeting this important class of receptors.

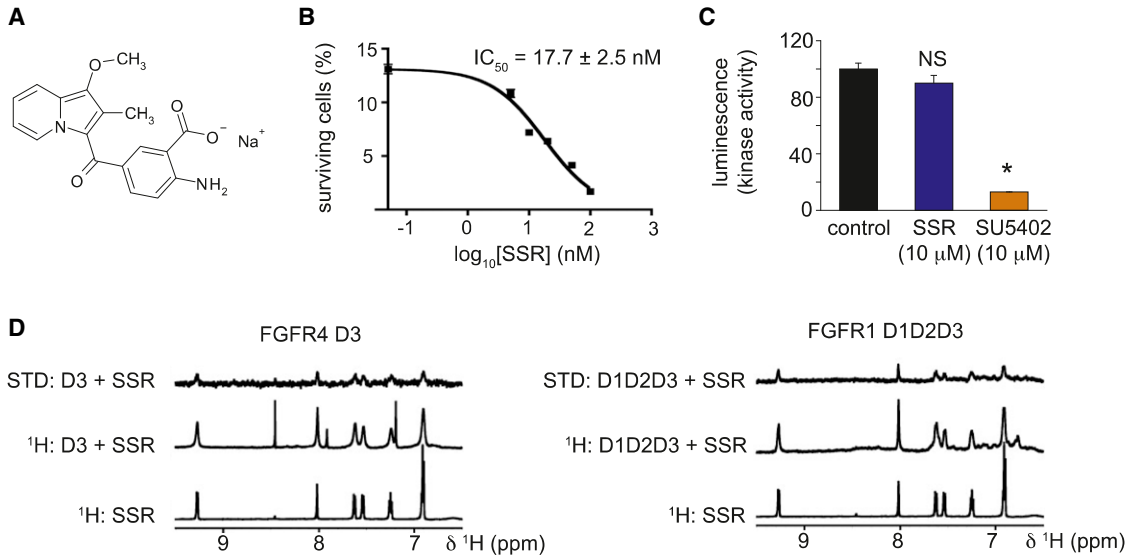

Figure 1. Chemical Structure, Cellular Effects, and NMR of SSR

(A) Chemical structure of SSR128129E (SSR).

(B) Apoptosis assay to study SSR's potency of inhibiting EC survival (mean ± SEM; n = 3).

(C) FGFR2-kinase assay to compare the effect of SSR and SU5402 (mean ± SEM; n = 3). The asterisk indicates that $p < 0.05$. NS, not significant.

(D) ^{1}H and STD-NMR spectra of SSR in the presence of FGFR1 and FGFR4 as compared to the ^{1}H-NMR spectrum of SSR alone.

See also Figure S1 and Table S1.

By using a high-throughput scintillation proximity binding assay (SPA), we identified compounds that inhibited binding of ^{125}I-FGF2 to the extracellular domain of FGFR1, comprising three immunoglobulin-like domains D1–D3 coupled to an Fc-fragment (FGFR1-D1D2D3/Fc). After screening >10^5 compounds and chemical optimization, one compound (SSR128129E, abbreviated as "SSR") inhibited ^{125}I-FGF2 binding with μM affinity, although this effect was not saturated (Bono et al., 2013). These findings suggested a modulation in fibroblast growth factor (FGF) binding but not necessarily binding competition. Further, SSR reduced FGFR phosphorylation but did not cross the plasma membrane, while inhibiting cell proliferation at nM potency. The discrepancy of the inhibition constants between the SPA results and proliferation assay led us to investigate the molecular mechanisms of SSR. Pharmacological experiments showed that this compound inhibited FGF receptor (FGFR) signaling via an allosteric mechanism (Bono et al., 2013), which we studied in more molecular detail here.

RESULTS

SSR128129E Inhibits FGFR and Binds to Its Extracellular Domain

We identified SSR128129E, referred to as "SSR" (Figure 1A), which inhibited the binding of ^{125}I-FGF2 to the extracellular domain (ECD) of FGFR1 at μM concentrations in a SPA assay (Bono et al., 2013). SSR dose-dependently inhibited the survival of endothelial cells (ECs) (IC_{50} < 30 nM; Figure 1B).

Since SSR's effects on FGFR signaling did not result from an inhibition of FGF binding to FGFRs (Bono et al., 2013), impaired dimerization of FGFRs or FGF ligands (Figures S1A and S1B available online), or TK inhibition (Figure 1C), we used saturation transfer difference (STD)-nuclear magnetic resonance (NMR) to analyze if, after FGFR irradiation, the NMR signal (saturation) would spread to SSR, which would indicate that SSR interacts with FGF. However, SSR did not bind FGF1 or FGF2 (Figure S1C).

We assessed if SSR bound FGFR-ECD, in which D2 and D3 constitute the major binding site for FGFs and coreceptors. STD-NMR showed that SSR bound all constructs containing D2 and/or D3 (Table S1). Figure 1D shows the STD-NMR spectra of FGFR1 and FGFR4 with SSR. Together with the functional assays, these data suggest a direct (orthosteric) or indirect (allosteric) inhibition of FGF binding to ECD of FGFR and/or the biological function of the receptor.

SSR Inhibits FGF-Induced Signaling and Endocytosis Pathways

To dissect how SSR interfered with FGFR, we studied its effect on ERK1/2 activation and FGFR endocytosis. SSR blocked the FGF2-induced increase in ERK1/2 phosphorylation (Figure 2A) and translocation of cell surface FGFR4 to the cytosol (Figure 2B). In addition, SSR inhibited the FGF2-induced intracellular accumulation of early endosomal antigen1 positive ($EEA1^+$) vesicles, the destination of internalized FGFRs (Figures 2C and 2D). Similar effects of SSR on FGFR internalization and phosphorylation of FRS-2 (target of FGFR2) and ERK1/2 were observed in human gastric SNU-16 cancer cells, in which these processes rely on FGF7/FGFR2 (Figures 2E and 2F), and in FGFR2-overexpressing L6 cells (see below). Blockage of FGFR internalization could explain the inhibition of FGFR signaling, though other opinions exist (Belleudi et al., 2007; Reilly et al., 2004).

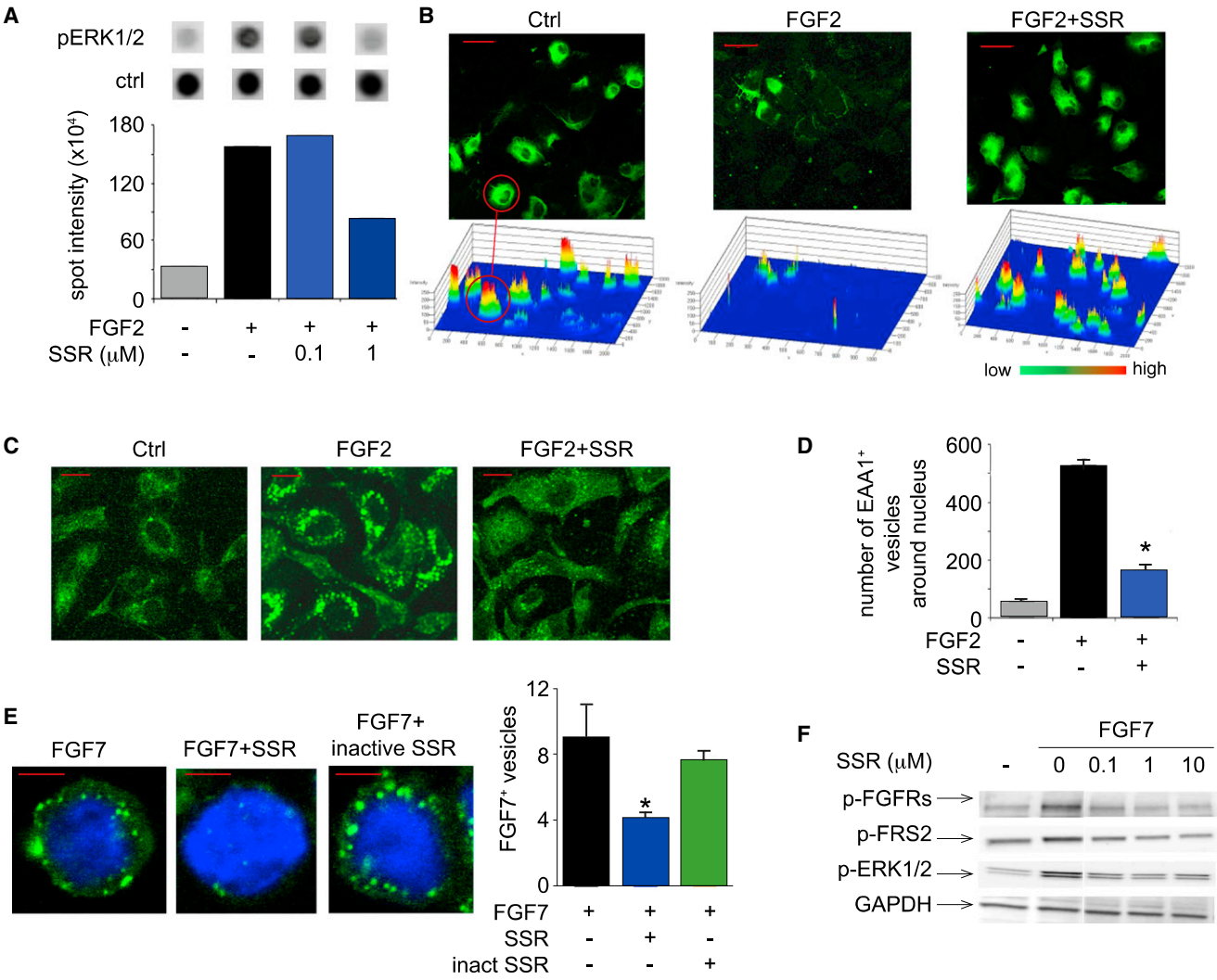

Figure 2. Effect of SSR on FGFR-Signaling and Endocytosis

(A) Phosphoproteome profiler array of ECs in baseline and response to FGF2 in the presence or absence of SSR (n = 3).

(B) Micrographs of cell surface-localized FGFR to study FGF2-induced internalization of FGFR4 with or without SSR (top). Immunoreactive signal for single cells is quantified in the 2.5D intensity plot (bottom).

(C and D) Staining of FGF2-stimulated ECs for EEA1 in the presence or absence of SSR. Representative images are shown in (C) and quantification result of EEA1$^+$ vesicles is shown in (D, n = 3).

(E) Stimulation of SNU-16 cells with FGF7-alexa488 to study SSR's effect on endosomal trafficking; SSR119501: inactive SSR-analog (n = 3).

(F) Immunoblotting of SNU-16 cell extracts to study the effect of SSR on FGF7-induced phosphorylation of FGFR2 (p-FGFR), FRS-2 (p-FRS-2), and ERK1/2 (p-ERK1/2). GAPDH: loading control. Scale bars: 50 μm (B); 20 μm (C); 10 μm (E). In (D) and (E): mean ± SEM. The asterisk indicates $p < 0.05$.

Structural Properties of Extracellular FGFR Domains D2 and D3

To map the interaction site of SSR with FGFR-ECD, we first generated two-dimensional (2D) ^{15}N-HSQC NMR spectra of FGFR-ECD in the absence of SSR to obtain the protein's fingerprint. Peaks in this spectrum correspond to amide groups (and nitrogen-containing side-chains). Since chemical shift perturbations (CSPs) of these peaks are sensitive to the chemical environment, this technique allows identification of SSR interaction sites with FGFR-ECD.

The spectrum of D2 showed sharp peaks and spectral dispersion, as expected for a well-folded domain with defined structure, and all NMR resonances were assigned to a particular residue. In contrast, the signals of D3 could not be detected, because they were broadened beyond detection, indicating that D3 does not adopt a stable, persistent three-dimensional (3D)-fold (Figures S2A–S2F). This behavior is consistent with a transiently unfolded flexible state, a phenomenon confirmed by D3's high tendency to aggregate (data not shown). Because this behavior can be an inherent property of the domain or, alternatively, a preparation artifact compromising the analysis of a potential interaction with SSR, we generated preparations of functional, structured D3. However, optimization of conditions to solubilize D3, variations of D3 constructs (with/without

membrane or D2D3-Linker), or attachment of solubilizing fusion constructs (thioredoxin, protein G) all failed to yield spectra consistent with a stable D3 fold, while the other domains remained readily detectable (Figures S2A–S2D).

Such a very flexible (intrinsically disordered; Tompa, 2011) state of proteins can be characterized by computer simulations that estimate the preferred conformational state and stability of various parts of the protein. We therefore performed multi-μs-long, unbiased, all-atom, explicit-solvent molecular dynamics (MD) computer simulations with the Amber99SB*-ILDN force field. In line with NMR data, D3 was marginally stable and partially disordered in solution. The Thr^{319}-Arg^{330} region, which has an extended β-conformation in the crystal structure, tended to adopt an α-helical conformation and to detach from the protein core, leading to partial unfolding of the domain. Plasticity of this region, in particular of the βC′-βE loop (Pro^{307}-Val^{332}) plays a key role in the specificity of FGF binding to FGFR splice variants (Beenken and Mohammadi, 2009). Noteworthy, the algorithm AGADIR also predicted a propensity for α helix conformation of the Thr^{319}-Arg^{330} region, thus independently confirming the MD computer simulations.

To assess if the flexibility of D3 corresponds to a completely random (random coil) or compact but unfolded (molten globule [MG]) state and to verify the chemical purity and quality of the protein used in the NMR experiments, we performed FGFR2-D2D3 crystallization trials. We resolved a similar structure of the FGFR2-FGF1 complex, as reported (Plotnikov et al., 1999; Schlessinger et al., 2000). A defined electron density of D3 revealed a stable structure, suggesting that D3 is only marginally unstable and ready to fold in conditions of crystallization and/or upon forces taking place in the crystal. These observations are compatible with a molten globule state of D3 (in line with the increased aggregation propensity and disappearance of NMR peaks). Control experiments showed that the amino acid composition of the urea-unfolded D2D3 polypeptide chain was correct (Figures S2E and S2F), that D3 folding was not enforced by crystallization conditions (Figures S2G and S2H), and that D2D3 interacted with FGF1 (Figures S2G and S2I). Since the crystal structure indicates that D2 and D3 are needed to interact with FGF (Plotnikov et al., 1999; Schlessinger et al., 2000), these findings show that D3 is present and functional. Thus, D2 is well folded, while D3 is in an unfolded MG state that is ready to fold.

Mode of Action of SSR: Effects on D2

We then explored to which sites SSR binds in the FGFR ECD and used 2D NMR to determine the CSP values upon addition of SSR to D2 of FGFR1, FGFR2, and FGFR4. SSR-induced CSPs were mapped on the X-ray structure of FGF2/FGFR1-D2D3/heparin (Protein Data Bank [PDB] code 1FQ9; Schlessinger et al., 2000). The CSPs suggested a conserved binding site of SSR in the vicinity of—but not overlapping with—the heparin binding site of D2 (red balls show residues interacting with SSR in D2 of FGFRs; Figures 3A and 3B). Chemical shift titration analysis yielded a binding affinity of SSR to D2 of FGFR1, −2 and −4 in the mM range (Table S2). These affinities are two to three orders of magnitude too low to explain the μM SPA data. Moreover, the computational estimation of the free binding energy of SSR to FGFR2-D2 (~5 kcal/mol) is in line with the mM range of the observed K_D values (Figure 3C). Thus, an interaction of SSR with D2 alone cannot account for the cellular effects.

We therefore performed binding experiments with FGF/FGFR complexes. Since NMR signals only appear if the protein is labeled with ^{15}N isotope, FGFR or FGF was labeled separately to dissect to which component SSR binds. The effect of SSR on the 2D NMR spectra of (^{15}N)FGFR2-D2D3/FGF1 and FGFR1-D1D2D3/(^{15}N)FGF2 is shown in Figure 3D and mapped on the crystal structure 1FQ9 in Figure 3E. The spatial CSP clustering indicates a binding site for SSR at the interface between D2 and FGF, in agreement with the binding of SSR to D2 alone. Confirming STD-NMR experiments that SSR does not bind to FGF1 or FGF2, SSR induced CSPs in FGF only when a FGF/FGFR complex was formed. When analyzing the complex between FGFR1-D1D2D3 and (^{15}N)FGF2, two additional CSPs were observed: Asn^{101} (facing D2 in crystal structure 1FQ9) and Ala^{57} (facing D3; black circle in Figure 3E, bottom), suggesting an additional binding site for SSR in D3. To evaluate SSR's affinity for FGFR/FGF, we performed NMR titration experiments of FGF1/FGFR1-D1D2D3 with SSR, yielding an affinity constant in the low μM range (~50 μM; Figure 3F). Due to the structural disorder of D3, a binding mode could not be deduced. Together, the CSP data indicate a binding site on the interface between FGF and D2 and a potential binding site on D3. A role for D3 in SSR binding is supported by the mM affinity of SSR to D2 alone, too low to explain the biological effect.

Mode of Action of SSR: Low Resolution FGF-FGFR Crystals

To further assess the molecular basis of the allosteric interaction, we performed X-ray crystallography. Crystals of FGF1/FGFR2-D2D3 complexes with SSR could not be optimized to a suitable diffraction quality, but it was possible to generate crystals with SR128545 (abbreviated as "SR"; Figure S3A), a SSR analog with comparable cellular activity (Figure S3B). Limited by a diffraction resolution of 4.2 Å, the exact binding position of SR could not be visualized, but conformational protein backbone changes induced by the interaction with SR were detectable. Molecular replacement (MR) statistics of Phaser (McCoy et al., 2007) were used to compare the observed X-ray diffraction pattern to existing 3D models. This revealed single solutions without structural clashes when independently using the three separate domains (FGF1, FGFR2-D2, and FGFR2-D3) of the FGF1/FGFR2/heparin crystal structure (PDB code 1E0O; Pellegrini et al., 2000). These results confirm that the obtained crystal structures were in agreement with published results (PDB codes 1CVS and 1DJS). We also analyzed the translation function Z-scores (TFZ), as they are a measure of how well the MR model fits to X-ray data (a high score indicates a good match). TFZ scores in the presence of SR were smaller for D3 than for D2 or FGF1 (FGF1/SR = 23.1, FGFR2-D2/SR = 15.7, and FGFR2-D3/SR = 7.5), showing that the structure solution cannot explain the entire scattering pattern in the presence of SR but rather suggests a structural change induced by SR.

To confirm the above findings and to determine conformational dynamics, we refined the structure of the FGFR2-D2D3/FGF1/heparin/SR complex by generating polyalanine models using Refmac5 to obtain a model that best explains the experimental data (Murshudov et al., 1996). The electron density of

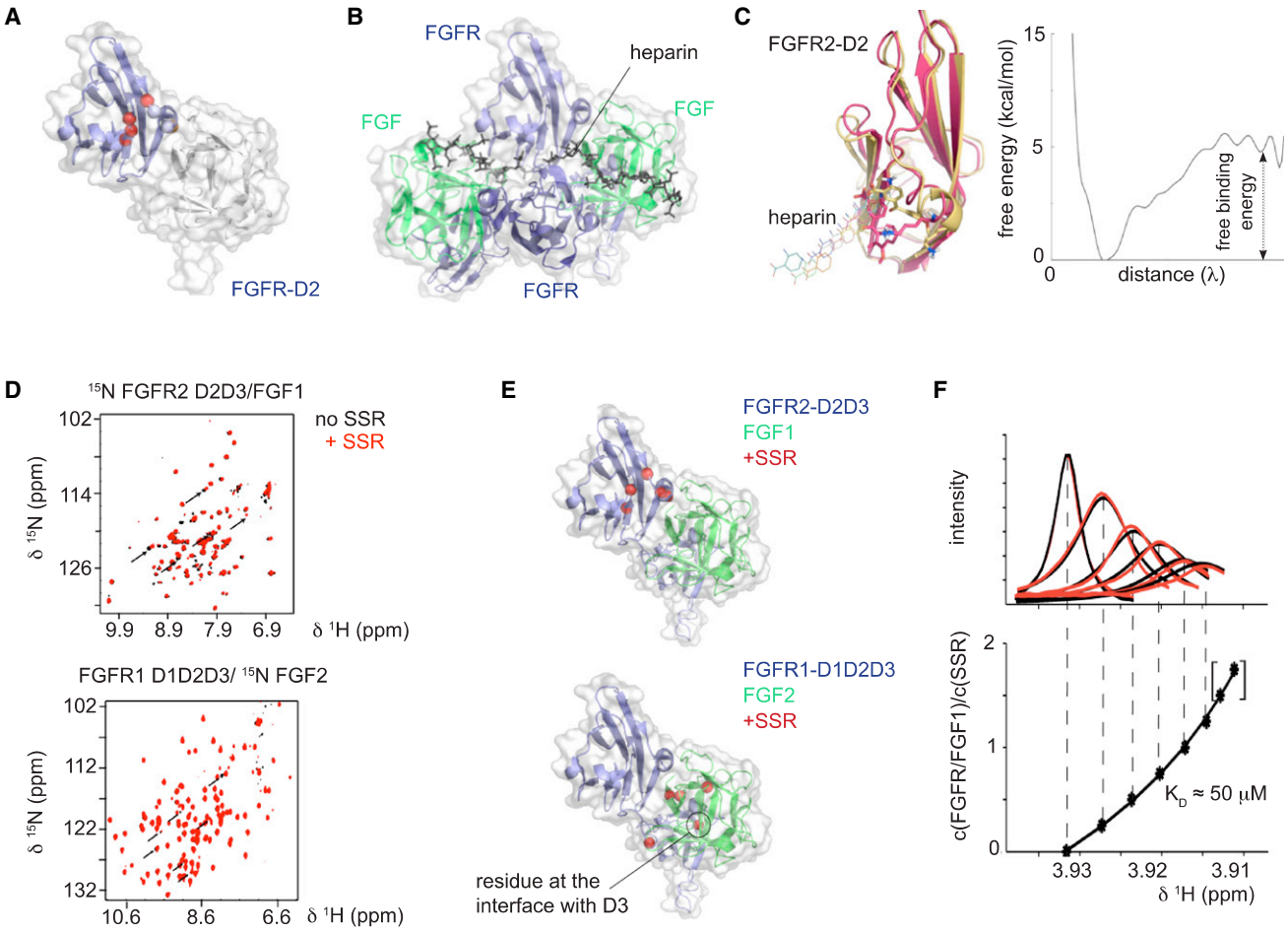

Figure 3. 2D-NMR Analysis and Free Energy Profiles

(A and B) Surface representation of FGFR (blue) and FGF (green), showing the SSR binding site in FGFR2 and FGFR4. Amide signals, shifting due to addition of SSR in 2D ^{15}N-HSQC NMR, were mapped onto the X-ray structure of FGFR1-D2D3/FGF2/heparin mimetic (1FQ9). (A) Highlight of the shifting amide residues of D2 of FGFR2 and FGFR4, induced by SSR. Red balls indicate residues shifting in both FGFRs (Thr^{150}, Phe^{170}, Arg^{171}, and Cys^{172}; numbering according to FGFR4). His^{151} and Arg^{154} (light blue balls) only shift in FGFR4-D2, and Lys^{164} (orange ball) is only affected in FGFR2-D2. For both receptors, an identical binding site of SSR was observed. For clarity, only one molecule of FGF and FGFR is shown. (B) For comparison, the binding sites of the saccharide heparin molecules are depicted in black/gray. The complex with heparin consists of two FGFs and FGFR-D2D3 molecules.

(C) Cartoon representation of the main binding mode of SSR to FGFR2-D2 (from NMR in this study, yellow; from MD modeling, pink) as predicted from free energy calculations and docking (left), with its corresponding binding free energy profile for SSR, as calculated by metadynamics (right). The low free binding energy corresponds to the low affinity (mM) of binding, as revealed by NMR studies. Binding of heparin is also shown.

(D) Overlay of the [^{1}H,^{15}N]-TROSY HSQC spectra, revealing CSPs induced by SSR on ^{15}N FGFR2-D2D3/FGF1 (top) and FGFR1-D1D2D3/^{15}N FGF2 (bottom); SSR-induced CSPs are indicated by arrows: black without SSR and red with SSR.

(E) CSPs induced by SSR in the experiments shown in (D) were mapped to the X-ray structure (1FQ9). Red balls denote residues showing CSP. Only one molecule of FGF and FGFR is shown.

(F) NMR titration experiments of the FGF1/FGFR1-D1D2D3 complex with SSR. Top: ^{1}H 1D signal of the SSR methoxy resonance. Black lines show the measured spectra; red lines indicate a least square fit using full signal simulation (performed by variation of K_D and k_{off}). Bottom: Chemical shift of the peak maximum (*x* axis) as a function of the ratio of complex to SSR concentration. Asterisks show the experimental values; the solid line results from a least square fit of the chemical shift data by variation of the reaction parameters.

See also Figure S2 and Table S2.

all domains was fully recovered by molecular replacement after separate deletion of single domains in the PDB file. In the presence of SR, the density of FGFR2-D3 was weak around a β sheet region (β2 at Asp^{272}-Val^{277} and β5 at Glu^{325}-Ile^{329}) located ~25 Å away from the orthosteric FGF-ligand-binding region in D3. Comparison of FGFR2-D2D3/FGF1 structures in the absence and presence of SR revealed no conformational differences. However, strong differences in the Debye-Waller factors (B-factors; higher values suggest flexibility) were observed. Surprisingly, the average B-factor of the X-ray protein structure in the presence of SR was strongly increased. Specific regions in FGFR2-D3 at β1β2 (Ala^{266}-Val^{277}) and α1β5 (Thr^{319}-Ile^{324}Glu^{325}-Ile^{329}) showed large decreases in the occupancy of atoms, resulting in high B-factors (Figure 4A). Together,

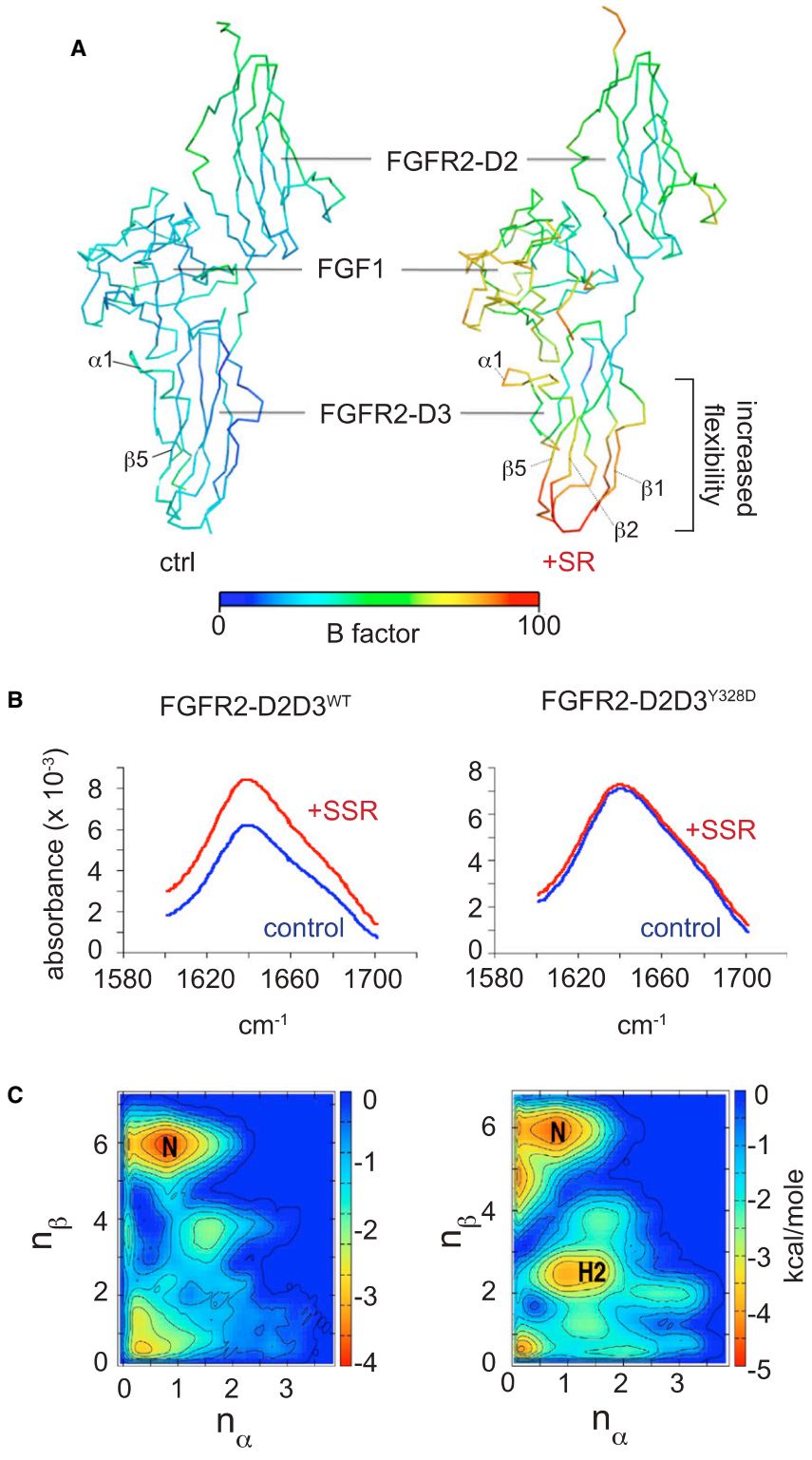

Figure 4. Crystallography, FTIR Analysis, and Free Energy Calculations

(A) 3D representation of the X-ray crystal structure of FGFR2-D2D3/FGF1 complex in the absence (left) and presence (right) of SR. The change in colors (B-factor values) suggests increased flexibility of D3 at α1/β5 after SR binding.

(B) FTIR measurements of FGFR2-D23^{WT} and FGFR2-D23^{Y328D} in the absence (blue) or presence (red) of SSR.

(C) Calculated free energy surfaces as a function of the β sheet and α helix content (nβ and nα, respectively; see Supplemental Information) in the absence (left) or presence (right) of SSR. The native state is marked with "N". Note the appearance of a new free energy minimum corresponding to the H2 state.

See also Figure S3.

Mode of Action of SSR: Effect of SSR on FGFR-D3

The finding of an intrinsically disordered D3 domain in NMR studies and MD simulations together with the SR-induced increase of its B-factors in the X-ray structure led us to further investigate the influence of SSR on D3 using Fourier transform infrared (FTIR) spectroscopy and in silico methods. By obtaining an infrared spectrum of absorption, FTIR provides information on the transition from one to another conformation. Addition of SSR to FGFR2-D2D3 increased the amplitude of the amide I band in the FTIR spectrum with a maximum at 1,640 cm^{-1} (Figure 4B), suggesting that binding of SSR leads to a conformational change of FGFR-D2D3 (similar results were obtained when analyzing FGFR2-D1D2D3), in agreement with the AGADIR prediction.

We used state-of-the-art free energy (ΔG) calculations and computer modeling to unravel how the conformational landscape and flexibility of D3 changed in the presence of SSR. The free energy calculations were performed with the Gromacs 4 package and PLUMED plug-in using metadynamics, bias exchange metadynamics, and steered MD approaches and the Amber99SB*-ILDN force-field (Best and Hummer, 2009; Piana and Laio, 2007). Similar techniques were used previously to predict the free energy landscapes associated with conformational changes and ligand binding in kinases (Lovera et al., 2012; Saladino et al., 2012). Comparison of the free energy landscapes of D3 as a function of the β sheet and α helix content predicted that SSR stabilizes helix α1 (Thr^{319}-Ile^{324}) and induces a β sheet to α helix transition of part of β5 (Gln^{325}-Ile^{329}), thereby nearly doubling the number of turns in helix α1. As a result, D3 undergoes a conformational rearrangement into an intermediate

the conformation of the FGF-FGFR complex and flexibility of FGFR2-D2 or FGF1 were not strongly affected by SR. However, TFZ scores, disturbed electron density maps, and increased B-factors suggest increased structural dynamics of D3, resulting from different conformational states induced by SR.

"H1" state, which progresses to state "H2," where a new hydrophobic cavity, not accessible in the native form of D3, is formed, in which the hydrophobic Tyr^{328} residue (solvent exposed in the native configuration) now faces the core of D3 (Figures 4C and S3C). The difference in free energy between the crystallographic fold of D3 and the refolded H2 state, calculated by two independent approaches (bias exchange metadynamics and steered MD simulations) was 2 to 3 kcal/mol. These data, in agreement with NMR and X-ray observations, suggest that D3 binds SSR and undergoes conformational rearrangements without becoming fully structured in the SSR-bound state.

Mode of Action of SSR: Helix-Breaker Mutations

To assess the importance of Tyr^{328} in the conformational changes of FGFR-D3, we mutated this residue to aspartate, which has known "helix-breaker" properties (to yield FGFR2-D2D3^{Y328D}, termed FGFR2^{Y328D}), as this mutation should reduce the helical tendency and impair the conformational change. Indeed, we hypothesized that the hydrophilic Asp^{328} would destabilize the α-helical conformation and that SSR would not be able to induce a conformational change in FGFR2^{Y328D}. FTIR revealed that FGFR2^{Y328D} did not exhibit a major shift in its spectrum in the absence of SSR, showing that its overall 3D configuration was preserved. Conformational analysis by FTIR showed, however, that SSR failed to induce a change in the spectrum of FGFR2^{Y328D} (Figure 4B). This effect was specific, as additional mutations of the Y328 residue (Y328R/I329K) still showed the same structural change as FGFR2^{WT} upon addition of SSR, illustrating that not any type of mutation of Y328 per se could rescue the SSR effects (data not shown).

The aforementioned observations suggest that SSR does not directly compete with FGF binding, but rather that it alters the conformational ensemble of FGFR-ECD, which allosterically propagates into receptor function changes. The β to α transition of the β5 helix (Glu^{325}-Ile^{329}) is critically involved in this allosteric effect. To assess the relevance of Tyr^{328} in transmitting SSR's allosteric activity, we generated HEK293 cell lines expressing wild-type FGFR2^{WT} or mutant FGFR2^{Y328D}. In the absence of SSR, FGFR2^{WT} and FGFR2^{Y328D} cells exhibited a similar ERK1/2 response to FGF2, showing that the mutation did not change FGFR's response to FGF. The mutation did also not alter orthosteric binding of ^{125}I-FGF2 (K_D: 54 ± 8 pM for FGFR2^{WT} versus 52 ± 9 pM for FGFR2^{Y328D}; n = 5; p = NS). However, SSR's ability to inhibit FGF2-induced ERK1/2 phosphorylation was reduced in FGFR2^{Y328D} cells (IC_{50} value: 121 ± 30 nM) as compared to FGFR2^{WT} cells (IC_{50} value: 28 ± 12 nM; $p < 0.05$) (Figures 5A and 5B). Similar data were obtained for FGFR2 phosphorylation and phospho-FRS2 signaling (Figures 5C and 5D).

We also stably overexpressed FGFR2^{WT} or FGFR2^{Y328D} in L6 myoblast cells (which lack endogenous FGFRs). Transduced cells were treated with AlexaFluor488-conjugated FGF2, leading to the formation of FGF2/FGFR2 at the cell membrane and its internalization in endocytic vesicles. Upon stimulation, FGFR2^{WT} and FGFR2^{Y328D} were comparably endocytosed (Figures 5E and 5F). Notably, SSR reduced endocytosis in FGFR2^{WT} but not in FGFR2^{Y328D} cells (Figures 5E and 5F). To unravel the endocytic pathway, inhibitors of clathrin- (Pitstop2) and caveolin-dependent (Dyngo-4a) pathways were used. Only Dyngo-4a affected endocytosis of FGFR2^{WT} and FGFR2^{Y328D}, indicating that the FGF2 endocytic pathway relies on caveolae-dependent internalization (Figures 5E and 5F), consistent with previous reports (Irschick et al., 2013). Thus, FGFR2^{WT} and FGFR2^{Y328D} showed similar profiles with respect to FGF2 affinity, ERK1/2 phosphorylation, and receptor internalization, but SSR inhibited signaling more efficiently in FGFR2^{WT} than FGFR2^{Y328D} cells. Thus, by altering the β to α transition of the β5 strand and thereby elongating the α1 helix, SSR modulates inhibition of FGFR signaling and internalization.

Mode of Action of SSR: Binding of SSR to D3 H2

Because of the flexibility in D3, we performed in silico binding studies using metadynamics, a recently developed method to dock ligands on receptors in water solution, allowing protein flexibility (Laio and Gervasio, 2008). This revealed that the free energy of binding to the hydrophobic cavity in the H2 state was −10.2 kcal/mol (Figure 6A), reflecting tight binding in the nM range. Overall, very long all-atom MD simulations and free energy calculations with metadynamics confirmed that SSR alters the flexibility and conformational propensity of D3. The stability of the helical region in FGFR2-D3 is enhanced by an initial step of low-affinity SSR binding, thereby making a new metastable H2 state accessible, which is stabilized by docking of SSR (Figures 6B–6D and S3C). Superposing D3′s structure in its SSR-bound H2 state with previously identified crystal structure of FGFR2-D2D3 showed that the FGF-interacting residues remain unaffected, in line with findings that SSR did not alter the affinity of FGFs.

In addition, free energy calculations showed that FGFR2^{Y328D} underwent helix elongation and adopted the conformational state H2, though H2 was less stable. This relates to the fact that stabilization of the cavity is largely due to interactions of the hydrophobic Tyr^{328} with the core of D3 and that these interactions are highly unfavorable in FGFR2-D3^{Y328D}, in which the hydrophilic Asp^{328} prefers solvent exposure rather than buried conformations. Our finding that Y328D reduces but does not eliminate SSR binding explains why FGFR2^{Y328D} is still capable of binding SSR but also why its signaling is inhibited less by SSR.

Structure-Activity Relationship Analysis

Experimental and computational approaches suggest a nonconventional allosteric regulation of FGFR function by binding of SSR to the disordered ensemble of D3. MD simulations outline the major structural features of the H2 state and schematic features of the arising binding cavity. To further probe the molecular details of the D3-SSR interaction, we analyzed the structure activity relationship (SAR) of a set of 19 SSR analogs by comparing their biological activity (inhibition of phospho-ERK1/2 signaling) to their capacity to dock into the in silico-identified binding pocket of D3 (H2 state) using the Schrödinger Glide XP package on the nonflexible H2 state of FGFR2-D3. As shown in Table S3, two active SSR analogs inhibited ERK1/2 phosphorylation with a comparable efficiency as SSR ($IC_{50} \sim$ 10–100 nM); their activity was reduced in FGFR2^{Y328D} cells (Table S4), confirming the specificity of their activity. Six other compounds had weak biological activity ($IC_{50} \sim$ 100–1,000 nM), while another ten molecules were inactive ($IC_{50} >$ 1,000 nM). One compound could not be tested because of insolubility. Docking experiments showed that the binding energy generally correlated

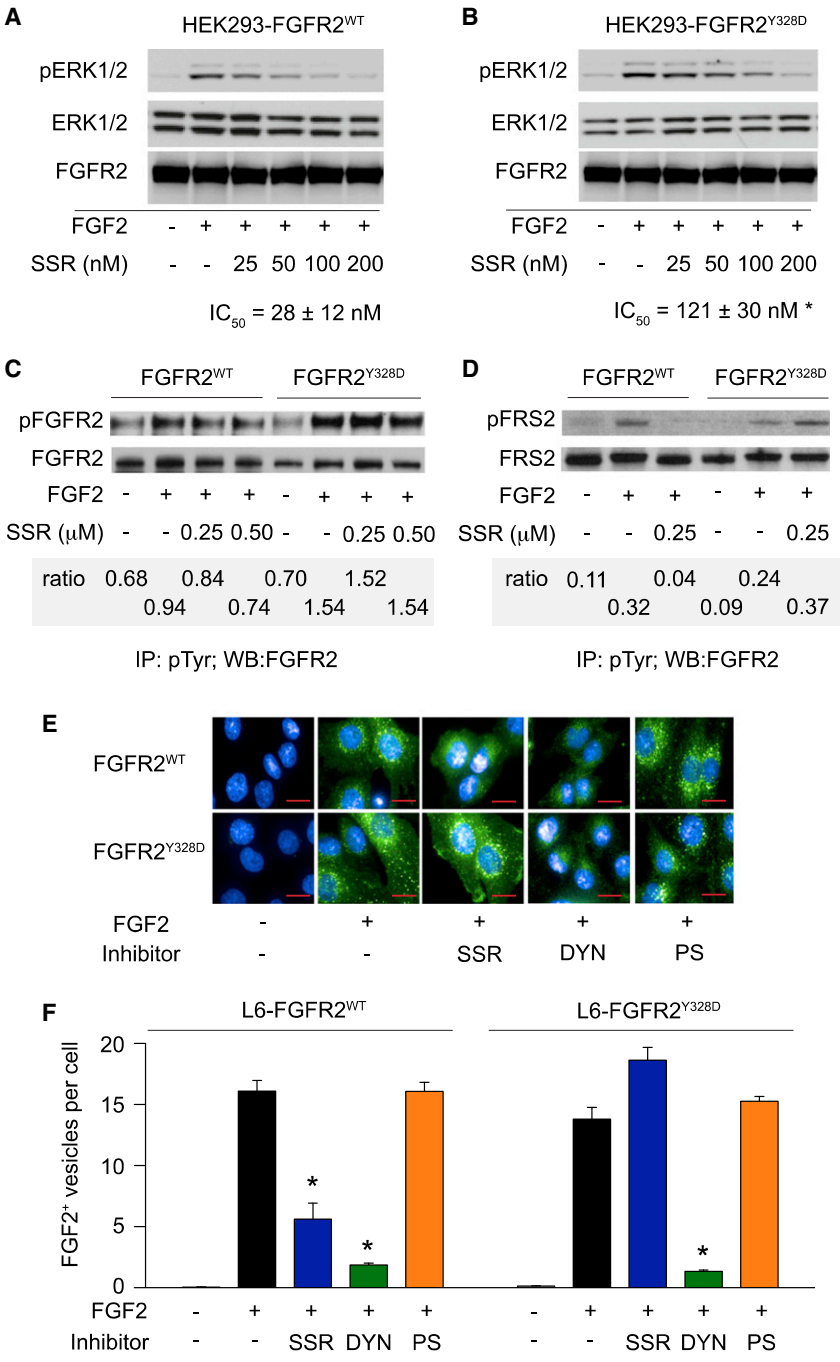

Figure 5. FGFR Signaling in FGFR2^{WT} and FGFR2^{Y328D} Cells

(A–D) Analysis of inhibition of FGFR2^{WT} or FGFR2^{Y328D} by SSR in HEK293 cells stably expressing these proteins using immunoblot. Phosphorylated ERK1/2 (pERK1/2) and total ERK1/2 (ERK1/2), upon FGF2 stimulation, were determined and ratios of pERK1/2 over total ERK1/2 were used to calculate IC_{50} values (A and B; mean ± SEM, n = 3). The asterisk indicates $p < 0.05$ versus FGFR2^{WT}. FGFR2 was used as loading control. Similar results were obtained when analyzing phosphorylation of FGFR2 (C) and FRS2 (D) upon prior immunoprecipitation for phosphotyrosine (pTyr) residues (the ratio of phospho- over total protein is shown).

(E and F) Analysis of endocytic vesicle formation in L6 myoblasts stably expressing FGFR2^{WT} or FGFR2^{Y328D} and stimulated with AlexaFluor488-conjugated FGF2 in the presence of control, SSR (1 μM), Dyngo-4a (3 μM, DYN), or Pitstop2 (1 μM, PS). Representative images are shown in (E) (scale bars: 20 μm), and the result of quantification of the number of AlexaFluor488-conjugated FGF2 endocytic vesicles is shown in (F). Each bar corresponds to the number of vesicles detected on 28–30 views from three different wells (mean ± SEM; n = 3). The asterisk indicates $p < 0.05$ versus FGF2 alone.

with biological inhibition and that the binding strength of the active compounds was significantly higher than of the weak and inactive compounds (Figure S4A).

Computational modeling suggested that several critical substitutes were adjacent to residues in the Thr^{319}-Arg^{330} region (i.e., R1 and R2 in the vicinity of Leu^{327}-Tyr^{328}-Ile^{329} and R′ and R″ pointing toward Thr^{319}-Thr^{320}-Glu^{323}-Ile^{324}; Figure 7A). More detailed analysis revealed the following insights (Table S3): (1) R′ group: a carboxylate group (or amide bioisostere) at R′ is required for full biological activity (compound 7); changing this group abrogated SSR's activity (compounds 10–13,16); switching the carboxyl group at R′ and the aniline group at R″ retains residual activity (compound 5), likely because of sufficient docking, but this configuration is less favorable because one charge-charge interaction (with Lys^{279}) and a H-bond between neutral groups (Thr^{319}, Thr^{320}) are replaced with H-bond interactions between charged and neutral groups; (2) R″ group: the aniline group is required as its removal (compound 4 and 17) or monomethylation (compound 6) lowered the activity, in line with the observation that these compounds had reduced polar and H-bond interactions in the H2 state; (3) R1 group: switching the methoxy group for a carboxyl group prevents docking into the H2 pocket (compound 11), but this group can be replaced by a hydrogen atom without losing activity (compound 3), highlighting the need for hydrophobic interactions not compatible with negative charge; and (4) R2 group: the methyl group can be substituted by a cyclopropyl group, retaining potency consistent with comparable hydrophobic interactions with the pocket (compound 2).

These data confirm that the Thr^{319}-Arg^{330} region is important for SSR binding and transduction of the allosteric information. Noteworthy, the R1 moiety facing Tyr^{328} is critical, explaining why SSR binding and inhibitory activity were impaired by the bulky methoxybenzamide and methoxybenzenesulfonamide at R1 (compounds 17 and 18). Likewise, the bulky CONHMe at R6 (compound 8) is not tolerated, probably because of steric clashes with the hydrophobic pocket. Other substitutions

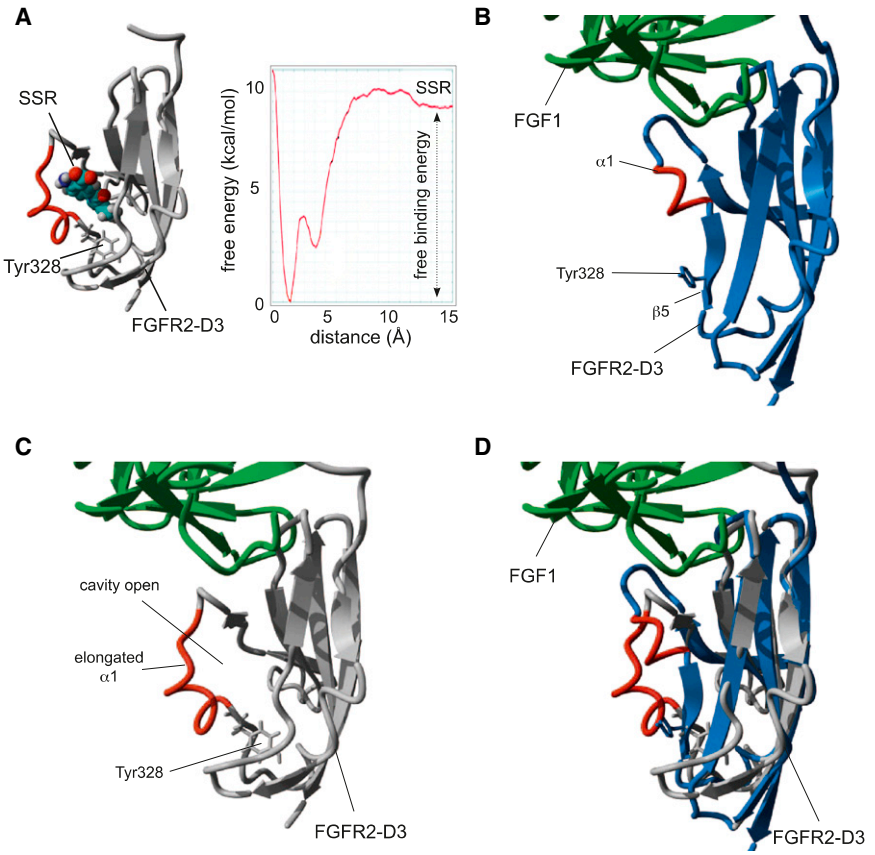

Figure 6. Free Energy Calculations and Conformational States

(A) Cartoon representation of the main binding mode of SSR to FGFR2-D3, as predicted from free energy calculations and docking (left) and the corresponding binding free energy profile for SSR as calculated by metadynamics (right).

(B–D) Cartoon representation of the conformation adopted by FGFR2-D3 in the native state (without SSR) (B) and in the H2 state in the presence of SSR (C), as obtained by calculating the free energy using molecular dynamics modeling (for reasons of clarity, SSR itself is not shown); the overlay is shown in (D). Note the elongated helix α1 and the position of Tyr^{328} pointing toward the hydrophobic core of the domain in the H2 state compared to the native state. FGF1, green; native FGFR2-D3, blue; FGFR2-D3 "H2" conformation, gray; helix α1, red.

abrogated the function, even though they did not interfere much with binding itself, which is compatible with the allosteric mode of action, in a sense that not binding per se but rather the conformational change induced by the SSR derivative matters.

On a subset of active, weak, and inactive compounds (Table 1), we performed biophysical (STD-NMR and waterLOGSY-NMR; Bretonnet et al., 2007) experiments to assess their binding capacity to FGF1/FGFR2-D2D3. Also, to allow flexibility of protein movements, we calculated the free binding energy (ΔG) of these compounds using metadynamics, which, in contrast to standard modeling on a rigid structure, also takes into account movements of the protein. The agreement between the calculated ΔG and biological activity is superior to that obtained with the Glide XP score (Table 1; Figures 7B and S4B). For instance, when we subtract the thermodynamic penalty of state H2 (2 to 3 kcal/mol) from the calculated binding free energies, we obtained −8/−9 and −9/−10 kcal/mol for SSR and compound 2, which is in very close agreement with the expected value of −8.5 kcal/mol for compounds in the 100 nM affinity range. An agreement is also obtained for weak and inactive compounds. The superior agreement of the free energy (calculated by Metadynamics) over the docking scores (calculated by Glide XP) stresses the importance of considering flexibility and explicit water hydration.

This view is also supported by NMR measurements, in which STD and waterLOGSY NMR were used to rank binding of this subset of compounds (Table 1). The NMR data are in good agreement with the calculated binding energy values and biological potency. Two compounds from the active group bound the strongest, and SSR itself was the third strongest binder, which also underscores that, besides binding strength itself, the compatibility with the structural allosteric transition is also important for the effect of the compound. Again, adding large groups at R1 induces the most profound effect (compound 17 being the weakest and compound 18 being undetectable by NMR due to protein precipitation). Overall, the binding affinity of SSR variants and their allosteric effect of binding generally correlate: the stronger a derivative binds, the more it drives the conformation of the receptor toward the inhibited ensemble.

DISCUSSION

In the accompanying paper (Bono et al., 2013), we identified SSR, a synthetic inhibitor of the FGF tyrosine kinase receptor, and provided pharmacological evidence for an allosteric mechanism. This orally deliverable, small-molecule, multi-FGFR inhibitor showed promising therapeutic anticancer efficacy (Bono et al., 2013). SSR does not affect orthosteric FGF ligand binding, cannot penetrate the membrane, and does not directly block the TK activity but exhibits typical pharmacological allosteric features. Indeed, the compound shows signaling bias by inhibiting ERK1/2 activation (relying on FGFR internalization) without altering phospholipase C (PLC)-γ phosphorylation, has a "ceiling" effect, and exhibits "probe dependence" (Bono et al., 2013). All these findings suggest an allosteric conformational effect that discriminatively affects the readout of receptor activation. In this study, efforts were made to unravel the molecular mechanisms of the allosteric activity of SSR. The challenge in these investigations is due to both the complexity of the FGFRs and the disordered, even unfolded nature of domain D3, which is prone to aggregation, invisible to NMR, and highly flexible in the X-ray structures in the presence of SSR.

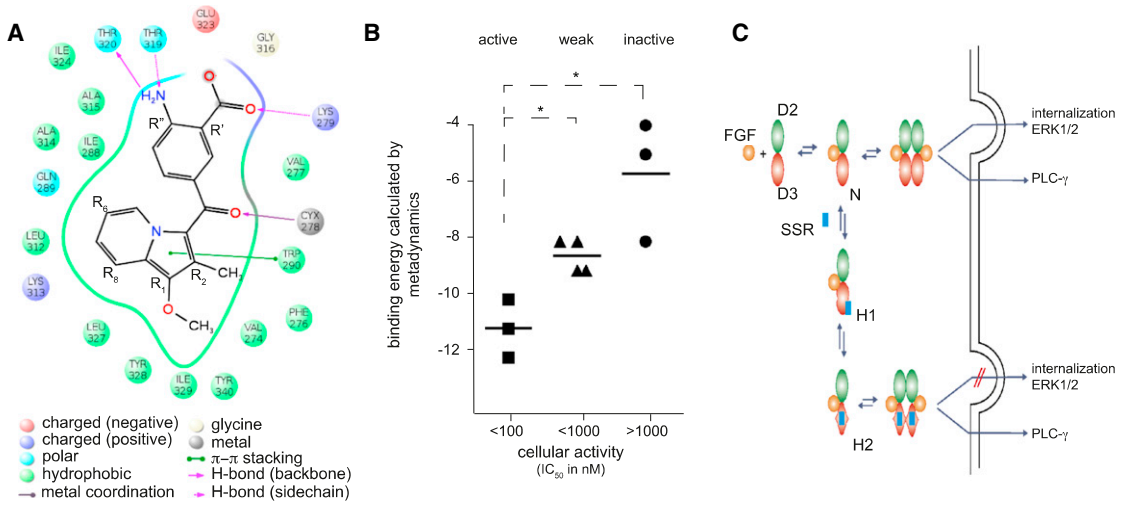

Figure 7. SAR and Hypothetical Model of the Allosteric Regulation of FGFR by SSR

(A) Scheme of the putative SSR binding pocket in the newly exposed cavity in the H2 state, used for the docking analysis to obtain the SAR. The position and type of individual amino acid residues and putative interactions are indicated. The colored band lining the cavity represents hydrophobicity (green is hydrophobic; blue is charged).

(B) Scatterplot analysis of calculated binding energy using metadynamics of the three different classes of compounds from the SAR analysis. The compounds of each group are shown in Table 1. The asterisk indicates $p < 0.05$ between the indicated conditions (dashed lines); horizontal full lines represent averages.

(C) Under normal conditions, heparin sulfate-bound FGF (orange circle) binds to FGFR ECD via D2 (green) and D3 (red). While D2 is well folded, D3 is in a disordered native (N, probably corresponding to a molten globule) state. The receptor can dimerize and induce distinct intracellular signaling pathways, such as receptor internalization (leading to ERK1/2 phosphorylation) and PLC-γ phosphorylation. Due to its inherent flexibility, D3 can transit to an alternative disordered state (H1), which is more open and competent for weak SSR binding. From this state, there is a transition to a third disordered state (H2), which binds SSR stronger. In this state, SSR does not inhibit FGF binding or dimerization, but, due to altering the conformational ensemble and/or dynamics of D3, it inhibits receptor internalization. Allostery of the system arises from SSR acting indirectly via long-range conformational effects in the disordered ensemble, attenuating membrane interaction.

See also Figure S4 and Tables S3 and S4.

At first, it may appear surprising that a small molecule like SSR is capable of inhibiting the responses of various FGFRs to multiple FGF ligands if steric hindrance of the orthosteric FGFR pocket was the desired mode of receptor targeting. However, an allosteric interaction with a small molecule can perturb the signaling of a large FGF ligand by inducing a conformational change in FGFR. The model that emerges from computer simulations and modeling reconciles the experimental findings by predicting a marginally stable D3 fold, a weak SSR binding site on D2, and a conformational change in D3 in the presence of SSR. The AGADIR software also independently predicted a conformational preference of α helix over β sheet structure. The conformational change gives rise to a new hydrophobic cavity, to which SSR can bind. A mutation that reduced the α-helical propensity in this region was predicted to suppress the SSR-induced conformational changes in silico and indeed counteracted SSR's ability to inhibit FGFR-driven cellular processes.

The key element of the model is the allosteric nature of SSR's action. Whereas this molecule was selected by using the SPA assay for FGF binding and has nM pharmacological effects, it does not interfere with FGF binding or receptor dimerization in a cellular context. Because SSR is not internalized, it acts on the extracellular part of the receptor. Direct SSR binding to FGFR was indeed demonstrated experimentally, as was the conformational change that is critical for affecting receptor function. Allostery also follows from the "ceiling" effect, the differential effect on distinct downstream signaling pathways, and "probe dependence" (Bono et al., 2013). All these observations can be reconciled with data from structural experiments and modeling calculations in the following model: (1) an SSR-induced conformational rearrangement of D3 is suggested by most techniques; (2) structural disorder of D3 is confirmed by NMR, MD simulations, and high-crystallographic B-factors; and (3) defective receptor internalization in the presence of SSR is shown in cellular assays and suggested by differential pharmacological effects.

Therefore, the structural underpinning of the system is that the actual structural state of domain D3 is probably a conformational ensemble corresponding to a MG state, with a global topology resembling the structure stabilized in crystallography. This domain thus falls into the growing family of intrinsically disordered proteins, which lack well-defined stable folds, yet play key regulatory and signaling roles in many cellular processes (Tompa, 2011). Its dimerization, even without a folding transition, can be envisaged, as in fuzzy complexes (Tompa and Fuxreiter, 2008) such as T-cell receptor zeta (Duchardt et al., 2007; Sigalov et al., 2004). As is the case with MG states, its various conformations are in an intermediate kinetic exchange regime that causes severe line broadening in NMR, making it invisible to the NMR (Park et al., 2011).

The native ensemble of D3 samples the minor state H1, in which the β5 region tends to adopt local helical conformations; this structural state is stabilized by weak interactions

Table 1. Structure Activity Relationship of SSR Analogs

Compound	R_1[a]	R_2	R′	R″	pERK Inhibition (IC_{50} Range, nM)[b]	ΔG of Binding (calculated, kcal/mol)	Glide XP Score	NMR Binding Event (fSTD/fWL)
Active								
1 (SSR)	OMe	Me	COOH	NH_2	<100	−11	−10.3	2.0/3.8
2	OMe	cPr	COOH	NH_2	<100	−12	−11.3	4.9/15.0
3	H	Me	COOH	NH_2	<100	−10[c]	−11.3	4.4/12.6
Weak								
5	OMe	Me	NH_2	COOH	<1,000	−8	−8.2	1.5/3.2
6	OMe	Me	COOH	NHMe	<1,000	−9	−9.8	3.8/11.6
7	OMe	Me	$CONH_2$	NH_2	<1,000	−9	−9.1	ND
9	Et	Me	COOH	NH_2	<1,000	−8	−12	ND
Inactive								
13	OMe	Me	COOMe	NH_2	>1,000	−8	−10.3	ND
14	OMe	Me	COOH	OH	>1,000	−5	−11.9	ND
17	3-Methoxybenzamide	Me	COOH	H	>1,000	−4	−4.7	0.7/1.9
18	3-Methoxybenzene-sulfonamide	Me	COOH	NH_2	>1,000	ND	−4.2	Not detectable

Compound 1 is SSR. ND, not determined; fSTD, STD amplification factor; fWL, quantitative waterLOGSY effect.
See also Tables S3 and S4.
[a]The position of the groups (R′, R″, R^1, R^2) is indicated in the chemical structure in Figure 7A.
[b]The inhibition of ERK1/2 phosphorylation was determined for four concentrations of each compound (i.e., 1, 10, 100, and 1,000 nM).
[c]A major induced fit effect on D3 is observed, increasing the uncertainty on this estimate.

with SSR, as indicated by an increase of B-factors upon SR binding, MD simulations, and FTIR. Local helical conformations are also underlined by AGADIR predictions. Overall, this transition is compatible with the ability of small molecules to bind to the disordered state, as observed in the inhibition of Myc-Max heterodimerization (Metallo, 2010). The SSR-FGFR interaction is likely heterogeneous, as suggested by the failure of observing electron density for the bound SR in the crystal structure.

MD simulations suggest that, upon transition to this transient and heterogeneous complex, a hydrophobic cavity becomes exposed, in which Tyr^{328} plays a key role. This transient complex may then relax into a more stable structural ensemble (H2), in which SSR is buried in the hydrophobic cavity (Figure S3C). This results in a much stronger interaction, which does not inhibit FGF binding but alters FGFR signaling, possibly due to interfering with membrane binding and/or internalization (Figure 7C). Disorder of this state is confirmed by increased crystallographic B-factors in the SR-complex and MD simulations and is also compatible with the allosteric nature of regulation of the receptor. Transitions in the ensemble N → H1 → H2 translate into different interactions with the membrane and/or different dynamics and orientations of receptor subunits in the dimer, resulting in inhibition of receptor internalization but not PLC-γ phosphorylation. In all, this scenario is fully compatible with recent concepts of allostery, which emphasize the importance of changes in dynamics without alteration of the equilibrium conformation (Tzeng and Kalodimos, 2009), and/or redistribution of the ensemble of intrinsically disordered protein structures (Hilser and Thompson, 2007). The outcome of these transitions, as seen in in cellulo assays, is an inhibition of slow and irreversible FGF-dependent receptor endocytosis abolishing ERK1/2 phosphorylation. A similar allosteric mechanism was described for the ganglioside GM3 and EGF receptor; the latter is closely related to FGFR (Coskun et al., 2011).

The allosteric effect was also confirmed by SAR analysis, which shows a good correlation of binding free energies of various SSR derivatives and their allosteric inhibition calculated by metadynamics modeling, while the docking scores, with their known limitations, also have an overall correlation with biological activity. This behavior would be fully incompatible with an orthosteric competitive inhibition of FGF binding and can be best explained by a binding model in which the allosteric activity of the compound stems from its ability to induce the proper shift in the conformational ensemble of the receptor. In most cases, altering substituent R1, which faces Tyr^{328}, impairs the allosteric activity of the compound, which points to the importance of this residue in the allosteric transitions.

Mutagenesis studies of Tyr^{328} are also in line with this conclusion, because the Tyr to Asp replacement does not basically affect the D3 structural ensemble, leaving its FGF-binding capacity and dimerization intact. On the other hand, it reduces the capacity of the structure to sample the local helical conformations, characteristic of H1 (and H2) states, thus altering SSR binding and its ability to interfere with signaling. This is in line with our FTIR experiments, MD simulations, and cellular assays. In addition, this disorder-based binding and allosteric mechanism is also compatible with the relaxed specificity of SSR, which is capable of interfering with different FGFR variants in distinct species. This would be difficult to reconcile with a well-folded (preformed) binding cavity on D3, which would limit FGFR isoform specificity toward SSR. Adaptability of the structural ensemble of intrinsically disordered proteins in binding is observed in many cases (Dunker et al., 2008). A corollary of this conserved allosteric regulation in all FGFR structures is that the receptor may have endogenous regulatory compound(s)

that act by a similar mechanism; identifying these molecules may open exciting avenues of FGFR research.

A final word is due on the difference of Ki values observed in the distinct in vitro and in vivo experiments. Such an enhanced response to small-molecule effectors in vivo is often observed (Hanoulle et al., 2007; Huppa et al., 2010), probably due to cellular conditions, such as the presence of additional (protein) factors or the vicinity of the membrane. The latter is probably signaled by the preferential inhibitory effect on receptor internalization rather than PLC-γ phosphorylation. In the case of FGFR, this effect may be augmented by the structural sensitivity of the conformational ensemble of the D3 domain.

What are the possible implications of this study? From a structural biology perspective, our study provides insight in fundamental mechanisms of how FGFRs transmit signals and provides unprecedented evidence for allosteric regulation of growth factor receptor tyrosine kinases. We show the importance of taking into account target flexibility in order to understand the mode of action of allosteric ligands. In addition, from a biopharmaceutical perspective, our results unveil the therapeutic potential for FGFR antagonists, perhaps wider than previously attributed to tyrosine kinase inhibitors, since SSR blocks not one but multiple FGFRs and because allosteric modulators are considered to have an improved benefit/risk ratio and to offer opportunities for fine-tuning biological responses in a manner that is not attainable with classic orthosteric modulators (Christopoulos, 2002). Finally, our results show that development of orally deliverable selective allosteric inhibitors of growth factor receptors is feasible, which creates formidable therapeutic opportunities for the future.

EXPERIMENTAL PROCEDURES

Compound Reconstitution

SSR was stored as pure powder at 4°C in the dark. For the different assays, SSR was dissolved in DMSO at a concentration of 100 mM and stored at −20°C until further use. SU5402 (Calbiochem) was also dissolved in DMSO at a concentration of 10 mM and stored at −20°C. For each assay, the same amount of DMSO was used for the control condition.

Materials

FGF1 and FGF7 were purchased from R&D Systems and FGF2 was produced and purified in-house. Human umbilical vein endothelial cells (HUVECs) are single-donor HUVECs from Promocell.

Cell Survival

Apoptotic cells were detected using fluorescein isothiocyanate-conjugated annexin V. Each assay was performed in triplicate and repeated three times.

FGFR2 Kinase Assay

Kinase activity measurements of the recombinant catalytic domain of FGFR2 was done using the ADP-Glo Kinase Assay and the Cyclex FGFR2 Kinase Assay/ Inhibitor screening kit (Sanbio, Uden, The Netherlands) according to the manufacturer's protocol.

Confocal Microscopy Studies

EEA-1 labeling was performed on HUVECs or SNU-16 cells starved for 24 hr in 1% fetal bovine serum containing medium and stimulated for 2 hr with FGFs diluted in prewarmed medium without fetal calf serum in the presence or absence of SSR. Cells were then rinsed with cold PBS and fixed for 15 min with paraformaldehyde 4% and then permeabilized with PBS-Triton 0.1% for 5 min. Following washing with cold PBS, nonspecific sites were saturated with 1% normal goat serum (Zymed) in PBS for 1 hr at room temperature. Early endosomal vesicles were detected using mouse anti-human EEA1 antibody (1/100, BD Biosciences) overnight at 4°C and revealed with AlexaFluor488-conjugated anti-mouse antibody (1/2,000, Invitrogen) for 2 hr at 4°C. Wells were rinsed twice with 1 ml PBS. Then, all liquids were removed and one drop of Fluoprep (Biomerieux) was added and mounted with a round coverslip (KnittelGläser). Confocal microscopy views were performed with a Zeiss LSM510. The number of EEA1-positive vesicles around the nucleus was counted with Columbus software (PekinElmer). For FGF-R4 staining, HUVEC were only fixed with Dako Cytomaton kit following supplier recommendations. FGF-R4 was detected with primary anti-FGFR4 MAB685 (1/100, R&D Systems).

Western Blot Analysis and Phosphoproteome Profiler Array

These studies were realized on 24 hr-starved cells that were then stimulated for 7 min with FGFs in the presence or absence of SSR. Immunoblots were carried out with anti-phosphoprotein antibodies against FGFRs (Santacruz Biotech, Sc30262), FRS2 (Cell Signaling Tech., 3864), Erk1/2 (Cell Signaling Tech., 4377), or anti-glyceraldehyde 3-phosphate dehydrogenase (GAPDH) (Cell Signaling Tech., 2118). The proteome array was run in accordance with supplier recommendations.

FTIR Measurements

FTIR was performed using a Bruker Tensor 37 FTIR spectrometer equipped with an AquaSpec flow cell. The sample compartment was thermostatted to 25°C and 100 spectra were averaged for a good signal-to-noise ratio. Proteins were purified as described in Supplemental Experimental Procedures. Immediately after the gel filtration, the proteins were dialyzed overnight in the same preparation of buffer (10 mM 4-[2-hydroxyethyl]-1-piperazineethanesulfonic acid pH 7.2, 150 mM NaCl) in the presence or absence of SSR. Dialysis buffer samples were used to subtract background signal. The analysis was performed using the OPUS software package provided by Bruker.

STD- and 1D-NMR Measurements

All STD- and 1D-NMR experiments were carried out on a BRUKER three-channel DRX600 and on a BRUKER four-channel DRX800 spectrometer at the standard temperature of 298 K and were referenced to the internal standard 3-trimethyl-2,2,3,3-tetradeuteropropionate sodium salt. A detailed description has been included in the Supplemental Information.

X-Ray Crystallography

Crystals of FGF1/FGFR2 D2D3 complexes with and without SR/SSR compounds could be obtained under crystallization conditions containing 0.1 M Tris/HCl pH 8, 1.8 M $(NH_4)_2SO_4$ at protein concentration of 2 mg/ml. Crystals with SSR diffracted up to 6 Å, whereas SR bound crystals diffracted up to 4 Å at SLS Villingen. Data could be integrated using XDS and phased with Phaser, using MR of separate domains FGF1, FGFR2 D2, and FGFR2 D3 of the crystal structure 1E0O. Because of bad resolution, all residues were mutated to alanine. The poly-A backbone model of FGF1/FGFR2 D2D3 was refined using Refmac5 and Coot.

In Silico Molecular Modeling and Metadynamics Modeling

All the detailed procedures are in the Supplemental Information.

Other Assays

For methods such as cell proliferation, survival, FGFR kinase assay, confocal microscopy, FTIR, and western blotting, we used standard protocols that are detailed in the Supplemental Experimental Procedures.

Statistics

All data represent the mean ± SEM of the indicated number of experiments. Statistical significance was calculated by Student's t test, considering $p < 0.05$ as statistically significant.

ACCESSION NUMBERS

The low resolution polyA backbone model of the FGFR2D2D3/FGF1/SSR128545 complex has been deposited in the RCSB Protein Data Bank under the ID code rcsb077498 and PDB ID code 4J23.

SUPPLEMENTAL INFORMATION

Supplemental Information includes four figures, four tables, and Supplemental Experimental Procedures and can be found with this article online at http://dx.doi.org/10.1016/j.ccr.2013.02.018.

ACKNOWLEDGMENTS

The authors would like to thank J. Fidelak for his contribution and L. Notebaert for help with the figures. G.S. and F.L.G. acknowledge partial support by Spanish Science and Innovation grant BIO2010-20166. F.D.S. was supported by the Flemish Institute for the Promotion of Scientific Research (IWT) and the Flemish Foundation for Scientific Research (FWO) Belgium. This work was also supported, in part, by grant numbers G.0567.05 and G.0405.05 from the FWO, Belgium; grant number GOA/2006/11 from the Concerted Research Activities, Belgium; grant number LSHG-CT-2004-503573 from the EU 6th Framework Program; the Belgian Science Policy (IAP numbers P5-02 and P6-30); and by long-term structural Methusalem funding from the Flemish Government (to P.C.). Funding for H.S. was derived from EXC 115 DFG, Cluster of Excellence: Macromolecular Complexes.

C.H., C.A., M.B., D.S., P.R., J.P.H., G.L., J.M.H., F.B. are employees of Sanofi-Aventis, Montpellier, France. P.C., J.S., F.R., F.D. are inventors on the international patent application "extracellular allosteric inhibitor binding domain from a tyrosine kinase receptor" with publication number WO2011/001413 and its national counterparts.

Received: July 24, 2012
Revised: December 12, 2012
Accepted: February 19, 2013
Published: April 15, 2013

REFERENCES

Beenken, A., and Mohammadi, M. (2009). The FGF family: biology, pathophysiology and therapy. Nat. Rev. Drug Discov. *8*, 235–253.

Belleudi, F., Leone, L., Nobili, V., Raffa, S., Francescangeli, F., Maggio, M., Morrone, S., Marchese, C., and Torrisi, M.R. (2007). Keratinocyte growth factor receptor ligands target the receptor to different intracellular pathways. Traffic *8*, 1854–1872.

Best, R.B., and Hummer, G. (2009). Optimized molecular dynamics force fields applied to the helix-coil transition of polypeptides. J. Phys. Chem. B *113*, 9004–9015.

Bono, F., De Smet, F., Herbert, C., DeBock, K., Georgiadou, M., Fons, P., Tjwa, M., Alcouffe, C., Ny, A., Bianciotto, M., et al. (2013). Inhibition of tumor angiogenesis and growth by a small-molecule multi-FGF receptor blocker with allosteric properties. Cancer Cell *23*, this issue, 477–488.

Bretonnet, A.S., Jochum, A., Walker, O., Krimm, I., Goekjian, P., Marcillat, O., and Lancelin, J.M. (2007). NMR screening applied to the fragment-based generation of inhibitors of creatine kinase exploiting a new interaction proximate to the ATP binding site. J. Med. Chem. *50*, 1865–1875.

Christopoulos, A. (2002). Allosteric binding sites on cell-surface receptors: novel targets for drug discovery. Nat. Rev. Drug Discov. *1*, 198–210.

Conn, P.J., Christopoulos, A., and Lindsley, C.W. (2009). Allosteric modulators of GPCRs: a novel approach for the treatment of CNS disorders. Nat. Rev. Drug Discov. *8*, 41–54.

Coskun, U., Grzybek, M., Drechsel, D., and Simons, K. (2011). Regulation of human EGF receptor by lipids. Proc. Natl. Acad. Sci. USA *108*, 9044–9048.

Duchardt, E., Sigalov, A.B., Aivazian, D., Stern, L.J., and Schwalbe, H. (2007). Structure induction of the T-cell receptor zeta-chain upon lipid binding investigated by NMR spectroscopy. ChemBioChem *8*, 820–827.

Dunker, A.K., Oldfield, C.J., Meng, J., Romero, P., Yang, J.Y., Chen, J.W., Vacic, V., Obradovic, Z., and Uversky, V.N. (2008). The unfoldomics decade: an update on intrinsically disordered proteins. BMC Genomics *9*(*Suppl 2*), S1.

Gasparini, G., Longo, R., Toi, M., and Ferrara, N. (2005). Angiogenic inhibitors: a new therapeutic strategy in oncology. Nat. Clin. Pract. Oncol. *2*, 562–577.

Hanoulle, X., Melchior, A., Sibille, N., Parent, B., Denys, A., Wieruszeski, J.M., Horvath, D., Allain, F., Lippens, G., and Landrieu, I. (2007). Structural and functional characterization of the interaction between cyclophilin B and a heparin-derived oligosaccharide. J. Biol. Chem. *282*, 34148–34158.

Hilser, V.J., and Thompson, E.B. (2007). Intrinsic disorder as a mechanism to optimize allosteric coupling in proteins. Proc. Natl. Acad. Sci. USA *104*, 8311–8315.

Huppa, J.B., Axmann, M., Mörtelmaier, M.A., Lillemeier, B.F., Newell, E.W., Brameshuber, M., Klein, L.O., Schütz, G.J., and Davis, M.M. (2010). TCR-peptide-MHC interactions in situ show accelerated kinetics and increased affinity. Nature *463*, 963–967.

Irschick, R., Trost, T., Karp, G., Hausott, B., Auer, M., Claus, P., and Klimaschewski, L. (2013). Sorting of the FGF receptor 1 in a human glioma cell line. Histochem. Cell Biol. *139*, 135–148.

Laio, A., and Gervasio, F.L. (2008). Metadynamics: a method to simulate rare events and reconstruct the free energy in biophysics, chemistry and material science. Rep. Prog. Phys. *71*, 126601.

Lovera, S., Sutto, L., Boubeva, R., Scapozza, L., Dölker, N., and Gervasio, F.L. (2012). The different flexibility of c-Src and c-Abl kinases regulates the accessibility of a druggable inactive conformation. J. Am. Chem. Soc. *134*, 2496–2499.

McCoy, A.J., Grosse-Kunstleve, R.W., Adams, P.D., Winn, M.D., Storoni, L.C., and Read, R.J. (2007). Phaser crystallographic software. J. Appl. Cryst. *40*, 658–674.

Metallo, S.J. (2010). Intrinsically disordered proteins are potential drug targets. Curr. Opin. Chem. Biol. *14*, 481–488.

Murshudov, G.N., Dodson, E.J., and Vagin, A.A. (1996). Application of maximum likelihood methods for macromolecular refinement. In CCP4 Study Weekend Proceedings: Macromolecular RefinementCCP4 Study Weekend Proceedings: Macromolecular Refinement (Warrington, United Kingdom: Daresbury Laboratory), pp. 93–104.

Overington, J.P., Al-Lazikani, B., and Hopkins, A.L. (2006). How many drug targets are there? Nat. Rev. Drug Discov. *5*, 993–996.

Park, S.J., Borin, B.N., Martinez-Yamout, M.A., and Dyson, H.J. (2011). The client protein p53 adopts a molten globule-like state in the presence of Hsp90. Nat. Struct. Mol. Biol. *18*, 537–541.

Pellegrini, L., Burke, D.F., von Delft, F., Mulloy, B., and Blundell, T.L. (2000). Crystal structure of fibroblast growth factor receptor ectodomain bound to ligand and heparin. Nature *407*, 1029–1034.

Piana, S., and Laio, A. (2007). A bias-exchange approach to protein folding. J. Phys. Chem. B *111*, 4553–4559.

Plotnikov, A.N., Schlessinger, J., Hubbard, S.R., and Mohammadi, M. (1999). Structural basis for FGF receptor dimerization and activation. Cell *98*, 641–650.

Reilly, J.F., Mizukoshi, E., and Maher, P.A. (2004). Ligand dependent and independent internalization and nuclear translocation of fibroblast growth factor (FGF) receptor 1. DNA Cell Biol. *23*, 538–548.

Saladino, G., Gauthier, L., Bianciotto, M., and Gervasio, F.L. (2012). Assessing the performance of metadynamics and path variables in predicting the binding free energies of p38 inhibitors. J. Chem. Theory Comput. *8*, 1165–1170.

Schlessinger, J., Plotnikov, A.N., Ibrahimi, O.A., Eliseenkova, A.V., Yeh, B.K., Yayon, A., Linhardt, R.J., and Mohammadi, M. (2000). Crystal structure of a ternary FGF-FGFR-heparin complex reveals a dual role for heparin in FGFR binding and dimerization. Mol. Cell *6*, 743–750.

Sigalov, A., Aivazian, D., and Stern, L. (2004). Homooligomerization of the cytoplasmic domain of the T cell receptor zeta chain and of other proteins containing the immunoreceptor tyrosine-based activation motif. Biochemistry *43*, 2049–2061.

Tompa, P. (2011). Unstructural biology coming of age. Curr. Opin. Struct. Biol. *21*, 419–425.

Tompa, P., and Fuxreiter, M. (2008). Fuzzy complexes: polymorphism and structural disorder in protein-protein interactions. Trends Biochem. Sci. *33*, 2–8.

Tzeng, S.R., and Kalodimos, C.G. (2009). Dynamic activation of an allosteric regulatory protein. Nature *462*, 368–372.

Zhang, J., Yang, P.L., and Gray, N.S. (2009). Targeting cancer with small molecule kinase inhibitors. Nat. Rev. Cancer *9*, 28–39.

Cancer Cell
Article

Inhibition of Tumor Angiogenesis and Growth by a Small-Molecule Multi-FGF Receptor Blocker with Allosteric Properties

Françoise Bono,[1,15] Frederik De Smet,[2,3,15] Corentin Herbert,[1] Katrien De Bock,[2,3] Maria Georgiadou,[2,3] Pierre Fons,[1] Marc Tjwa,[2,3] Chantal Alcouffe,[1] Annelii Ny,[2,3] Marc Bianciotto,[1] Bart Jonckx,[2,3] Masahiro Murakami,[4] Anthony A. Lanahan,[4] Christof Michielsen,[5] David Sibrac,[1] Frédérique Dol-Gleizes,[1] Massimiliano Mazzone,[2,3] Serena Zacchigna,[2,3] Jean-Pascal Herault,[1] Christian Fischer,[2,3] Patrice Rigon,[1] Carmen Ruiz de Almodovar,[2,3] Filip Claes,[2,3] Isabelle Blanc,[1] Koen Poesen,[2,3] Jie Zhang,[5] Inmaculada Segura,[2,3] Geneviève Gueguen,[1] Marie-Françoise Bordes,[1] Diether Lambrechts,[2,3] Roselyne Broussy,[1] Marlies van de Wouwer,[2,3] Corinne Michaux,[1] Toru Shimada,[8] Isabelle Jean,[1] Silvia Blacher,[10] Agnès Noel,[10] Patrick Motte,[10] Eran Rom,[11] Jean-Marie Rakic,[9] Susumu Katsuma,[8] Paul Schaeffer,[1] Avner Yayon,[11] Ann Van Schepdael,[5] Harald Schwalbe,[12] Francesco Luigi Gervasio,[13] Geert Carmeliet,[6] Jef Rozensky,[7] Mieke Dewerchin,[2,3] Michael Simons,[4] Arthur Christopoulos,[14] Jean-Marc Herbert,[1,15] and Peter Carmeliet[2,3,15,*]

[1]Early to Candidate Department and Lead Generation and Candidate Realization Department, Sanofi, 31036 Toulouse, France
[2]Laboratory of Angiogenesis and Neurovascular Link, Vesalius Research Center, Department of Oncology, University of Leuven, Leuven, B-3000, Belgium
[3]Laboratory of Angiogenesis and Neurovascular link, Vesalius Research Center, VIB, Leuven, B-3000, Belgium
[4]Section of Cardiovascular Medicine, Department of Internal Medicine, Yale University School of Medicine, New Haven, CT 06520, USA
[5]Laboratory for Pharmaceutical Analysis, Pharmaceutical and Pharmacological Sciences
[6]Laboratory for Clinical and Experimental Endocrinology
[7]Medicinal Chemistry, Rega Instituut
KU Leuven, B-3000 Leuven, Belgium
[8]Department of Agricultural and Environmental Biology, School Agricultural and Life Sciences, University of Tokyo, 113-8657 Tokyo, Japan
[9]Department of Ophthalmology, University Hospital, CHU, Sart-Tilman, B-4000 Liège, Belgium
[10]Laboratory of Tumor and Development Biology, GIGA, University of Liège, B-4000 Liège, Belgium
[11]ProCore, Ltd., 10400 Nes Ziona, Israel
[12]Institute for Organic Chemistry and Chemical Biology, Center for Biomolecular Magnetic Resonance (BMRZ), University of Frankfurt, D-60438 Frankfurt, Germany
[13]Computational Biophysics Group, Spanish National Cancer Research Center (CNIO), E-28029 Madrid, Spain
[14]Drug Discovery Biology, Monash Institute of Pharmaceutical Sciences, Monash University, 3052 Victoria, Australia
[15]These authors contributed equally to this work
*Correspondence: peter.carmeliet@vib-kuleuven.be
http://dx.doi.org/10.1016/j.ccr.2013.02.019

SUMMARY

Receptor tyrosine kinases (RTK) are targets for anticancer drug development. To date, only RTK inhibitors that block orthosteric binding of ligands and substrates have been developed. Here, we report the pharmacologic characterization of the chemical SSR128129E (SSR), which inhibits fibroblast growth factor receptor (FGFR) signaling by binding to the extracellular FGFR domain without affecting orthosteric FGF binding. SSR exhibits allosteric properties, including probe dependence, signaling bias, and ceiling effects. Inhibition by SSR is highly conserved throughout the animal kingdom. Oral delivery of SSR inhibits arthritis and tumors that are relatively refractory to anti-vascular endothelial growth factor receptor-2 antibodies. Thus, orally-active extracellularly acting small-molecule modulators of RTKs with allosteric properties can be developed and may offer opportunities to improve anticancer treatment.

Significance

Receptor tyrosine kinases (RTK) represent key targets for anticancer drug development. Classic examples of RTK blockers include antibodies inhibiting orthosteric ligand binding, but small molecules that bind the extracellular domain of RTKs have traditionally not been considered because they are thought to be too small to competitevely block binding of the much larger polypeptide ligands. We identified a small-molecule chemical compound, SSR128129E (SSR), which inhibits fibroblast growth factor receptor (FGFR) signaling through allosteric mechanisms after binding to the extracellular FGFR domain. Oral delivery of SSR inhibits tumor growth and amplifies anti-angiogenic drug therapy. These results offer incentives to develop orally-active small-molecule RTK inhibitors with allosteric properties and opportunities for improved anticancer treatment.

INTRODUCTION

Cell-surface receptors represent key targets for drug development. Historically, drug discovery programs have been dominated by efforts to develop antagonists that compete for binding with endogenous ligands at orthosteric sites. Drugs that bind to allosteric sites, i.e., topographically distinct domains from those used by orthosteric ligands (if the target is a receptor) or substrates (if the target is an enzyme) that modulate a protein's activity, have been more difficult to identify. Recently, allosteric modulators have been identified for ligand-gated ion channels, G protein-coupled receptors (GPCRs), and kinases (Chahrour et al., 2012; Conn et al., 2009; Cox et al., 2011; Thaker et al., 2012).

Allosteric kinase inhibitors have been developed (Chahrour et al., 2012), but an extracellularly acting small-molecule allosteric inhibitor of receptor tyrosine kinases (RTKs) is not available. Yet, this receptor superfamily is of immense biomedical significance (Lemmon and Schlessinger, 2010). Furthermore, allosteric drugs offer therapeutic advantages over traditional orthosteric drugs, including greater safety and/or selectivity (Christopoulos, 2002). Most drugs targeting RTKs are antibodies against growth factor receptors that inhibit ligand binding or receptor dimerization or are small molecules inhibiting tyrosine kinase (TK) activity (Chung and Ferrara, 2011; Tvorogov et al., 2010). However, it is becoming increasingly clear that formation of receptor signaling complexes requires allosteric conformational changes in the extracellular domain to position the TK domains for signal transduction (Brozzo et al., 2012; Landgraf et al., 2010). Whether small molecules can inhibit or modulate RTK signaling by acting extracellularly remains unexplored.

Anti-angiogenic therapy would benefit from other RTK small-molecule inhibitors. Vascular endothelial growth factor (VEGF)-targeted agents prolong the survival of patients with cancer, but their success is restricted by refractoriness, escape, and in some models, increased metastasis (Bergers and Hanahan, 2008; Ebos and Kerbel, 2011). Combinatorial delivery of anti-angiogenic agents may help overcome these challenges (You et al., 2011).

Receptors for basic fibroblast growth factors (FGFs) are attractive drug candidates (Daniele et al., 2012; Itoh and Ornitz, 2011). FGF receptor (FGFR) signaling has been implicated in cancer, inflammation, and the escape of tumor vascularization from VEGF inhibitor treatment (Ahmad et al., 2012; Beenken and Mohammadi, 2009; Casanovas et al., 2005; Fischer et al., 2007; Malemud, 2007; Turner and Grose, 2010; Wesche et al., 2011). Nonetheless, the FGFR superfamily with its 18 ligands and four receptors has received little attention for drug development, partly because of redundancy (Beenken and Mohammadi, 2009). Selective TK inhibitors (TKIs) of FGFRs have not been clinically approved, and only broad-spectrum TKIs targeting primarily VEGF receptors (VEGFRs) and, less potently, FGFRs are available (Daniele et al., 2012; McDermott et al., 2005). This study characterizes an orally-active, extracellularly acting small-molecule inhibitor of FGFRs.

RESULTS

Identification of SSR128129E

The compound SSR128129E ("SSR"; Figure 1A) was identified in a high-throughput screen, designed originally to discover orthosteric FGFR inhibitors. In this screen, we used a scintillation proximity assay (SPA) assay to identify chemicals blocking binding of ^{125}I-FGF2 to the extracellular domain of FGFR1-D1D2D3/Fc, the extracellular domain with 3 Ig-like domains D1-3 coupled to a Fc-fragment. A 10- to 100-fold molar excess of unlabeled FGF2 or anti-FGFR1 Fab (αFGFR1) inhibited ^{125}I-FGF2 binding completely, indicating that the assay identifies compounds inhibiting ligand binding via a competitive (orthosteric) mechanism (not shown). SSR emerged from this screen as a low-affinity antagonist (half maximal inhibitory concentration [IC_{50}]: 1.9 ± 1.4 μM).

Surprisingly, SSR was effective in the nanomolar range in cellular assays. Because FGF2 affects endothelial cells (ECs) in vitro, we used human umbilical venous endothelial cells (HUVECs) that express FGFR1 and lower levels of FGFR2 and FGFR4. SSR dose-dependently inhibited FGF2-induced EC proliferation (IC_{50}: 31 ± 1.6 nM; Figure 1B), migration (IC_{50}: 15.2 ± 4.5 nM; Figure 1C), and lamellipodia formation (Figure S1A available online). Thus, SSR inhibited EC responses with nanomolar potency, yet antagonized FGF binding only at micromolar levels. This puzzling result suggested that SSR was not acting as a classic orthosteric inhibitor and/or that its pharmacology was highly sensitive to the cellular environment and conformational properties of intact FGFR. We thus characterized its pharmacological properties.

SSR Is a Multi-FGFR Inhibitor

We investigated if SSR blocked the response to other FGFs, known to bind selectively to distinct FGFR subtypes. We therefore used cells from different species, expressing one or more FGFRs, and stimulated them with various FGF ligands. SSR inhibited responses mediated by FGFR1-4. For instance, SSR blocked EC migration in response to FGF1, a ligand of FGFR1 and FGFR4 (Figure 1C), and capillary tube formation in response to FGF19, a ligand of FGFR4 (Figure S1B). Proliferation and migration of the murine pancreatic Panc02 tumor cell line in response to FGF7 were also blocked by SSR (Figures 1D and 1E), showing that SSR inhibits FGFR subtypes of other species as well. Table 1 lists the nanomolar potency activities of SSR in blocking different FGFR subtypes in various cell lines used to analyze migratory, mitogenic, and other responses to FGF ligands. Notably, SSR inhibited FGFR paralogues in various species across the animal kingdom, including *Danio rerio* (zebrafish) (Figures S1C–S1F), *Drosophila melanogaster* (fruit fly) (Figures S1G-S1I), *Spodoptera frugiperda* (moth) (Figure S1J), and *Bombyx mori* (silkworm) (not shown).

The effect of SSR was not due to nonspecific toxicity because SSR (1 μM) failed to affect the mitogenic response to other stimuli of B9 myeloma cells or L6 myoblasts, which did not express FGFRs (not shown). Heparin (30 μg/ml) did not alter the inhibitory activity of SSR on the mitogenic or chemotactic response of FGFs (not shown).

SSR Inhibits FGFRs but Not Other Related RTKs

We then determined if SSR blocked the FGFR superfamily selectively. SSR did not affect responses to ligands activating structurally related RTKs (Figures 1E, 1F, and S1K). When FGF7 and VEGF were added together to test the migration of Panc02 tumor cells, SSR only blocked the response to

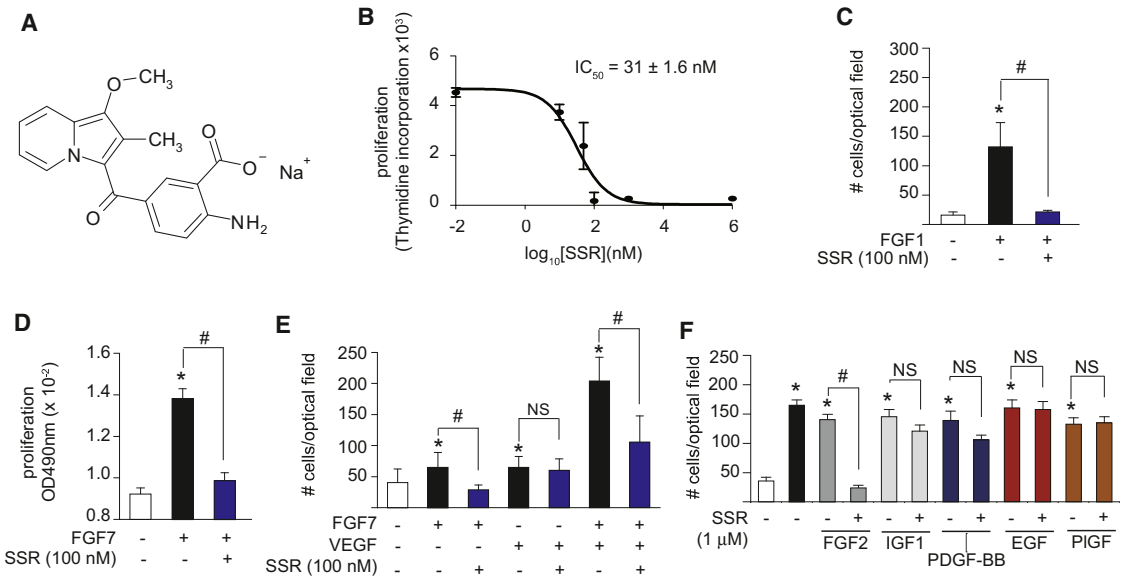

Figure 1. Activity and FGFR Specificity of SSR

(A) Chemical structure of SSR128129E (SSR).

(B) Effect of SSR on FGF2-induced EC proliferation.

(C) Effect of SSR (100 nM) on FGF1-driven EC migration (n = 3; *p < 0.05 versus control, #p < 0.05 versus FGF1 alone).

(D) Effect of SSR (100 nM) on FGF7-driven proliferation of Panc02 tumor cells (n = 3; *p < 0.05 versus control, #p < 0.05 versus FGF7 alone).

(E) Effect of SSR (100 nM) on migration of Panc02 tumor cells in response to single or combined stimulation with FGF7 and VEGF (n = 3; *p < 0.05 versus control, #p < 0.05 versus indicated condition).

(F) Effect of SSR (1 μM) on migration of ECs in response to different growth factors (n = 3; *p < 0.05 versus control, #p < 0.05 versus indicated condition). Data are presented as mean ± SEM.

See also Figure S1 and Tables S1 and S2.

FGF7 (Figure 1E). Similar results were obtained for the responses of ECs to VEGF plus FGF1 (not shown) or to VEGF plus FGF2 (Figure S1L), or of Panc02 cell responses to VEGF plus FGF7 (not shown). Genetic experiments in zebrafish to silence both *fgfr1* and *fgfr2* showed that SSR recapitulated quantitatively and qualitatively the phenotypic pharyngeal arch and cartilage defects, induced by combined silencing of *fgfr1* and *fgfr2*, underscoring that SSR is a multi-FGFR inhibitor (Figures S1M–S1T). SSR failed however to induce additional anomalies in zebrafish embryos lacking multiple FGFRs, showing that SSR specifically inhibited multiple FGFRs in an intact animal model without causing off-target effects (Figures S1U and S1V).

In contrast to a 10- or 100-fold molar excess of a neutralizing competitor or antibody, SSR failed to inhibit binding of VEGF, VEGF-B, placental growth factor, platelet-derived growth factor (PDGF)-BB, or PDGF-CC to their receptors, whose extracellular domains exhibit the highest homology to FGFRs. SSR also failed to inhibit phosphorylation of VEGFR2 or hepatocyte growth factor-receptor MET (Figures S1W and S1X; Table S1). SSR also did not alter receptor binding of interleukin-8, transforming growth factor-β, tumor necrosis factor-α, or epidermal growth factor, which are structurally more divergent from FGFs (Table S2). SSR also did not inhibit binding of >100 distinct ligands with related structural homology or entirely different chemical composition from FGFs, even when used at concentrations up to 10 μM (Table S2). Overall, SSR inhibited FGFR-driven responses while not affecting other related RTKs.

SSR Is Not a Potent Inhibitor of Orthosteric FGF Binding to FGFR

We then aimed at determining SSR's pharmacologic mechanism. The weak inhibition of the binding of ^{125}I-FGF2 to FGFR1-D1D2D3/Fc in the scintillation proximity assay (SPA) could be reconciled with a low-affinity orthosteric interaction or a low-affinity allosteric interaction exhibiting negative binding cooperativity (Christopoulos and Kenakin, 2002). However, such modest effects on the binding affinity of ^{125}I-FGF2 alone could not explain the greater potency of SSR in assays of cellular function. This would require a difference in binding affinity of SSR at the intact receptor expressed in a native environment and/or an allosteric effect on signal transduction (in addition to any negative cooperativity on orthosteric agonist binding).

To address these possibilities, we determined the potency of SSR as an inhibitor of the binding of ^{125}I-FGF2 to FGFRs when expressed in their native configuration in natural conditions on the EC surface. Under these conditions, the potency of SSR was reduced even more than in the SPA such that it was unable to inhibit ^{125}I-FGF2 binding to its receptors even at high micromolar concentrations (Figure 2A). In contrast, orthosteric inhibitors such as unlabeled FGF2, a neutralizing anti-FGF2 antibody or anti-FGFR1 (αFGFR1) blocked ^{125}I-FGF2 binding (Figure 2A). Thus, in this cellular binding assay, SSR did not act as a strong orthosteric inhibitor. Such contextual assay-dependent results are inconsistent with a simple competitive mechanism that relies on steric hindrance for an overlapping binding domain because the latter would yield consistent

Table 1. Effects of SSR on Cellular Responses to Different FGFRs

FGF Receptor	FGF Ligand	Cell Line	Cellular Assay	SSR Concentration Resulting in ≥50% Inhibition[a]
FGFR1IIIcα	FGF1	PAE-hFGFR1	Proliferation	100 nM[b]
	FGF2	PAE-hFGFR1	Proliferation	100 nM[b]
FGFR1IIIcβ	FGF1	HUVEC	Proliferation, migration	100 nM[b]
	FGF2	HUVEC	Proliferation, migration, survival	15–22 nM
	FGF4	HUVEC	Proliferation, migration	100 nM[b]
FGFR2IIIcα	FGF2	HEK-hFGFR2^{WT}	ERK activation	28 nM
FGFR2IIIb	FGF7	mPanc02	Proliferation, migration	100 nM[b]
FGFR3IIIcα	FGF1	hB9-myeloma	Proliferation	25 nM[b]
FGFR4IIIcα	FGF2	HUVEC	Proliferation, migration, survival	15–22 nM
	FGF19	HUVEC	Tube formation	10 nM[b]

PAE, porcine aortic endothelial cells.
[a]IC_{50} value of SSR (nM) determined by using various concentrations.
[b]Only two or three concentrations of SSR were tested without determining the precise IC_{50} value; in these cases, the indicated concentration already resulted in >50% inhibition.

inhibition of binding in all assays (as observed for unlabeled FGF2, αFGF2, and αFGFR1). Rather, these findings are characteristic of small-molecule allosteric modulators of other receptor classes that exert minimal effects on orthosteric ligand affinity (i.e., low negative cooperativity in the case of FGFR1-D1D2D3/Fc or neutral cooperativity in the case of intact FGFR) but have profound effects on orthosteric ligand signaling (Litschig et al., 1999). Indeed, the ability to mediate differential effects on the binding and function of orthosteric ligands in an assay-dependent manner is a typical feature of allosteric receptor modulators, referred to as "probe dependence" (Christopoulos and Kenakin, 2002; Litschig et al., 1999; Price et al., 2005).

Pharmacological Validation of an Allosteric Mechanism for SSR

SSR's inhibitory activity on FGFR signaling was not due to inhibition of dimerization of FGF receptors or ligands (Herbert et al., 2013). We thus used ECs and HEK293 cells stably expressing FGFR1 or FGFR3, respectively, to study whether SSR reduced FGFR phosphorylation in response to FGF1. FGFR immunoprecipitation, followed by blotting for phosphotyrosine, revealed that FGFR tyrosine phosphorylation in response to FGF1 was reduced by nanomolar SSR concentrations (Figures 2B and 2C). We thus explored if inhibition by SSR of FGFR-TK activity was consistent with an allosteric mechanism. At least four characteristic features of allosteric antagonists have been identified for other classes of cell-surface receptors, including: (1) the ability to act at a topographically distinct site away from orthosteric or substrate-binding sites; (2) the ability to display "probe dependence" (see above); (3) a saturability, or ceiling level, to the allosteric effect, above which no further antagonism is observed irrespective of ligand concentration; and (4) different degrees of inhibition depending on the signal pathway that is being modulated, a phenomenon referred to as "pathway bias" (Keov et al., 2011).

SSR Interacts with a Topographically Distinct Site

FGFR-TKIs, which competitively block binding of ATP to its orthosteric site in the TK domain, must cross the plasma membrane. High-performance liquid chromotography analysis indicated that lysates of cells treated with 10 μM SSR contained only background traces of SSR (Figure S2), indicating that SSR failed to cross the plasma membrane and did not accumulate at high levels intracellulary. Calculation by theoretical prediction of the octanol-water partition coefficient (theoretical $LogP_{OW}$: −2.018), a measure of the lipophilicity of the compound, also showed that SSR was preferentially distributed in a hydrophilic rather than hydrophobic milieu and thus unlikely to cross the plasma membrane.

Use of a recombinant FGFR1-TK domain revealed that even supraphysiologic concentrations of SSR failed to inhibit the TK activity in contrast to the FGFR-TK inhibitor SU5402 (Figure 2D). We also used B9 myeloma cells because they express a constitutively active FGFR3^{K650E} mutant, which stimulates cell proliferation in the absence of FGF. If SSR would be cell permeable and inhibit TK, then SSR should block the growth of FGFR3^{K650E} cells. In cells expressing wild-type FGFR3 (FGFR3^{WT}), FGF1 enhanced proliferation and this response was reduced by SSR (Figure 2E). As expected, FGF1 failed to further stimulate growth of FGFR3^{K650E} cells, while SSR was ineffective in reducing constitutively activated proliferation (Figure 2E). In contrast, SU5402 inhibited proliferation of both FGFR3^{WT} and FGFR3^{K650E} expressing B9 cells (Figure 2E).

Given that SSR indirectly blocked the FGFR-TK activity yet failed to cross the plasma membrane, we analyzed if SSR interacted with the extracellular domain of FGFR. We purified FGFR2-D2D3, a fragment of the extracellular domain of FGFR2 consisting of domain D2 and D3, and used mass spectrometry to determine if SSR bound to this fragment. Spectral analysis showed the predicted mass of FGFR2-D2D3 when measured in the absence of SSR (Mr = 24,493 Da) and revealed that the mass was augmented in the presence of a 10-fold molar excess of SSR by 322 Da, e.g., the molecular weight of SSR without Na^+ and H_2O (Figure 3A). This indicates that SSR binds with a stoichiometry of n = 1 to FGFR2-D2D3. SSR did not bind to FGFR2-D2L, consisting of D2 plus adjacent linker, indicating that SSR binds to D3 (Figure 3B). Because FGFR2-D2L contains the binding pocket for FGF, the lack of binding of SSR to FGFR2-D2L also supports our finding that SSR is unable to block orthosteric FGF binding. As negative control, no binding of SSR to FGF1 was detected (not shown), consistent with nuclear magnetic resonance studies (Herbert et al., 2013).

SSR Displays a Ceiling Level to Its Antagonism of FGFR Phosphorylation

SSR (100 nM) reduced tyrosine phosphorylation of FGFR1 and FGFR3 (see above). Remarkably, even a supramaximal

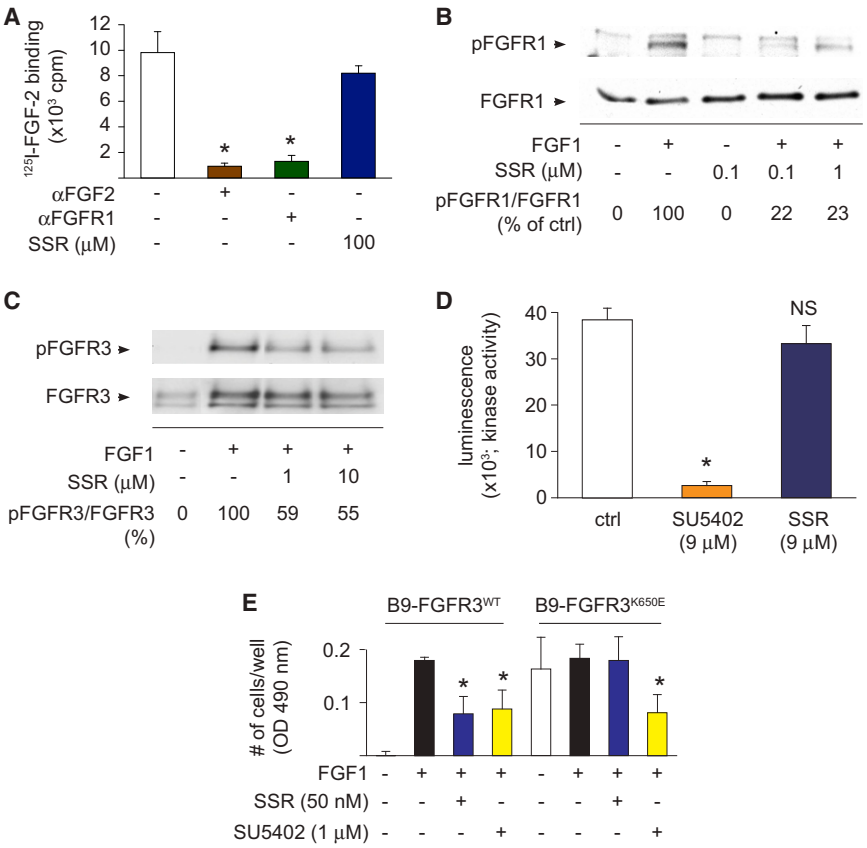

Figure 2. Mode of Action of SSR: Binding and Phosphorylation Assays

(A) Binding of ^{125}I-FGF2 to porcine aortic ECs (PAE) overexpressing FGFR1 with and without the orthosteric inhibitors anti-FGF2 (αFGF2) or anti-FGFR1 Fab (αFGFR1), or a 100-fold molar excess of SSR (100 μM). Data are corrected for residual background binding in the presence of 100-fold molar excess of unlabeled FGF2 (n = 3; *p < 0.05).

(B) Immunoblotting with densitometric quantification of FGF1-induced tyrosine phosphorylation of FGFR1 in ECs in the absence or presence of SSR.

(C) Immunoblotting with densitometric quantification of FGF1-induced phosphorylation of wild-type FGFR3 in HEK293 cells in the absence or presence of SSR.

(D) Effect of SSR in a phosphorylation assay using the isolated kinase domain of FGFR1. The RTKI SU5402 was used as positive control (n = 3; *p < 0.05).

(E) Effect of SSR on FGF1-induced proliferation of B9 myeloma cells expressing FGFR3^{WT} or the constitutively active FGFR3^{K650E} mutant. The RTKI SU5402 was used as positive control (n = 3; *p < 0.05). Ctrl, control vehicle (DMSO). Quantitative data are presented as mean ± SEM.

See also Figure S2.

concentration of SSR (10 μM) did not completely eliminate FGFR but left a residual level of FGFR autophosphorylation (Figures 2B and 2C). This phenomenon cannot be reconciled with a competitive orthosteric mechanism and is another hallmark of allosteric interactions, namely a "ceiling level" to the actions of the allosteric modulator, above which no further pharmacologic effect is observed irrespective of modulator concentration (Conn et al., 2009; May et al., 2007). These findings suggest a limited negative cooperativity on FGFR signaling, in essence "tuning down" the degree of autophosphorylation to a new (lower) set-point. Similar data were obtained when analyzing tyrosine phosphorylation of FGFR1 and FGFR2 in HEK293 cells in response to FGF1 or FGF2 (not shown). We also analyzed the effect of increasing concentrations of SSR on the mitogenic response to different concentrations of FGF2, showing a shift to the right with increased sigmoidicity of the curve (Figure 3C), another hallmark of allostery (Christopoulos, 2002). This observation is comparable to effects observed for the allosteric antagonist 7-hydroxyimino-cyclopropan[b]chromen-1a-carboxylic acid ethyl ester of glutamate receptor 1 (Knoflach et al., 2001).

SSR Displays Pathway-Biased Antagonism of FGFR Signaling

Based on studies of allosteric modulators for other receptor classes, there is no a priori reason why conformational changes resulting from binding of the allosteric modulator should display equivalent degrees of allosteric modulation across different signaling pathways, if the allosteric interaction predominantly modulates orthosteric ligand efficacy rather than affinity (Leach et al., 2007)—a phenomenon referred to as "functional selectivity", "stimulus-trafficking", or "biased antagonism" (Urban et al., 2007). To assess if SSR induced biased antagonism, we generated a phosphomap of two major FGFR signaling pathways, i.e., FRS2-ERK1/2 and PLC-γ (Beenken and Mohammadi, 2009).

In FGFR2-expressing HEK293 cells (HEK-FGFR2), levels of phosphorylated FRS2 (pFRS2) and ERK1/2 (pERK1/2) were minimal in baseline and upregulated by FGF2 (Figures 3D and 3E). SSR and the pan-FGFR-TKI SU5402 inhibited phosphorylation of FRS2 and ERK1/2 (Figures 3D and 3E). However, unlike SU5402, SSR did not eliminate all FRS2 and ERK1/2 phosphorylation, in line with SSR's ceiling effect. Higher concentrations of FGF2 could not overcome the inhibition of ERK1/2 phosphorylation by SSR, further supporting the ceiling phenomenon (not shown). In the same cells, FGF2 elevated the levels of phosphorylated PLC-γ (pPLC-γ) (Figure 3F). In contrast to its inhibitory effect on FRS2 and ERK1/2, activation of PLC-γ was not blocked by SSR at the concentration (1 μM) that inhibited FRS2/ERK phosphorylation (Figure 3F). This induction of pPLC-γ was fully blocked by SU5402 (Figure 3F). Thus, SSR does not inhibit all FGFR signaling pathways indiscriminatively but selectively blocks particular signaling pathways, dependent on the cellular context. This biased antagonism of a RTK by a small molecule interacting with the extracellular domain can only be achieved via an allosteric mechanism. Collectively, our pharmacologic studies show that SSR exhibits all characteristic features of a small-molecule allosteric receptor inhibitor of FGF-driven cellular processes in vitro.

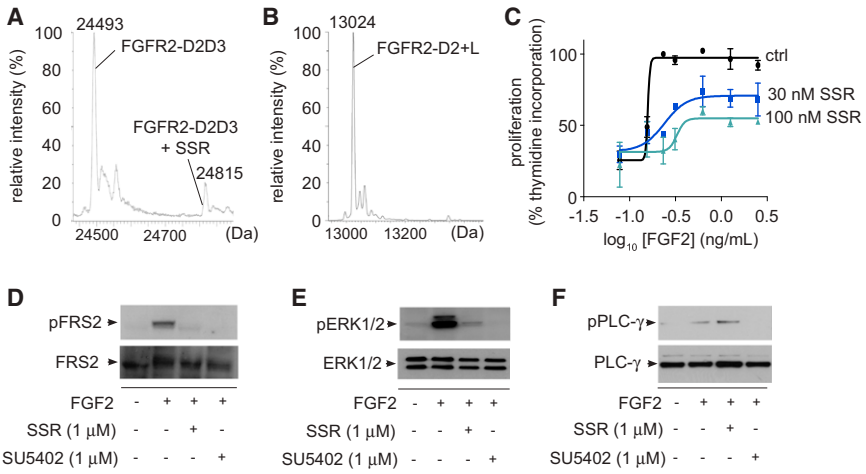

Figure 3. SSR-FGFR Binding Spectra and Effect on FGF-Signaling Pathways

(A and B) Spectra analysis of SSR binding to recombinant extracellular domain fragments of FGFR2. (A) The highest peak on the left corresponds to the expected molecular mass of the FGFR2-D2-3 fragment (24,493 Da); the peak on the right corresponds to the mass of FGFR2-D2-3 plus a single molecule of SSR (24,815 Da). (B) The highest peak corresponds to the expected molecular mass of FGFR2-D2L (13,024 Da).

(C) Effect of increasing SSR concentrations on the mitogenic response of ECs to increasing FGF2 concentrations. Ctrl, control vehicle (DMSO). Quantitative data are presented as mean ± SEM.

(D–F) Immunoblots for FGF2-induced tyrosine phosphorylation of FRS2 (D), ERK1/2 (E), or PLC-γ (F) in the absence or presence of SSR. The RTKI SU5402 was used as positive control.

SSR Inhibits Angiogenesis, Inflammation, and Bone Resorption in Arthritis

We then explored if SSR is capable of inhibiting inflammatory and malignant diseases, known as FGFR-driven processes (Malemud, 2007). Oral administration of SSR (30 mg/kg/day from day 3 onward; unless otherwise specified) reduced the number of limbs affected by redness, swelling, and deformity (3.6 ± 0.1 in controls versus 1.2 ± 0.1 after SSR; n = 10–14; $p < 0.001$). SSR reduced the severity of clinical symptoms (Figures 4A–4C) and slowed down its progression (day of maximal clinical score: 12.7 ± 0.3 days in controls versus 15.3 ± 0.8 days after SSR; n = 10; $p < 0.01$). Radiography revealed that SSR protected the mice against bone and joint damage (Figures 4D and 4E). SSR-treated mice also performed better in an exercise endurance test and ran longer on a treadmill (Figure 4F).

SSR reduced angiogenesis in the inflamed joints ($CD31^+$ vessels per optic field: 3.4 ± 1.6 in normal joints; 28.6 ± 4.2 in arthritic joints of controls versus 11.9 ± 4.6 in arthritic joints after SSR; n = 10–18; $p < 0.05$; Figures 4G and 4H). The antiangiogenic activity of SSR was confirmed in a matrigel model (hemoglobin content: 57 ± 10 mg/ml in control versus 12 ± 3 mg/ml in SSR mice; n = 5; $p < 0.05$). SSR attenuated synovial hyperplasia, inflammation, and pannus formation (Figures 4I, 4J,and 4M), and inhibited the infiltration of $CD45^+$ leukocytes ($CD45^+$ area, percentage of synovial area after 1 week: 14.5% ± 2.3% in controls versus 7.2% ± 1.5% after SSR; n = 5, $p < 0.05$) and osteoclast-mediated cartilage breakdown (safranin-O^+ area/μm: 12.1 ± 1.2 μm^2 in controls versus 16.5 ± 2.2 μm^2 after SSR; n = 18; $p < 0.05$; Figures 4K and 4L).

Oral SSR Delivery Delays Tumor Growth and Metastasis

We also analyzed if SSR inhibited tumor angiogenesis, growth, and metastasis using syngeneic and orthotopic tumor models and human xenograft tumor models. Oral delivery of SSR (30 mg/kg/day, from day 3) inhibited growth of orthotopic Panc02 tumors by 44% (Figures 5A, 5C, and 5E) and delayed growth of Lewis lung carcinoma (LLC) (end-stage tumor size and weight: 1,120 ± 120 mm^3 and 750 ± 80 mg in controls versus 720 ± 133 mm^3 and 430 ± 90 mg after SSR; n = 15; $p < 0.05$; Figure 5F). In murine 4T1 breast tumors, oral SSR (30 mg/kg/day, from day 5) reduced tumor size and weight by 53% and 40%, respectively (end-stage tumor size and weight: 2,050 ± 172 mm^3 and 840 ± 80 mg in controls versus 970 ± 127 mm^3 and 510 ± 80 mg after SSR; n = 15; $p < 0.001$; Figure 5G). In addition, SSR inhibited the growth of subcutaneous CT26 colon tumors by 34% (Figure 5H) and of the multidrug resistant MCF7/ADR breast cancer xenograft model by 40% (end-stage tumor volume: 250 ± 50 mm^3 in controls versus 152 ± 25 mm^3 after SSR; n = 15; $p < 0.01$). Tumor cells in these models expressed one or several FGFRs, while various FGF ligands were also detectable (not shown).

SSR reduced tumor invasiveness because the incidences of tumor invasion in healthy duodenum and of hemorrhagic ascites were lower in SSR-treated mice (75% and 58% of controls versus 15% and 8% of SSR-treated mice, respectively; n = 13; $p < 0.05$). Moreover, SSR inhibited metastasis of Panc02 tumor cells to peritoneal lymph nodes (metastatic nodules/mouse: 24 ± 2.6 in controls versus 8.3 ± 2.3 after SSR; n = 21; $p < 0.05$; Figures 5B and 5D). The reduced number of metastatic lymph nodes upon SSR treatment was not attributable to a reduction in tumor growth only because SSR decreased the metastatic index (metastatic nodes/gram tumor: 41 ± 3 for controls versus 30 ± 3 for SSR; n = 10; $p < 0.05$). In the LLC model, SSR reduced the number of pulmonary metastatic nodules by 43% after 3 weeks (lung metastases: 3.5 ± 0.3 in control versus 2.0 ± 0.3 after SSR; n = 15; $p < 0.05$). Similar results were obtained after orthotopic injection of 4T1 cells into the mammary gland (metastases per lung: 12.7 ± 1.4 in control versus 5.4 ± 0.4 after SSR; n = 15; $p < 0.001$). Altogether, SSR inhibited both the growth of primary tumors and metastasis.

SSR Enhances Tumor Growth Inhibition by Anti-VEGFR2

A substantial fraction of patients with cancer do not or only minimally respond to VEGFR inhibitor therapy (Ebos and Kerbel, 2011). Combinations of anti-angiogenic agents with complementary mechanisms may offer opportunities to overcome resistance. We therefore analyzed if SSR acts via a complementary mechanism to that of the anti-VEGFR2 antibody DC101 (αVEGFR2) (Witte et al., 1998) and if delivery of SSR enhanced the antitumor activity of αVEGFR2 using a model

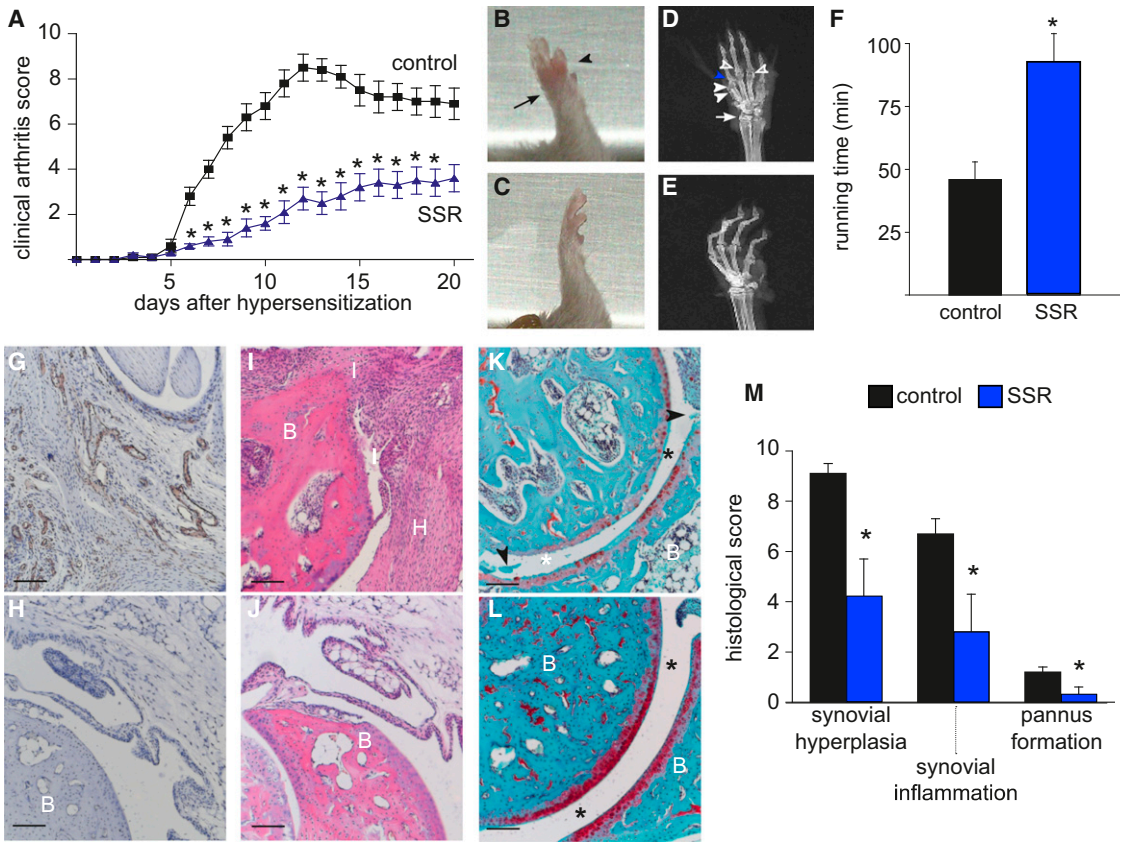

Figure 4. SSR Treatment of Inflammatory Joint Disease

(A) Clinical score of forelimbs and hindlimbs in arthritic mice treated with vehicle or SSR (30 mg/kg/day orally) (n = 10–14; $p < 0.001$ by repeated-measurement ANOVA; *$p < 0.05$ versus control at each time point).

(B and C) Micrographs of forelimb of mice treated with vehicle (B) or SSR (C). Black arrows and arrowheads point to swelling and redness of wrist or digits, respectively.

(D and E) X-ray images of forelimb of mice treated with vehicle (D) or SSR (E). White arrows: radiographic signs of aberrant bone formation; white arrowheads: osteolytic lesions, bone fractures, and bone remodeling; open arrowheads: loss or remodeling of joint space; blue arrowheads: joint fusion.

(F) Endurance treadmill exercise of control and SSR-treated arthritic mice at day 20 after hypersensitization (n = 7–12; *$p < 0.05$).

(G and H) Immunostaining of synovial blood vessels (CD31; brown) in control (G) and SSR-treated mice (H).

(I and J) Hematoxylin and eosin staining to visualize synovial hyperplasia and inflammation in control (I) and SSR-treated mice (J). B, bone; I, synovial inflammation; H, synovial hyperplasia.

(K and L) Safranin-O staining (red) of cartilage proteoglycans in control (K) and SSR-treated mice (L). Asterisks, the joint space; black arrowheads, presence of erosive bone fragment.

(M) Histologic score of synovial hyperplasia, inflammation, and pannus formation in control and SSR-treated mice (n = 5–9. *$p < 0.05$ versus control by Mann-Whitney). Scale bars: 100 μm (G–L). All quantitative data are presented as mean ± SEM.

that is more sensitive (Panc02 tumor) or more refractory (CT26 tumor) to VEGFR inhibitor therapy. In the Panc02 model, a low dose of αVEGFR2 (5 mg/kg; three times per week) inhibited tumor growth by ~40% (Figure 5E), which is comparable to the ~30% inhibition of tumor growth by a high dose of αVEGFR2 (50 mg/kg; three times per week; Figure 5H) in the CT26 model.

Mechanistically, both SSR and αVEGFR2 inhibited angiogenesis in Panc02 tumors ($CD31^+$ area: 5.0% ± 0.4% in control; 3.8% ± 0.3% after SSR; 2.9% ± 0.3% after DC101; n = 10; $p < 0.05$ for all treatments and for SSR versus αVEGFR2). SSR differed however from αVEGFR2 in its effect on macrophage infiltration. Indeed, in contrast to the lack of effect by αVEGFR2, SSR inhibited inflammatory cell infiltration in tumors (Figures 5I–5K). Similar findings were obtained for CT26 tumors (not shown). Thus, SSR inhibits tumor growth via mechanisms that differ from those utilized by αVEGFR2.

We therefore tested if a combination of SSR plus αVEGFR2 inhibited Panc02 tumor growth more extensively. SSR and αVEGFR2 each inhibited tumor growth by ~40%, while the combination treatment inhibited tumor growth by ~70% (Figure 5E). Similar results were obtained when analyzing the metastatic index (41% ± 3% for control; 30% ± 3% for SSR; 33% ± 3% for αVEGFR2 and 20% ± 1% for combination; n = 10; $p < 0.05$ for all treatments and for SSR versus αVEGFR2). When using the VEGFR inhibitor-refractory CT26 tumor model, the combination treatment inhibited tumor growth more than each monotherapy alone (Figure 5H). Thus, SSR acted via different mechanisms from those used by the VEGFR2 inhibitor,

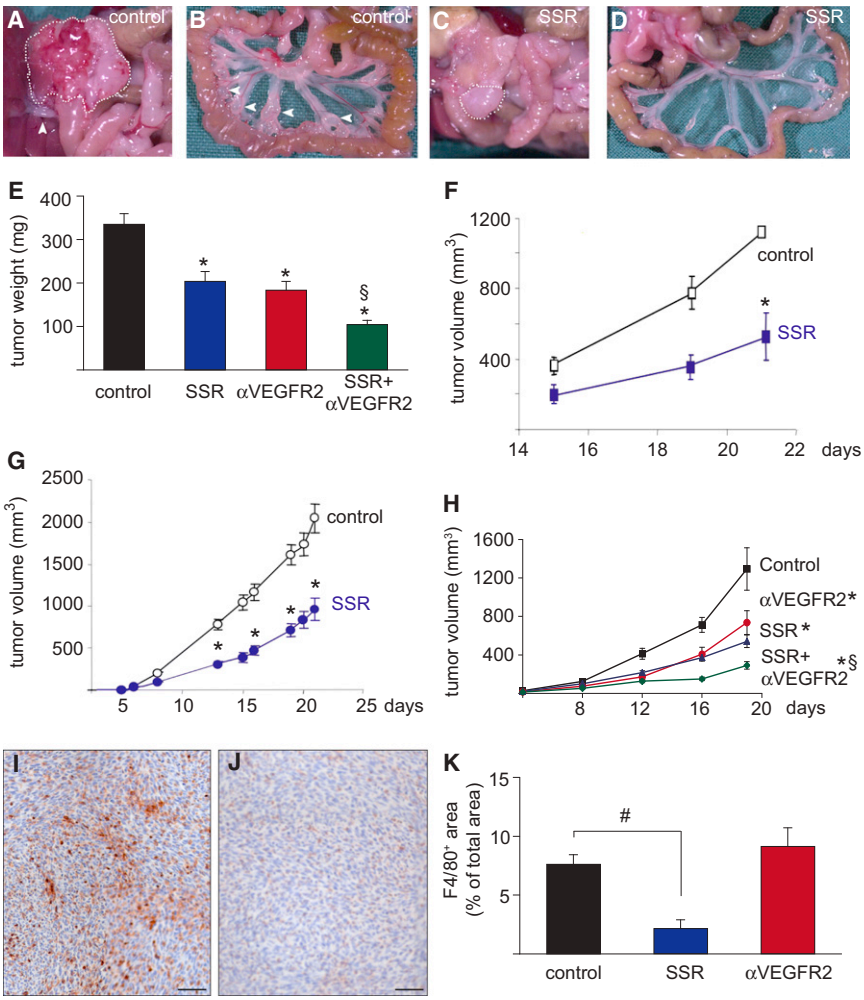

Figure 5. SSR Treatment of Malignant Disorders

(A–D) Effect of SSR (30 mg/kg/day orally) on orthotopic pancreatic Panc02 tumor growth. Representative images of the primary tumor (dashed line) in a control (A) or SSR-treated mouse (C). The white arrowhead in A denotes local infiltration of the primary tumor in the stomach and duodenum and a tumor-infiltrated celiac lymph node. Representative images show tumor-infiltrated mesenterial lymph nodes (white arrowheads) in control (B) and SSR-treated mice (D).

(E) Effect of single and combined treatment of orthotopically implanted Panc02 tumors with SSR (30 mg/kg/day) or αVEGFR2 (5 mg/kg; three times per week) on tumor weight as compared to vehicle-treated tumors (8–10 mice per group, n = 3; *$p < 0.05$ versus control; §$p < 0.05$ versus either monotherapy).

(F and G) Growth curve of subcutaneously implanted LLC tumors (F) and 4T1 breast tumors (G), upon treatment with vehicle (control) or SSR (30 mg/kg/day) (n = 3; *$p < 0.05$).

(H) Effect of single or combined treatment of subcutaneously implanted CT26 colon tumors with SSR (30 mg/kg/day) or αVEGFR2 (5 mg/kg; three times per week intraperitoneally) on tumor weight as compared to vehicle-treated tumors (8–10 mice per group, n = 3; *$p < 0.05$ versus control, §$p < 0.05$ versus either monotherapy).

(I–K) F4/80 immunostaining for macrophages in tumors of SSR-treated (J) versus control (I) mice. (K) shows quantification of tumor infiltration by F4/80$^+$ macrophages in SSR-treated compared to control or αVEGFR2-treated mice (n = 3; *$p < 0.05$). All quantitative data are presented as mean ± SEM. Scale bars: 100 μm (I, J).

inhibited growth of VEGFR inhibitor-refractory and -sensitive tumor models, and enhanced the antitumor activity of a VEGFR inhibitor.

Safety Profile

We assessed the safety profile of SSR by administering it to healthy mice during 3 weeks (30 mg/kg/day). A therapeutic dose of SSR did not cause vessel pruning (tracheal FITC$^+$ vessel area, percentage of total: 11.6% ± 1.1% in control versus 11.0% ± 0.6% after SSR; n = 6, p = NS), did not alter the mean arterial blood pressure (86 ± 3 mm Hg in controls versus 91 ± 4 mm Hg after SSR; n = 5; p = NS), and only minimally elevated plasma levels of the prothrombotic PAI-1 (1.0 ± 0.8 ng/ml in control versus 2.7 ± 0.6 ng/ml in SSR-treated mice; n = 5, $p < 0.05$). Hematologic parameters were normal after SSR, except for a minor anemia (red blood cells: 8.8 ± 0.1 10^6/ml in controls versus 8.3 ± 0.1 10^6/ml after SSR; n = 5; $p < 0.05$). SSR did also not significantly alter the body weight (21.2 ± 0.7 g in controls versus 19.3 ± 1.0 g after SSR; p = NS). In addition, daily treatment of Apo-E knockout mice with SSR for >6 months did not alter plasma cholesterol and triglyceride levels (not shown). Consistent with findings that SSR did not cross the blood-brain barrier, SSR did not impair neurologic performance (not shown).

DISCUSSION

We identified a small-molecule multi-FGFR inhibitor that does not block orthosteric ligand binding and does not act as a classic FGFR-TKI either. Instead, SSR negatively modulates selected FGFR signaling pathways with a pharmacologic profile characteristic of an allosteric mechanism.

Targeting the Fibroblast Growth Factor Receptor Superfamily by SSR

At least two reasons can explain the anti-inflammatory and anticancer activity of SSR. First, SSR is a multi-FGFR blocker with a broad action radius. This is necessary to overcome the substantial redundancy in this superfamily. Blocking a single FGFR with a monoclonal antibody may be beneficial for cancers arising from amplification or constitutive activation of a particular FGFR subtype (Ahmad et al., 2012; Qing et al., 2009; Turner and Grose, 2010). However, in most cancers, multiple FGFs are upregulated and various FGFR subtypes on tumor and stromal cells are activated (Turner and Grose, 2010). In such conditions, blocking a single FGFR may not suffice to yield therapeutic benefit. This may be particularly relevant for ECs, where FGFRs compensate for each other's loss. Indeed, mice,

zebrafish, or tadpoles lacking FGF/FGFRs do not exhibit vessel defects (Arman et al., 1998; Miller et al., 2000; Reifers et al., 2000; Zhou et al., 1998). Also, a genetic mouse study documented redundant roles of FGFRs in coronary vessel formation (Lavine et al., 2006). Hence, by blocking multiple FGFRs simultaneously, SSR not only has a broader action radius, but may also prevent compensatory rescue by other FGFR members.

A second explanation is that SSR inhibits multiple and diverse biologic processes that together synergistically fuel inflammation and tumorigenesis. FGFs induce multiple responses in nearly every cell type in the inflamed or malignant milieu (Malemud, 2007; Pietras et al., 2008). Consistent with findings that aberrant FGF-signaling stimulates tumor cell proliferation and migration, and induces epithelial-to-mesenchymal transition of tumor cells (Billottet et al., 2008; Strutz et al., 2002; Turner and Grose, 2010), SSR blocked FGF-driven proliferation and migration of tumor cells in vitro and slowed down tumor growth and reduced invasiveness and metastasis in vivo. FGFs can also activate FGFRs on ECs directly or stimulate angiogenesis indirectly by inducing the release of angiogenic factors from other cell types (Murakami and Simons, 2008; Presta et al., 2009). In accordance, SSR reduced FGF-driven EC proliferation, migration, and capillary tube formation in vitro and tumor angiogenesis in vivo. But FGFs also stimulate myeloid cells (Berardi et al., 1995), tumor-associated macrophages (Tsunoda et al., 2009), cancer-associated fibroblasts (Itoh, 2007; Kharitonenkov, 2009), and osteoclasts (Collin-Osdoby et al., 2002). Consistently, SSR reduced the accumulation of fibroblasts and myeloid cells in tumors and osteoclast-mediated breakdown of cartilage in arthritic joints. Thus, the anticancer/anti-inflammatory potential of SSR is likely due to a combined effect on many cell types. Because of the broad repertoire of cellular targets for FGFs, a multi-FGFR inhibitor like SSR might be expected to be instrumental in blocking a wider range of inflammatory and malignant diseases than analyzed in this study.

A Multi-Fibroblast Growth Factor Receptor Inhibitor with Allosteric Properties

Several lines of evidence indicate that SSR does not act as a classic orthosteric inhibitor of FGF binding because it failed to competitively antagonize binding of FGF2 to FGFRs in a natural context. SSR also did not act as a classic RTK inhibitor because it exhibits a hydrophilic partition coefficient, did not cross the plasma membrane, and failed to block the kinase activity of FGFR TK domains and a constitutively active TK of FGFR3 in cells.

Instead, SSR exhibits pharmacologic characterstics of an allosteric modulator. Mass spectrometry showed that SSR bound to a site in extracellular D2 or D3 of FGFR2 and failed to bind to a fragment containing D2 and its adjacent linker, implying that SSR likely binds a site in D3. Additional biophysical studies support binding of SSR to D3 (Herbert et al., 2013). Because D2 and its adjacent linker are critical for orthosteric FGF binding, the absence of binding of SSR to this fragment provides circumstantial evidence that SSR does not interfere with orthosteric FGF binding. It would be otherwise puzzling to explain how a small molecule like SSR is capable of inhibiting the responses of FGFRs to multiple FGF ligands via steric hindrance of the orthosteric FGFR pocket, given that FGFs are large polypeptides that utilize multiple epitopes for interaction with their receptors (Beenken and Mohammadi, 2009).

Instead, an allosteric mechanism more likely explains how a small molecule can perturb binding and signaling of a much larger ligand, and our pharmacologic analyses indicate that SSR displays typical pharmacologic hallmarks of an allosteric modulator. For instance, a characteristic of SSR's allosteric interactions was the phenomenon of "probe dependence" i.e., variations in magnitude and direction of an allosteric interaction depending on the nature of the orthosteric ligand-receptor complex with which the modulator is interacting (Christopoulos and Kenakin, 2002; Litschig et al., 1999; May et al., 2007; Price et al., 2005). Binding cooperativity was negative in the SPA with a predimerized Fc-coupled extracellular domain of FGFR2, while it was neutral in the cellular binding assays to a naturally folded and signaling-capable FGFR2. An additional key allosteric feature was the ceiling level (limit) to the degree of inhibition of FGFR tyrosine phosphorylation and ERK1/2 phosphorylation by SSR at high concentrations, as observed for other allosteric modulators (May et al., 2007). SSR also showed a bias toward antagonizing selected FGFR signaling pathways to the relative exclusion of others. This phenomenon cannot be explained by a competitive orthosteric mechanism; if SSR's mode of antagonism was based on steric hindrance of FGF ligands, then all pathways should be blocked nondiscriminatively to the same extent. Overall, rather than acting as an allosteric "affinity modulator", SSR acts as an allosteric "efficacy modulator" (Conn et al., 2009). The finding that SSR inhibits FGFR orthologues and paralogues throughout the animal kingdom suggests that it binds to a conserved allosteric site in the FGFRs. In the accompanying manuscript (Herbert et al., 2013), we characterized the molecular mechanisms of the allosteric properties of the SSR compound.

Possible Implications

From a therapeutic perspective, our studies highlight opportunities for multi-FGFR inhibitors in arthritis and cancer. An intriguing question is if SSR might be useful as an anticancer agent for the treatment of VEGFR-inhibitor-resistant tumors, given that FGFs belong to a class of "rescue" angiogenic factors, when tumor-bearing mice or patients are treated with VEGF inhibitors (Ebos and Kerbel, 2011).

Most anticancer drugs are administered at maximal tolerable dose to block the target's activity as maximally as possible. However, such a strategy may cause adverse effects. Preclinical studies report that high doses of orthosteric VEGF blockers, causing high-grade inhibition of VEGF signaling, induce undesired erythrocytosis (Tam et al., 2006) and fuel metastasis in preclinical models in particular (Ebos and Kerbel, 2011; You et al., 2011). In contrast, irrespective of its dose, an allosteric inhibitor has a ceiling effect and cannot completely wipe out RTK signaling, thus leaving a residual level of baseline signaling that may suffice to ensure cellular homeostasis and prevent evocation of undesired responses. Studies of GPCRs and ion channels show that an allosteric mode of drug-receptor interaction offers opportunities for fine-tuning biologic responses in a manner that is not attainable via classic orthosteric mechanisms (Conn et al., 2009). Finally, from a drug development perspective, our data offer an incentive to develop orally

deliverable small-molecule allosteric RTK inhibitors that bind to an extracellular domain.

EXPERIMENTAL PROCEDURES

Compound Characteristics

Chemical features of SSR128129E are described in the Supplemental Experimental Procedures. Upon oral treatment of mice with 30 mg/kg, a maximal plasma concentration (C_{max}) of 15.2 ± 0.5 mg/l was achieved at 15 min after treatment. The half-life ($T_{1/2}$) was 18.4 hr and the area under the curve at 0–48 hr (AUC_{0-48hr}) was 138.5 mg/hr/l. When rats were treated orally with 10 mg/kg, the C_{max} was 5.3 mg/l, the $T_{1/2}$ was 5.6 hr, the AUC_{0-24h} was 28.3 mg/hr/l, and the V_{ss} was 1.7 l/kg, and 64% of administered SSR was available in the plasma. SSR was not detectable in the cerebrospinal fluid, showing that it was unable to pass through the blood-brain barrier while it did accumulate in peripheral organs (tissue/plasma ratio for liver is 2–3; for brain, 0.01).

Binding Experiments

SPA were performed using FGFR1IIIcβ/Fc and ^{125}I-FGF2, and cellular binding assays by using ^{125}I-FGF2 or ELISA. Binding assays listed in Table S1 were performed by CEREP (Poitiers, France).

Cell Proliferation and Migration Assays

HUVECs, freshly isolated from different donors and used between passage two and five, were cultured in M199 medium (Invitrogen, Life Technologies, Ghent, Belgium) supplemented with 20% fetal bovine serum (FBS), 2 mM L-glutamine, 30 mg/l endothelial cell growth factor supplements (EGCS), 10 units/ml heparin, and penicillin/streptomycin (Lonza, Braine l'Alleud, Belgium). For proliferation, ECs were starved overnight in growth factor-depleted M199 medium containing 2% FBS and stimulated for 24 hr with 10 ng/ml bFGF with SSR or DMSO. Proliferation was assessed the last 2 hr by incubation with 1 μCi/ml [^{3}H]thymidine (Perkin Elmer, Zaventem, Belgium). Proliferation of porcine aortic endothelial (PAE) and tumor cell lines was measured using the CellTiter 96 Aqueous One Solution Cell Proliferation Assay (Promega, Madison, Wisconsin, USA), and cell migration was assessed by a modified Boyden chamber assay, as detailed in the Supplemental Experimental Procedures. Lamellipodia formation and capillary tube formation was assessed as described (Mazzone et al., 2009). Each assay was performed in triplicate and repeated at least three times. B9-FGFR3^{WT} and B9-FGFR3^{K650E} were obtained from S. Trudel (Toronto, ON, Canada).

Fibroblast Growth Factor Receptor Phosphorylation and Tyrosine Kinase Assay

Rat fat-pad endothelial (RFPE) cells expressing FGFR1IIIcα-hemaglutinin, Sf-9 cells expressing His-tagged *Bmbtl*, and HEK293 cells expressing FGFR1IIIca, FGFR2IIIca, or FGFR1IIIcβ were stimulated with FGFs in the presence or absence of SSR. HA-tagged proteins or FGFRs were immunoprecipitated with an anti-HA-antibody and immunoblotted with HRP-conjugated anti-PY or HRP-conjugated anti-HA. Kinase activity measurements of the recombinant catalytic domain of FGFR1 (Sigma-Aldrich, Bornem, Belgium) were done using the ADP-Glo Kinase Assay (Promega, Madison, Wisconsin, USA).

Mass Spectrometry

Mass spectra using purified FGFR2$^{\partial 23}$ and FGFR2$^{\partial 2+L}$ were acquired on a quadrupole orthogonal acceleration time-of-flight mass spectrometer equipped with standard electrospray source. Sample solutions were prepared in acetonitrile/water (1/1 v/v) containing 1% (v/v) acetic acid. The electrospray capillary voltage was 3,000 V and cone voltage 30 V. Nitrogen gas was used for nebulization and desolvation. Spectra were deconvoluted using the MaxEnt algorithm.

Animal Experiments

All procedures and care of animals were approved by the Institutional Animal Care and Research Advisory Committee (KU Leuven, Belgium) and Use Committees of Sanofi-Synthelabo Recherche (France). All animal experiments were performed in accordance with the institutional and national guidelines and regulations and are described extensively in the Supplemental Experimental Procedures.

Statistics

All data represent the mean ± SEM of the indicated number of experiments. We used SPSS v.11.0 for statistical calculations. IC_{50} values were calculated using Prism v4.0b. Statistical significance was calculated by the indicated test, considering $p < 0.05$ as statistically significant.

A more extended version of the materials and methods can be found in the Supplemental Experimental Procedures.

SUPPLEMENTAL INFORMATION

Supplemental Information includes two figures, two tables, and Supplemental Experimental Procedures and can be found with this article online at http://dx.doi.org/10.1016/j.ccr.2013.02.019.

ACKNOWLEDGMENTS

H.S. is supported by the DFG-Cluster of Excellence (EXC115) and by the state of Hesse. M.S. and M.M. are supported by NIH grant HL53793. A.C. is a Senior Research Fellow of the National Health and Medical Research Council of Australia. This work is supported, in part, by grants G.0567.05, G.0405.05, G.0405.06, and G.0789.11 from the FWO, Belgium; GOA/2006/11 from the Concerted Research Activities, Belgium; grant #LSHG-CT-2004-503573 from the EU 6th Framework Program; the Belgian Science Policy (IAP #P5-02 and IAP #P6-30); Leducq Network of Excellence; and long-term structural Methusalem funding by the Flemish Government to P.C. The authors are grateful to M. Krasnow for providing *Btl*-EGFP fruitflies, S. Trudel and Zhihua Li for providing B9 myeloma cell lines, and Lena Claesson-Welsh for providing PAE-FGFR1 cells.

F.B., C.H., C.A., M.B., D.S., F.D.-G., J.P.H., P.R., I.B., G.G., M.F.B., R.B., C.M., I.J., P.S., and J.M.H. are employees of Sanofi-Aventis, Toulouse, France. This work was sponsored in part by a grant from Sanofi-Aventis (to P.C.). P.C., C.H., and F.D. are inventors on the international patent application "extracellular allosteric inhibitor binding domain from a tyrosine kinase receptor" with publication number WO2011/001413 and its national counterparts.

Received: March 17, 2012
Revised: July 24, 2012
Accepted: February 19, 2013
Published: April 15, 2013

REFERENCES

Ahmad, I., Iwata, T., and Leung, H.Y. (2012). Mechanisms of FGFR-mediated carcinogenesis. Biochim. Biophys. Acta *1823*, 850–860.

Arman, E., Haffner-Krausz, R., Chen, Y., Heath, J.K., and Lonai, P. (1998). Targeted disruption of fibroblast growth factor (FGF) receptor 2 suggests a role for FGF signaling in pregastrulation mammalian development. Proc. Natl. Acad. Sci. USA *95*, 5082–5087.

Beenken, A., and Mohammadi, M. (2009). The FGF family: biology, pathophysiology and therapy. Nat. Rev. Drug Discov. *8*, 235–253.

Berardi, A.C., Wang, A., Abraham, J., and Scadden, D.T. (1995). Basic fibroblast growth factor mediates its effects on committed myeloid progenitors by direct action and has no effect on hematopoietic stem cells. Blood *86*, 2123–2129.

Bergers, G., and Hanahan, D. (2008). Modes of resistance to anti-angiogenic therapy. Nat. Rev. Cancer *8*, 592–603.

Billottet, C., Tuefferd, M., Gentien, D., Rapinat, A., Thiery, J.P., Broët, P., and Jouanneau, J. (2008). Modulation of several waves of gene expression during FGF-1 induced epithelial-mesenchymal transition of carcinoma cells. J. Cell. Biochem. *104*, 826–839.

Brozzo, M.S., Bjelić, S., Kisko, K., Schleier, T., Leppänen, V.M., Alitalo, K., Winkler, F.K., and Ballmer-Hofer, K. (2012). Thermodynamic and structural

description of allosterically regulated VEGFR-2 dimerization. Blood *119*, 1781–1788.

Casanovas, O., Hicklin, D.J., Bergers, G., and Hanahan, D. (2005). Drug resistance by evasion of antiangiogenic targeting of VEGF signaling in late-stage pancreatic islet tumors. Cancer Cell *8*, 299–309.

Chahrour, O., Cairns, D., and Omran, Z. (2012). Small molecule kinase inhibitors as anti-cancer therapeutics. Mini Rev. Med. Chem. *12*, 399–411.

Christopoulos, A. (2002). Allosteric binding sites on cell-surface receptors: novel targets for drug discovery. Nat. Rev. Drug Discov. *1*, 198–210.

Christopoulos, A., and Kenakin, T. (2002). G protein-coupled receptor allosterism and complexing. Pharmacol. Rev. *54*, 323–374.

Chung, A.S., and Ferrara, N. (2011). Developmental and pathological angiogenesis. Annu. Rev. Cell Dev. Biol. *27*, 563–584.

Collin-Osdoby, P., Rothe, L., Bekker, S., Anderson, F., Huang, Y., and Osdoby, P. (2002). Basic fibroblast growth factor stimulates osteoclast recruitment, development, and bone pit resorption in association with angiogenesis in vivo on the chick chorioallantoic membrane and activates isolated avian osteoclast resorption in vitro. J. Bone Miner. Res. *17*, 1859–1871.

Conn, P.J., Christopoulos, A., and Lindsley, C.W. (2009). Allosteric modulators of GPCRs: a novel approach for the treatment of CNS disorders. Nat. Rev. Drug Discov. *8*, 41–54.

Cox, K.J., Shomin, C.D., and Ghosh, I. (2011). Tinkering outside the kinase ATP box: allosteric (type IV) and bivalent (type V) inhibitors of protein kinases. Fut Med. Chem. *3*, 29–43.

Daniele, G., Corral, J., Molife, L.R., and de Bono, J.S. (2012). FGF receptor inhibitors: role in cancer therapy. Curr. Oncol. Rep. *14*, 111–119.

Ebos, J.M., and Kerbel, R.S. (2011). Antiangiogenic therapy: impact on invasion, disease progression, and metastasis. Nature reviews. Clin. Oncol. *8*, 210–221.

Fischer, C., Jonckx, B., Mazzone, M., Zacchigna, S., Loges, S., Pattarini, L., Chorianopoulos, E., Liesenborghs, L., Koch, M., De Mol, M., et al. (2007). Anti-PlGF inhibits growth of VEGF(R)-inhibitor-resistant tumors without affecting healthy vessels. Cell *131*, 463–475.

Herbert, C., Schieborr, U., Saxena, K., Juraszek, J., De Smet, F., Alcouffe, C., Bianciotto, M., Saladino, G., Sibrac, D., Kudlinzki, D., et al. (2013). Molecular mode of action of SSR128129E, a small molecule allosteric inhibitor of FGF receptor signaling. Cancer Cell. *23*, this issue, 489–501.

Itoh, N. (2007). The Fgf families in humans, mice, and zebrafish: their evolutional processes and roles in development, metabolism, and disease. Biol. Pharm. Bull. *30*, 1819–1825.

Itoh, N., and Ornitz, D.M. (2011). Fibroblast growth factors: from molecular evolution to roles in development, metabolism and disease. J. Biochem. *149*, 121–130.

Keov, P., Sexton, P.M., and Christopoulos, A. (2011). Allosteric modulation of G protein-coupled receptors: a pharmacological perspective. Neuropharmacology *60*, 24–35.

Kharitonenkov, A. (2009). FGFs and metabolism. Curr. Opin. Pharmacol. *9*, 805–810.

Knoflach, F., Mutel, V., Jolidon, S., Kew, J.N., Malherbe, P., Vieira, E., Wichmann, J., and Kemp, J.A. (2001). Positive allosteric modulators of metabotropic glutamate one receptor: characterization, mechanism of action, and binding site. Proc. Natl. Acad. Sci. USA *98*, 13402–13407.

Landgraf, K.E., Santell, L., Billeci, K.L., Quan, C., Young, J.C., Maun, H.R., Kirchhofer, D., and Lazarus, R.A. (2010). Allosteric peptide activators of prohepatocyte growth factor stimulate Met signaling. J. Biol. Chem. *285*, 40362–40372.

Lavine, K.J., White, A.C., Park, C., Smith, C.S., Choi, K., Long, F., Hui, C.C., and Ornitz, D.M. (2006). Fibroblast growth factor signals regulate a wave of Hedgehog activation that is essential for coronary vascular development. Genes Dev. *20*, 1651–1666.

Leach, K., Sexton, P.M., and Christopoulos, A. (2007). Allosteric GPCR modulators: taking advantage of permissive receptor pharmacology. Trends Pharmacol. Sci. *28*, 382–389.

Lemmon, M.A., and Schlessinger, J. (2010). Cell signaling by receptor tyrosine kinases. Cell *141*, 1117–1134.

Litschig, S., Gasparini, F., Rueegg, D., Stoehr, N., Flor, P.J., Vranesic, I., Prézeau, L., Pin, J.P., Thomsen, C., and Kuhn, R. (1999). CPCCOEt, a noncompetitive metabotropic glutamate receptor 1 antagonist, inhibits receptor signaling without affecting glutamate binding. Mol. Pharmacol. *55*, 453–461.

Malemud, C.J. (2007). Growth hormone, VEGF and FGF: involvement in rheumatoid arthritis. Clin. Chim. Acta *375*, 10–19.

May, L.T., Leach, K., Sexton, P.M., and Christopoulos, A. (2007). Allosteric modulation of G protein-coupled receptors. Annu. Rev. Pharmacol. Toxicol. *47*, 1–51.

Mazzone, M., Dettori, D., Leite de Oliveira, R., Loges, S., Schmidt, T., Jonckx, B., Tian, Y.M., Lanahan, A.A., Pollard, P., Ruiz de Almodovar, C., et al. (2009). Heterozygous deficiency of PHD2 restores tumor oxygenation and inhibits metastasis via endothelial normalization. Cell *136*, 839–851.

McDermott, L.A., Simcox, M., Higgins, B., Nevins, T., Kolinsky, K., Smith, M., Yang, H., Li, J.K., Chen, Y., Ke, J., et al. (2005). RO4383596, an orally active KDR, FGFR, and PDGFR inhibitor: synthesis and biological evaluation. Bioorg. Med. Chem. *13*, 4835–4841.

Miller, D.L., Ortega, S., Bashayan, O., Basch, R., and Basilico, C. (2000). Compensation by fibroblast growth factor 1 (FGF1) does not account for the mild phenotypic defects observed in FGF2 null mice. Mol. Cell. Biol. *20*, 2260–2268.

Murakami, M., and Simons, M. (2008). Fibroblast growth factor regulation of neovascularization. Curr. Opin. Hematol. *15*, 215–220.

Pietras, K., Pahler, J., Bergers, G., and Hanahan, D. (2008). Functions of paracrine PDGF signaling in the proangiogenic tumor stroma revealed by pharmacological targeting. PLoS Med. *5*, e19.

Presta, M., Andrés, G., Leali, D., Dell'Era, P., and Ronca, R. (2009). Inflammatory cells and chemokines sustain FGF2-induced angiogenesis. Eur. Cytokine Netw. *20*, 39–50.

Price, M.R., Baillie, G.L., Thomas, A., Stevenson, L.A., Easson, M., Goodwin, R., McLean, A., McIntosh, L., Goodwin, G., Walker, G., et al. (2005). Allosteric modulation of the cannabinoid CB1 receptor. Mol. Pharmacol. *68*, 1484–1495.

Qing, J., Du, X., Chen, Y., Chan, P., Li, H., Wu, P., Marsters, S., Stawicki, S., Tien, J., Totpal, K., et al. (2009). Antibody-based targeting of FGFR3 in bladder carcinoma and t(4;14)-positive multiple myeloma in mice. J. Clin. Invest. *119*, 1216–1229.

Reifers, F., Walsh, E.C., Léger, S., Stainier, D.Y., and Brand, M. (2000). Induction and differentiation of the zebrafish heart requires fibroblast growth factor 8 (fgf8/acerebellar). Development *127*, 225–235.

Strutz, F., Zeisberg, M., Ziyadeh, F.N., Yang, C.Q., Kalluri, R., Müller, G.A., and Neilson, E.G. (2002). Role of basic fibroblast growth factor-2 in epithelial-mesenchymal transformation. Kidney Int. *61*, 1714–1728.

Tam, B.Y., Wei, K., Rudge, J.S., Hoffman, J., Holash, J., Park, S.K., Yuan, J., Hefner, C., Chartier, C., Lee, J.S., et al. (2006). VEGF modulates erythropoiesis through regulation of adult hepatic erythropoietin synthesis. Nat. Med. *12*, 793–800.

Thaker, T.M., Kaya, A.I., Preininger, A.M., Hamm, H.E., and Iverson, T.M. (2012). Allosteric mechanisms of G protein-Coupled Receptor signaling: a structural perspective. Methods Mol. Biol. *796*, 133–174.

Tsunoda, S., Sakurai, H., Saito, Y., Ueno, Y., Koizumi, K., and Saiki, I. (2009). Massive T-lymphocyte infiltration into the host stroma is essential for fibroblast growth factor-2-promoted growth and metastasis of mammary tumors via neovascular stability. Am. J. Pathol. *174*, 671–683.

Turner, N., and Grose, R. (2010). Fibroblast growth factor signalling: from development to cancer. Nat. Rev. Cancer *10*, 116–129.

Tvorogov, D., Anisimov, A., Zheng, W., Leppänen, V.M., Tammela, T., Laurinavicius, S., Holnthoner, W., Heloterä, H., Holopainen, T., Jeltsch, M., et al. (2010). Effective suppression of vascular network formation by combination of antibodies blocking VEGFR ligand binding and receptor dimerization. Cancer Cell *18*, 630–640.

Urban, J.D., Clarke, W.P., von Zastrow, M., Nichols, D.E., Kobilka, B., Weinstein, H., Javitch, J.A., Roth, B.L., Christopoulos, A., Sexton, P.M., et al. (2007). Functional selectivity and classical concepts of quantitative pharmacology. J. Pharmacol. Exp. Ther. *320*, 1–13.

Wesche, J., Haglund, K., and Haugsten, E.M. (2011). Fibroblast growth factors and their receptors in cancer. Biochem. J. *437*, 199–213.

Witte, L., Hicklin, D.J., Zhu, Z., Pytowski, B., Kotanides, H., Rockwell, P., and Böhlen, P. (1998). Monoclonal antibodies targeting the VEGF receptor-2 (Flk1/KDR) as an anti-angiogenic therapeutic strategy. Cancer Metastasis Rev. *17*, 155–161.

You, W.K., Sennino, B., Williamson, C.W., Falcón, B., Hashizume, H., Yao, L.C., Aftab, D.T., and McDonald, D.M. (2011). VEGF and c-Met blockade amplify angiogenesis inhibition in pancreatic islet cancer. Cancer Res. *71*, 4758–4768.

Zhou, M., Sutliff, R.L., Paul, R.J., Lorenz, J.N., Hoying, J.B., Haudenschild, C.C., Yin, M., Coffin, J.D., Kong, L., Kranias, E.G., et al. (1998). Fibroblast growth factor 2 control of vascular tone. Nat. Med. *4*, 201–207.

Cancer Cell
Article

SIRT4 Has Tumor-Suppressive Activity and Regulates the Cellular Metabolic Response to DNA Damage by Inhibiting Mitochondrial Glutamine Metabolism

Seung Min Jeong,[1,6] Cuiying Xiao,[3,6] Lydia W.S. Finley,[1] Tyler Lahusen,[3] Amanda L. Souza,[4] Kerry Pierce,[4] Ying-Hua Li,[2] Xiaoxu Wang,[2] Gaëlle Laurent,[1] Natalie J. German,[1] Xiaoling Xu,[3] Cuiling Li,[3] Rui-Hong Wang,[3] Jaewon Lee,[1] Alfredo Csibi,[1] Richard Cerione,[5] John Blenis,[1] Clary B. Clish,[4] Alec Kimmelman,[2] Chu-Xia Deng,[3,*] and Marcia C. Haigis[1,*]
[1]Department of Cell Biology
[2]Division of Genomic Stability and DNA Repair, Department of Radiation Oncology, Dana-Farber Cancer Institute
Harvard Medical School, Boston, MA 02115, USA
[3]Mammalian Genetics Section, Genetics of Development and Disease Branch, National Institute of Diabetes, Digestive and Kidney Diseases, National Institutes of Health, Bethesda, MD 20892, USA
[4]Metabolite Profiling Platform, Broad Institute of MIT and Harvard, Cambridge, MA 02142, USA
[5]Department of Molecular Medicine, Cornell University, Ithaca, NY 14853, USA
[6]These authors contributed equally to this work
*Correspondence: chuxiad@bdg10.niddk.nih.gov (C.-X.D.), marcia_haigis@hms.harvard.edu (M.C.H.)
http://dx.doi.org/10.1016/j.ccr.2013.02.024

SUMMARY

DNA damage elicits a cellular signaling response that initiates cell cycle arrest and DNA repair. Here, we find that DNA damage triggers a critical block in glutamine metabolism, which is required for proper DNA damage responses. This block requires the mitochondrial SIRT4, which is induced by numerous genotoxic agents and represses the metabolism of glutamine into tricarboxylic acid cycle. SIRT4 loss leads to both increased glutamine-dependent proliferation and stress-induced genomic instability, resulting in tumorigenic phenotypes. Moreover, SIRT4 knockout mice spontaneously develop lung tumors. Our data uncover SIRT4 as an important component of the DNA damage response pathway that orchestrates a metabolic block in glutamine metabolism, cell cycle arrest, and tumor suppression.

INTRODUCTION

DNA damage initiates a tightly coordinated signaling response to maintain genomic integrity by promoting cell cycle arrest and DNA repair. Upon DNA damage, ataxia telangiectasia mutated (ATM) and ataxia telangiectasia and RAD3-related protein (ATR) are activated and induce phosphorylation of CHK1, CHK2, and γ-H2AX to trigger cell cycle arrest and to initiate assembly of DNA damage repair machinery (Abraham, 2001; Ciccia and Elledge, 2010; Su, 2006). Cell cycle arrest is a critical outcome of the DNA damage response (DDR), and defects in the DDR often lead to increased incorporation of mutations into newly synthesized DNA, the accumulation of chromosomal instability, and tumor development (Abbas and Dutta, 2009; Deng, 2006; Negrini et al., 2010).

The cellular metabolic response to DNA damage is not well elucidated. Recently, it has been shown that DNA damage causes cells to upregulate the pentose phosphate pathway (PPP) to generate nucleotide precursors needed for DNA repair (Cosentino et al., 2011). Intriguingly, a related metabolic switch to increase anabolic glucose metabolism has been observed for tumor cells and is an important component of rapid generation of biomass for cell growth and proliferation (Jones and Thompson, 2009; Koppenol et al., 2011). Hence, cells exposed to genotoxic stress face a metabolic challenge; they must be able to upregulate nucleotide biosynthesis to facilitate DNA repair, while at the same time limiting proliferation and inducing cell cycle arrest to limit the accumulation of damaged DNA. The molecular events that regulate this specific metabolic program in response to DNA damage are still unclear.

Significance

Genomic instability and altered metabolism are key features of many cancer cells. Thus, defining the factors that are involved in regulating DNA damage responses and metabolic processes may have profound implications for the development of strategies to prevent or treat cancer. We find that SIRT4, a mitochondria-localized sirtuin, functions as a tumor suppressor by regulating metabolic responses to DNA damage and repressing mitochondrial glutamine metabolism. Importantly, we also show that SIRT4 knockout mice spontaneously develop several types of tumors and SIRT4 expression is decreased in many human cancers. Our findings suggest that SIRT4 may be a potential therapeutic target against tumors.

Sirtuins are a highly conserved family of nicotinamide adenine dinucleotide (NAD^+)-dependent deacetylases, deacylases, and ADP-ribosyltransferases that play various roles in metabolism, stress response, and longevity (Finkel et al., 2009; Haigis and Guarente, 2006). In this study, we studied the role of SIRT4, a mitochondria-localized sirtuin, in cellular metabolic response to DNA damage and tumorigenesis.

RESULTS

DNA Damage Represses Glutamine Metabolism

To investigate how cells might balance needs for continued nucleotide synthesis, while also preparing for cell cycle arrest, we assessed the metabolic response to DNA damage by monitoring changes in the cellular consumption of two important fuels, glucose and glutamine, after DNA damage. Strikingly, treatment of primary mouse embryonic fibroblasts (MEFs) with camptothecin (CPT), a topoisomerase 1 inhibitor that causes double-stranded DNA breaks (DSBs), resulted in a pronounced reduction in glutamine consumption (Figure 1A). Glutamine metabolism in mammalian cells is complex and contributes to a number of metabolic pathways. Glutamine is the primary nitrogen donor for protein and nucleotide synthesis, which are essential for cell proliferation (Wise and Thompson, 2010). Additionally, glutamine provides mitochondrial anaplerosis. Glutamine can be metabolized via glutaminase (GLS) to glutamate and NH_4^+ and further converted to the tricarboxylic acid (TCA) cycle intermediate α-ketoglutarate via glutamate dehydrogenase (GDH) or aminotransferases. This metabolism of glutamine provides an important entry point of carbon to fuel the TCA cycle (Jones and Thompson, 2009) and accounts for the majority of ammonia production in cells (Yang et al., 2009). CPT-induced reduction of glutamine consumption was accompanied by a reduction in ammonia secretion from cells (Figure 1B). Notably, under these conditions, we observed no obvious decrease in glucose uptake and lactate production (Figures 1C and 1D), consistent with previous studies showing that intact glucose utilization through the PPP is important for a normal DNA damage response (Cosentino et al., 2011). Preservation of glucose uptake also suggests that repression of glutamine consumption may be a specific metabolic response to genotoxic stress and not reflective of a nonspecific metabolic crisis.

To examine the metabolic response to other forms of genotoxic stress, we monitored the metabolic response to ultraviolet (UV) exposure in primary MEFs. Similar to CPT treatment, UV exposure reduced glutamine uptake without significant changes in glucose consumption (Figures 1E and 1F). Similarly, two human cell lines, HepG2 and HEK293T, also demonstrated marked reductions in glutamine uptake in response to DNA damaging agents without comparable changes in glucose uptake (Figures 1G, 1H, S1A, and S1B available online). Taken together, these results suggest that a variety of primary and tumor cell lines (murine or human) respond to genotoxic stress by downregulating glutamine metabolism.

To examine in more detail the changes in cellular glutamine metabolism after genotoxic stress, we performed a global metabolomic analysis with transformed MEFs before and after DNA damage. As previously reported, we observed that PPP intermediates were increased in response to DNA damage (Figures 1I and 1J). Remarkably, we observed a decrease in measured TCA cycle intermediates after UV exposure (Figures 1I and 1K). Moreover, we found that HepG2 cells showed a similar metabolomic shift in response to DNA damage (Figure S1D). We did not observe a clear, coordinated repression of nucleotides or glutamine-derived amino acids after exposure to DNA damage (Figure S1C).

To determine whether reduction in TCA cycle metabolites was the consequence of reduced glutamine metabolism, we performed a time-course tracer study to monitor the incorporation of [U-$^{13}C_5$]glutamine into TCA cycle intermediates at 0, 2, and 4 hr after UV treatment. We observed that, after UV exposure, cells reduced contribution of glutamine to TCA cycle intermediates in a time-dependent manner (Figure 1L). Moreover, the vast majority of the labeled fumarate and malate contained four carbon atoms derived from [U-$^{13}C_5$]glutamine (Figure S1F, M+3 versus M+4), indicating that most glutamine was used in the nonreductive direction toward succinate, fumarate, and malate production. We were able to observe little contribution of glutamine flux into nucleotides or glutathione in control or UV-treated cells at these time points (data not shown), suggesting that the mitochondrial metabolism of glutamine accounts for the majority of glutamine consumption in these cells. Taken together, the metabolic flux analysis demonstrates that DNA damage results in a reduction of mitochondrial glutamine anaplerosis, thus limiting the critical refueling of carbons into the TCA cycle.

To assess the functional relevance of decreased glutamine metabolism after DNA damage, we deprived cells of glucose, thereby shifting cellular dependence to glutamine to maintain viability (Choo et al., 2010; Dang, 2010). If DNA damage represses glutamine usage, we reasoned that cells would be more sensitive to glucose deprivation. Indeed, following 72 hr of glucose deprivation, cell death in primary MEFs was significantly elevated at 10 hr after UV exposure (Figure S1E). However, cells cultured with glucose remained viable in these conditions. Thus, these data demonstrate that genotoxic stress limits glutamine entry into the central mitochondrial metabolism of the TCA cycle.

SIRT4 Is Induced in Response to Genotoxic Stress

Because sirtuins regulate both cellular metabolism and stress responses (Finkel et al., 2009; Schwer and Verdin, 2008), we examined whether sirtuins were involved in the metabolic adaptation to DNA damage. We first examined the expression of sirtuins in the response to DNA damage. Specifically, we probed SIRT1, which is involved in stress responses (Haigis and Guarente, 2006), as well as mitochondrial sirtuins (SIRT3–SIRT5), which have been shown to regulate amino acid metabolism (Haigis et al., 2006; Hallows et al., 2011; Nakagawa et al., 2009). Remarkably, *SIRT4* messenger RNA (mRNA) levels were induced by nearly 15-fold at 15 hr after CPT treatment and 5-fold after etoposide (ETS), a topoisomerase 2 inhibitor, in HEK293T cells (Figure 2A). Interestingly, the induction of *SIRT4* was significantly higher than the induction of *SIRT1* and mitochondrial *SIRT3* (~2-fold), sirtuins known to be induced by DNA damage and regulate cellular responses to DNA damage (Sundaresan et al., 2008; Vaziri et al., 2001; Wang et al., 2006). Moreover, overall mitochondrial mass was increased by only

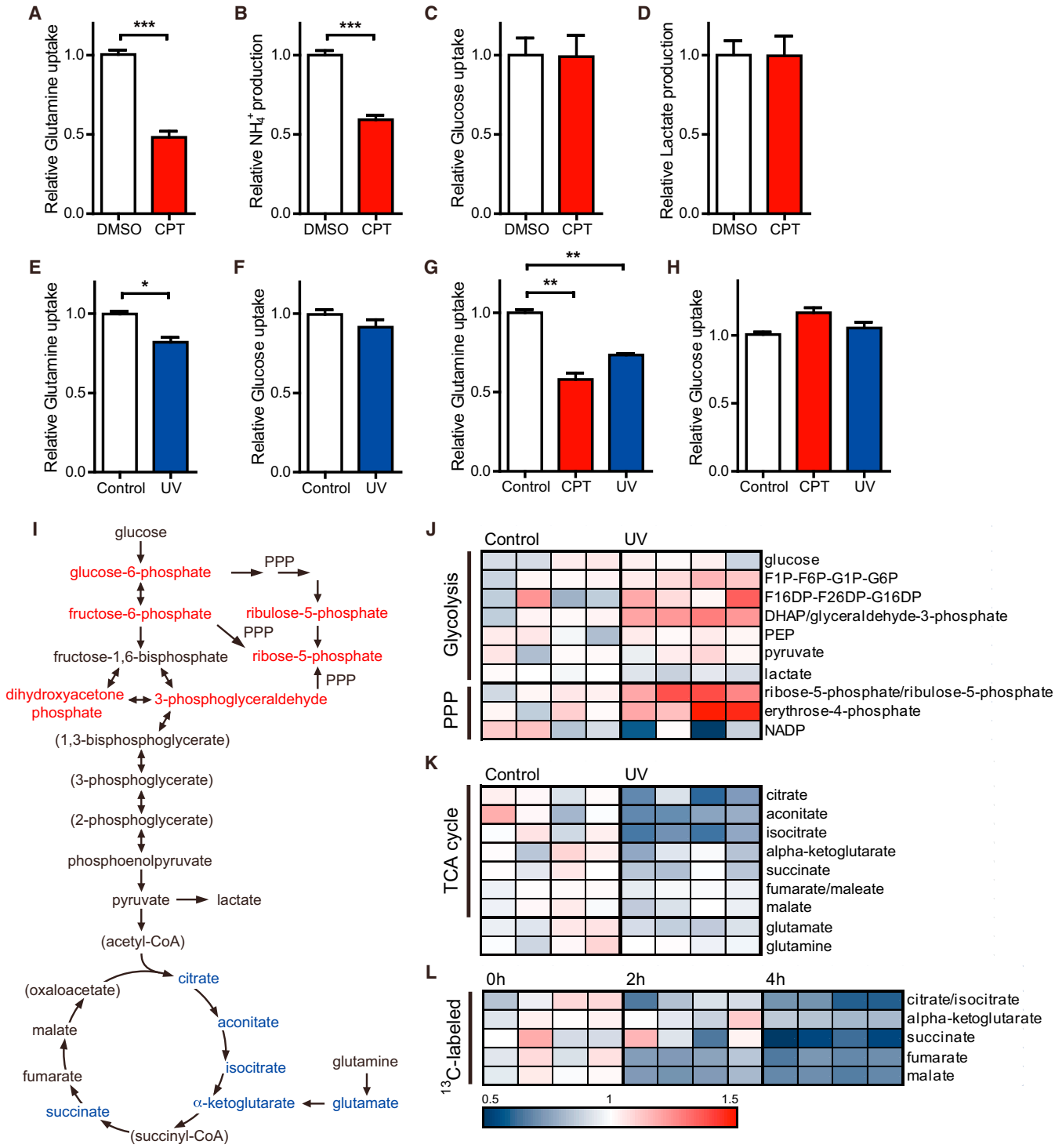

Figure 1. Glutamine Metabolism Is Repressed by Genotoxic Stress

(A and B) Glutamine uptake (A) and ammonia production (B) in primary MEFs incubated with or without 14 μM CPT for 12 hr (n = 8–9).

(C and D) Glucose uptake (C) and lactate production (D) in primary MEFs treated as indicated in Figure 1A (n = 8–9).

(E and F) Glutamine (E) and glucose (F) uptake in primary MEFs measured at 6 hr after 30 J/m^2 UV exposure (n = 3).

(G and H) Glutamine (G) and glucose (H) uptake in HepG2 cells treated with or without 14 μM CPT for 12 hr or at 6 hr after 30 J/m^2 UV exposure (n = 3–6).

(I) Schematic illustrating the metabolites that are increased (red) or decreased (blue) in transformed MEFs at 4 hr after 20 J/m^2 UV exposure (n = 4; $p < 0.05$). Metabolites in parentheses were not measured.

(J and K) Heat map comparing relative levels of intermediates in transformed MEFs measured at 4 hr after 20 J/m^2 UV exposure when compared with an untreated control (n = 4 samples of each condition). Blue and red indicates down- or upregulation, respectively.

(legend continued on next page)

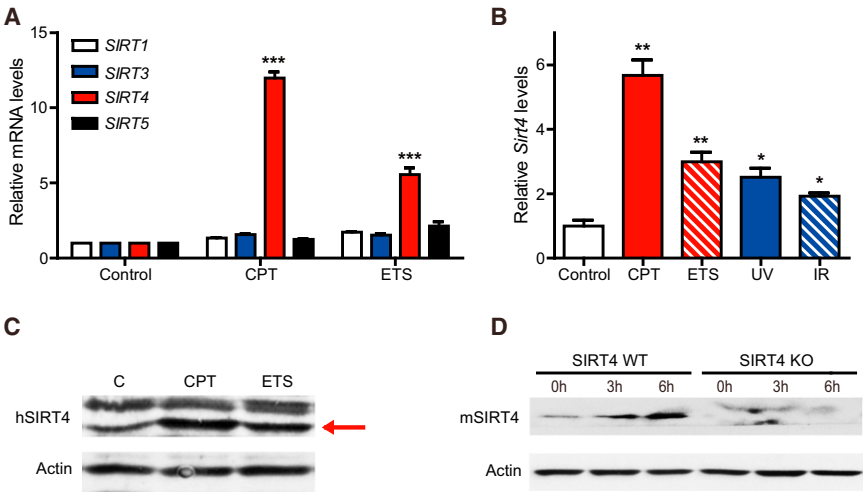

Figure 2. SIRT4 Is Induced by DNA Damage Stimuli

(A) Relative mRNA expression levels of indicated sirtuins in HEK293T cells treated with 14 μM CPT or 25 μM ETS for 15 hr were measured by quantitative RT-PCR (qRT-PCR) (n = 4). β-actin was used as an endogenous control for qRT-PCR.

(B) Relative *Sirt4* mRNA levels in primary MEFs at 12 hr after treatment with CPT (14 μM), ETS (25 μM), IR (5 Gy), or UV (30 J/m^2) were measured by qRT-PCR (n = 3–4). β-actin was used as an endogenous control for qRT-PCR.

(C) SIRT4 protein in whole cell lysates from HEK293T cells treated with CPT (14 μM) or ETS (25 μM) for 15 hr was detected by immunoblotting with anti-human SIRT4. β-actin serves as a loading control.

(D) SIRT4 protein in transformed WT and SIRT4 KO MEFs treated CPT (14 μM) for the indicated times. β-actin serves as a loading control.

Data are means ± SEM. *p < 0.05, **p < 0.005, and ***p < 0.0001.

See also Figure S2.

10% in comparison with control cells (Figure S2A), indicating that the induction of *SIRT4* is not an indirect consequence of mitochondrial biogenesis. These data hint that SIRT4 may have an important, previously undetermined role in the DDR.

To test the induction of *SIRT4* in the general genotoxic stress response, we treated cells with other types of DNA damage, including UV and gamma-irradiation (IR). *SIRT4* mRNA levels were also increased by these genotoxic agents (Figures S2B and S2C), and low doses of CPT and UV treatment also induced *SIRT4* expression (Figures S2D and S2E). We observed similar results with MEFs (Figures 2B, 2D, and S2F) and HepG2 cells (Figure S2G). DNA-damaging agents elevated *SIRT4* in p53-inactive HEK293T cells (Figures 2A and 2C) and in *p53* null PC3 human prostate cancer cells (Figure S2H), suggesting that *SIRT4* can be induced in a p53-independent manner.

To examine whether the induction of *SIRT4* occurred as a result of cell cycle arrest, we measured *SIRT4* levels after the treatment of nocodazole, which inhibits microtubule polymerization to block mitosis. While treatment with nocodazole completely inhibited cell proliferation (data not shown), *SIRT4* expression was not elevated (Figure S2I). In addition, we analyzed *SIRT4* expression in distinct stages of the cell cycle in HepG2 cells synchronized with thymidine block (Figure S2J, left). *SIRT4* mRNA levels were measured at different times after release and were not elevated during G1 or G2/M phases (Figure S2J, right), suggesting that *SIRT4* is not induced as a general consequence of cell cycle arrest. Next, we re-examined the localization of SIRT4 after DNA damage. SIRT4 localizes to the mitochondria of human and mouse cells under basal, unstressed conditions (Ahuja et al., 2007; Haigis et al., 2006). Following CPT treatment, SIRT4 colocalized with MitoTracker, a mitochondrial-selective marker, indicating that SIRT4 retains its mitochondrial localization after exposure to DNA damage (Figure S2K). Taken together, our findings demonstrate that SIRT4 is induced by multiple forms of DNA damage in numerous cell types, perhaps to coordinate the mitochondrial response to genotoxic stress.

SIRT4 Represses Glutamine Anaplerosis

We observed that glutamine anaplerosis is repressed by genotoxic stress (Figure 1) and SIRT4 is induced by DNA damage (Figure 2). Additionally, previous studies reported that SIRT4 represses glutamine anaplerosis (Haigis et al., 2006). We next tested whether SIRT4 directly regulates cellular glutamine metabolism and contribution of glutamine to the TCA cycle. Like DNA damage, SIRT4 overexpression (SIRT4-OE) in HepG2, HeLa, or HEK293T cells resulted in the repression of glutamine consumption (Figures 3A and S3A–S3C). Conversely, SIRT4 knockout (KO) MEFs consumed more glutamine than did wild-type (WT) cells (Figure 3B).

Mitochondrial glutamine catabolism refuels the TCA cycle and is essential for viability in the absence of glucose (Choo et al., 2010; Yang et al., 2009). Thus, we examined the effect of SIRT4 on cell survival during glucose deprivation. Overexpression of SIRT4 in HEK293T or HeLa cells increased cell death in glucose-free media compared to control cells (Figure 3C; Figure S3D). Importantly, this cell death was completely rescued by the addition of pyruvate or cell permeable dimethyl α-ketoglutarate (DM-KG), demonstrating that SIRT4 overexpression reduced the ability of cells to utilize glutamine for mitochondrial energy production. Moreover, cell death was equally maximized in the absence of glucose and presence of the mitochondrial ATPase inhibitor oligomycin (Figure 3C). These findings are in line with the model that SIRT4 induction with DNA damage limits glutamine metabolism and utilization by the TCA cycle.

We next utilized a metabolomic approach to interrogate glutamine usage in the absence of SIRT4. SIRT4 KO MEFs

(L) Heat map of ^{13}C-glutamine contributed to labeled TCA cycle intermediates at 0, 2, and 4 hr after 20 J/m^2 UV exposure (n = 4 samples of each condition). All changes are relative incorporation compared to each non-UV treated control after pulse of ^{13}C-glutamine.

Data are means ± SEM. *p < 0.05, **p < 0.005, and ***p < 0.0001.

See also Figure S1.

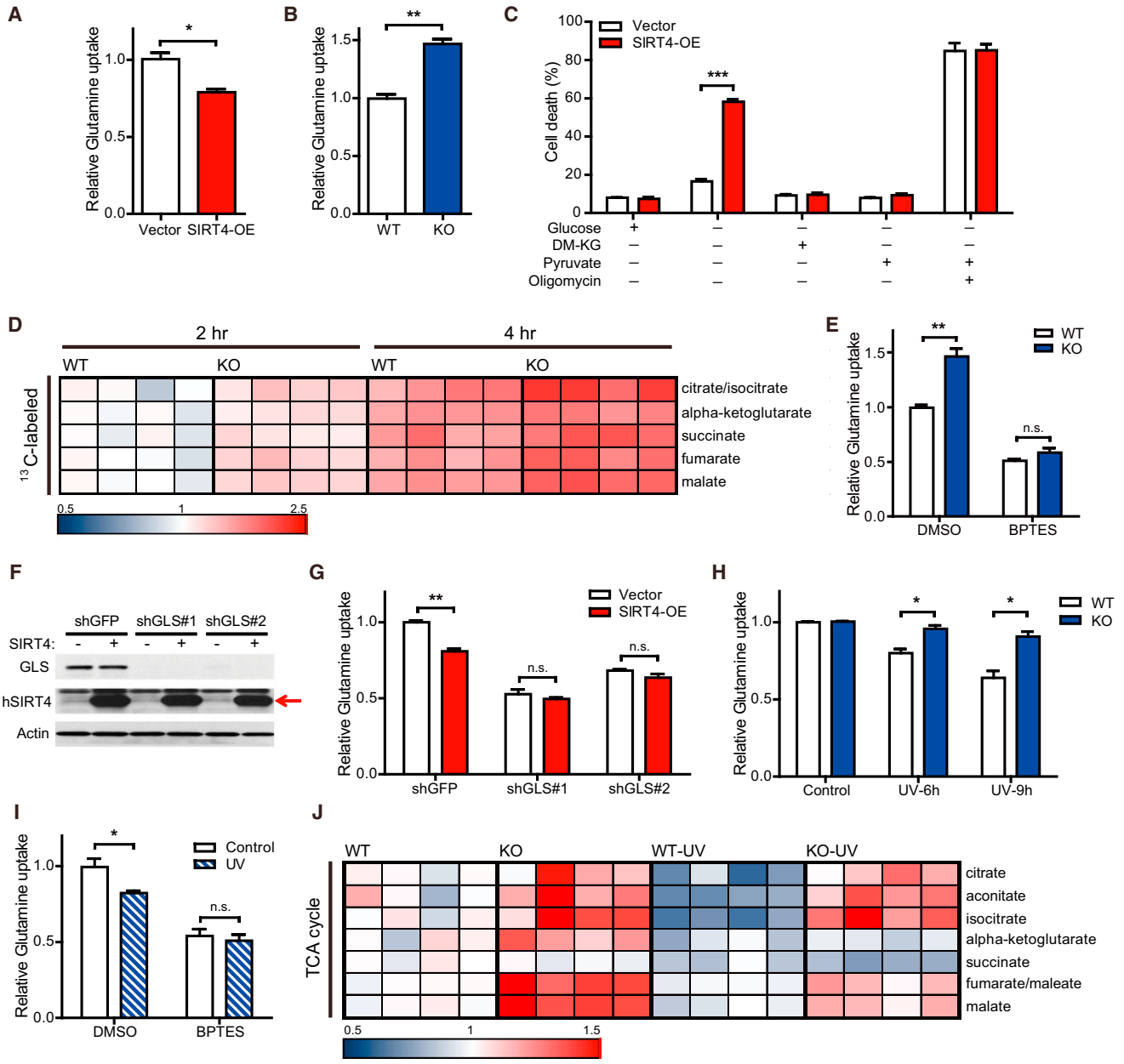

Figure 3. SIRT4 Represses Mitochondrial Glutamine Metabolism in Response to DNA Damage

(A and B) Glutamine uptake in HepG2 cells stably expressing empty vector (Vector) or SIRT4 (SIRT4-OE) (A) or in immortalized WT and SIRT4 KO MEFs (B) (n = 3).

(C) HEK293T Vector or SIRT4-OE cells deprived of glucose were given DM-KG (7 mM), pyruvate (1 mM), and/or oligomycin (5 μg/ml). Cell viability was measured via PI exclusion assay (n = 3).

(D) Relative abundance of ^{13}C-labeled TCA cycle intermediates (M+5 for α-ketoglutarate or M+4 for others) to the unlabeled from transformed WT and SIRT4 KO MEFs at the indicated times after pulse of ^{13}C-glutamine (n = 4 samples of each condition).

(E) Glutamine uptake in immortalized WT and SIRT4 KO MEFs treated with DMSO or BPTES (10 μM) (n = 3–4).

(F) GLS1 protein levels in HEK293T cells expressing GLS1-specific (shGLS#1 and shGLS#2) or control (shGFP) shRNAs. β-actin serves as a loading control.

(G) Glutamine uptake in control (shGFP) or GLS-knockdown (shGLS#1 and shGLS#2) cells after transfection with empty vector (Vector) and SIRT4 (SIRT4-OE) (n = 3).

(H) Relative glutamine uptake to each control in transformed WT and SIRT4 KO MEFs measured at the indicated times after 20 J/m^2 UV exposure (n = 3).

(I) Glutamine uptake in DMSO or BPTES (10 μM)-treated, immortalized MEFs after 20 J/m^2 UV exposure (n = 3).

(J) Heat map comparing relative levels of TCA cycle intermediates in transformed WT and SIRT4 KO MEFs at 4 hr after 20 J/m^2 UV exposure (n = 4).

Data are means ± SEM. n.s., not significant. *p < 0.05, **p < 0.005, and ***p < 0.0001.

See also Figure S3.

demonstrated elevated levels of TCA cycle intermediates (Figure 3J, WT versus KO), whereas intermediates of glycolysis were comparable with WT cells (data not shown). Nucleotides and other metabolites downstream of glutamine metabolism were not coordinately regulated by SIRT4 loss (Figure S3E; data not shown). Next, we analyzed glutamine flux in WT and SIRT4 KO MEFs in medium containing [U-$^{13}C_5$]glutamine for 2 or 4 hr and measured isotopic enrichment of TCA cycle intermediates. Loss of SIRT4 promoted a higher rate of incorporation of ^{13}C-labeled metabolites derived from [U-$^{13}C_5$]glutamine in all TCA cycle intermediates measured (Figure 3D). These data provide direct evidence that SIRT4 loss drives increased entry of glutamine-derived carbon into the TCA cycle.

Next, we examined the mechanisms involved in this repression of glutamine anaplerosis. GLS is the first required enzyme for mitochondrial glutamine metabolism (Curthoys and Watford, 1995), and its inhibition limits glutamine flux into the TCA cycle (Wang et al., 2010; Le et al., 2012; Yuneva et al., 2012). Treatment with bis-2-(5-phenylacetoamido-1,2,4-thiadiazol-2-yl)ethyl sulfide (BPTES) (Robinson et al., 2007), an inhibitor of GLS1, repressed glutamine uptake and completely rescued the increased glutamine consumption of SIRT4 KO cells (Figure 3E). Moreover, SIRT4 overexpression no longer inhibited glutamine uptake when GLS1 was reduced by using short hairpin RNAs (shRNAs) (Figures 3F and 3G), demonstrating that SIRT4 regulates mitochondrial glutamine metabolism. SIRT4 is a negative regulator of GDH activity (Haigis et al., 2006), and SIRT4 KO MEFs exhibited increased GDH activity in comparison with WT MEFs (Figure S3F). To test whether SIRT4 regulates mitochondrial glutamine metabolism via inhibiting GDH activity, we measured glutamine uptake in WT and SIRT4 KO cells in the presence of epigallocatechin gallate (EGCG), a GDH inhibitor (Choo et al., 2010; Li et al., 2006). The treatment of EGCG partially rescued the increased glutamine uptake of KO cells (Figure S3G), suggesting that GDH contributes to the role of SIRT4 in glutamine metabolism.

SIRT4 Represses Mitochondrial Glutamine Metabolism after DNA Damage

The induction of SIRT4 after DNA damage and regulation of glutamine metabolism by SIRT4 led us to speculate that SIRT4 may repress glutamine anaplerosis in response to DNA damage. Thus, we measured cellular glutamine consumption after UV exposure with transformed and nontransformed WT and SIRT4 KO MEFs. As expected, UV treatment suppressed glutamine uptake in WT cells (Figures 3H and S3H). Strikingly, we found that KO cells were unable to repress glutamine uptake in response to DNA damage (Figures 3H and S3H). We tested the involvement of glutamine anaplerosis by treating cells with chemical inhibitors of GLS1. Intriguingly, UV treatment could not further repress glutamine uptake in the presence of BPTES (Figure 3I), indicating that DNA damage inhibits mitochondrial glutamine metabolism. In addition, we observed similar results with the compound 968, a small molecule inhibitor of GLS1 (Figure S3I; Wang et al., 2010).

To probe further whether SIRT4 limits glutamine utilization to repress the TCA cycle after DNA damage, we performed metabolomic analysis with WT and SIRT4 KO MEFs with or without UV exposure. The levels of several TCA cycle intermediates remained elevated in KO cells compared to WT cells after UV exposure (Figure 3J), corroborating the idea that SIRT4 is required for the proper repression of mitochondrial glutamine metabolism in response to DNA damage.

SIRT4 Regulates Cell Cycle Progression and Genomic Fidelity in Response to DNA Damage

DNA damage initiates cell cycle arrest, which is crucial for maintenance of genomic integrity and ultimately for the prevention of cancer (Ciccia and Elledge, 2010). Glutamine is an essential metabolite for proliferation (Gaglio et al., 2009; Jones and Thompson, 2009; Wise and Thompson, 2010) and required for transition from G_1 to S phase (Colombo et al., 2011). Because our studies demonstrate that SIRT4 is induced by DNA damage to repress the utilization of glutamine, we interrogated the role of SIRT4 in cell cycle progression after DNA damage. To induce DNA damage independently of the rate of proliferation, we treated WT and SIRT4 KO MEFs with UV radiation and then pulsed with bromodeoxyuridine (BrdU) for 30 min, followed by staining with anti-BrdU fluorescein isothiocyanate (FITC) and 7-aminoactinomycin D. As expected, the population of the BrdU-labeled [BrdU$^+$ (S phase), (a) + (b)] cells was decreased in WT cells in a time-dependent manner (Figures 4A and S4A). However, this inhibition of BrdU incorporation was significantly delayed in KO MEFs, and this difference was most noticeable in cells in early S phase (Figure 4A, (a)). These cells were in G1 phase at the time of UV treatment and entered S phase during pulsing with BrdU. We observed similar results with IR treatment (Figure S4B). At 6 hr after IR treatment, G1 phase cells were nearly absent in KO cells but still present in WT cells (Figure S4B, red circle).

To probe the connection between glutamine metabolism and cell cycle arrest after DNA damage, we tested whether the inhibition of DNA synthesis upon DNA damage would be affected by the addition of a downstream metabolite of glutamine. We treated cells with dimethyl-glutamate (DMG), a cell-permeable glutamate donor (Maechler and Wollheim, 1999), and measured the level of BrdU$^+$ cells after UV treatment. To our surprise, DMG treatment promoted BrdU incorporation in response to DNA damage, as more cells entered early S phase by the addition of DMG (Figures 4B and S4C, PBS versus DMG). DMG treatment did not augment normal cell cycle proliferation (Figure S4D). Although the treatment of DMG caused a mild increase in the proportion of BrdU$^+$ cells in the KO cells, the fraction of BrdU$^+$ cells in WT cells increased robustly upon DMG treatment compared to PBS treatment (Figure S4E). These data suggest that reduced glutamine metabolism may limit proliferation, contributing to a metabolic checkpoint in response to genotoxic stress. Bypassing this checkpoint by adding soluble metabolites downstream of glutamine can partially promote cell cycle progression, even in the presence of DNA-damaging conditions.

Defects in the DDR may lead to accumulation of DNA damage and also may promote cell death. To assess whether SIRT4 affects genomic integrity in response to genotoxic stress, WT and SIRT4 KO cells were irradiated and then the number of γH2AX foci, known to localize at DSBs (Rogakou et al., 1998), was counted. The clearance of γH2AX foci was significantly impaired in KO cells (Figure 4C), while SIRT4 overexpression accelerated the clearance of foci (Figure 4D). Moreover, SIRT4

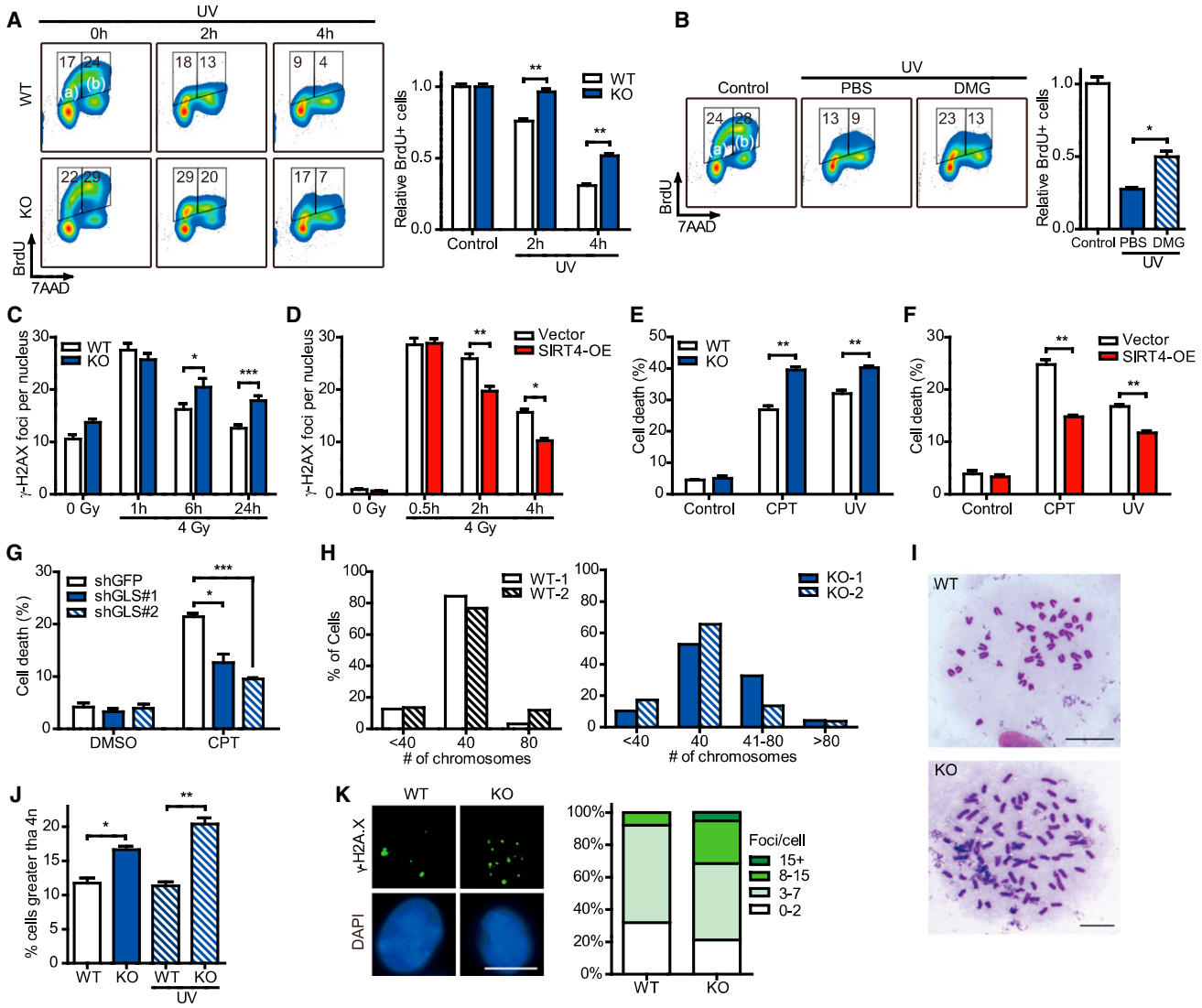

Figure 4. SIRT4 Is Involved in Cellular DNA Damage Responses

(A) The measurement of BrdU$^+$ cells and total DNA content in transformed WT and SIRT4 KO MEFs at the indicated times after 20 J/m^2 UV exposure (n = 3).

(B) The BrdU$^+$ cell and total DNA content in transformed WT MEFs incubated with PBS or DMG (10 mM) after UV exposure (n = 3).

(C and D) The number of γ-H2AX foci in immortalized WT and SIRT4 KO MEFs (C) or Vector and SIRT4-OE HeLa cells (D) was counted at the indicated times after IR treatment.

(E and F) Survival of immortalized WT and SIRT4 KO MEFs (E) or Vector and SIRT4-OE HepG2 cells (F) treated with or without CPT (14 μM) or UV (30 J/m^2) (n = 3–4). Cell viability was measured via PI exclusion assay.

(G) Survival of HepG2 cells expressing control (shGFP) or GLS1-specific (shGLS#1 and shGLS#2) shRNAs were treated with DMSO or CPT (14 μM) for 24 hr (n = 3). Cell viability was measured via PI exclusion assay.

(H and I) The percentage of chromosome number (H) and representative images of chromosome spread (I) of WT and SIRT4 KO MEFs at passage 2. Numbers of spreads counted were 64, 61, 142, and 104 for WT-1, WT-2, KO-1, and KO-2, respectively. Scale bar, 10 μm.

(J) Transformed WT and SIRT4 KO MEFs were treated with or without 20 J/m^2 UV, and the percentage of cells containing greater than 4n is analyzed by flow cytometry (n = 3).

(K) Immunofluorescent staining of transformed WT and SIRT4 KO MEFs using nuclear (DAPI) and DSBs (γ-H2AX) markers (left). Scale bar, 10 μm. The percentage of nuclei with the indicated number of γH2AX foci (right). WT MEFs (n = 119); KO MEFs (n = 71).

Data are means ± SEM. *p < 0.05, **p < 0.005, and ***p < 0.0001.

See also Figure S4.

KO cells showed significantly elevated levels of cell death compared to WT cells (Figure 4E), while SIRT4 overexpression was protective (Figure 4F). We next examined survival of control and GLS1 knockdown cells against DNA damage and discovered that inhibition of mitochondrial glutamine metabolism can mirror the protective role of SIRT4 overexpression (Figure 4G), demonstrating a link between mitochondrial glutamine metabolism and the DDR.

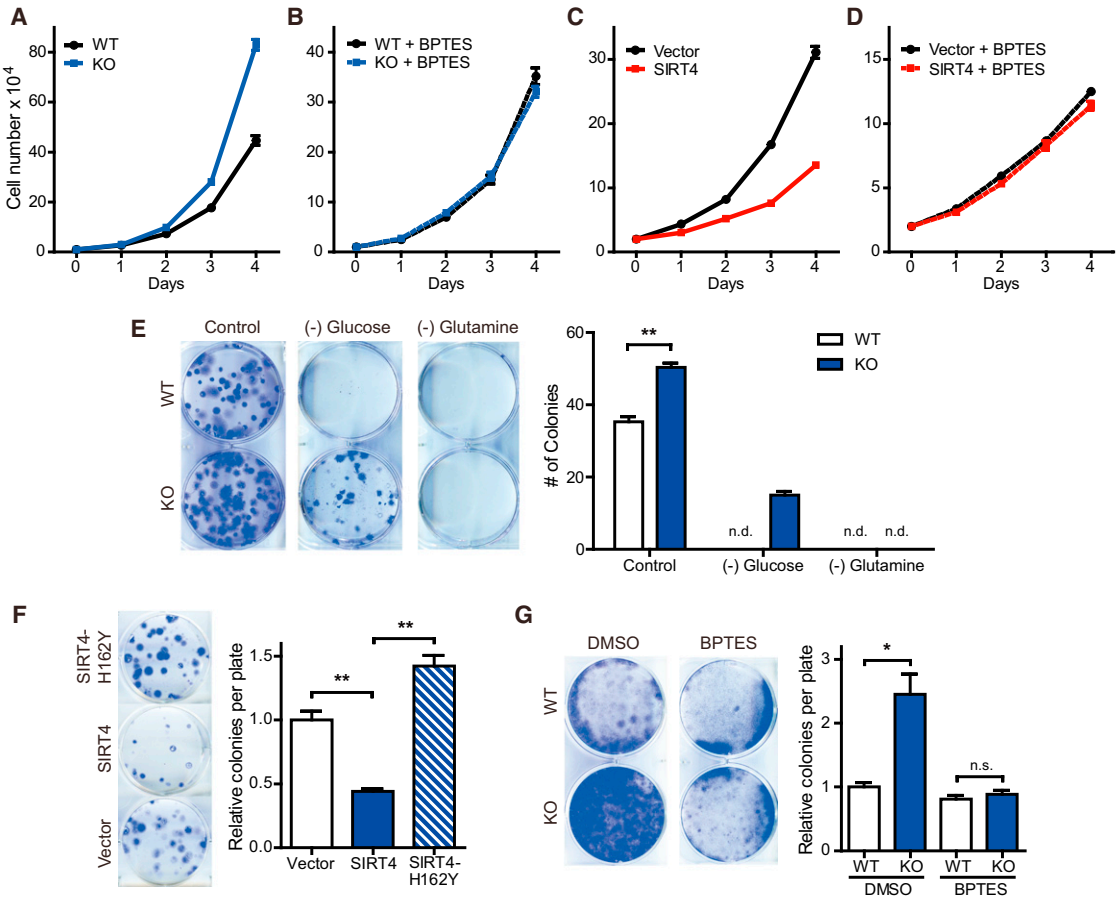

Figure 5. SIRT4 Has Tumor-Suppressive Function

(A and B) Growth curves of WT and SIRT4 KO MEFs (n = 3) cultured in standard media (A) or media supplemented with BPTES (10 μM) (B). Data are means ± SD.

(C and D) Growth curves of Vector and SIRT4-OE HeLa cells (n = 3) cultured in standard media (C) or media supplemented with BPTES (10 μM) (D). Data are means ± SD.

(E) Focus formation assays with transformed WT and SIRT4 KO MEFs (left). Cells were cultured with normal medium or medium without glucose or glutamine for 10 days and stained with crystal violet. The number of colonies was counted (right) (n = 3 samples of each condition). n.d., not determined.

(F) Focus formation assays with transformed KO MEFs reconstituted with SIRT4 or a catalytic mutant of SIRT4 (n = 3). Cells were cultured for 8 days and stained with crystal violet.

(G) Contact inhibited cell growth of transformed WT and SIRT4 KO MEFs cultured in the presence of DMSO or BPTES (10 μM) for 14 days (left). The number of colonies was counted (right). Data are means ± SEM. n.s., not significant. *$p < 0.05$ and **$p < 0.005$.

See also Figure S5.

Given the role for SIRT4 in regulating the metabolic checkpoint in response to DNA damage, we analyzed whether SIRT4 loss influenced chromosome stability. Chromosome spreads from two pairs of WT and SIRT4 KO primary MEFs revealed that KO cells possessed more aneuploidy (Figures 4H and 4I). Furthermore, more polyploidy cells were found in transformed KO cells compared to WT cells, and this phenotype became more severe after UV treatment (Figure 4J). Aberrant activation of the retinoblastoma (Rb)-E2F pathway by oncogenes leads to the replication-induced DSBs and formation of γH2AX foci (Bester et al., 2011). Hence, we analyzed the formation of γH2AX foci of WT and SIRT4 KO MEFs transformed with Ras and E1A, known to inactivate Rb (Harbour and Dean, 2000) and observed elevated γH2AX foci in KO cells (Figure 4K). Taken together, findings from multiple approaches demonstrate that SIRT4 is a critical regulator of genome fidelity.

SIRT4 Represses Tumor Proliferation

Genomic instability is one hallmark of tumorigenicity. Another feature of tumor cells is rapid cell proliferation, fueled in some cases by elevated glutamine utilization (Jones and Thompson, 2009; Wise and Thompson, 2010). Thus, we tested the idea that increased glutamine metabolism in SIRT4 KO MEFs may support proliferation. Indeed, KO cells significantly grew faster than did WT cells (Figure 5A). To test whether enhanced glutamine metabolism contributed to the proliferative phenotype of KO cells, we cultured cells with GLS1 inhibitors and measured proliferation. Remarkably, BPTES and 968 completely abrogated the increased proliferation of KO cells (Figures 5B and S5A). To probe the contribution of GDH, we measured proliferation in presence of EGCG and found it likewise abrogated the proliferative phenotype of KO cells (Figure S5B). In contrast, overexpression of SIRT4 in HeLa cells, which use glutamine as

a major energy source, significantly inhibited their growth (Figure 5C). Importantly, control and SIRT4-overexpressing cells proliferated at similar rates when cultured in media containing BPTES or 968 (Figures 5D and S5C), highlighting the role of SIRT4 in this pathway.

Defects in the proper regulation of DNA damage responses can result in the accumulation of DNA lesions, leading to cancer development (Lapenna and Giordano, 2009). Moreover, glutamine metabolism is critical for oncogenic transformation and cancer cell proliferation (DeBerardinis et al., 2007; Wang et al., 2010; Weinberg et al., 2010). Thus, we reasoned that SIRT4 would have the potential to suppress tumorigenesis by repressing glutamine metabolism and/or genomic instability. Thus, we assessed tumorigenic properties of transformed SIRT4 KO MEFs. KO MEFs formed more colonies than WT MEFs in colony formation assays (Figure 5E). Neither KO cells nor WT cells were able to form colonies on glutamine-deficient media. In contrast, SIRT4 KO MEFs were able to form a few colonies under glucose-deprived conditions, while WT cells were not, demonstrating that SIRT4 loss facilitates glutamine utilization to support colony formation. We found that reconstitution of KO cells with SIRT4 can reverse the phenotype, whereas reconstitution with a catalytic mutant of SIRT4 cannot (Figures 5F and S5D).

We next probed the contribution of glutamine anaplerosis in the transformative properties of SIRT4 KO cells. Cancer cells exhibit loss of contact inhibition of proliferation, resulting in uncontrolled cell proliferation. WT and SIRT4 KO MEFs were transformed in media supplemented with DMSO or BPTES, and colony-forming activities were determined. KO cells possessed increased colony-forming activity compared to WT cells (Figure 5G). This difference was inhibited by GLS or GDH inhibitors (Figures 5G and S5E), indicating that glutamine anaplerosis contributes to the tumorigenic phenotype of *SIRT4* null cells.

SIRT4 Represses Tumor Formation In Vivo

To investigate SIRT4 function in human cancers, we examined changes in *SIRT4* expression. *SIRT4* mRNA level was reduced in several human cancers, such as small-cell lung carcinoma (Garber et al., 2001), gastric cancer (Wang et al., 2012), bladder carcinoma (Blaveri et al., 2005), breast cancer (The Cancer Genome Atlas; http://tcga-data.nci.nih.gov/tcga/), and leukemia (Choi et al., 2007; Figure 6A). Of note, lower *SIRT4* expression was associated with shorter time to death in lung tumor patients (Shedden et al., 2008; Figure 6B). Overall, the expression data is consistent with the model that SIRT4 may play a tumor-suppressive role in human cancers.

To extend the cellular findings to in vivo models, we used multiple approaches. First, we performed allograft tumor formation assays in nude mice using transformed MEFs. Accordant with cellular models, loss of SIRT4 promoted larger tumor volume and weight compared to WT tumors in the recipient mice (Figure 6C). We next examined spontaneous tumor formation in two independent SIRT4 KO mouse strains, including in another strain of whole-body SIRT4 KO mice, generated by deleting exons 3 and 4 (Figure S6A). Like the previously reported SIRT4 KO model (Haigis et al., 2006), these SIRT4 KO mice demonstrated normal development and size. Strikingly, SIRT4 loss increased spontaneous tumor incidence throughout life (Figure 6D). Approximately 63% (22/35) of the *Sirt4* null animals developed several types of tumors, most frequently lung tumors at 18–26 months of age, while 20% (5/25) of aged WT littermates developed lung tumors (Figures 6E and S6B). Lung tumors from SIRT4 KO mice were categorized according to tumor types, revealing 41% (7/17) adenomas, and 59% (10/17) carcinomas, including bronchioloalveolar carcinoma and adenocarcinomas (Figure 6F). To further characterize these tumors, we performed immunohistochemistry to detect thyroid transcription factor-1 (TTF1), a transcription factor expressed specifically in epithelial cells of the thyroid and lung, providing a clinical marker in the diagnosis of tumors of lung origin (Kendall et al., 2007; Weir et al., 2007). Lung tumors from SIRT4 KO mice were positive for TTF1 (Figure 6G). Moreover, we found that 60% (9/15) of female *Sirt4* null animals also developed cystic endometrial hyperplasia, while only 15% (2/13) WT mice exhibited mild endometrial hyperplasia (Figure 6E).

The previously reported strain of SIRT4 KO mice (Haigis et al., 2006) demonstrated the same phenotype; these SIRT4 KO animals developed lung tumors (45.5%) more frequently than WT mice (8.3%) between 18 and 22 months of age (Figure S6C). Thus, two independently derived strains of SIRT4 KO mice possessed increased spontaneous lung tumor incidence.

SIRT4 Regulates Glutamine Metabolism in Lung Tissue

To test further the biological relevance of this pathway in lung, we examined whether SIRT4 is induced in vivo after exposure to DNA-damaging IR treatment. Remarkably, *Sirt4* was significantly induced in lung tissue after IR exposure (Figure 7A). We next examined whether IR repressed glutamine metabolism in vivo, as observed in cell culture by examining GDH activity in lung tissue from WT and SIRT4 KO mice with or without IR exposure. GDH activity was elevated in lung tissue extracts from SIRT4 KO mice compared with WT lung tissue (Figure 7B). Importantly, GDH activity was significantly decreased in lung tissue from WT mice after IR exposure, whereas not in lung tissue from KO mice (Figure 7C). Thus, these findings recapitulate our cellular studies and are in line with the model that SIRT4 induction with DNA damage limits mitochondrial glutamine metabolism and utilization.

To assess whether the functions of SIRT4 can be reproduced in these lung tumors, cells derived from SIRT4 KO lung tumors were reconstituted with wild-type SIRT4 (Figure S7A). As expected, SIRT4 reconstitution reduced glutamine uptake but not glucose uptake (Figures 7D and 7E) and repressed proliferation (Figure S7B) of lung tumor cells. Finally, we tested whether SIRT4 repressed genomic instability in these tumor cells after DNA damage. When we examined the chromosome abnormalities after irradiation, the reconstituted tumor cells with SIRT4 exhibit decreased genomic instability (Figure 7F). Taken together, these results provide critical evidence that SIRT4 regulates both glutamine metabolism and genomic instability in tumor cells and that loss of this critical regulatory node contributes to cancer susceptibility.

DISCUSSION

Here, we report that SIRT4 has an important role in cellular metabolic response to DNA damage by regulating mitochondrial

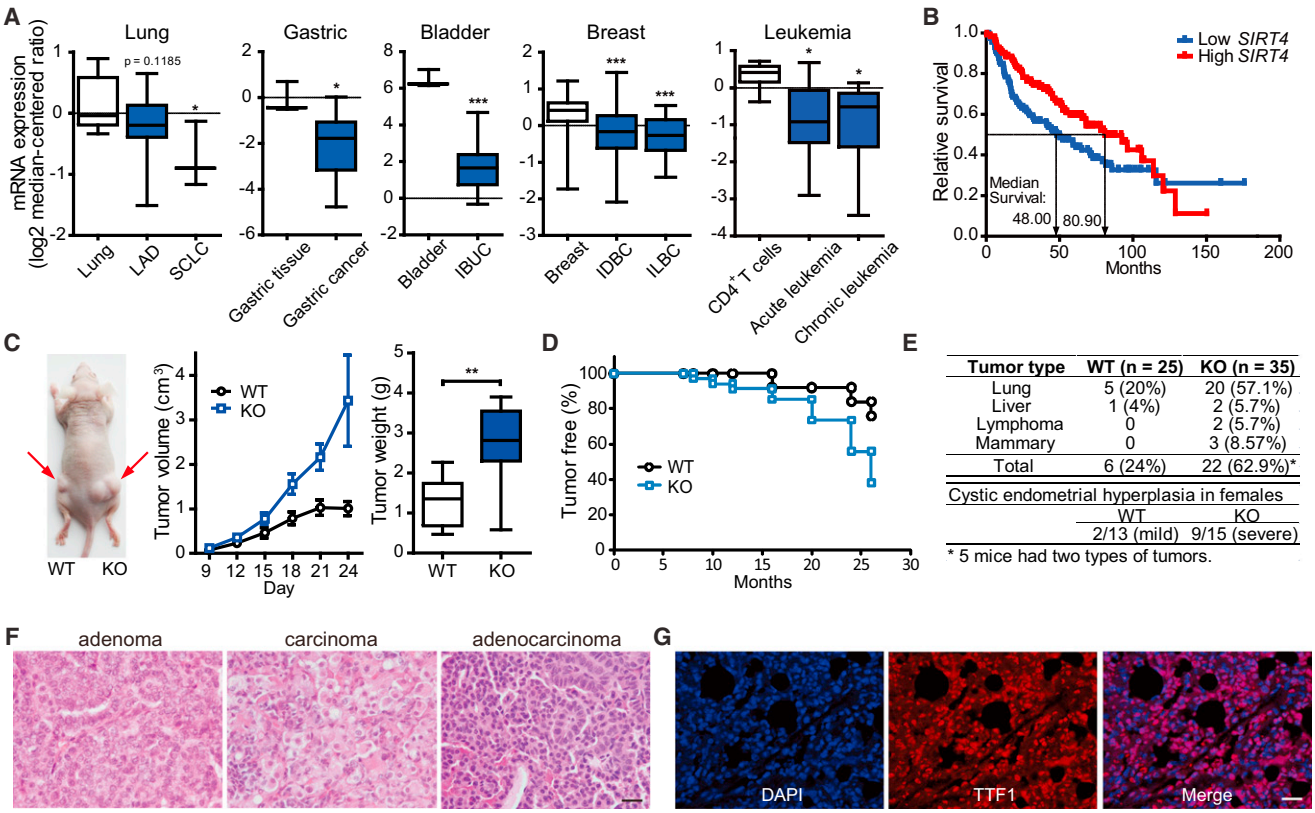

Tumor type	WT (n = 25)	KO (n = 35)
Lung	5 (20%)	20 (57.1%)
Liver	1 (4%)	2 (5.7%)
Lymphoma	0	2 (5.7%)
Mammary	0	3 (8.57%)
Total	6 (24%)	22 (62.9%)*
Cystic endometrial hyperplasia in females		
	WT	KO
	2/13 (mild)	9/15 (severe)

* 5 mice had two types of tumors.

Figure 6. SIRT4 Is a Mitochondrial Tumor Suppressor

(A) *SIRT4* mRNA levels were determined using the Oncomine microarray database (http://www.oncomine.org) in normal versus lung, gastric, bladder, breast cancer, and leukemia. The boxes represent the interquartile range; whiskers represent the 10th–90th percentile range; bars represent the median. LAD, lung adenocarcinoma; SCLC, small-cell lung carcinoma; IBUC, infiltrating bladder urothelial carcinoma; IDBC, invasive ductal breast carcinoma; ILBC, invasive lobular breast carcinoma.

(B) Kaplan-Meier curve comparing time to survival between lung adenocarcinomas with the lowest (<25th percentile) versus highest (>25th percentile) *SIRT4* expression was determined using the Oncomine database. p = 0.0354, log rank test.

(C) Representative image of tumors resulting from allograft with transformed WT and SIRT4 KO MEFs. Tumor volume and weight were measured (n = 8 tumors/genotypes). The boxes represent the interquartile range; whiskers represent the 10th–90th percentile range; bars represent the median.

(D and E) Tumor-free curve (D) and analysis of tumor types (E) in WT and SIRT4 KO mice. p = 0.0035, log rank test.

(F) Histological sections of representative lung tumors from SIRT4 KO mice with H&E staining. Scale bar, 20 μm.

(G) Immunofluorescent staining of a representative lung adenocarcinoma from SIRT4 KO mice using nuclear (DAPI) and lung (TTF1) markers. Scale bar, 20 μm.

Data are means ± SEM. *p < 0.05, **p < 0.005, and ***p < 0.0001.

See also Figure S6.

glutamine metabolism with important implication for the DDR and tumorigenesis. First, we discovered that DNA damage represses cellular glutamine metabolism (Figure 1). Second, we found that SIRT4 is induced by genotoxic stress (Figure 2) and is required for the repression of mitochondrial glutamine metabolism (Figure 3). This metabolic response contributes to the control of cell cycle progression and the maintenance of genomic integrity in response to DNA damage (Figure 4). Loss of SIRT4 increased glutamine-dependent tumor cell proliferation and tumorigenesis (Figure 5). In mice, SIRT4 loss resulted in spontaneous tumor development (Figure 6). We demonstrate that SIRT4 is induced in normal lung tissue in response to DNA damage, where it represses GDH activity. Finally, the glutamine metabolism-genomic fidelity axis is recapitulated in lung tumor cells derived from SIRT4 KO mice via SIRT4 reconstitution (Figure 7). Our studies therefore uncover SIRT4 as an important regulator of cellular metabolic response to DNA damage that coordinates repression of glutamine metabolism, genomic stability, and tumor suppression.

The DDR is a highly orchestrated and well-studied signaling response that detects and repairs DNA damage. Upon sensing DNA damage, the ATM/ATR protein kinases are activated to phosphorylate target proteins, leading to cell cycle arrest, DNA repair, transcriptional regulation, and initiation of apoptosis (Ciccia and Elledge, 2010; Su, 2006). Dysregulation of this pathway is frequently observed in many tumors. Emerging evidence has suggested that cell metabolism also plays key roles downstream of the DDR-induced pathways. For example, ATM has been reported to repress the rapamycin-sensitive mammalian target of rapamycin (mTORC1) pathway by activating the serine/threonine kinase LKB1/AMP-activated protein kinase (AMPK) metabolic pathway (Alexander et al., 2010). Several studies also

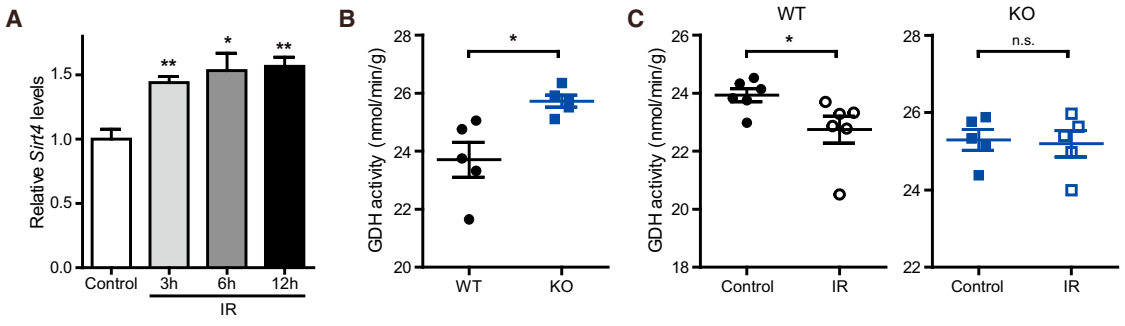

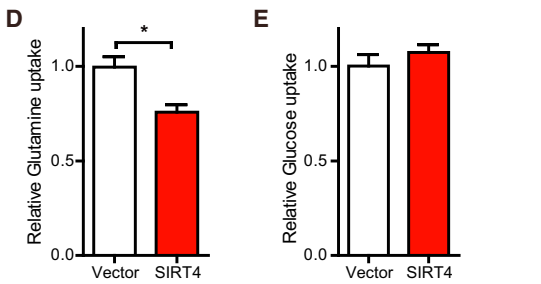

F

Abnormality	Vector (n = 36)	SIRT4 (n = 35)
gross abnormalities	25 (69.4%)	22 (62.9%)
premature segregation	5 (13.9%)	2 (5.7%)
multiple quadriradial chromosomes	4 (11.1%)	1 (2.9%)
1 quadriradial chromosomes	0 (0%)	1 (2.9%)

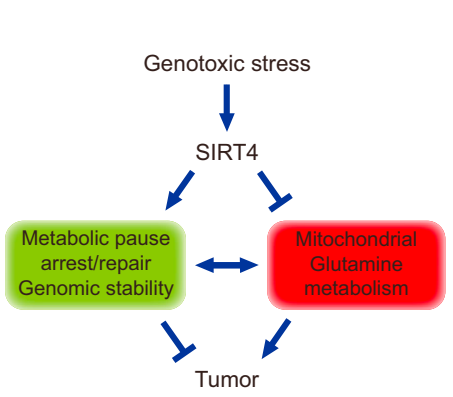

Figure 7. SIRT4 Inhibits Mitochondrial Glutamine Metabolism In Vivo

(A) Relative *Sirt4* mRNA levels in lung tissues for the indicated times after whole-body IR (10 Gy) were determined by qRT-PCR (n = 3). β-actin was used as an endogenous control for qRT-PCR.

(B) GDH activity in lung tissue extracts from WT and SIRT4 KO mice (n = 5 animals/genotype).

(C) GDH activity in lung tissue extracts from WT (left) and SIRT4 KO (right) mice at 12 hr after whole body IR (10 Gy) (n = 5–6 mice of each condition).

(D and E) Glutamine (D) and glucose (E) uptake in SIRT4 KO lung tumor cells reconstituted with SIRT4 (n = 3).

(F) Chromosomal abnormalities were examined in SIRT4 KO lung tumor cells reconstituted with SIRT4 after IR (5 Gy) treatment.

(G) A proposed model illustrating the regulation of metabolic response to DNA damage by SIRT4.

Data are means ± SEM. n.s., not significant. *$p < 0.05$ and **$p < 0.005$.

See also Figure S7.

indicate that AMPK is activated downstream of p53 via p53 target genes, sestrin 1 and sestrin 2 (Shackelford and Shaw, 2009). Moreover, damaged cells upregulate the PPP to facilitate DNA repair by generating precursors for nucleotide biosynthesis (Cosentino et al., 2011). The role of SIRT4 in the metabolic response to genotoxic stress synergizes with changes in cellular signaling pathways. SIRT4 contributes to this stress response by repressing glutamine entry into TCA cycle.

How does diminished glutamine metabolism regulate cellular responses to genotoxic stress? Proliferating cells use precursors derived from TCA cycle intermediates to synthesize NAD phosphate (NADPH), lipids, proteins, and nucleic acids (DeBerardinis et al., 2007; Wise and Thompson, 2010). For example, mitochondrial citrate is exported to the cytosol and is used for lipid synthesis and protein acetylation. However, continuous export of TCA cycle intermediates would result in the loss of mitochondrial integrity by stalling the TCA cycle, limiting anabolic pathways, and decreasing substrates for cellular respiration. Thus, refilling the mitochondrial carbon pool by glutamine is essential for the maintenance of mitochondrial integrity and its biosynthetic roles, as has been previously demonstrated (DeBerardinis et al., 2007). We find that this pathway is repressed in response to cellular stress and additionally demonstrate that SIRT4 regulates glutamine anaplerosis.

Although our current work highlights the regulation of glutamine anaplerosis by SIRT4, other glutamine metabolism pathways may also be important for the DDR and tumorigenesis. For example, glutamine contributes to de novo synthesis of glutathione (GSH), an intracellular antioxidant that plays a critical role in cellular defense against oxidative stress (Lu, 2009). Our studies did not find a significant difference in the levels of GSH and GSH dimers and no measurable flux of glutamine into GSH under these conditions and at short time points after damage (data not shown). Glutamine metabolism also contributes to lipid synthesis, nucleotide synthesis, and NADPH levels. Sirtuins have several targets and synergically regulate the same pathway. For example, SIRT3 has been shown to bind and regulate multiple enzymes in mitochondrial fatty-acid oxidation (Hallows et al., 2011; Hirschey et al., 2010). Thus, it will be interesting for future studies to examine systematically whether

SIRT4 regulates mitochondrial glutamine metabolism and other branches of glutamine metabolism via other targets.

This study identifies an important role for SIRT4 in suppressing tumor growth using a combination of human data and cellular and mouse experiments. In humans, *SIRT4* mutations have been identified in colon, lung, and uterine carcinomas (http://www.cbioportal.org). Moreover, *SIRT4* expression is decreased in human tumors and correlates with prognosis in lung cancer patients. Our cellular and animal studies also reveal that SIRT4 loss increases tumorigenesis, importantly in a glutamine-dependent manner. These findings also share parallels with the role of SIRT3, another mitochondrial sirtuin, in tumorigenesis. Like SIRT3, the tumors in SIRT4 KO mice arise in an age-dependent manner—after 1 year. Thus, as with SIRT3, SIRT4 loss on its own may not be the initiating event in tumorigenesis, but its loss appears to create a tumor-permissive environment to promote both increased genomic instability and anabolic growth, supporting tumor cell survival and proliferation.

Several other sirtuins have been shown to play critical roles in genome maintenance and tumorigenesis. For example, SIRT1- and SIRT6-deficient cells showed an impaired DSB repair and SIRT2, SIRT3, and SIRT6 KO mice exhibit spontaneous genomic instability (Kim et al., 2010; Mao et al., 2011; Mostoslavsky et al., 2006; Oberdoerffer et al., 2008; Wang and Tong, 2009). As sirtuins are important modulators of cell metabolism (Haigis and Guarente, 2006; Houtkooper et al., 2012), it will be interesting to examine whether these sirtuins coordinately regulate genomic fidelity and tumorigenesis, in part via modulating fuel switching.

In sum, our studies reveal an important role for the mitochondrial sirtuin, SIRT4, in cancer biology and connect two hallmarks of tumor cells: genomic instability and dysregulation of glutamine metabolism. Given the importance of metabolism in cellular proliferation and tumorigenesis, these findings hold profound implications for understanding the normal metabolic response to stress as well as for the development of cancer therapy.

EXPERIMENTAL PROCEDURES

Animal Studies

Animal studies were performed according to protocols approved by the Institutional Animal Care and Use Committee, the Standing Committee on Animals at Harvard. Age-matched SIRT4 WT and KO mice were sacrificed and subjected to pathological examination. For allograft studies, 10^6 transformed SIRT4 WT or KO MEFs in Matrigel (BD Bioscience) for a total volume of 100 μl were injected subcutaneously in right and left flanks of 8-week-old male nude mice (Charles River). Visible tumor volume was measured on the indicated days with calipers. At the termination of the experiment, tumors were excised and weighed. For generation of *SIRT4* mutant mice, chimeric mice were mated with NIH Black Swiss females (Taconic) to screen for germline transmission. Male mice bearing germline transmission were mated with female FVB EIIa-Cre mice to generate whole body exons 3 and 4 deletion of the *Sirt4* gene. All experiments were approved by the Animal Care and Use Committee of the National Institute of Diabetes, Digestive and Kidney Diseases.

Histological Analysis

Tumors were dissected from mice and fixed in 10% neutral-buffered formalin (Sigma) at room temperature overnight and placed in 70% ethanol for at least one day. Then, the tumor tissues were dehydrated through a graded alcohol series, xylene and paraffin, and then embedded in paraffin. Sections of 5 μm were cut and stained by hematoxylin and eosin (H&E).

Flow Cytometric Measurement of Cell Death and BrdU Incorporation

Cells at less than 80% confluency were treated with DNA damage agents. After treatments, cells were harvested by trypsinization, pelleted by centrifugation, and resuspended in PBS containing 3% fetal bovine serum. The measurement of cell death was performed by flow cytometry using propidium iodide (PI) staining, as previously described. The incorporation of BrdU into the genomic DNA was measured with BrdU Flow Kit (BD PharMingen) according to the manufacturer's instructions.

γH2AX Immunofluorescence

Cells grown on coverslips or eight-well microscopy slides were fixed for 20 min with 4% paraformaldehyde and permeabilized by 0.1% Triton X-100 for 3 min. Cells were then incubated overnight at 4° with mouse monoclonal antibodies against γH2AX (Ser139) (Millipore, 1:200 dilution) followed by goat anti-mouse immunoglobulin G-FITC (Santa Cruz, 1:300). Cell images were taken under a Zeiss microscope using a 63X objective and analyzed for foci/nucleus.

Glutamine and Glucose Measurements

Glutamine, ammonia, glucose, and lactate levels in culture media were measured using the BioProfile FLEX analyzer (Nova Biomedical), as previously described (Finley et al., 2011). Briefly, fresh media were added to a six-well plate of cells, and metabolite levels in the media were measured 6–9 hr later and normalized to the number of cells in each well.

Metabolites Profiling

Metabolites were extracted and analyzed as previously described (Finley et al., 2011). Briefly, SIRT4 WT and KO MEFs were plated, then metabolites were extracted at 4 hr after 20 J/m^2 UV exposure. Metabolite levels were normalized to the total of all metabolites detected.

Statistical Analysis

Unpaired two-tailed Student's t tests were performed unless otherwise noted. All experiments were performed at least two or three times. For the tumor incidence and survival study, the log rank (Mantel-Cox) test was performed.

SUPPLEMENTAL INFORMATION

Supplemental Information includes seven figures and Supplemental Experimental Procedures and can be found with this article online at http://dx.doi.org/10.1016/j.ccr.2013.02.024.

ACKNOWLEDGMENTS

We thank Roderick T. Bronson for analyzing tumors, Moon Hee Yang for help with allograft assays, Annie Lee for technical assistance, and the Nikon Imaging Center at Harvard Medical School. We thank Kevin Haigis for critical reading of the manuscript. S.M.J. was supported in part by a National Research Foundation of Korea grant funded by the Korean Government (NRF-2010-357-C00087). M.C.H. is supported in part by NIH grant AG032375, the Glenn Foundation for Medical Research, and the American Cancer Society New Scholar Award. A.K. is supported by the National Cancer Institute grant R01 CA157490, the Kimmel Scholar Award, and an AACR-PanCAN Career Development Award. This work was also supported in part by the Intramural Research Program of the National Institute of Diabetes, Digestive and Kidney Diseases, National Institutes of Health, USA.

Received: June 21, 2012
Revised: November 30, 2012
Accepted: February 21, 2013
Published: April 4, 2013

REFERENCES

Abbas, T., and Dutta, A. (2009). p21 in cancer: intricate networks and multiple activities. Nat. Rev. Cancer *9*, 400–414.

Abraham, R.T. (2001). Cell cycle checkpoint signaling through the ATM and ATR kinases. Genes Dev. *15*, 2177–2196.

Ahuja, N., Schwer, B., Carobbio, S., Waltregny, D., North, B.J., Castronovo, V., Maechler, P., and Verdin, E. (2007). Regulation of insulin secretion by SIRT4, a mitochondrial ADP-ribosyltransferase. J. Biol. Chem. *282*, 33583–33592.

Alexander, A., Cai, S.L., Kim, J., Nanez, A., Sahin, M., MacLean, K.H., Inoki, K., Guan, K.L., Shen, J., Person, M.D., et al. (2010). ATM signals to TSC2 in the cytoplasm to regulate mTORC1 in response to ROS. Proc. Natl. Acad. Sci. USA *107*, 4153–4158.

Bester, A.C., Roniger, M., Oren, Y.S., Im, M.M., Sarni, D., Chaoat, M., Bensimon, A., Zamir, G., Shewach, D.S., and Kerem, B. (2011). Nucleotide deficiency promotes genomic instability in early stages of cancer development. Cell *145*, 435–446.

Blaveri, E., Simko, J.P., Korkola, J.E., Brewer, J.L., Baehner, F., Mehta, K., Devries, S., Koppie, T., Pejavar, S., Carroll, P., and Waldman, F.M. (2005). Bladder cancer outcome and subtype classification by gene expression. Clin. Cancer Res. *11*, 4044–4055.

Choi, Y.L., Tsukasaki, K., O'Neill, M.C., Yamada, Y., Onimaru, Y., Matsumoto, K., Ohashi, J., Yamashita, Y., Tsutsumi, S., Kaneda, R., et al. (2007). A genomic analysis of adult T-cell leukemia. Oncogene *26*, 1245–1255.

Choo, A.Y., Kim, S.G., Vander Heiden, M.G., Mahoney, S.J., Vu, H., Yoon, S.O., Cantley, L.C., and Blenis, J. (2010). Glucose addiction of TSC null cells is caused by failed mTORC1-dependent balancing of metabolic demand with supply. Mol. Cell *38*, 487–499.

Ciccia, A., and Elledge, S.J. (2010). The DNA damage response: making it safe to play with knives. Mol. Cell *40*, 179–204.

Colombo, S.L., Palacios-Callender, M., Frakich, N., Carcamo, S., Kovacs, I., Tudzarova, S., and Moncada, S. (2011). Molecular basis for the differential use of glucose and glutamine in cell proliferation as revealed by synchronized HeLa cells. Proc. Natl. Acad. Sci. USA *108*, 21069–21074.

Cosentino, C., Grieco, D., and Costanzo, V. (2011). ATM activates the pentose phosphate pathway promoting anti-oxidant defence and DNA repair. EMBO J. *30*, 546–555.

Curthoys, N.P., and Watford, M. (1995). Regulation of glutaminase activity and glutamine metabolism. Annu. Rev. Nutr. *15*, 133–159.

Dang, C.V. (2010). Glutaminolysis: supplying carbon or nitrogen or both for cancer cells? Cell Cycle *9*, 3884–3886.

DeBerardinis, R.J., Mancuso, A., Daikhin, E., Nissim, I., Yudkoff, M., Wehrli, S., and Thompson, C.B. (2007). Beyond aerobic glycolysis: transformed cells can engage in glutamine metabolism that exceeds the requirement for protein and nucleotide synthesis. Proc. Natl. Acad. Sci. USA *104*, 19345–19350.

Deng, C.X. (2006). BRCA1: cell cycle checkpoint, genetic instability, DNA damage response and cancer evolution. Nucleic Acids Res. *34*, 1416–1426.

Finkel, T., Deng, C.X., and Mostoslavsky, R. (2009). Recent progress in the biology and physiology of sirtuins. Nature *460*, 587–591.

Finley, L.W., Carracedo, A., Lee, J., Souza, A., Egia, A., Zhang, J., Teruya-Feldstein, J., Moreira, P.I., Cardoso, S.M., Clish, C.B., et al. (2011). SIRT3 opposes reprogramming of cancer cell metabolism through HIF1α destabilization. Cancer Cell *19*, 416–428.

Gaglio, D., Soldati, C., Vanoni, M., Alberghina, L., and Chiaradonna, F. (2009). Glutamine deprivation induces abortive s-phase rescued by deoxyribonucleotides in k-ras transformed fibroblasts. PLoS ONE *4*, e4715.

Garber, M.E., Troyanskaya, O.G., Schluens, K., Petersen, S., Thaesler, Z., Pacyna-Gengelbach, M., van de Rijn, M., Rosen, G.D., Perou, C.M., Whyte, R.I., et al. (2001). Diversity of gene expression in adenocarcinoma of the lung. Proc. Natl. Acad. Sci. USA *98*, 13784–13789.

Haigis, M.C., and Guarente, L.P. (2006). Mammalian sirtuins—emerging roles in physiology, aging, and calorie restriction. Genes Dev. *20*, 2913–2921.

Haigis, M.C., Mostoslavsky, R., Haigis, K.M., Fahie, K., Christodoulou, D.C., Murphy, A.J., Valenzuela, D.M., Yancopoulos, G.D., Karow, M., Blander, G., et al. (2006). SIRT4 inhibits glutamate dehydrogenase and opposes the effects of calorie restriction in pancreatic beta cells. Cell *126*, 941–954.

Hallows, W.C., Yu, W., Smith, B.C., Devries, M.K., Ellinger, J.J., Someya, S., Shortreed, M.R., Prolla, T., Markley, J.L., Smith, L.M., et al. (2011). Sirt3 promotes the urea cycle and fatty acid oxidation during dietary restriction. Mol. Cell *41*, 139–149.

Harbour, J.W., and Dean, D.C. (2000). The Rb/E2F pathway: expanding roles and emerging paradigms. Genes Dev. *14*, 2393–2409.

Hirschey, M.D., Shimazu, T., Goetzman, E., Jing, E., Schwer, B., Lombard, D.B., Grueter, C.A., Harris, C., Biddinger, S., Ilkayeva, O.R., et al. (2010). SIRT3 regulates mitochondrial fatty-acid oxidation by reversible enzyme deacetylation. Nature *464*, 121–125.

Houtkooper, R.H., Pirinen, E., and Auwerx, J. (2012). Sirtuins as regulators of metabolism and healthspan. Nat. Rev. Mol. Cell Biol. *13*, 225–238.

Jones, R.G., and Thompson, C.B. (2009). Tumor suppressors and cell metabolism: a recipe for cancer growth. Genes Dev. *23*, 537–548.

Kendall, J., Liu, Q., Bakleh, A., Krasnitz, A., Nguyen, K.C., Lakshmi, B., Gerald, W.L., Powers, S., and Mu, D. (2007). Oncogenic cooperation and coamplification of developmental transcription factor genes in lung cancer. Proc. Natl. Acad. Sci. USA *104*, 16663–16668.

Kim, H.S., Patel, K., Muldoon-Jacobs, K., Bisht, K.S., Aykin-Burns, N., Pennington, J.D., van der Meer, R., Nguyen, P., Savage, J., Owens, K.M., et al. (2010). SIRT3 is a mitochondria-localized tumor suppressor required for maintenance of mitochondrial integrity and metabolism during stress. Cancer Cell *17*, 41–52.

Koppenol, W.H., Bounds, P.L., and Dang, C.V. (2011). Otto Warburg's contributions to current concepts of cancer metabolism. Nat. Rev. Cancer *11*, 325–337.

Lapenna, S., and Giordano, A. (2009). Cell cycle kinases as therapeutic targets for cancer. Nat. Rev. Drug Discov. *8*, 547–566.

Le, A., Lane, A.N., Hamaker, M., Bose, S., Gouw, A., Barbi, J., Tsukamoto, T., Rojas, C.J., Slusher, B.S., Zhang, H., et al. (2012). Glucose-independent glutamine metabolism via TCA cycling for proliferation and survival in B cells. Cell Metab. *15*, 110–121.

Li, C., Allen, A., Kwagh, J., Doliba, N.M., Qin, W., Najafi, H., Collins, H.W., Matschinsky, F.M., Stanley, C.A., and Smith, T.J. (2006). Green tea polyphenols modulate insulin secretion by inhibiting glutamate dehydrogenase. J. Biol. Chem. *281*, 10214–10221.

Lu, S.C. (2009). Regulation of glutathione synthesis. Mol. Aspects Med. *30*, 42–59.

Maechler, P., and Wollheim, C.B. (1999). Mitochondrial glutamate acts as a messenger in glucose-induced insulin exocytosis. Nature *402*, 685–689.

Mao, Z., Hine, C., Tian, X., Van Meter, M., Au, M., Vaidya, A., Seluanov, A., and Gorbunova, V. (2011). SIRT6 promotes DNA repair under stress by activating PARP1. Science *332*, 1443–1446.

Mostoslavsky, R., Chua, K.F., Lombard, D.B., Pang, W.W., Fischer, M.R., Gellon, L., Liu, P., Mostoslavsky, G., Franco, S., Murphy, M.M., et al. (2006). Genomic instability and aging-like phenotype in the absence of mammalian SIRT6. Cell *124*, 315–329.

Nakagawa, T., Lomb, D.J., Haigis, M.C., and Guarente, L. (2009). SIRT5 Deacetylates carbamoyl phosphate synthetase 1 and regulates the urea cycle. Cell *137*, 560–570.

Negrini, S., Gorgoulis, V.G., and Halazonetis, T.D. (2010). Genomic instability—an evolving hallmark of cancer. Nat. Rev. Mol. Cell Biol. *11*, 220–228.

Oberdoerffer, P., Michan, S., McVay, M., Mostoslavsky, R., Vann, J., Park, S.K., Hartlerode, A., Stegmuller, J., Hafner, A., Loerch, P., et al. (2008). SIRT1 redistribution on chromatin promotes genomic stability but alters gene expression during aging. Cell *135*, 907–918.

Robinson, M.M., McBryant, S.J., Tsukamoto, T., Rojas, C., Ferraris, D.V., Hamilton, S.K., Hansen, J.C., and Curthoys, N.P. (2007). Novel mechanism of inhibition of rat kidney-type glutaminase by bis-2-(5-phenylacetamido-1,2,4-thiadiazol-2-yl)ethyl sulfide (BPTES). Biochem. J. *406*, 407–414.

Rogakou, E.P., Pilch, D.R., Orr, A.H., Ivanova, V.S., and Bonner, W.M. (1998). DNA double-stranded breaks induce histone H2AX phosphorylation on serine 139. J. Biol. Chem. *273*, 5858–5868.

Schwer, B., and Verdin, E. (2008). Conserved metabolic regulatory functions of sirtuins. Cell Metab. *7*, 104–112.

Shackelford, D.B., and Shaw, R.J. (2009). The LKB1-AMPK pathway: metabolism and growth control in tumour suppression. Nat. Rev. Cancer *9*, 563–575.

Shedden, K., Taylor, J.M., Enkemann, S.A., Tsao, M.S., Yeatman, T.J., Gerald, W.L., Eschrich, S., Jurisica, I., Giordano, T.J., Misek, D.E., et al.; Director's Challenge Consortium for the Molecular Classification of Lung Adenocarcinoma. (2008). Gene expression-based survival prediction in lung adenocarcinoma: a multi-site, blinded validation study. Nat. Med. *14*, 822–827.

Su, T.T. (2006). Cellular responses to DNA damage: one signal, multiple choices. Annu. Rev. Genet. *40*, 187–208.

Sundaresan, N.R., Samant, S.A., Pillai, V.B., Rajamohan, S.B., and Gupta, M.P. (2008). SIRT3 is a stress-responsive deacetylase in cardiomyocytes that protects cells from stress-mediated cell death by deacetylation of Ku70. Mol. Cell. Biol. *28*, 6384–6401.

Vaziri, H., Dessain, S.K., Ng Eaton, E., Imai, S.I., Frye, R.A., Pandita, T.K., Guarente, L., and Weinberg, R.A. (2001). hSIR2(SIRT1) functions as an NAD-dependent p53 deacetylase. Cell *107*, 149–159.

Wang, F., and Tong, Q. (2009). SIRT2 suppresses adipocyte differentiation by deacetylating FOXO1 and enhancing FOXO1's repressive interaction with PPARgamma. Mol. Biol. Cell *20*, 801–808.

Wang, C., Chen, L., Hou, X., Li, Z., Kabra, N., Ma, Y., Nemoto, S., Finkel, T., Gu, W., Cress, W.D., and Chen, J. (2006). Interactions between E2F1 and SirT1 regulate apoptotic response to DNA damage. Nat. Cell Biol. *8*, 1025–1031.

Wang, J.B., Erickson, J.W., Fuji, R., Ramachandran, S., Gao, P., Dinavahi, R., Wilson, K.F., Ambrosio, A.L., Dias, S.M., Dang, C.V., and Cerione, R.A. (2010). Targeting mitochondrial glutaminase activity inhibits oncogenic transformation. Cancer Cell *18*, 207–219.

Wang, Q., Wen, Y.G., Li, D.P., Xia, J., Zhou, C.Z., Yan, D.W., Tang, H.M., and Peng, Z.H. (2012). Upregulated INHBA expression is associated with poor survival in gastric cancer. Med. Oncol. *29*, 77–83.

Weinberg, F., Hamanaka, R., Wheaton, W.W., Weinberg, S., Joseph, J., Lopez, M., Kalyanaraman, B., Mutlu, G.M., Budinger, G.R., and Chandel, N.S. (2010). Mitochondrial metabolism and ROS generation are essential for Kras-mediated tumorigenicity. Proc. Natl. Acad. Sci. USA *107*, 8788–8793.

Weir, B.A., Woo, M.S., Getz, G., Perner, S., Ding, L., Beroukhim, R., Lin, W.M., Province, M.A., Kraja, A., Johnson, L.A., et al. (2007). Characterizing the cancer genome in lung adenocarcinoma. Nature *450*, 893–898.

Wise, D.R., and Thompson, C.B. (2010). Glutamine addiction: a new therapeutic target in cancer. Trends Biochem. Sci. *35*, 427–433.

Yang, C., Sudderth, J., Dang, T., Bachoo, R.M., McDonald, J.G., and DeBerardinis, R.J. (2009). Glioblastoma cells require glutamate dehydrogenase to survive impairments of glucose metabolism or Akt signaling. Cancer Res. *69*, 7986–7993.

Yuneva, M.O., Fan, T.W., Allen, T.D., Higashi, R.M., Ferraris, D.V., Tsukamoto, T., Matés, J.M., Alonso, F.J., Wang, C., Seo, Y., et al. (2012). The metabolic profile of tumors depends on both the responsible genetic lesion and tissue type. Cell Metab. *15*, 157–170.

Cancer Cell
Article

1B50-1, a mAb Raised against Recurrent Tumor Cells, Targets Liver Tumor-Initiating Cells by Binding to the Calcium Channel α2δ1 Subunit

Wei Zhao,[1,7] Limin Wang,[1,7] Haibo Han,[1] Kemin Jin,[2] Na Lin,[3] Ting Guo,[1] Yangde Chen,[4] Heping Cheng,[3] Fengmin Lu,[5] Weigang Fang,[6] Yu Wang,[1] Baocai Xing,[2,*] and Zhiqian Zhang[1,*]
[1]Key Laboratory of Carcinogenesis and Translational Research (Ministry of Education), Department of Cell Biology
[2]Department of Hepatobiliary Surgery I
Peking University Cancer Hospital and Institute, Beijing 100142, People's Republic of China
[3]State Key Laboratory of Biomembrane and Membrane Biotechnology, Institute of Molecular Medicine, Peking-Tsinghua Center for Life Sciences, Peking University, Beijing 100871, People's Republic of China
[4]Biologics Discovery, Genzyme, a Sanofi Company, Framingham, MA 01701, USA
[5]Department of Microbiology
[6]Department of Pathology
Peking University Health Science Center, Beijing 100191, People's Republic of China
[7]These authors contributed equally to this work
*Correspondence: xingbaocai88@sina.com (B.X.), zlzqzhang@bjmu.edu.cn (Z.Z.)
http://dx.doi.org/10.1016/j.ccr.2013.02.025

SUMMARY

The identification and targeted therapy of cells involved in hepatocellular carcinoma (HCC) recurrence remain challenging. Here, we generated a monoclonal antibody against recurrent HCC, 1B50-1, that bound the isoform 5 of the α2δ1 subunit of voltage-gated calcium channels and identified a subset of tumor-initiating cells (TICs) with stem cell-like properties. A surgical margin with cells detected by 1B50-1 predicted rapid recurrence. Furthermore, 1B50-1 had a therapeutic effect on HCC engraftments by eliminating TICs. Finally, α2δ1 knockdown reduced self-renewal and tumor formation capacities and induced apoptosis of TICs, whereas its overexpression led to enhanced sphere formation, which is regulated by calcium influx. Thus, α2δ1 is a functional liver TIC marker, and its inhibitors may serve as potential anti-HCC drugs.

INTRODUCTION

Hepatocellular carcinoma (HCC) is one of the deadliest cancers, mainly due to its high rate of recurrence, which can be as high as 70% following conventional treatments such as surgical resection, arterial embolization, and radiofrequency ablation (Llovet and Bruix, 2008; Xu et al., 2010). The cellular origin of HCC recurrence remains poorly understood, and, as yet, no specific treatment strategy has been developed that focuses on HCC recurrence.

HCC, like other cancer types, is composed of phenotypically and functionally diverse cell types (Shackleton et al., 2009; Visvader, 2011). It is hypothesized that a rare subset of cancer cells, often operationally referred to as cancer stem cells or tumor-initiating cells (TICs), behave like stem cells in that they are capable of self-renewal and of giving rise to a hierarchical organization of heterogeneous cancer cells. These cells are resistant to conventional chemotherapy and radiotherapy and, hence, are responsible for sustaining tumor growth and recurrence. Therapies that can eradicate these cells may eventually lead to cancer cures (Alison et al., 2011; Clarke et al., 2006; Rosen and Jordan, 2009; Visvader and Lindeman, 2012; Zhang et al., 2010). $CD133^+$, $CD13^+$, $CD24^+$, and $EpCAM^+$ cells, as well as some side populations from HCC cell lines and/or biopsies, have been identified as TICs, but their roles in HCC recurrence and therapeutic strategies to target these cells have only recently

Significance

This study identified a population of cells with the TIC properties and expressing α2δ1 in primary HCC and some surgical margins using the monoclonal antibody, 1B50-1. These TICs have prognostic value. α2δ1 was found to play an essential role in modulating calcium oscillation amplitude, which may be important in maintaining the properties of TICs. The study also suggested that α2δ1 could serve as a therapeutic target in the treatment of HCC. Additionally, 1B50-1 bound α2δ1 on TICs and could potentially be developed into an anti-HCC drug. These findings contribute to the understanding of HCC recurrence at both the cellular and molecular levels and advance the development of prognostic and therapeutic strategies.

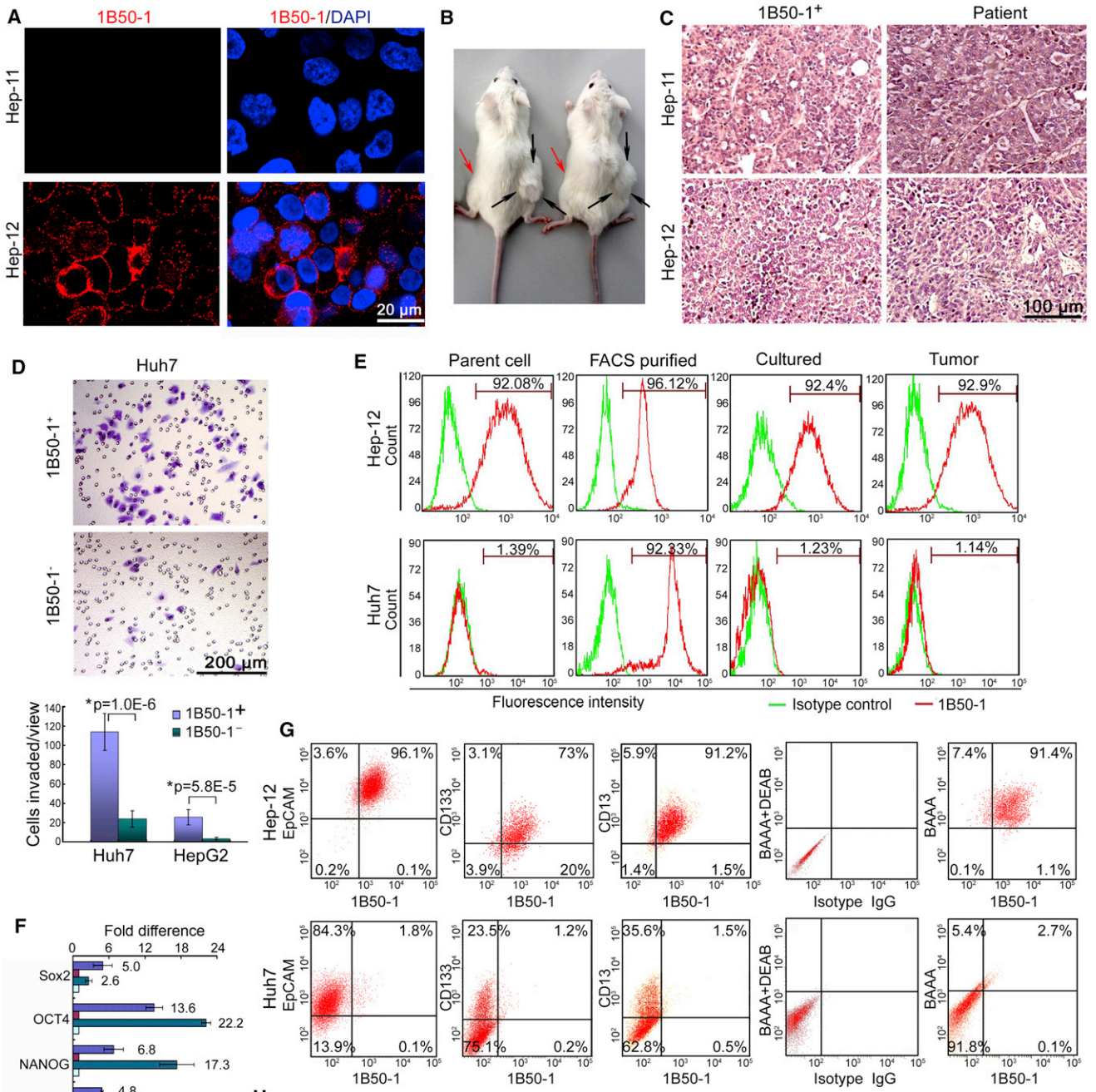

Markers	Tumor formation		Frequency of tumorigenic cells (95% CI)	p value
	10^3	10^2		
1B50-1$^+$CD133$^+$ (A)	5/5	5/5	1/1 (1/126-1/1)	4.67E-06 (A *vs* B)
1B50-1$^-$CD133$^+$ (B)	2/5	2/5	1/1061 (1/3129-1/360)	0.689 (B *vs* C)
1B50-1$^-$CD133$^-$ (C)	2/5	1/5	1/1445 (1/4728-1/442)	1.48E-06 (A *vs* C)
1B50-1$^+$CD13$^+$ (D)	5/5	4/5	1/62.6 (1/185-1/21.4)	2.28E-06 (D *vs* E)
1B50-1$^-$CD13$^+$ (E)	1/5	0/5	1/4983.8 (1/35192-1/706.2)	1.0 (E *vs* F)
1B50-1$^-$CD13$^-$ (F)	1/5	0/5	1/4983.8 (1/35192-1/706.2)	2.28E-06 (D *vs* F)
1B50-1$^+$EpCAM$^+$ (G)	5/5	5/5	1/1 (1/80.3-1/1)	8.5E-10 (G *vs* H)
1B50-1$^-$EpCAM$^+$ (H)	2/5	3/5	1/725 (1/1891.2-1/278)	0.11 (H *vs* I)
1B50-1$^-$EpCAM$^-$ (I)	1/5	1/5	1/2458 (1/10394.2-1/582)	8.9E-125 (G *vs* I)

Web 3C

(legend on next page)

begun to be investigated (Chiba et al., 2006; Haraguchi et al., 2010; Lee et al., 2011; Ma et al., 2010; Mishra et al., 2009; Yamashita et al., 2009).

Antibody-based targeted cancer therapy, either alone or in combination with standard chemotherapy regimens, has shown increasing clinical and commercial success (Deonarain et al., 2009). The current antibody-based anticancer therapies do not result in complete remission, but trials using antibodies targeting the surface molecules of TICs, such as DLL4, CD123, CD133, and interleukin-4 (IL-4), have shown promising therapeutic effects in a variety of cancers (Hoey et al., 2009; Jin et al., 2009; Rappa et al., 2008; Todaro et al., 2007). However, systematic identification of TIC biomarkers suitable for targeting antibody development is currently hindered by the sparseness of the TIC population in a given specimen.

We previously established a pair of HCC cell lines with the same clonal origin, Hep-11 and Hep-12, by primary culture from the same patient's primary and recurrent HCC tissues, respectively. Hep-12 cells are enriched for TICs, whereas Hep-11 cells do not form tumors in nonobese diabetic/severe combined immunodeficient (NOD/SCID) mice up to 6 months after injection of 5×10^6 cells (Xu et al., 2010). These two cell lines thus provide a unique cellular model system for characterizing the nature of the cells related to HCC recurrence and for identifying biomarkers for targeted therapy, specifically against recurrent HCC and perhaps for TICs in general. In this study, we used these two cell lines to generate monoclonal antibodies (mAbs) aiming to identify and target cells specifically related to HCC recurrence and to investigate the nature of these cells.

RESULTS

1B50-1 Identifies a Highly Tumorigenic and Invasive Subpopulation of HCC Cells

We used a whole-cell subtractive immunization approach (Brooks et al., 1993; Rasmussen and Ditzel, 2009) to generate mAbs that specifically reacted with Hep-12 cells. From three batches of cell fusions with the spleens of mice immunized with Hep-12 cells, a total of 37 hybridoma clones secreting mAbs that reacted strongly with Hep-12 cells, but weakly with Hep-11 cells, were obtained after screening with a cell-based ELISA method. One of these antibodies, named 1B50-1, recognized a subset of highly tumorigenic Hep-12 cells and appeared to be cytotoxic in vivo in our preliminary tumorigenicity assay. 1B50-1 bound to an antigen on the Hep-12 cell membrane, while it recognized few Hep-11 cells (Figure 1A). The percentage of cells bound by 1B50-1 (1B50-1$^+$) cells varied from 0.5% to less than 5% across HCC cell lines, with the exception of Hep-12 cells, more than 90% of which were 1B50-1$^+$ (Table 1).

To confirm that 1B50-1$^+$ cells have tumor initiation ability, we first purified 1B50-1$^+$ and 1B50-1$^-$ cells from five HCC cell lines by fluorescence-activated cell sorting (FACS) and performed tumorigenicity assays in NOD/SCID mice with limiting dilution. As shown in Table 1, as few as 100 purified 1B50-1$^+$ cells from the Huh7, Hep-12, HepG2, and SMMC7721 cell lines initiated tumor formation in almost all transplanted mice. For the least tumorigenic Hep-11 cell line, 1,000 purified 1B50-1$^+$ cells also resulted in tumor formation in five of five transplanted mice. The 1B50-1$^-$ counterparts either were completely nontumorigenic or formed tiny nodules only occasionally (Figure 1B; Figure S1A available online). We then tested the tumorigenic potential of 1B50-1$^+$ and 1B50-1$^-$ cells sorted from primary HCC-derived cells of four HCC patients. Again, 100 or 1,000 1B50-1$^+$ cells were consistently more tumorigenic than their 1B50-1$^-$ counterparts (Table 1; Figure S1A). Hematoxylin and eosin (H&E) staining demonstrated that the histological features of tumors formed by the 1B50-1$^+$ fractions resembled the tumors from which they derived, retaining the phenotypic heterogeneity, except those from Hep-12 cells, whose tumor morphology was slightly different from the original patient tissue (Figure 1C; Figure S1B).

We also compared the invasive property of 1B50-1$^+$ and 1B50-1$^-$ cells on Matrigel with a Boyden chamber assay. As shown in Figure 1D, 1B50-1$^+$ cells were more invasive than their 1B50-1$^-$ counterparts.

Differentiation Properties of 1B50-1$^+$ Cells

We next evaluated the differentiation potential of purified 1B50-1$^+$ cells from Hep-12 and Huh7 cell lines. After purified 1B50-1$^+$ Huh7 cells were cultured in vitro for 2 weeks, the percentage of 1B50-1$^+$ cells decreased from 92.33% to 1.23%, a value similar to that of the parental Huh7 population (Figure 1E). Furthermore, analysis of single-cell clones from Huh7 cells indicated that 1B50-1$^+$ cells underwent differentiation, giving rise to both 1B50-1$^+$ and 1B50-1$^-$ populations, whereas the percentage of 1B50-1$^+$ cells in the clones from the 1B50-1$^-$ fraction was unchanged (Figures S1C and S1D). It is important to note that the percentage of 1B50-1$^+$ cells in tumors formed by purified 1B50-1$^+$ Huh7 cells in NOD/SCID mice also decreased

Figure 1. Characterization of 1B50-1$^+$ HCC Cells

(A) Immunofluorescence staining for 1B50-1 in HCC cell lines. Nuclei were stained by DAPI.

(B) Representative photograph showing tumor formation in NOD/SCID mice injected s.c. with 1,000 sorted 1B50-1$^+$ (black arrows) and 1B50-1$^-$ (red arrows) Hep-11 cells.

(C) The histology of the tumors formed by 1B50-1$^+$ cells was compared with that of the HCC tissues from the original patient by H&E staining.

(D) Sorted 1B50-1$^+$ and 1B50-1$^-$ cells were assayed for their invasive ability on Matrigel using a Boyden chamber assay. Bars represent the mean ± SD of three independent experiments. *Student's t test.

(E) Flow cytometry results showing the percentage of 1B50-1$^+$ cells in parental cells, FACS-purified 1B50-1$^+$ cells and purified 1B50-1$^+$ cells cultured in 10% serum-containing medium for 2 weeks (Cultured) or transplanted into NOD/SCID mice (Tumor).

(F) qRT-PCR analysis of the expression of stem cell markers and drug-resistance-related genes in purified 1B50-1$^+$ and 1B50-1$^-$ populations. Data presented as fold difference over 1B50-1$^-$ cells for each gene, which was defined as 1 (calibrator). Error bars indicate SD.

(G) Representative flow cytometry results from analyzing indicated markers. For the ALDH assay, cells incubated with Aldefluor substrate BAAA and the ALDH-specific inhibitor DEAB were used to set the gate.

(H) Tumorigenic cell frequency in each fraction of Huh7 cells was determined with limiting dilution assay in NOD/SCID mice.

See also Figure S1.

Table 1. Tumorigenicity of 1B50-1$^+$ and 1B50-1$^-$ Cells Sorted from HCC Cell Lines and Clinical Specimen-Derived Cells in NOD/SCID Mice

	Percentage of Positive Cells				Positive in 1B50-1$^+$ Cells (%)			Tumor Formation (Tumor Formed/Mice Injected)			
								1B50-1 Positive		1B50-1 Negative	
Cells	1B50-1[a]	CD133	CD13	EpCAM	CD133	CD13	EpCAM	10^3	10^2	10^3	10^2
Huh7	0.9–2.2	24.7	37.1	86.1	85.7	75	94.7	5/5(3.8 ± 1.9)[b]	5/5	3/5(0.09 ± 0.06)[b]	0/5
Hep-11	0.4–0.7	91.2	97.4	99.9	100	100	97.8	5/5	1/5	0/5	0/5
Hep-12	92.1–94.8	76.3	97.1	99.7	78.5	98.4	99.9	5/5(4.5 ± 1.1)[b]	5/5	3/5(1.3 ± 0.3)[b]	0/5
HepG2	0.5–2.1	4.2	53.4	4.8	85.5	94.3	85.7	4/5	4/5	0/5	0/5
SMMC7721	0.5–0.6	4.8	23.2	3.6	94.3	86	85.1	5/5	5/5	0/5	0/5
Case-1[c]	1.7–3.3	2.4	30.3	28.8	84.3	92.1	97.6	5/5(3.5 ± 1.0)[b]	5/5	3/5(0.12 ± 0.04)[b]	0/5
Case-2[c]	0.6–2.1	2.1	87.7	2.5	90.3	97.6	78.7	3/5	2/5	0/5	0/5
Case-3[c]	0.4–1.8	1.5	85.5	15.8	96.8	91.7	95.2	5/5(1.3 ± 0.6)[b]	3/5	5/5(0.6 ± 0.4)[b]	1/5
Case-4[c]	0.6–1.3	8.6	13.7	4.1	89.8	93.7	91.8	2/5	0/5	0/5	0/5

[a]The results of two to eight flow cytometry analyses.
[b]The data in the parentheses are the average volume ± SD of tumors formed (cm^3).
[c]HCC specimens were undergone primary culture and expanded in vitro for less than ten passages.

to 1.14% (Figure 1E). These data suggest that 1B50-1$^+$ cells are able to differentiate into 1B50-1$^-$ cells but not vice versa. However, purified 1B50-1$^+$ Hep-12 cells retained their high percentage of 1B50-1$^+$ cells whether they were kept in culture or in vivo, like the parental Hep-12 cells (Figure 1E; Figure S1E).

1B50-1$^+$ Cells Express Multiple Stem Cell Genes

To confirm that 1B50-1$^+$ cells represent cells with stem cell-like properties at the molecular level, the expression of a panel of genes associated with liver progenitor cells (Sell and Leffert, 2008) was compared between 1B50-1$^+$ and 1B50-1$^-$ populations purified from Hep-12 and Huh7 cells by quantitative reverse transcription (qRT)-PCR (Figure 1F). Compared with 1B50-1$^-$ cells, 1B50-1$^+$ cells from both cell lines consistently expressed higher levels of *OCT4*, *SOX2*, *NANOG*, *BMI1*, *AFP*, and *CTNNB*. Furthermore, the expression of the drug efflux transporter gene *ABCG2* and the multidrug resistance gene *MDR1* was elevated in the 1B50-1$^+$ fractions.

It is interesting that 1B50-1$^+$ cells overlapped with CD133$^+$, EpCAM$^+$, CD13$^+$, and ALDH$^+$ populations of Hep-12 cells (Figure 1G). Although the majority of 1B50-1$^+$ cells were also positive for CD133, EpCAM, CD13, and ALDH in Huh7 cells, only a small fraction of CD133$^+$, EpCAM$^+$, CD13$^+$, or ALDH$^+$ cells were 1B50-1$^+$ (Figure 1G). A similar correlation between 1B50-1 and these reported HCC TIC markers was also found in other HCC cell lines and patient-derived cells (Table 1). Thus, 1B50-1$^+$ cells represent fractions of CD133$^+$, EpCAM$^+$, and CD13$^+$ populations but not vice versa.

1B50-1$^+$ Cells Are a More Restricted Subset of Highly Tumorigenic Cells among CD13$^+$, CD133$^+$, and EpCAM$^+$ HCC TIC Populations

The relationship of 1B50-1 to the other liver TIC markers CD13, CD133, and EpCAM and the fact that the 1B50-1$^+$ fraction of nontumorigenic Hep-11 cells, which were more than 91% positive for CD13, CD133, and EpCAM, was tumorigenic led us to propose that the previously reported HCC TIC population defined by CD13$^+$, CD133$^+$, or EpCAM$^+$ might be mainly attributed to the existence of their respective 1B50-1$^+$ subsets. To confirm this, we compared the tumor-forming ability of different fractions of Huh7 cells (Figure 1H). As few as 100 cells of 1B50-1$^+$CD13$^+$, 1B50-1$^+$CD133$^+$, and 1B50-1$^+$EpCAM$^+$ subsets formed tumors in almost all the transplanted mice, whereas only small nodules were occasionally found in all other fractions that were 1B50-1$^-$. Cells only positive for CD13, CD133, or EpCAM did not have significantly higher tumor formation ability compared with each corresponding double-negative fraction.

Clinical Significance of 1B50-1$^+$ Cells in HCC and Surgical Margin Tissues

Because 1B50-1 did not stain formalin-fixed tissues, we examined its staining by fluorescence immunohistochemistry using 86 paired frozen HCC and paracancerous tissues that were obtained from the hepatectomy margins, six recurrent HCC tissues, and five normal liver samples from hepatic hemangioma patients. As shown in Figure 2A, 1B50-1 reacted with an antigen on the cell surface in the positive tissues and 1B50-1$^+$ cells showed a scattered distribution in 72.1% of HCC tissues, whereas they were detected in only 46.5% of paracancerous tissues (Table S1). Furthermore, 1B50-1$^+$ staining in paracancerous tissues was only found in those patients with positive staining in their tumor tissues. No 1B50-1$^+$ cells were observed in the five normal liver tissues. It is important to note that 1B50-1$^+$ cells were enriched in the recurrent HCC tissues of four patients out of six tested.

Next, we examined the tumorigenic capability of 1B50-1$^+$ and 1B50-1$^-$ cells sorted directly from freshly resected HCC and paracancerous tissues of three patients (Figure 2B). 1B50-1$^+$ cells isolated from the tumor tissues of all three patients gave rise to tumor growth after transplantation of as few as 1,000 cells, while those purified from the paracancerous tissues in two out of three patients also initiated tumor growth within 8 weeks after transplantation. As many as 10^5 1B50-1$^-$ cells isolated from either tumor or paracancerous tissues caused no visible tumor formation after 4 months. H&E staining showed no difference in the

histology formed by 1B50-1$^+$ cells from tumor versus peritumor tissues, which both resembled that of the tumor tissue of the patient (Figure 2C).

Finally, we analyzed the correlation between the clinicopathologic characteristics and 1B50-1 staining status (Table S1). No significant correlation was found between the 1B50-1$^+$ staining in HCC tissues and any clinicopathologic factor. However, the presence of 1B50-1$^+$ cells in the paracancerous tissues did correlate significantly with hepatic cirrhosis, very rapid recurrence, and a lower rate of 4-year overall survival postsurgery. Kaplan-Meier curves revealed that the 1B50-1 staining status in the tumor tissues did not correlate with disease-free or overall survival of these patients, but the median disease-free survival and the 75th percentile overall survival time postsurgery in the patients with 1B50-1$^-$ staining in the paracancerous tissues were approximately 4.5 and 10.1 times, respectively, those with positive staining (Figures 2D–2G). Multivariant Cox regression analysis also showed that 1B50-1$^+$ staining in HCC paracancerous tissues was an independent risk factor of poor prognosis for HCC patients (Figure 2H).

Self-Renewal Property of 1B50-1$^+$ Cells

To further confirm that 1B50-1$^+$ cells have stem cell-like properties, we first performed sphere formation assays to determine their in vitro self-renewal ability. 1B50-1$^+$ cells purified from various HCC cell lines and clinical specimens displayed significantly higher sphere-forming efficiency compared with their respective 1B50-1$^-$ counterparts. Furthermore, the sphere-forming ability of 1B50-1$^+$ cells expanded in subsequent serial propagations (Figures 3A and 3B). We then performed in vivo serial transplantation assays with resorted cells from tumors formed by 1B50-1$^+$ cells. Once again, 1B50-1$^+$ cells formed tumors in the second transplanted mice, while their 1B50-1$^-$ counterparts remained nontumorigenic (Figure 3C). These results demonstrate that 1B50-1$^+$ cells have self-renewal ability both in vitro and in vivo.

In Vitro Effects of 1B50-1 on HCC Cells

To evaluate if 1B50-1 could have some effects on liver TICs, we first tested the sphere-forming ability of 1B50-1$^+$ cells following 1B50-1 treatment. As shown in Figure 3D, 1B50-1 at 10 μg/ml significantly suppressed the sphere formation of 1B50-1$^+$ cells purified from all HCC cell lines and patient-derived specimens tested.

We then examined the effect of 1B50-1 on the apoptosis of 1B50-1$^+$ cells by a terminal deoxynucleotidyl transferase dUTP nick-end labeling (TUNEL) assay. 1B50-1 induced apoptosis of the cultured Hep-12 cells in a dose-dependent manner. The apoptosis-inducing effect was also confirmed in 1B50-1$^+$ fractions purified from other cell lines. No significant cell apoptosis was observed for unpurified Hep-11 cells upon 1B50-1 treatment (Figures 3E and 3F; Figure S2).

Finally, we treated cultured HCC cells with 1B50-1 at 10 μg/ml for 48 hr, followed by transplanting the cells into NOD/SCID mice subcutaneously (s.c.) with limiting dilution. While 10^6 cells of control groups (treated with immunoglobulin G [IgG]) formed tumors in all the transplanted mice within 3–4 weeks after injection, none of the mice transplanted with 1B50-1-treated cells showed tumor formation after 12 weeks (Figure 3G). These data indicate that tumorigenic cells are eradicated by ex vivo 1B50-1 treatment.

1B50-1 Suppresses the Growth of HCC In Vivo and Eradicates TICs

Next, we examined whether 1B50-1 could have a therapeutic effect on established HCC engraftments by administering 1B50-1 intraperitoneally (i.p.). As shown in Figures 4A–4C, the growth of both Hep-12 and Huh7 cells was dramatically suppressed by 1B50-1 treatment in a dose-dependent manner, although the percentages of positive cells varied greatly between the two cell lines (Table 1). Some of the tumors formed by Hep-12 cells almost completely disappeared following 1B50-1 treatment. The suppression effect of 1B50-1 was also detected on xenografts derived from a HCC primary culture (Figure 4D).

Because 1B50-1 treatment alone retarded tumor growth only to a moderate degree, we examined the therapeutic efficacy of the combination of 1B50-1 and doxorubicin (DXR). By injecting 800 μg 1B50-1 and 1.5 mg/kg DXR i.p. per mouse, the growth of Huh7 engraftments was inhibited by as much as 89.0% compared with the control, representing a further 46.5% inhibition compared with DXR alone (Figures 4E and 4F). A similar effect with combined therapy was also observed for tumor xenografts directly derived from two HCC patients (patient-derived xenograft [PDX]) (Figures 4G and 4H). The survival of mice was also improved following combined therapy in the PDX models (Figures 4I and 4J).

We then analyzed the TICs in the residues of treated Huh7 engraftments. Although the tumor inhibition of 1B50-1 was less effective than DXR, the proportion of 1B50-1$^+$ cells decreased upon antibody treatment, whereas the population of 1B50-1$^+$ cells was significantly enriched after DXR treatment (Figure 4K). Moreover, serial transplantation of 10^4 cells into secondary NOD/SCID mice from tumors that received 1B50-1 treatment formed tumors in two out of 10 mice, while the cells from the control and DXR-treated tumors subsequently formed tumors in nine out of 10 and five out of five injected mice, respectively, with DXR-treated cells developing tumors more rapidly. Notably, only a tiny nodule was found in one out of five mice transplanted with residual cells from an engraftment treated with 1B50-1 plus DXR (Figures 4L and 4M), suggesting TICs were reduced following combined treatment in vivo.

We next detected apoptotic cells by TUNEL assay in the xenografts following 1B50-1 treatment. Consistent with in vitro results, the apoptotic cell percentage increased significantly in both Hep-12 and HuH7 engraftments treated with 800 μg 1B50-1 per mouse (Figures 4N and 4O; Figure S3).

These data demonstrate that 1B50-1 has a therapeutic effect on HCC by targeting TICs, which is augmented by combination with DXR.

The Antigen Recognized by 1B50-1 Is α2δ1, Isoform 5

To identify the antigen recognized by 1B50-1, we performed immunoprecipitation and mass spectrometry analysis using Hep-11 and Hep-12 cells. Unlike in Hep-11 cells, immunoprecipitation of Hep-12 cell lysates with 1B50-1 resulted in several dominant bands observed by SDS-PAGE (Figure 5A). Only the ~150 kDa band was predicted to be a membrane protein with a matched molecular weight of glycosylated α2δ1,

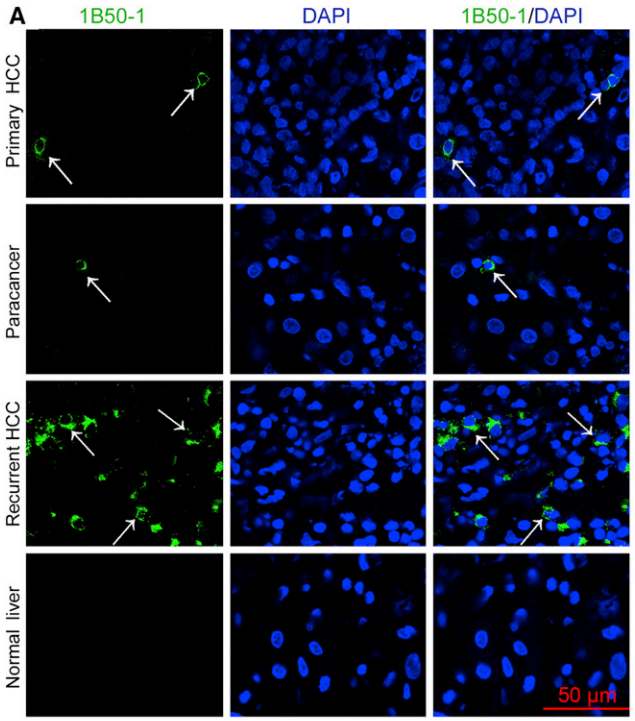

B

Patient	Age (Year)	Gender	Venous thrombosis	AFP (ng/ml)	Tumorigenicity (Tumor)# 1B50-1+	Tumorigenicity (Tumor)# 1B50-1-	Tumorigenicity (PCa)# 1B50-1+	Tumorigenicity (PCa)# 1B50-1-
Case-5	40	Female	Yes	9621	1/1 (10^4)	0/1 (2×10^4)	1/1 (10^4)	0/1 (10^4)
Case-6	70	Male	No	63	1/1 (10^3)	0/1 (2×10^4)	1/1 (2×10^4)	0/1 (2×10^4)
Case-7	55	Male	No	430	1/1 (5×10^3)	0/1 (10^5)	0/1 (10^4)	0/1 (10^5)

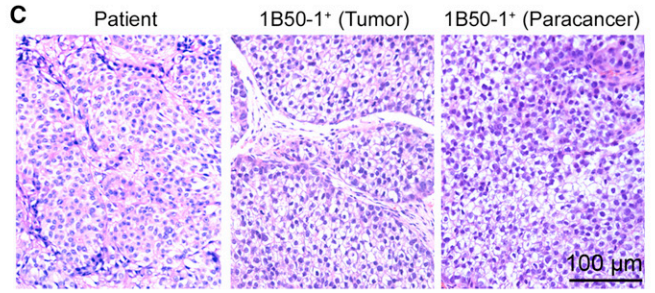

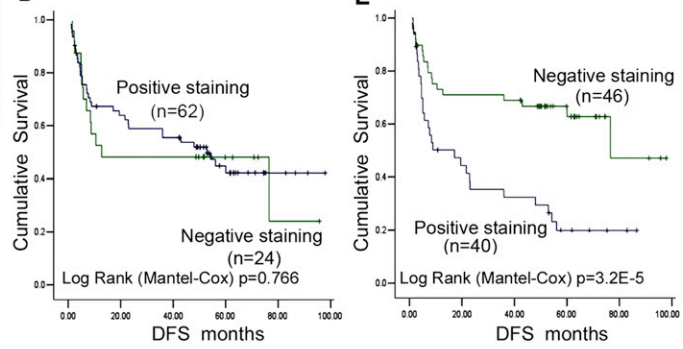

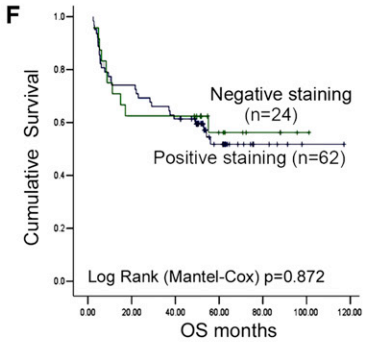

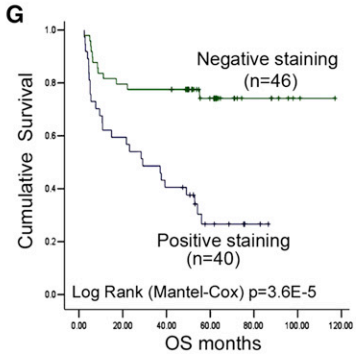

H

Variable		Cases (n)	4-year survival rate (%)	Univariate p value*	Multivariate (Cox-regression) RR (95% CI)	Multivariate (Cox-regression) p value
Gender	Male	75	64.0	0.155	0.732 (0.316-1.697)	0.467
	Female	11	36.4			
Age (Year)	≤60	63	54.0	0.073	1.525 (0.589-3.950)	0.385
	>60	23	78.3			
Cirrhosis	Absent	27	81.5	0.007	0.476 (0.190-1.189)	0.112
	Present	59	50.8			
Size	≤5 cm	46	80.4	0.00005	2.908 (0.917-9.226)	0.070
	>5 cm	40	2.5			
Venous invasion	Absent	64	70.3	0.001	0.457 (0.216-0.967)	0.041
	Present	22	31.8			
1B50-1 (PCa)	Negative	46	80.4	0.00005	0.211 (0.089-0.503)	0.0004
	Positive	40	37.5			
1B50-1 (Ca)	Negative	24	62.5	0.810	1.306 (0.550-3.098)	0.545
	Positive	62	59.7			

Figure 2. Clinical Significance of 1B50-1$^+$ Cells in HCC Patients

(A) Immunohistochemical staining of cryostat sections of primary and recurrent HCC tissues, paracancerous tissues and normal liver with 1B50-1. Nuclei were stained with DAPI. Arrows indicate positive cells.

(B) The tumorigenicity of 1B50-1$^+$ and 1B50-1$^-$ cells purified directly from freshly resected HCC and matched paracancerous tissues. #The data are expressed as number of tumors formed/number of sites injected, and the numbers of cell injected are shown in parentheses.

(C) H&E staining of the tumors formed in (B) by 1B50-1$^+$ cells from both the tumor and paracancerous tissues, as well as the original patient HCC tissue (case-5).

(D–G) Kaplan-Meier curves for disease-free (DFS) and overall survival (OS) were compared according to 1B50-1 staining status in HCC tissues (D and F) and the paracancerous tissues (E and G).

(legend continued on next page)

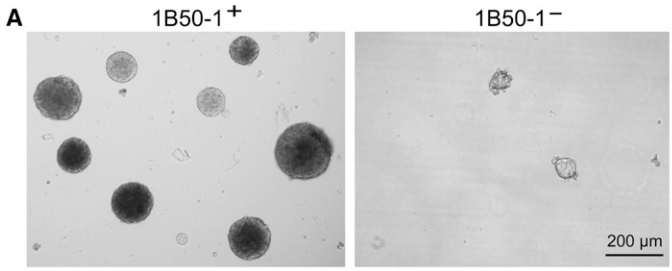

C

Cells	1B50-1 positive		1B50-1 negative	
	10^3	10^2	10^3	10^2
Huh7	5/5	5/5	0/5	0/5
Hep-11	5/5	ND	0/5	ND
Case-5#	3/3	1/3	0/3	0/3
Case-7	3/3	3/3	0/3	0/3

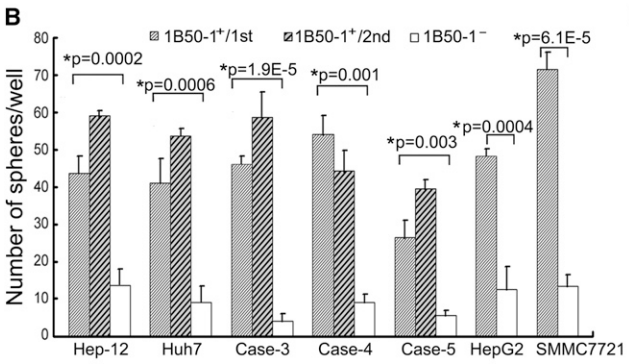

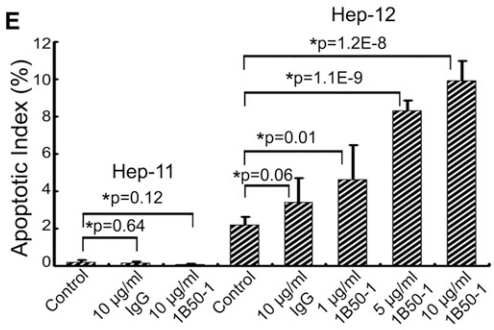

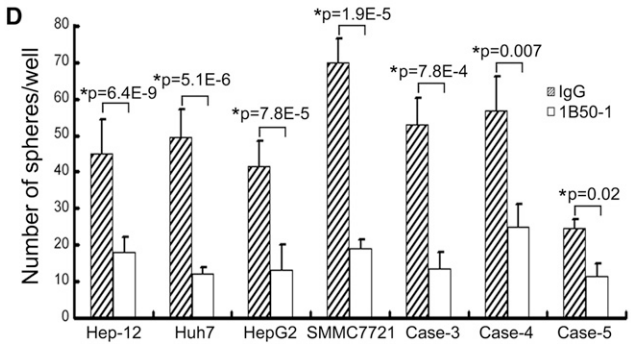

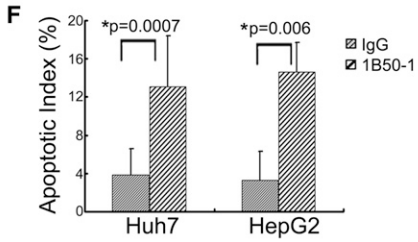

G

Cells	Control		1B50-1	
	10^6	10^5	10^6	10^5
Hep-12	5/5	3/5	0/5	0/5
Huh7	5/5	3/5	0/5	0/5
SMMC7721	3/3	ND	0/3	ND

Figure 3. The Self-Renewal Property of 1B50-1$^+$ HCC Cells and the Effects of 1B50-1 In Vitro

(A) Representative phase contrast micrographs show the spheroids formed by 1B50-1$^+$ and 1B50-1$^-$ HCC cells.

(B) Histograms showing the spheroid forming efficiency of FACS-sorted 1B50-1$^+$ and 1B50-1$^-$ fractions from indicated sources. The ability of the spheres formed by 1B50-1$^+$ cells to form secondary spheroid was also shown (1B50-1$^+$/2nd). One hundred cells per well were plated (n = 6). Spheroids ($\geq$100 μm) were counted under a stereomicroscope.

(C) Tumor formation of serial transplantation assay: 1B50-1$^+$ and 1B50-1$^-$ subsets sorted from xenografted tumors by 1B50-1$^+$ cells in Table 1 and Figure 2B were transplanted s.c. into secondary NOD/SCID mice. #The tumor formed by paracancerous 1B50-1$^+$ cells were used.

(D) Histograms showing the effect of 1B50-1 (10 μg/ml) on spheroid formation of sorted 1B50-1$^+$ cells (n = 6).

(E and F) Histograms showing the effect of 1B50-1 on apoptosis of Hep-11 and Hep-12 cell lines (E) or purified 1B50-1$^+$ subsets from indicated HCC cell lines (F). Cells were treated with 10 μg/ml 1B50-1 for 48 hr in vitro and processed using TUNEL assay followed by flow cytometry.

(G) The tumorigenicity of HCC cells treated with 10 μg/ml 1B50-1 or nonrelated IgG (control) for 48 hr in vitro and subsequently transplanted into NOD/SCID mice.

All error bars indicate SD. *Student's t test. ND, not done.

See also Figure S2.

a composing subunit of a voltage-dependent calcium channel (Figures S4A and S4B). Hence, it was selected for further analysis.

An analysis of α2δ1, which is encoded by *CACNA2D1*, was conducted to examine whether its expression was associated with 1B50-1 staining. qRT-PCR showed that the α2δ1 mRNA

(H) Univariate and multivariate analysis predicts risk factors of poor survival for HCC patients. *Chi-square test. Note: 1B50-1$^+$ staining is defined as the presence of at least one 1B50-1$^+$ cell in a whole cryostat slice, which was screened under a microscope with a 10× lens blindly by two experienced researchers. Negative staining indicates that no 1B50-1$^+$ cells were found. Ca, cancer; PCa, paracancer; RR, relative risk.

See also Table S1.

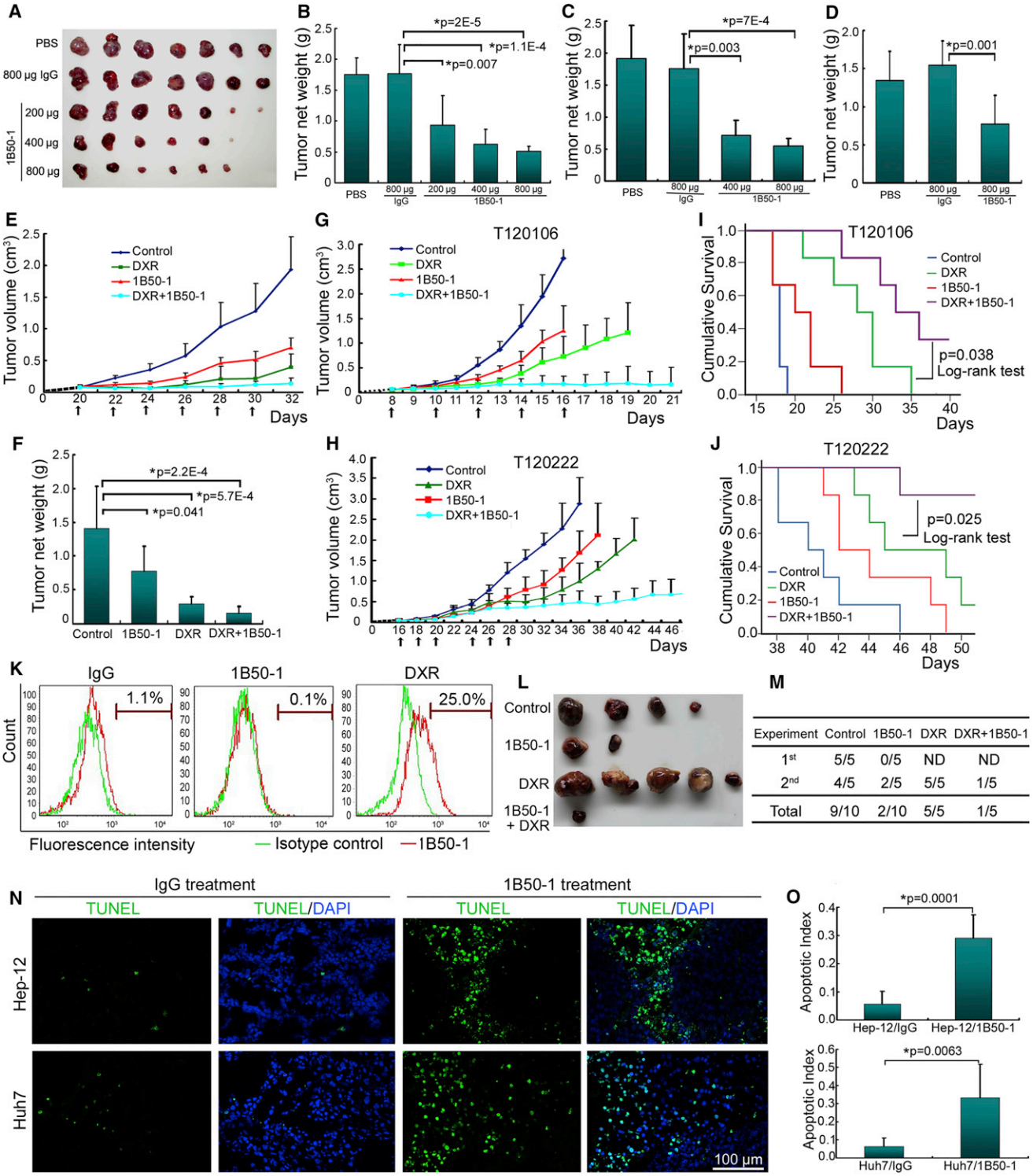

Figure 4. The Therapeutic Effects of 1B50-1 on Established HCC Engraftments in NOD/SCID Mice

(A–D) The mice transplanted s.c. with Hep-12 (A and B, n = 7), Huh7 (C, n = 5), and primary HCC cells (D, n = 5) were injected i.p. with PBS, nonrelated IgG, or 1B50-1 at indicated doses every other day for a total of seven times after the tumors were visible. Tumors were dissected and weighed at experiment termination.

(E and F) Growth curves of Huh7 engraftments treated with 800 μg 1B50-1, 1.5 mg/kg doxorubicin (DXR), or the combination of both, per mouse as indicated by arrows in (E). The histogram in (F) shows the average weight of the dissected tumors (n = 7).

(G and H) Growth curves of two HCC PDX tumors injected i.p. with 800 μg 1B50-1, 1.5 mg/kg DXR, or the combination of both, per mouse as indicated by arrows (n = 6).

(I and J) Kaplan-Meier survival curves of the PDX models in (G) and (H) following the treatments.

(legend continued on next page)

was highly expressed in Hep-12 cells compared with Hep-11 cells (Figure 5B) and in 1B50-1$^+$ subsets compared with their 1B50-1$^-$ counterparts from HCC cell lines and primary tumor-derived cells (Figure 5C). Furthermore, western blot with a commercial α2δ1 mAb showed that Hep-12 cells and 1B50-1$^+$ HCC specimens expressed high levels of α2δ1 protein, while it was undetectable in Hep-11 cells and IB50-1$^-$ paracancerous tissues (Figures 5D and 5E). Additionally, double staining of Hep-12 cells and HCC specimens with 1B50-1 and a rabbit polyclonal α2δ1 antibody confirmed that both antibodies colocalized (Figure 5F).

Because α2δ1 has five isoforms, we determined if 1B50-1 is isoform specific. Double staining (with MYC and 1B50-1 antibodies) of COS-7 cells transiently transfected with each MYC-tagged α2δ1 isoform revealed that 1B50-1 specifically recognized isoform 5, while it weakly cross-reacted with the other four isoforms (Figure 5G). Further PCR cloning and sequencing verified that the mRNA encoding the target protein in 1B50-1$^+$ HCC cells was indeed that of α2δ1 isoform 5 (Figures S4C and S4D). Consistently, skeletal muscle, which expresses isoform 1 of α2δ1, was positively stained by the commercial polyclonal α2δ1 antibody but was negative for 1B50-1 staining (Figure 5F), further suggesting that 1B50-1 specifically recognizes isoform 5 of α2δ1. Finally, knockdown with shRNAs specifically targeting α2δ1 resulted in decreased 1B50-1 staining in Hep-12 cells (Figures 5H–5J). All of these data confirm that the antigen recognized by 1B50-1 is indeed isoform 5 of α2δ1.

The Effects of α2δ1 Knockdown and Overexpression on TIC Properties

If 1B50-1 functions by blocking α2δ1, knockdown of its expression should mimic the effects of 1B50-1 treatment. To validate this hypothesis, we performed RNAi experiments. Knockdown of α2δ1 led to reduced sphere formation, enhanced apoptosis, and decrease of tumorigenic cells among Hep-12 cells (Figures 5K–5M; Figure S4E). In addition, knockdown of α2δ1 in purified 1B50-1$^+$ cells from other HCC cell lines and primary HCC-derived cells reduced sphere formation and tumorigenicity and increased cell apoptosis (Figures 5K, 5L, and 5N).

We also overexpressed α2δ1 isoform 5 in Hep-11 cells and 1B50-1$^-$ populations purified from other HCC cell lines. Although overexpression of α2δ1 did not lead to a significant change in tumorigenicity of Hep-11 cells, it increased hepatosphere-forming efficiency. Similar results were obtained in other 1B50-1$^-$ populations upon α2δ1 overexpression (Figure 5O).

α2δ1 Regulates Calcium Influx in Liver TICs

To determine whether 1B50-1 binding of α2δ1, which is a subunit of a voltage-dependent calcium channel, affects calcium influx, we first measured changes in intracellular calcium concentration ($[Ca^{2+}]_i$) with the Ca^{2+} indicator Fluo-4AM. $[Ca^{2+}]_i$ in Hep-12 cells was significantly higher than that of nontumorigenic Hep-11 cells, as shown by the intensity of fluorescence. Treatment of Hep-12 cells with 10 μg/ml 1B50-1 for 24 hr resulted in a 25.5% decrease of fluorescence intensity, which was statistically significant compared with IgG-treated cells, whereas Hep-11 cells were not affected by 1B50-1 treatment (Figure 6A). Furthermore, analysis of $[Ca^{2+}]_i$ in other HCC cell lines and primary HCC-derived cells revealed that the average $[Ca^{2+}]_i$ level in 1B50-1$^+$ fractions was significantly higher than that of 1B50-1$^-$ subsets, and 1B50-1 treatment resulted in a marked reduction of $[Ca^{2+}]_i$ in 1B50-1$^+$ cells (Figure 6B; Figure S5A). Overexpression of α2δ1 resulted in elevation of $[Ca^{2+}]_i$ in Hep-11 cells (Figure 6C; Figure S5B), whereas knockdown of α2δ1 in Hep-12 cells led to decrease in $[Ca^{2+}]_i$ (Figure 6D). All these data show that α2δ1 plays a role in the calcium influx in 1B50-1$^+$ liver TICs.

Next, we monitored time-dependent changes in $[Ca^{2+}]_i$ in individual cells. Irregular calcium transients were observed in most Hep-12 cells. They appeared more frequently and with more varied intervals in Hep-12 cells compared with Hep-11 cells, in which transients were only observed in approximately 1%–2% of cells (Figures 6E–6G). Calcium transients diminished when extracellular Ca^{2+} was chelated with EGTA and restored when calcium was added into the culture medium (Figures S5C and S5D), suggesting that spontaneous $[Ca^{2+}]_i$ oscillations in TIC-enriched Hep-12 cells depended on the influx of extracellular calcium. Treatment of Hep-12 cells with 1B50-1 did not alter the frequency of spontaneous $[Ca^{2+}]_i$ oscillations, but their amplitude was significantly suppressed (Figures 6H–6J). α2δ1 knockdown in Hep-12 cells gave similar results (Figures 6K and 6L). These data confirm that α2δ1 plays an essential role in calcium oscillations in HCC TICs and that 1B50-1 inhibits the function of α2δ1.

The Hepatosphere-Forming Ability of 1B50-1$^+$ Liver TICs Depends on L- and N-type Calcium Channels

Given that α2δ1 may function through both calcium channel-dependent and independent mechanisms and that multiple calcium channels may be involved in calcium influx, we first determined which calcium channel is involved in the TIC self-renewal regulated by α2δ1 using specific calcium channel blockers. As shown in Figure 6M, the hepatosphere formation ability of 1B50-1$^+$ liver TICs isolated from different HCC cell lines, as well as that of α2δ1-overexpressing Hep-11 cells, was inhibited by L-type and N-type but not T-type calcium channel blockers, indicating that α2δ1 regulates TIC self-renewal through at least L-type and N-type calcium channels.

We then determined whether other subunits of functional voltage-gated calcium channels were present in the TICs by performing RT-PCR analysis of the mRNAs coding for all known 10 α1 subunits and three β subunits of voltage-gated calcium

(K) Residual tumors of (E) were digested into single cells, stained by 1B50-1 after depleting red blood cells, and analyzed by flow cytometry to detect the percentage of 1B50-1$^+$ cells in the residual tumors after treatment.
(L and M) The tumor-initiating ability of the Huh7 engraftment residues after each drug treatment was assayed by retransplanting 10^4 cells with Matrigel into NOD/SCID mouse. The data in (M) are from two independent experiments, and the photograph in (L) shows the dissected tumors of one experiment. ND, not done.
(N and O) Apoptotic cells in engraftments treated with 800 μg 1B50-1 per mouse were detected in situ using the TUNEL assay. The apoptotic index was assessed by the ratio of TUNEL-positive cells/total number of cells from six randomly selected high-power fields (400×). All error bars indicate SD. *Student's t test.
See also Figure S3.

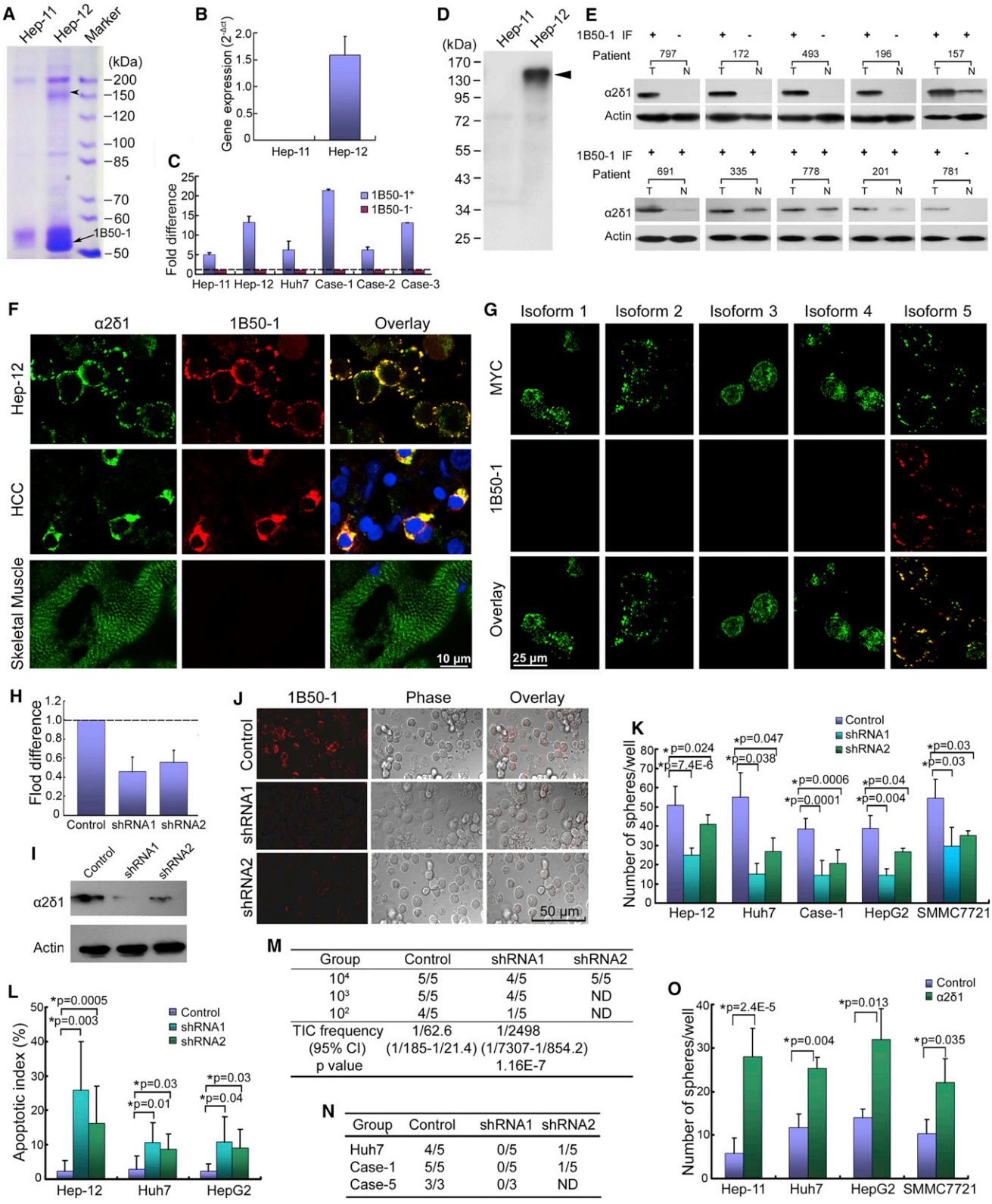

Group	Control	shRNA1	shRNA2
10^4	5/5	4/5	5/5
10^3	5/5	4/5	ND
10^2	4/5	1/5	ND
TIC frequency (95% CI)	1/62.6 (1/185-1/21.4)	1/2498 (1/7307-1/854.2)	
p value		1.16E-7	

Group	Control	shRNA1	shRNA2
Huh7	4/5	0/5	1/5
Case-1	5/5	0/5	1/5
Case-5	3/3	0/3	ND

Figure 5. The Roles of α2δ1 in HCC TICs

(A) SDS-PAGE analysis of 1B50-1 immunoprecipitation products from Hep-11 and Hep-12 cells. The arrowhead indicates the band that was cut out for mass spectrometry analysis.

(B) qRT-PCR analysis of the α2δ1 mRNA level relative to *GAPDH* mRNA level in Hep-11 and Hep-12 cell lines.

(legend continued on next page)

channels. As shown in Figure S5E, the mRNAs encoding α1B, α1C, and α1F subunits were highly expressed in Hep-12 cells compared with Hep-11 cells, while those for α1A, α1D, α1G, α1H, β1, and β3 subunits were equally expressed in both cell lines. Furthermore, when α2δ1 was transfected into Hep-11 cells, the expression of α1B, α1C, and α1F mRNAs was induced. The data were further confirmed with qRT-PCR analysis of α1B, α1C, α1D, and α1F mRNAs in these cells and sorted 1B50-1$^+$ and 1B50-1$^-$ subsets (Figure 6N). These data suggest that the most important subunits of a functional calcium channel do exist in TICs and that α2δ1 could upregulate the expression of α1B, α1C, and α1F subunits.

α2δ1 Knockdown Inhibits ERK1/2 Phosphorylation and Triggers Apoptosis

Because calcium oscillations play a pivotal role in activating signaling cascades that regulate gene transcription and various cell functions, we performed western blots to investigate the molecular mechanisms underlying the effects of 1B50-1 treatment and α2δ1 knockdown. As shown in Figure 7A, the phosphorylation of ERK1/2 in Hep-12 cells was suppressed upon 1B50-1 treatment and α2δ1 knockdown, while both the overall protein and phosphorylation levels of PI3K and AKT were unaffected. Furthermore, consistent with its apoptosis-inducing effects, both 1B50-1 treatment and α2δ1 shRNA knockdown resulted in downregulation of the antiapoptotic protein BCL2 and upregulation of BAX and BAD, as well as activation of caspases 3, 8, and 9, as shown by increased levels of cleaved proteins. Notably, the expression of ABCG2 and BMI1, which is important for stem cell self-renewal (Chiba et al., 2008), was also downregulated.

Next, we validated the aforementioned data in cells purified from primary HCC-derived cells by western blot analysis of some representative proteins. Compared with their 1B50-1$^-$ counterparts, 1B50-1$^+$ cells expressed higher levels of ABCG2, BMI1, BCL2, and OCT4, as well as phosphorylated ERK1/2 (p-ERK1/2). 1B50-1 treatment of 1B50-1$^+$ cells resulted in downregulation of these proteins and dephosphorylation of ERK1/2 (Figure 7B).

It is important to note that the expression of those proteins downregulated by α2δ1 blocking, such as BMI1, OCT4, ABCG2, BCL2, and p-ERK1/2, was upregulated upon α2δ1 overexpression (Figure 7C).

An ERK1/2 Inhibitor, U0126, Mimics the Effects of α2δ1 Blocking

The aforementioned findings indicate that the MAPK pathway regulates liver TIC properties. To test this hypothesis, we treated Hep-12 cells and 1B50-1$^+$ fractions from other HCC cell lines with an ERK1/2 inhibitor, U0126. The expression of BMI1, OCT4, ABCG2, and BCL2 were downregulated by 10 μM U0126 treatment for 48 hr (Figure 7D). The hepatosphere formation of Hep-12 cells, purified 1B50-1$^+$ subsets from various HCC cell lines, and α2δ1-overexpressing Hep-11 cells was also suppressed upon U0126 treatment (Figures 7E and 7F). These data suggest that ERK1/2 inhibition mimics the effects of 1B50-1 treatment and α2δ1 knockdown, suggesting that ERK1/2 activity is essential for the maintenance of HCC TIC properties.

DISCUSSION

The TICs are proposed to be responsible for tumor recurrence according to the cancer stem cell hypothesis (Visvader and Lindeman, 2012). Here, we identified a population of HCC TIC expressing α2δ1 in primary HCC and some surgical margins using a mAb, 1B50-1, generated against the recurrent HCC-derived cell line Hep-12, suggesting these α2δ1$^+$ TICs might be the cell of origin for HCC recurrence.

The differentiation capability of 1B50-1$^+$ cells from the recurrent HCC-originated Hep-12 cells, which have a block of differentiation capacity in vitro or in vivo (Xu et al., 2010), is quite different from those purified from primary HCC-derived cells in that they established equilibrium at a different percentage of 1B50-1$^+$ cells. This observation indicates that, during tumor progression, the same TIC population undergoes clonal evolution under selection pressures that enable these cells to acquire additional characteristics and to remain in a more stable state.

α2δ1 was previously proposed as a potential hepatic progenitor cell marker (Yovchev et al., 2007). We confirmed that 1B50-1 recognized many cells in resected mouse liver as well as in colony-forming units of normal mouse liver (data not shown).

(C) qRT-PCR analysis of the α2δ1 mRNA level in purified 1B50-1$^+$ fractions relative to that in their 1B50-1$^-$ counterparts of indicated sources.
(D and E) Western blot analysis with a α2δ1 mAb in HCC cell lines (D) or paired tumor (T) and paracancerous (N) tissues from HCC patients (E). The corresponding 1B50-1 immunofluorescence staining status (1B50-1 IF) is also given above each lane for comparison. +, positive; −, negative.
(F) Cultured Hep-12 cells, cryostat sections of HCC tissue and skeletal muscle were fixed with methanol, double-stained with 1B50-1 and a rabbit polyclonal α2δ1 antibody, and observed under a confocal microscope. The HCC tissue and the skeletal muscle were also counterstained with DAPI.
(G) Immunofluorescent staining of COS-7 cells transiently transfected with indicated MYC-tagged isoform of α2δ1 with MYC and 1B50-1 antibodies without fixation.
(H and I) α2δ1 mRNA (H) and protein (I) levels of Hep-12 cells stably infected with lentivirus harboring scramble (control) or shRNA1 or shRNA2 targeting α2δ1.
(J) Hep-12 cells stably infected with indicated lentivirus were immunostained by 1B50-1.
(K) Histogram showing the sphere-forming ability of purified 1B50-1$^+$ subsets after α2δ1 knockdown. Sorted 1B50-1$^+$ cells were incubated with indicated lentivirus for 4 hr, and were plated at 100 cells per well (n = 6).
(L) Sorted 1B50-1$^+$ cells were infected with indicated lentivirus and cultured in serum-free medium for 72 hr, and apoptotic cells were detected by flow cytometry analysis of TUNEL-stained cells.
(M) Hep-12 cells stably infected with indicated lentivirus were transplanted s.c. in NOD/SCID mice at indicated numbers to assay their tumorigenicity.
(N) The tumorigenicity of 1B50-1$^+$ cells purified from indicated sources after α2δ1 shRNA knockdown. 1B50-1$^+$ cells were incubated with indicated lentivirus for 4 hr, and 1,000 cells per mouse were injected.
(O) The sphere-forming ability of sorted 1B50-1$^-$ cells infected with α2δ1 (isoform 5) lentivirus (100 cells per well plated, n = 6). All error bars indicate SD. *Student's t test. ND, not done.
See also Figure S4.

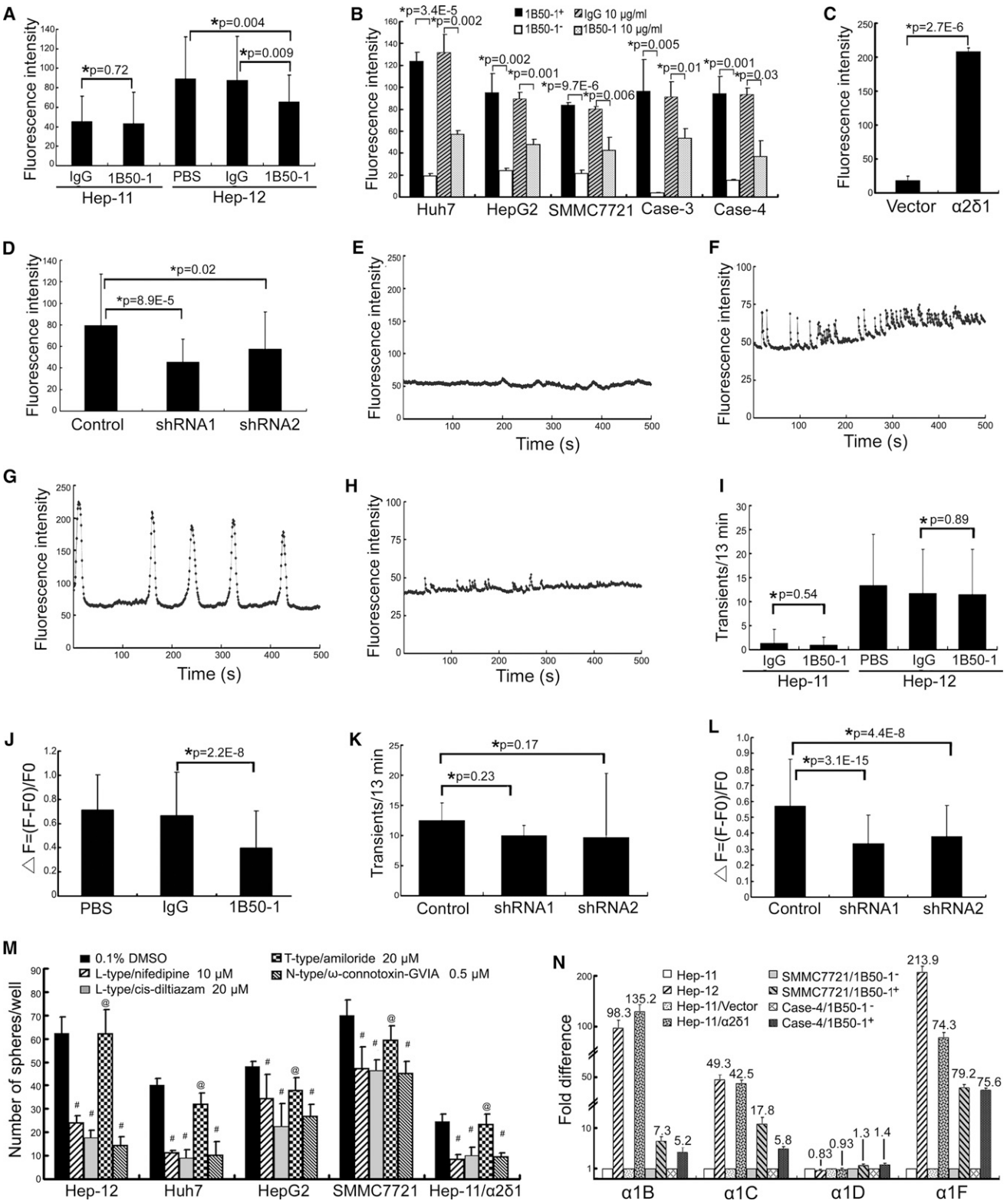

Figure 6. Characterization of Calcium Influx in 1B50-1$^+$ TICs

(A) $[Ca^{2+}]_i$ levels in Hep-11 and Hep-12 cells after treated with IgG or 1B50-1 at 10 μg/ml for 24 hr measured by the fluorescence intensity using confocal microscopy after cells were loaded with Fluo-4AM.

(B) $[Ca^{2+}]_i$ levels in 1B50-1$^+$ and their 1B50-1$^-$ counterparts, as well as in 1B50-1$^+$ subsets treated with IgG or 1B50-1 at 10 μg/ml for 24 hr measured by flow cytometry.

(legend continued on next page)

Its identification as a TIC marker here demonstrates TICs' close correlation with normal liver progenitors. Furthermore, our inability to find cells reacted with 1B50-1 in normal human liver specimens is consistent with the notion that liver progenitors are rare and are not readily detectable in human normal adult liver (Darwiche and Petersen, 2010). Finally, the finding that the cells detected by 1B50-1 in paracancerous tissues also have TIC properties may explain why those patients who have undergone hepatectomy still relapse, and this could have prognostic value. This finding also indicates that specific therapeutic strategies to eradicate these cells should be used for HCC patients with $\alpha2\delta1^+$ cells at the surgical margins.

Our data demonstrate that 1B50-1 has a therapeutic effect on HCC by targeting TICs. Of course, ideally, tumors will disappear when TICs are disrupted completely, according to the TIC hypothesis. However, it is difficult to obtain complete pharmacokinetic control, especially in vivo (as shown by this study and many others; Haraguchi et al., 2010; Visvader and Lindeman, 2012), with an antibody alone, most likely because of inefficient penetration of the antibody to the cells inside the tumor mass and because of the presence of other transit-amplifying tumorigenic cells. Instead, combination therapy of 1B50-1 with other anti-HCC drugs such as DXR, which most likely disrupt TICs and fast-proliferating non-TICs, respectively, would be required to achieve a drastic regression, as demonstrated here.

The target of 1B50-1 was identified and validated as isoform 5 of $\alpha2\delta1$, a subunit of voltage-gated calcium channel complexes (De Jongh et al., 1990; Eroglu et al., 2009). Currently, little is known about the expression pattern and specific function of isoform 5 of $\alpha2\delta1$, although other members of the $\alpha2\delta$ family have been extensively investigated. Here, we reveal an essential role of $\alpha2\delta1$ isoform 5 for the modulation of calcium influx and the maintenance of many HCC TIC properties. In addition, it is undetectable in most normal tissues, so cytotoxicity unlikely would be a concern. Hence, $\alpha2\delta1$ isoform 5 could serve as a therapeutic target for the development of drugs against HCC that specifically eradicate TICs.

Our study identified the roles of $\alpha2\delta1$ isoform 5 in liver TICs were related to its calcium influx regulation function through L- and N-type voltage-gated calcium channels. However, the activation of voltage-dependent calcium channels is regulated by polarization and depolarization of membranes, which are often caused by influx of cations. Polarization/depolarization-related signaling pathways and some other calcium channels, such as nicotinic acetylcholine receptors, are also found to be related to tumorigenesis (Hung et al., 2008; Lee et al., 2010). It would be interesting to determine if these molecules are also highly expressed in $\alpha2\delta1^+$ liver TICs and, if so, what the roles are of these molecules in the maintenance of TIC properties.

We identified p-ERK1/2 as a key downstream target of $\alpha2\delta1$ function in liver TICs. This finding is consistent with a previous report that signaling to the nucleus by an L-type calcium channel is transduced through the MAPK pathway (Dolmetsch et al., 2001). Because other signaling pathways, such as the noncanonical Wnt pathway, may also be involved in calcium signaling (MacLeod et al., 2007), further studies are needed to clarify whether these signaling pathways are also involved in the maintenance of cancer stem cell-like properties of HCC TICs by $\alpha2\delta1$.

Spontaneous calcium oscillations occur in cells originating from excitable tissues, such as muscle and neuronal tissues, but they also occur in embryonic stem cells, mesenchymal stem cells, immature dendritic cells, and G0/G1-phase cells, although the regulatory mechanisms and biological functions have not been elucidated in many cases (Ferreira-Martins et al., 2009; Kapur et al., 2007; Vukcevic et al., 2010). $[Ca^{2+}]_i$ oscillations, one of the major forms of calcium signaling, can promote the expression of specific genes, and this is related to the amplitude and duration of calcium transients, possibly by keeping transcription factors in the nucleus at high enough levels to bind enhancer sites and initiate transcription (Dolmetsch et al., 1997; Dolmetsch et al., 1998; Vukcevic et al., 2010). Here, we observed that spontaneous $[Ca^{2+}]_i$ oscillations were present in HCC TICs and were controlled by calcium influx. Because many TIC properties, such as self-renewal, tumorigenicity, and survival, were affected by 1B50-1 treatment and knockdown of $\alpha2\delta1$ and because these treatments resulted in changes in gene expression and a strong decrease in the amplitude of $[Ca^{2+}]_i$ oscillations, we propose that $\alpha2\delta1$ is involved in "amplitude-encoding" signals that maintain the properties of HCC TICs and that inhibition of this signaling could serve as a therapeutic strategy for HCC.

EXPERIMENTAL PROCEDURES

Cell Lines and Clinical Samples

The HCC cell lines Hep-11, Hep-12, HuH7, SMMC-7721, and HepG2 were cultured in RPMI 1640 medium supplemented with 10% fetal bovine serum,

(C) $[Ca^{2+}]_i$ levels in Hep-11 cells after $\alpha2\delta1$ overexpression measured by flow cytometry.
(D) $[Ca^{2+}]_i$ levels in Hep-12 cells following $\alpha2\delta1$ knockdown measured by confocal microscopy.
(E–G) Representative recordings of the fluorescence of individual cells plotted as a function of time showing the change of $[Ca^{2+}]_i$ in the majority of Hep-11 (E) and Hep-12 cells (F). A representative type of $[Ca^{2+}]_i$ oscillation for a minor Hep-11 population was shown in (G).
(H) A representative recording of $[Ca^{2+}]_i$ change with time in Hep-12 cells treated with 1B50-1 at 10 μg/ml for 24 hr.
(I) The frequency of $[Ca^{2+}]_i$ oscillations in indicated cells treated with IgG or 1B50-1 at 10 μg/ml for 24 hr.
(J) The effect of 1B50-1 treatment (10 μg/ml for 24 hr) on the amplitude of $[Ca^{2+}]_i$ oscillations in Hep-12 cells.
(K and L) $[Ca^{2+}]_i$ oscillation frequency (K) and amplitudes (L) in Hep-12 cells after $\alpha2\delta1$ stable knockdown.
(M) The effects of specific calcium channel blockers on spheroid formation were tested using FACS-purified 1B50-1^+ cells from indicated sources or $\alpha2\delta1$-overexpressing Hep-11 cells (100 cells per well plated, n = 6).
(N) qRT-PCR analysis of the mRNAs encoding some $\alpha1$ calcium channel subunits in indicated cells. The fold difference of Hep-12, Hep-11/$\alpha2\delta1$, and 1B50-1^+ subsets was calculated over the level of each gene in Hep-11, Hep-11/Vector, and 1B50-1^- cells, respectively. Error bars in all panels indicate SD. The data in (I) through (L) are the mean of 40 cells for each group of four independent experiments.
*, #, and @, Student's t test; $^{\#}p < 0.05$, and $^{@}p > 0.05$ versus 0.1% DMSO.
See also Figure S5.

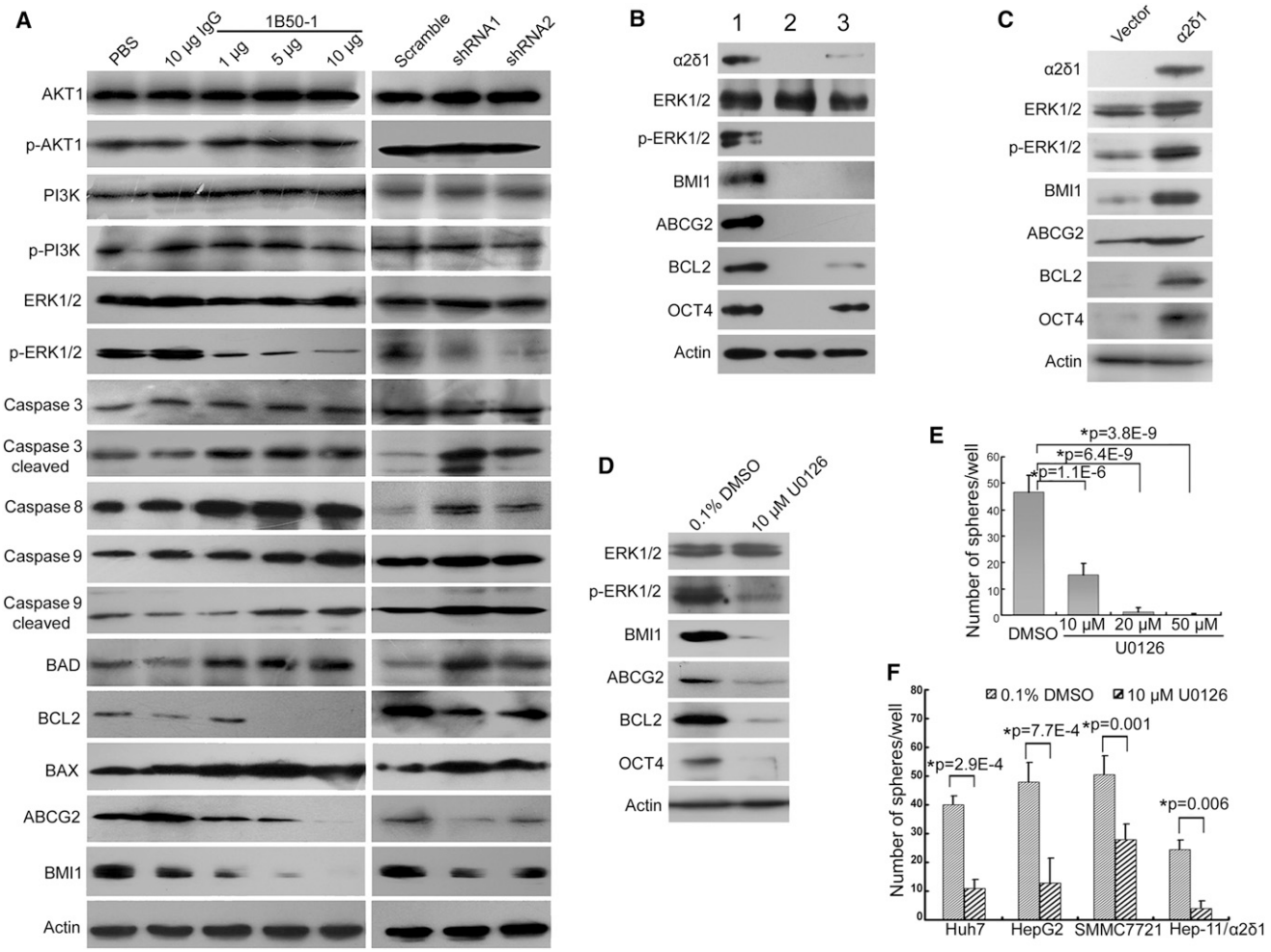

Figure 7. Molecular Mechanisms Underlying the Effects of α2δ1 Blocking

(A) Western blot analysis using lysates of Hep-12 cells treated with IgG or 1B50-1 at indicated doses (per ml) for 48 hr or stable pools infected with lentivirus harboring scramble or shRNA1 or shRNA2 targeting α2δ1.

(B) Western blot analysis using lysates of 1B50-1$^+$ (lane 1), 1B50-1$^-$ (lane 2), and 1B50-1$^+$ cells treated with 10 μg/ml 1B50-1 for 48 hr (lane 3). 1B50-1 fractions were sorted from Case-4 HCC-derived cells.

(C) Western blot analysis to detect the change of representative molecules associated with HCC TICs in Hep-11 cells after α2δ1 (isoform 5) overexpression.

(D) Western blot results show the expression of HCC TIC-related molecules in Hep-12 cells treated with U0126 for 48 hr.

(E) The sphere-forming ability of Hep-12 cells treated with an ERK1/2 inhibitor, U0126.

(F) The effect of U0126 on the sphere-forming ability of sorted 1B50-1$^+$ cells from indicated sources and α2δ1-overexpressing Hep-11 cells. One hundred cells per well were plated (n = 6). All error bars indicate SD. *Student's t test.

100 U/ml penicillin, and 100 μg/ml streptomycin (Invitrogen, Grand Island, NY, USA) in a humidified atmosphere of 5% CO_2 at 37°C.

Primary HCC specimens and matched adjacent normal tissues were collected and snap-frozen into liquid nitrogen from patients who received a hepatectomy with written informed consent. Some fresh HCC tissues were mechanically minced and collagenase IV digested, followed by FACS or primary culture in RPMI 1640 medium containing 10% fetal bovine serum and expansion after removal of fibroblasts. The PDX models were established using mechanically minced fresh HCC specimens. Acquisition and use of these tissues were approved by the Ethics Committee of Peking University Cancer Hospital.

Antibody Production

Subtractive immunization was used to generate antibodies recognizing the epitopes specifically enriched in Hep-12 cells. In brief, mice were immunized with Hep-11 cells, administered 200 mg/kg cyclophosphamide (Sigma-Aldrich, St. Louis, MO, USA), and boosted three times with Hep-12 cells. Fusion, hybridoma screening, antibody production, and purification were performed using standard protocols.

Cell Labeling and Flow Cytometry Analysis

For flow cytometry analysis or FACS, cells were dispersed, labeled, and analyzed as previously described (Xu et al., 2010). 1B50-1 was directly labeled with PE-Cy5 or fluorescein using the respective Lightning conjugation kits following the vendor's protocol (Innova Biosciences Ltd., Cambridge, UK).

Tumorigenicity Assay in NOD/SCID Mice

For the tumorigenicity assay, various numbers of FACS-purified cells were suspended in 50 μl of a 1:1 mix of plain RPMI 1640 and Matrigel (BD Biosciences, Bedford, MA, USA) and transplanted s.c. into the armpit of 4- to 6-week-old NOD/SCID mice (Vitalriver, Beijing, China). Tumor formation was monitored weekly.

To test the therapeutic effect of 1B50-1, cells were s.c. injected into the back of 4- to 6-week-old NOD/SCID mice (2×10^6 cells per mouse). When all the tumors were visible, mice with comparably sized tumors were randomly separated into control and treatment groups and injected i.p. with PBS, nonrelated IgG, 1B50-1, or DXR. The tumor volume was determined using the formula $V = L \times W^2 \times 0.5$, where L and W represent the largest and the smallest diameters, respectively.

All animal experiments were performed in accordance with the National Institutes of Health Guide for the Care and Use of Laboratory Animals with protocols approved by the Animal Care and Use Committee at Peking University Cancer Hospital.

Immunohistochemistry Staining

Frozen tissues were sectioned with a cryostat and fixed with methanol for 30 s. After blocking with 5% nonfat milk in PBS, slides were incubated with 1B50-1 mAb alone or combined with a polyclonal antibody against α2δ1 (Catalog #HPA008213, Sigma, St. Louis, MO, USA) at 4°C overnight, followed by reaction with fluorescein isothiocyanate (FITC)-goat antimouse IgG or both FITC-goat antimouse IgG and rhodamine-goat antirabbit IgG. Nuclei were stained with 4,6-diamidino-2-phenylindole dihydrochloride (DAPI; Polysciences, Warrington, PA, USA) at 0.5 μg/ml. Specimens were mounted in 90% glycerol/PBS containing 2.5% 1, 4-diazabicyclo(2,2,2)octane. Slides were examined with a Leica SP5 confocal microscope (Leica, Wetzlar, Germany).

Sphere Formation Assay

To assay sphere formation efficiency, cells were plated in Ultra Low Attachment 96-well plates (Corning Incorporated Life Sciences, Acton, MA, USA) and cultured in Dulbecco's modified Eagle's medium/F12 (Invitrogen) supplemented with B27 (Invitrogen), 20 ng/ml epidermal growth factor, 20 ng/ml basic fibroblast growth factor (Peprotech), 10 ng/ml hepatocyte growth factor (Peprotech, Rocky Hill, NJ, USA), and 1% methylcellulose (Sigma). Cells were incubated in a CO_2 incubator for 2–3 weeks, and spheres were counted under a stereomicroscope (Olympus, Tokyo, Japan).

Intracellular Calcium Measurement

For the confocal laser scanning microscope method, cells were rinsed twice with warmed Tyrode's solution (140 mM NaCl, 5.0 mM KCl, 1.0 mM $MgCl_2$, 5.5 mM glucose, 10 mM HEPES, 1.8 mM $CaCl_2$, pH 7.2) and labeled with Fluo-4/AM in Tyrode's solution for 15 min at room temperature (RT). After washing, fluorescence was measured at RT using a Zeiss confocal imaging system with a 40× water immersion lens (Carl Zeiss, Jena, Germany). A total of 500 images for each field were captured at intervals of 1.56 s, and the fluorescence was quantified over all the cells in three to six random fields using ImageJ software (http://rsb.info.nih.gov/ij/). The change in $[Ca^{2+}]_i$ was expressed as $\Delta F = (F - F0)/F0$, where F = fluorescence intensity and F0 = resting fluorescence.

For flow cytometry measurement of $[Ca^{2+}]_i$ level, trypsin-digested cells were loaded with Fluo-4/AM as described earlier and analyzed with a flow cytometer.

Statistical Analysis

Using the SPSS 13.0 software, the significance of differences was determined with a double-sided Student's t test or a χ^2 test unless otherwise specified. Tumorigenic cell frequency was calculated based on extreme limiting dilution analysis using the webtool at http://bioinf.wehi.edu.au/software/elda/ (Hu and Smyth, 2009). $p \leq 0.05$ was considered statistically significant.

SUPPLEMENTAL INFORMATION

Supplemental Information includes five figures, one table, and Supplemental Experimental Procedures and can be found with this article online at http://dx.doi.org/10.1016/j.ccr.2013.02.025.

ACKNOWLEDGMENTS

Thanks are given to Professor Cheng Qian for providing the Huh7 cell line and to the FACS Core Facility of Peking University Cancer Hospital for performing FACS assays. This work was supported by the National Basic Research Program of China (the "973" Program, No. 2010CB529402), National Natural Science Foundation of China (grant numbers 81071733 and 31221002), the "863" Project (2007AA02Z133), Beijing NSF (5122012), and Beijing Outstanding Talents Training Funds in Health Sciences (grant No. 2011-2-24). Y.C. is an employee of Genzyme, a Sanofi Company.

Received: September 5, 2012
Revised: December 12, 2012
Accepted: February 27, 2013
Published: April 15, 2013

REFERENCES

Alison, M.R., Lim, S.M., and Nicholson, L.J. (2011). Cancer stem cells: problems for therapy? J. Pathol. *223*, 147–161.

Brooks, P.C., Lin, J.M., French, D.L., and Quigley, J.P. (1993). Subtractive immunization yields monoclonal antibodies that specifically inhibit metastasis. J. Cell Biol. *122*, 1351–1359.

Chiba, T., Kita, K., Zheng, Y.-W., Yokosuka, O., Saisho, H., Iwama, A., Nakauchi, H., and Taniguchi, H. (2006). Side population purified from hepatocellular carcinoma cells harbors cancer stem cell-like properties. Hepatology *44*, 240–251.

Chiba, T., Miyagi, S., Saraya, A., Aoki, R., Seki, A., Morita, Y., Yonemitsu, Y., Yokosuka, O., Taniguchi, H., Nakauchi, H., and Iwama, A. (2008). The polycomb gene product BMI1 contributes to the maintenance of tumor-initiating side population cells in hepatocellular carcinoma. Cancer Res. *68*, 7742–7749.

Clarke, M.F., Dick, J.E., Dirks, P.B., Eaves, C.J., Jamieson, C.H., Jones, D.L., Visvader, J., Weissman, I.L., and Wahl, G.M. (2006). Cancer stem cells—perspectives on current status and future directions: AACR Workshop on cancer stem cells. Cancer Res. *66*, 9339–9344.

Darwiche, H., and Petersen, B.E. (2010). Biology of the adult hepatic progenitor cell: "ghosts in the machine". Prog. Mol. Biol. Transl. Sci. *97*, 229–249.

De Jongh, K.S., Warner, C., and Catterall, W.A. (1990). Subunits of purified calcium channels. Alpha 2 and delta are encoded by the same gene. J. Biol. Chem. *265*, 14738–14741.

Deonarain, M.P., Kousparou, C.A., and Epenetos, A.A. (2009). Antibodies targeting cancer stem cells: a new paradigm in immunotherapy? MAbs *1*, 12–25.

Dolmetsch, R.E., Lewis, R.S., Goodnow, C.C., and Healy, J.I. (1997). Differential activation of transcription factors induced by Ca2+ response amplitude and duration. Nature *386*, 855–858.

Dolmetsch, R.E., Xu, K., and Lewis, R.S. (1998). Calcium oscillations increase the efficiency and specificity of gene expression. Nature *392*, 933–936.

Dolmetsch, R.E., Pajvani, U., Fife, K., Spotts, J.M., and Greenberg, M.E. (2001). Signaling to the nucleus by an L-type calcium channel-calmodulin complex through the MAP kinase pathway. Science *294*, 333–339.

Eroglu, C., Allen, N.J., Susman, M.W., O'Rourke, N.A., Park, C.Y., Ozkan, E., Chakraborty, C., Mulinyawe, S.B., Annis, D.S., Huberman, A.D., et al. (2009). Gabapentin receptor alpha2delta-1 is a neuronal thrombospondin receptor responsible for excitatory CNS synaptogenesis. Cell *139*, 380–392.

Ferreira-Martins, J., Rondon-Clavo, C., Tugal, D., Korn, J.A., Rizzi, R., Padin-Iruegas, M.E., Ottolenghi, S., De Angelis, A., Urbanek, K., Ide-Iwata, N., et al. (2009). Spontaneous calcium oscillations regulate human cardiac progenitor cell growth. Circ. Res. *105*, 764–774.

Haraguchi, N., Ishii, H., Mimori, K., Tanaka, F., Ohkuma, M., Kim, H.M., Akita, H., Takiuchi, D., Hatano, H., Nagano, H., et al. (2010). CD13 is a therapeutic target in human liver cancer stem cells. J. Clin. Invest. *120*, 3326–3339.

Hoey, T., Yen, W.-C., Axelrod, F., Basi, J., Donigian, L., Dylla, S., Fitch-Bruhns, M., Lazetic, S., Park, I.-K., Sato, A., et al. (2009). DLL4 blockade inhibits tumor growth and reduces tumor-initiating cell frequency. Cell Stem Cell *5*, 168–177.

Hu, Y., and Smyth, G.K. (2009). ELDA: Extreme limiting dilution analysis for comparing depleted and enriched populations in stem cell and other assays. J. Immunol. Methods *347*, 70–78.

Hung, R.J., McKay, J.D., Gaborieau, V., Boffetta, P., Hashibe, M., Zaridze, D., Mukeria, A., Szeszenia-Dabrowska, N., Lissowska, J., Rudnai, P., et al. (2008).

A susceptibility locus for lung cancer maps to nicotinic acetylcholine receptor subunit genes on 15q25. Nature *452*, 633–637.

Jin, L., Lee, E.M., Ramshaw, H.S., Busfield, S.J., Peoppl, A.G., Wilkinson, L., Guthridge, M.A., Thomas, D., Barry, E.F., Boyd, A., et al. (2009). Monoclonal antibody-mediated targeting of CD123, IL-3 receptor alpha chain, eliminates human acute myeloid leukemic stem cells. Cell Stem Cell *5*, 31–42.

Kapur, N., Mignery, G.A., and Banach, K. (2007). Cell cycle-dependent calcium oscillations in mouse embryonic stem cells. Am. J. Physiol. Cell Physiol. *292*, C1510–C1518.

Lee, C.-H., Huang, C.-S., Chen, C.-S., Tu, S.-H., Wang, Y.-J., Chang, Y.-J., Tam, K.-W., Wei, P.-L., Cheng, T.-C., Chu, J.-S., et al. (2010). Overexpression and activation of the α9-nicotinic receptor during tumorigenesis in human breast epithelial cells. J. Natl. Cancer Inst. *102*, 1322–1335.

Lee, T.K., Castilho, A., Cheung, V.C., Tang, K.H., Ma, S., and Ng, I.O. (2011). CD24+ Liver Tumor-Initiating Cells Drive Self-Renewal and Tumor Initiation through STAT3-Mediated NANOG Regulation. Cell Stem Cell *9*, 50–63.

Llovet, J.M., and Bruix, J. (2008). Molecular targeted therapies in hepatocellular carcinoma. Hepatology *48*, 1312–1327.

Ma, S., Tang, K.H., Chan, Y.P., Lee, T.K., Kwan, P.S., Castilho, A., Ng, I., Man, K., Wong, N., To, K.F., et al. (2010). miR-130b Promotes CD133(+) liver tumor-initiating cell growth and self-renewal via tumor protein 53-induced nuclear protein 1. Cell Stem Cell *7*, 694–707.

MacLeod, R.J., Hayes, M., and Pacheco, I. (2007). Wnt5a secretion stimulated by the extracellular calcium-sensing receptor inhibits defective Wnt signaling in colon cancer cells. Am. J. Physiol. Gastrointest. Liver Physiol. *293*, G403–G411.

Mishra, L., Banker, T., Murray, J., Byers, S., Thenappan, A., He, A.R., Shetty, K., Johnson, L., and Reddy, E.P. (2009). Liver stem cells and hepatocellular carcinoma. Hepatology *49*, 318–329.

Rappa, G., Fodstad, O., and Lorico, A. (2008). The stem cell-associated antigen CD133 (Prominin-1) is a molecular therapeutic target for metastatic melanoma. Stem Cells *26*, 3008–3017.

Rasmussen, N., and Ditzel, H.J. (2009). Scanning the cell surface proteome of cancer cells and identification of metastasis-associated proteins using a subtractive immunization strategy. J. Proteome Res. *8*, 5048–5059.

Rosen, J.M., and Jordan, C.T. (2009). The increasing complexity of the cancer stem cell paradigm. Science *324*, 1670–1673.

Sell, S., and Leffert, H.L. (2008). Liver cancer stem cells. J. Clin. Oncol. *26*, 2800–2805.

Shackleton, M., Quintana, E., Fearon, E.R., and Morrison, S.J. (2009). Heterogeneity in cancer: cancer stem cells versus clonal evolution. Cell *138*, 822–829.

Todaro, M., Alea, M.P., Di Stefano, A.B., Cammareri, P., Vermeulen, L., Iovino, F., Tripodo, C., Russo, A., Gulotta, G., Medema, J.P., and Stassi, G. (2007). Colon cancer stem cells dictate tumor growth and resist cell death by production of interleukin-4. Cell Stem Cell *1*, 389–402.

Visvader, J.E. (2011). Cells of origin in cancer. Nature *469*, 314–322.

Visvader, J.E., and Lindeman, G.J. (2012). Cancer stem cells: current status and evolving complexities. Cell Stem Cell *10*, 717–728.

Vukcevic, M., Zorzato, F., Spagnoli, G., and Treves, S. (2010). Frequent calcium oscillations lead to NFAT activation in human immature dendritic cells. J. Biol. Chem. *285*, 16003–16011.

Xu, X.L., Xing, B.C., Han, H.B., Zhao, W., Hu, M.H., Xu, Z.L., Li, J.Y., Xie, Y., Gu, J., Wang, Y., and Zhang, Z.Q. (2010). The properties of tumor-initiating cells from a hepatocellular carcinoma patient's primary and recurrent tumor. Carcinogenesis *31*, 167–174.

Yamashita, T., Ji, J., Budhu, A., Forgues, M., Yang, W., Wang, H.Y., Jia, H., Ye, Q., Qin, L.X., Wauthier, E., et al. (2009). EpCAM-positive hepatocellular carcinoma cells are tumor-initiating cells with stem/progenitor cell features. Gastroenterology *136*, 1012–1024.

Yovchev, M.I., Grozdanov, P.N., Joseph, B., Gupta, S., and Dabeva, M.D. (2007). Novel hepatic progenitor cell surface markers in the adult rat liver. Hepatology *45*, 139–149.

Zhang, M., Atkinson, R.L., and Rosen, J.M. (2010). Selective targeting of radiation-resistant tumor-initiating cells. Proc. Natl. Acad. Sci. USA *107*, 3522–3527.

Cancer Cell
Article

A Human ICAM-1 Antibody Isolated by a Function-First Approach Has Potent Macrophage-Dependent Antimyeloma Activity In Vivo

Niina Veitonmäki,[1,5,6] Markus Hansson,[2,5] Fenghuang Zhan,[3] Annika Sundberg,[1] Tobias Löfstedt,[1] Anne Ljungars,[1] Zhan-Chun Li,[1] Titti Martinsson-Niskanen,[1] Ming Zeng,[4] Ye Yang,[3] Lena Danielsson,[1] Mathilda Kovacek,[1] Andrea Lundqvist,[1] Linda Mårtensson,[1] Ingrid Teige,[1] Guido Tricot,[3] and Björn Frendéus[1,*]

[1]BioInvent International, Sölvegatan 41, 22370 Lund, Sweden
[2]Department of Hematology, BMC 13, Skåne University Hospital, Lund University, 221 84 Lund, Sweden
[3]Division of Hematology, Oncology, and Blood and Marrow Transplantation, Department of Internal Medicine, University of Iowa, Iowa City, IA 52242, USA
[4]School of Public Health, Central South University, 110 Xiangya Road, Changsha, Hunan 410078, PR China
[5]These authors contributed equally to this work
[6]Present address: Alligator Bioscience, 223 81 Lund, Sweden
*Correspondence: bjorn.frendeus@bioinvent.com
http://dx.doi.org/10.1016/j.ccr.2013.02.026

SUMMARY

We isolated a tumor B-cell-targeting antibody, BI-505, from a highly diversified human phage-antibody library, using a pioneering "function-first" approach involving screening for (1) specificity for a tumor B cell surface receptor, (2) induction of tumor programmed cell death, and (3) enhanced in vivo antitumor activity compared to currently used treatments. BI-505 bound to intercellular adhesion molecule-1, identifying a previously unrecognized role for this receptor as a therapeutic target in cancer. The BI-505 epitope was strongly expressed on the surface of multiple myeloma cells from both newly diagnosed and relapsed patients. BI-505 had potent macrophage-dependent antimyeloma activity and conferred enhanced survival compared to currently used treatments in advanced experimental models of multiple myeloma.

INTRODUCTION

Targeted immunotherapy plays an increasingly important role in the treatment of cancer (Weiner et al., 2010). Still, antibodies with antitumor activity have yet to be generated for several types of cancer, and a significant proportion of patients who initially respond to the currently available therapies develop resistance (Smith, 2003). The search for antitumor antibodies is thus critical for the further development of targeted immunotherapy.

A common first step of conventional antibody discovery approaches is to isolate antibodies with specificity for a predefined target structure, which may be previously uncharacterized or well validated with respect to cancer therapy. Therapeutic efficacy is not, however, easily predicted from antibody target specificity; antibodies to the same target receptor may vary greatly in therapeutic efficacy independent of their binding affinity (Beers et al., 2008; Cragg and Glennie, 2004), and antibodies against alternative molecular targets may show promising, and sometimes unexpected, therapeutic potential (Beck et al., 2010; Cheson and Leonard, 2008). It is therefore important to use a "function-first," rather than a target specificity-based, approach to therapeutic antibody discovery.

We have developed an approach that allows screening of large numbers of antibodies for useful antitumor activity without prior identification of the target receptors (Fransson et al., 2006). This high-throughput, function-first approach allows rapid identification of candidates that display key properties for an antitumor antibody, e.g., specificity for differentially expressed

Significance

Antibody therapy plays a growing role in the treatment of cancer. Antibodies may exert their therapeutic function by targeting ligand-receptor signaling pathways and/or by triggering of antibody-unique effector functions. Here, we describe potent in vivo antimyeloma activity of an antibody isolated by target-unbiased functional screening for tumor cell death. Mechanism-of-action studies demonstrated that the antibody induced apoptosis in target tumor cells and activated macrophage-dependent host antitumor immunity in a manner that would not have been predicted from currently available information on the receptor targeted by the antibody. Our results help illustrate how functional screening may complement predefined target approaches to broaden therapeutic target space by discovering functions of known targets.

tumor cell surface receptors, significant ability to confer programmed cell death (PCD) in tumors, and significant antitumor activity in vivo compared to currently used treatments.

When applied to find antibodies with improved antitumor activity against B cell malignancies, the process identified several tumor PCD-inducing antibodies—specific for different tumor B-cell-associated receptors—that showed better antitumor activity compared to rituximab, a CD20-specific monoclonal antibody used for treatment of CD20-expressing B cell cancers (Fransson et al., 2006).

Interestingly, among antibodies identified were several specific for intercellular adhesion molecule 1 (ICAM-1), a receptor not previously associated with tumor PCD. ICAM-1 is highly expressed in several human malignancies and is believed to be involved in their pathogenesis (Aalinkeel et al., 2004; Hideshima et al., 2007; Huang et al., 1995; Johnson et al., 1988; Schmidmaier et al., 2006). Notably, ICAM-1 was recently reported to be overexpressed and associated with advanced disease and poor survival in multiple myeloma (MM) (Sampaio et al., 2009; Schmidmaier et al., 2006). Further, evidence suggests that ICAM-1 is upregulated and causally related to MM patient development of resistance to chemotherapy (Sampaio et al., 2009; Schmidmaier et al., 2006; Zheng et al., 2009). ICAM-1, by binding to integrin β2 receptors and muc-1, is involved in cell-adhesive events that trigger multiple cell-signaling pathways promoting MM cell proliferation, migration, resistance to apoptosis, and development of cell adhesion molecule-induced drug resistance (Hideshima et al., 2007; Schmidmaier et al., 2004; Zheng et al., 2009). There is no curative treatment for MM, and the currently available therapy is associated with significant toxicity and development of drug resistance (Kyle and Rajkumar, 2004). MM plasma cells typically do not express the B cell antigen CD20 or show low and heterogeneous CD20 expression, making CD20-targeted therapies ineffective in this disease (Kapoor et al., 2008; Richardson et al., 2011).

Here, we characterize MM plasma cells for expression of the ICAM-1 epitope targeted by our function-first-isolated antibody BI-505, and we investigate BI-505's therapeutic activity and mechanism-of-action in well-established experimental models of MM.

RESULTS

A Human ICAM-1 Antibody Isolated by a Function-First Approach Has Significant Antitumor Activity against B Cell Cancer Xenografts

We isolated multiple antibodies inducing programmed cell death (PCD) in B cell lymphomas, targeting different tumor-cell-associated surface receptors, by means of a sequential process involving differential biopanning and high-throughput PCD screening of antibodies from the n-CoDeR (Söderlind et al., 2000) human antibody library (Figures S1A–S1C available online). The high specificity for ICAM-1 of one of these antibodies, BI-505 (appears as B11 in Fransson et al., 2006), is shown in Figure S1C. BI-505 dose-dependently induced PCD in ICAM-1-expressing Ramos, Raji, and Daudi lymphoma cells (Fransson et al., 2006; Figure 2D).

In order to further investigate the therapeutic potential of PCD-inducing ICAM-1 antibodies, we screened BI-505 for in vivo antitumor activity in tumor models comprising SCID mice transplanted with the lymphoblastic cell lines ARH-77 or Daudi. Both cell lines express the CD20 antigen, making it possible to compare antitumor efficacy and potency of antibodies identified here with those of the clinically validated CD20-specific monoclonal antibody rituximab.

Subcutaneous injection of ARH-77 cells resulted in rapid establishment and growth in SCID mice, with tumors being readily palpable between 12 and 14 days. Twice-weekly injections of 20 mg/kg of BI-505 commencing 1 day after tumor cell inoculation prevented tumor growth in 9 out of 10 injected mice (Figure 1A). Rituximab conferred significant antitumor activity at the same dose but was less efficacious than BI-505 (Figure 1A). Furthermore, BI-505 administered at a 100 times lower dose (0.2 mg/kg) was equally efficacious compared to 20 mg/kg rituximab in conferring survival (Figure 1B). The high efficacy and potency of BI-505 was confirmed in mice carrying ARH-77 tumors established for 12 days before the start of antibody treatment (Figures 1C and 1D). In this model, rituximab failed to reduce tumor growth or promote animal survival ($p > 0.05$), whereas BI-505 both significantly reduced tumor growth (Figure 1C; $p < 0.05$) and prolonged animal survival (Figure 1D; $p < 0.05$). Thus, in this aggressive model of CD20-positive B cell malignancy, BI-505 was more efficacious and more potent in conferring antitumor activity and survival than rituximab.

We also tested BI-505's antitumor activity against Daudi B cell lymphoma xenografts. Again, BI-505 significantly prevented tumor growth (Figures 1E and 1G; $p < 0.001$) and prolonged survival (Figures 1F and 1H; $p < 0.001$) of tumor-bearing mice when administered 1 day following tumor cell injection (Figures 1E and 1F) or when established tumors were treated (Figures 1G and 1H), this time with equal efficacy compared to rituximab (Figures 1E–1H). The overall stronger antitumor activity of BI-505 compared with rituximab was not caused by a higher number of tumor cell epitopes for BI-505 than for rituximab. In contrast, flow cytometric analysis revealed that both ARH-77 (Figure 1I) and Daudi (Figure 1J) cells expressed significantly fewer BI-505 epitopes than rituximab epitopes, and immunohistochemical analysis of tumor tissue harvested from mice treated with BI-505, rituximab, or isotype control antibodies showed that tumors expressed both rituximab and BI-505 epitopes at the completion of experimentation (Figure S1D).

To establish the potency of BI-505 in vivo and the lowest dose achieving maximal antitumor activity, we performed a dose-titration experiment using the SCID/ARH-77 model system. BI-505 showed dose-dependent antitumor activity, which followed a sigmoidal curve, peaking at the 2 mg/kg dose and remaining near maximal at a dose of 0.2 mg/kg (Figures 2A and 2B). Antibody concentrations in mouse sera were determined by ELISA and were plotted as a function of maximal in vivo antitumor activity (Figure 2C). The relationship between BI-505 concentration-dependent in vivo antitumor activity, in vitro antitumor (PCD) activity (Figure 2D), and in vitro receptor occupancy (Figure 2E) was then examined by overlaying generated curves in a single graph (Figure 2F). BI-505 concentration-dependent receptor occupancy correlated nearly perfectly with BI-505 in vitro and in vivo antitumor activity (Figure 2F). This result is consistent with ICAM-1-dependent direct cell cytotoxicity underlying BI-505's antitumor activity.

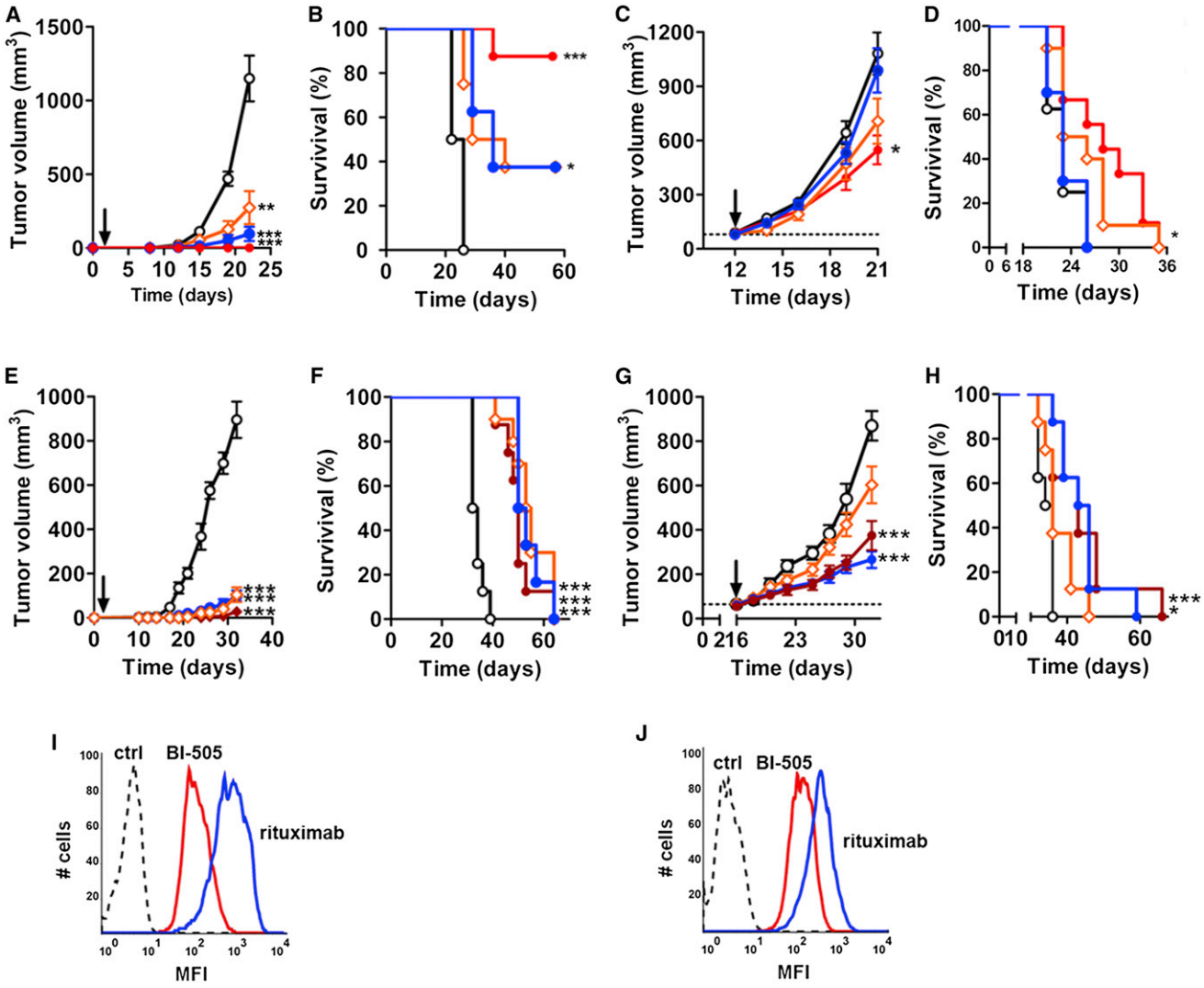

Figure 1. BI-505 Has Significant In Vivo Antitumor Activity against CD20-Expressing Tumors Compared with Rituximab

(A–H) Mean tumor volumes (A, C, E, and G) and survival (B, D, F, and H) of mice xenografted with CD20-expressing ARH-77 (A–D) or Daudi (E–H) cells and treated with BI-505 (bright red line = 20 mg/kg BI-505; maroon line = 2 mg/kg BI-505; and orange line = 0.2 mg/kg BI-505), rituximab (20 mg/kg, blue line), or isotype control (20 mg/kg, black line) antibodies in prophylactic (A, B, E, and F) or established (C, D, G, and H) tumor models. There were eight to ten animals per treatment/dose group. Tumor cells were injected day 0, and antibody treatment started as indicated in the graphs (black arrow). *$p < 0.05$, **$p < 0.01$, and ***$p < 0.001$. Error bars show ± SD. (I and J) FACS analysis of BI-505 and rituximab epitopes on the surface of ARH-77 (I) and Daudi (J) tumor cells. Antibodies were used at binding saturating concentrations.

See also Figure S1.

We conclude that BI-505 confers potent and direct antitumor activity against different types of B cell cancer.

ICAM-1 and the BI-505 Epitope Are Strongly Expressed in Multiple Myeloma

We next evaluated expression of the BI-505 epitope on bone marrow cells in patients with MM and related diseases (plasmacytoma, plasma cell leukemia, and light-chain amyloidosis) by flow cytometry (Figure 3; Table 1). Myeloma cells were identified using fluorescent antibodies against surface antigens CD38, CD138, CD45, and CD56 (Figure S2A), according to the European Myeloma Network guidelines on multiparametric flow cytometry in MM (Rawstron et al., 2008) and confirming monoclonal MM cells with intracellular staining of λ and κ light chains. All MM patients expressed the BI-505 epitope on most (97% ± 4%, mean ± SD, patient n = 22) myeloma cells (Figure 3; Table 1). The BI-505 epitope was generally very highly expressed on these cells, with a median expression level that was ten times higher than on normal B cells from the same patients. Similar results were obtained with a commercially available anti-ICAM-1 antibody (data not shown). Furthermore, the BI-505 epitope was highly expressed on myeloma cells in a patient in relapse who had received several different lines of therapy (Figure S2B). Thus, ICAM-1 and the BI-505 epitope are strongly expressed on the surface of MM plasma cells.

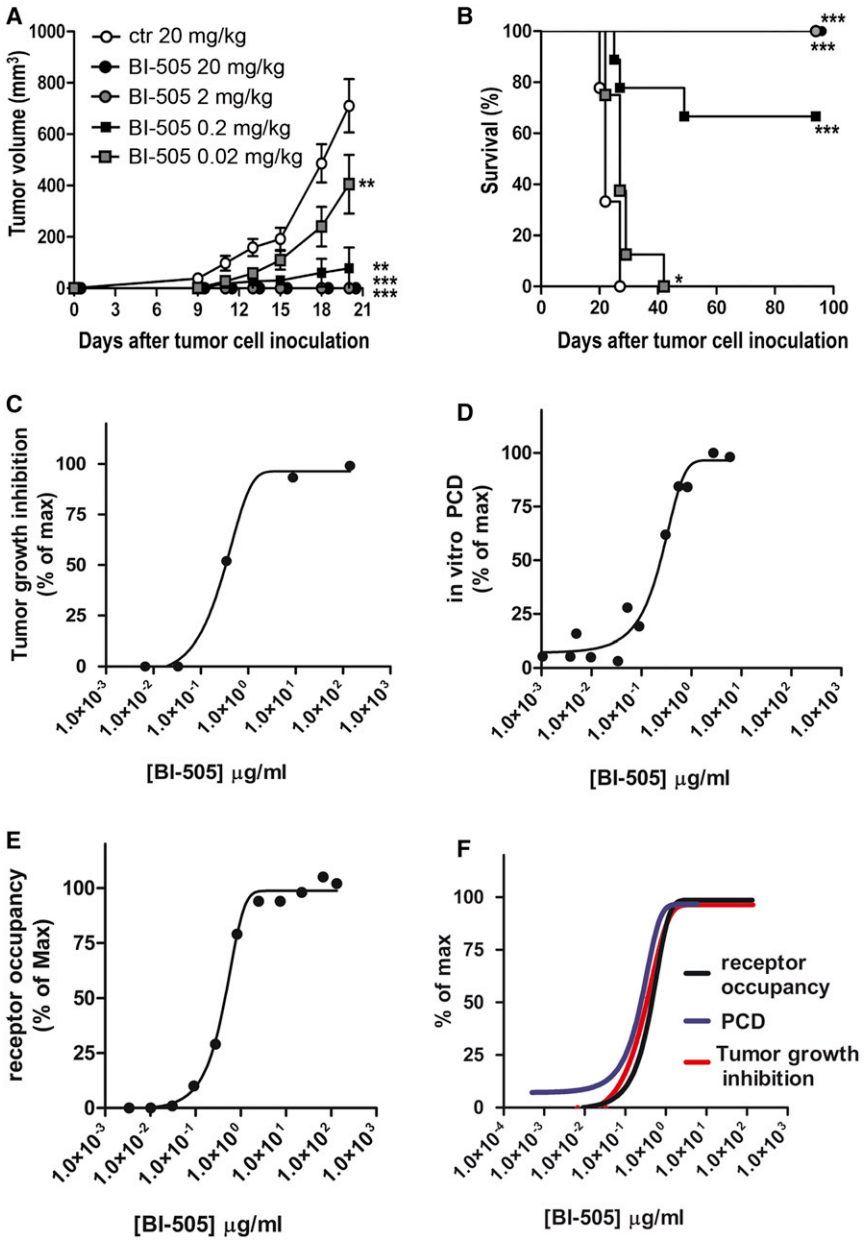

Figure 2. BI-505 Dose-Dependent Antitumor Activity Correlates with ICAM-1 Receptor Occupancy on Tumor Cell Surfaces

(A and B) Mean tumor volumes (A) and mean survival (B) of mice treated with different doses of BI-505 in the ARH-77 tumor model. Error bars show ± SD. *$p < 0.05$, **$p < 0.01$, and ***$p < 0.001$. (C–E) BI-505 concentration-dependent in vivo antitumor activity (C), in vitro antitumor (tumor PCD) activity (D), and receptor occupancy of tumor cell-expressed ICAM-1 (E).

(F) A combined plot of (C)–(E). There were eight to ten animals per treatment group.

BI-505 Has Broad Antimyeloma Activity In Vivo

Because we found high expression of the BI-505 epitope in human MM, we proceeded to screen BI-505 for in vivo antimyeloma activity using SCID/xenograft models comprising four well-characterized MM cell-lines. These cell lines express the myeloma markers CD38 and CD138 but do not express CD20. Twice-weekly dosing with 2 mg/kg of BI-505 starting 1 day after tumor cell injection reduced myeloma tumor growth in mice xenografted with ICAM-1-expressing cell lines EJM, RPMI-8226, and NCI-H929 by 98%, 96%, and 99%, respectively (Figures 4A and 4B). In contrast, BI-505 did not affect tumor growth in mice xenografted with the ICAM-1-negative cell line OPM-2 (Figures 4A and 4B). Taken together, these studies indicated that BI-505 had highly efficacious, broad, and ICAM-1-dependent in vivo antimyeloma activity.

BI-505 Has Potent Antimyeloma Activity in Clinically Relevant Models of Advanced Myeloma

To assess the therapeutic potential of BI-505 for treatment of MM, we next compared the antimyeloma effects of BI-505 to current gold-standard treatment in disseminated experimental models of MM sharing characteristics with human disease. These models resemble the manifestation and progression of human MM disease in many respects, including tumor dissemination and establishment in bone marrow, and the appearance of osteolytic bone lesions and hypercalcemia (Mitsiades et al., 2003; Yaccoby et al., 1998). First, we compared the antimyeloma activity of BI-505 with currently used treatments in an advanced disseminated MM model comprising RPMI-8226 myeloma cells. In this model, therapeutic treatment with 2 mg/kg BI-505 was started 5 days after intravenous grafting of MM cells to allow for homing and establishment of MM cells in bone marrow. BI-505 significantly enhanced survival and delayed disease onset compared to treatment with the comparator drugs bortezomib, lenalidomide, melphalan, or dexamethasone (Figure 5A), all approved and currently used for MM therapy. Importantly, Figure 5A shows the effect of the comparator drugs used at maximally efficacious, and clinically relevant, doses. Higher doses of some of the comparator drugs were shown to be toxic, but not more efficacious, to animals (data not shown).

Primary human MM cells depend on interactions with bone marrow stromal cells to proliferate and survive. The SCID-hu mouse harbors a human microenvironment, where primary patient MM cells proliferate and induce pathology similar to human clinical MM (Yaccoby et al., 1998). MM-cell-derived human immunoglobulin G (IgG) titers were detected (>10 μg/ml) in the serum of SCID-hu mice 4 weeks after implantation of human MM cells to transplanted human bones, at which time treatment with antibodies (2 mg/kg) or bortezomib (1 mg/kg) began. Human IgG titers increased steadily in control-treated SCID-hu

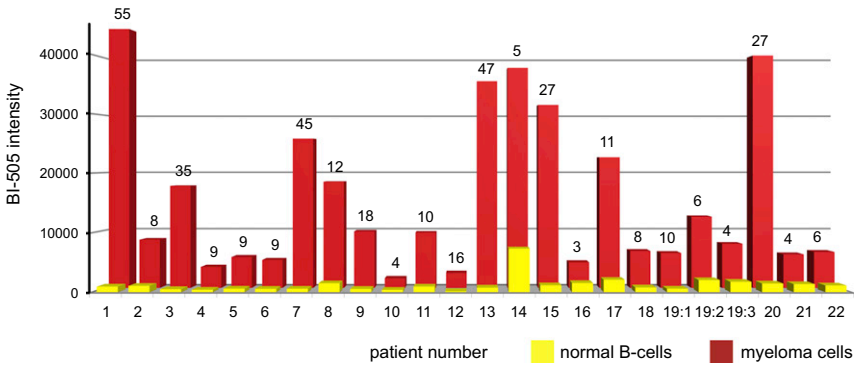

Figure 3. The BI-505 Epitope Is Highly Expressed on the Surface of Primary MM Plasma Cells

FACS analysis of BI-505 epitope expression on the cell surface of patients' MM cells (red bars) versus normal B cells (yellow bars). Numbers on top of bars indicate fold increase of the BI-505 epitope on surface of MM cells compared to normal B cells. Patient numbers correspond to those shown in Table 1.

See also Figure S2.

mice over the course of experimentation to reach maximal concentrations of 40 ± 5 μg/ml just before sacrifice (Figures 5B and S3). In contrast, therapeutic treatment with BI-505 or bortezomib halted or reduced serum human IgG levels to below pretreatment levels ($hIgG_{BI\text{-}505}$ = 91% ± 22%), demonstrating a significant anti-MM effect. Two independent experiments were performed with similar results (Figures 5B and S3), each with MM cells from two different patient donors (n = 4). Immunohistochemical staining for human CD138-expressing cells in harvested human bone implants indicated that BI-505 antimyeloma effects correlated with decreased tumor burden (Figure 5C). BI-505 antimyeloma effects correlated with protection against MM-induced bone pathology as demonstrated by decreased bone remodeling with decreased loss of bone mineral density (Figure 5D). Staining of a limited number of bone sections indicated reduced numbers of bone osteoclasts (Figure 5E) and total infiltrated nucleated cells (Figure 5F) in BI-505- or bortezomib-treated mice compared to control-treated mice.

Thus, in two clinically relevant experimental models BI-505 anti-MM activity was equal to or greater than currently available drugs.

BI-505 Confers Fc-FcγR-Dependent Antitumor Activity through Macrophages

Previous studies have demonstrated PCD-inducing properties of BI-505 in a wide range of tumor B cell lines (Fransson et al., 2006). BI-505 PCD was enhanced by antibody crosslinking in vitro, indicating that in vivo antitumor activity might be enhanced by crosslinking provided by FcγR-expressing cells (Wilson et al., 2011). Given the critical importance of FcγR-mediated antitumor mechanisms for the clinical and in vivo therapeutic activity of clinically validated cancer mAbs (Clynes et al., 2000; Musolino et al., 2008; Weng and Levy, 2003), we addressed the contribution of antibody Fc: host FcγR-dependent mechanisms for BI-505's therapeutic activity. To this end, we engineered BI-505 variants with abolished ($IgG_{1\ N297Q}$, "Fc-mut"), or reduced (BI-505-IgG_4) FcγR-binding compared to wild-type BI-505 IgG_1, and investigated their respective in vivo therapeutic activities. The Fc-switch variants retained affinities for ICAM-1 as evidenced by near identical EC_{50} values for binding to recombinant or cell-surface-expressed ICAM-1 (Figures S4A–S4C). The in vivo antitumor activity of BI-505 Fc-variants (Figure 6A) correlated perfectly with binding to mouse FcγRIV (Figure 6B)—the structural and functional homolog of human FcγRIIIa and a principal murine FcγR conferring antibody-mediated cell cytotoxicity in vivo (Nimmerjahn et al., 2005)—increasing in the order of $IgG_{1\ N297Q} < IgG_4 < IgG_1$. Importantly, mice treated with IgG_1, IgG_4, and $IgG_{1\ N297Q}$ variant antibodies of BI-505 had similar serum antibody titers at the end of experimentation, indicating that the different antibody variants had similar in vivo half-lives and demonstrating that differential antitumor activity did not result from differential pharmacokinetics (Table S1). These findings demonstrated that BI-505 in vivo antitumor activity was Fc: FcγR-dependent.

Fc-FcγR-interactions, in addition to enhancing antibody-induced negative signaling and tumor PCD (Wilson et al., 2011), may involve both innate and adaptive arms of cellular immunity (Alduaij and Illidge, 2011; Park et al., 2010). We used different approaches to assess the role of NK cells and macrophages—two principal cell types capable of conferring FcγR-dependent antitumor effects—for BI-505 therapeutic activity. First, we examined the relative abundance of these cell types in tumor tissue harvested from BI-505 or control-antibody-treated mice. By immunohistochemistry, we found that macrophages ($F4/80^+$ cells) constituted the vast majority of FcγR-expressing cells in BI-505-treated tumors (Figure 6D). In contrast, very few intratumoral NK cells could be detected ($CD49b^+$ $CD31^-$ cells). Furthermore, and interestingly, treatment with BI-505 significantly increased tumor macrophage infiltration but—conversely—decreased tumor NK cell content (Figure 6D). Together, these data suggested that macrophages, but not NK cells, were principal FcγR-expressing cells conferring BI-505 antitumor activity in vivo. To verify this, we depleted macrophages or NK cells, using clodronate liposomes and anti-asialo antibodies, respectively, from SCID mice bearing established RPMI-8226 myeloma tumors and examined the effect on BI-505 antimyeloma activity. A period of 3 weeks of macrophage and NK cell depletion was chosen as readout because this was the longest time period in which neither treatment affected animal well-being. Cell depletion did not per se impact tumor growth over this period of time (Figures S4D and S4E). Figure 6E clearly demonstrates that macrophage depletion completely abolished BI-505 in vivo antitumor activity. Tumors of macrophage depleted BI-505-treated mice had doubled in size compared with tumors from animals receiving BI-505 treatment alone ($V_{BI\text{-}505}$ = 95 ± 39 mm^3, $V_{BI\text{-}505+clodro}$ = 189 ± 94 mm^3, $p < 0.001$) but were similarly sized compared to tumors from control-antibody-treated mice ($V_{ctrl\ IgG}$ = 198 ± 90 mm^3, $p > 0.05$). NK cell depletion, in contrast, had little or no effect on BI-505 antitumor activity. Tumor volumes of NK-cell-depleted

Table 1. Expression of the BI-505 Epitope in a Cohort of 29 Patients with Plasma Cell Disorders

Patient Characteristics										BI-505 Epitope Expression	
Patient Number[a]	Age (year)	Sex[b]	Ig[c]	M- comp (g/l)	Skel. Dest[d] (n)	MM Cells[e] (%)	ISS[f]	T[g] (n)	Diagnosis[h]	Intensity[i]	Positive Cells (%)
1	38	m	IgG	10	0	14	I	0	MM	+++	98
2	46	m	IgG	38	0	34	II	0	MM	+++	97
3	53	f	IgG	14	>10	6	I	0	MM	+++/++	100
4	54	m	–	–	3	22	III	2	nsMM	+++	100
5	59	m	IgG	32	>10	29	I	0	MM	++	100
6	60	f	IgG	4	3	2	II	1	MM	+++	98
7	60	f	IgA	26	1	10	I	0	MM	+++	98
8	61	m	IgG	28	0	23	II	0	MM	+++	100
9	62	m	IgG	69	>10	30	II	0	MM	++	100
10	62	f	IgG	70	>10	80	III	1	MM	+	95
11	68	m	IgA	36	>10	60	I	0	MM	+++	100
12	69	m	–	–	3	50	I	1	nsMM	+++/+	95
13	71	m	IgG	26	0	30	I	0	MM	+++	100
14	72	m	IgG	13	0	29	I	0	MM	+++	100
15	74	m	IgG	20	0	23	I	0	MM	+++	100
16	75	m	IgA	40	0	78	II	0	MM	++	88
17	77	m	IgG	45	0	34	II	0	MM	+++	100
18	79	f	IgG	23	0	16	I	0	MM	+++	100
19:1	79	m	IgG	24	7	50	III	0	MM	+++	93
19:2	79	m	IgG	3	n/a	n/a	–	1	MM	+++	95
19:3	80	m	IgG	3	n/a	16	–	2	MM	+++	91
20	82	m	IgA	29	0	44	III	0	MM	+++	100
21	83	f	IgG	39	0	89	III	0	MM	+++	93
22	84	m	IgA	17	0	38	III	0	MM	+++	86
23	61	m	IgA	7	2	24	–	0	AL	++	97
24	64	f	–	–	n/a	6	–	0	AL	+++	100
25	72	f	–	–	0	1	–	0	LCDD/MM	+++	98
26	61	f	IgA	42	n/a	80	–	4	PCL	+++	76
27	75	m	IgG	18	>10	8	–	4	PCL	+	77
28	52	m	IgG	1	1	5	–	1	PC	+++	93
29	60	f	IgG	4	1	2	–	1	PC	+++	100

n/a, not analyzed.
[a]Corresponds to number found in Figure 3.
[b]m, male; f, female.
[c]Immunoglobulin class of M-component.
[d]Number of skeletal destructions.
[e]Multiple myeloma cells counted as percent of all nucleated cells in bone marrow smears.
[f]International Staging System of MM.
[g]Number of different MM treatment regimens before BI-505 analysis.
[h]MM, multiple myeloma; nsMM, nonsecretory multiple myeloma; AL, amyloid light-chain amyloidosis; LCDD, light-chain deposit disease; PCL, plasma cell leukemia; PC, plasmacytoma.
[i]Measured by FACS on MM cells. Two patients (no. 3 and 12) had two MM cell populations with differential BI-505 expression.

BI-505-treated mice were not significantly different from mice treated with BI-505 only (V_{BI-505} = 95 ± 39 mm^3, $V_{BI-505+asialo}$ = 130 ± 53 mm^3, $p > 0.05$) but were significantly smaller compared to control-antibody-treated animals ($p < 0.01$, Figure 6E). BI-505 also had significant antitumor activity in two different aggressively growing NK-cell-deficient MM mouse models comprising RPMI-8226 or U266 cells grafted to NOD/Shi-*scid*/*IL-2Rγ*$^{-/-}$ mice (Figures 6F and 6G). Taken together, our data identify macrophages, but not NK cells, as critical effector cells conferring BI-505 FcγR-dependent in vivo antitumor activity.

We next investigated BI-505's ability to mediate Fc:FcγR-dependent macrophage phagocytosis (antibody-dependent cell phagocytosis [ADCP]) of human MM cells in vitro. As expected, BI-505 IgG_1 bound to human FcγR (Figure 6C) and

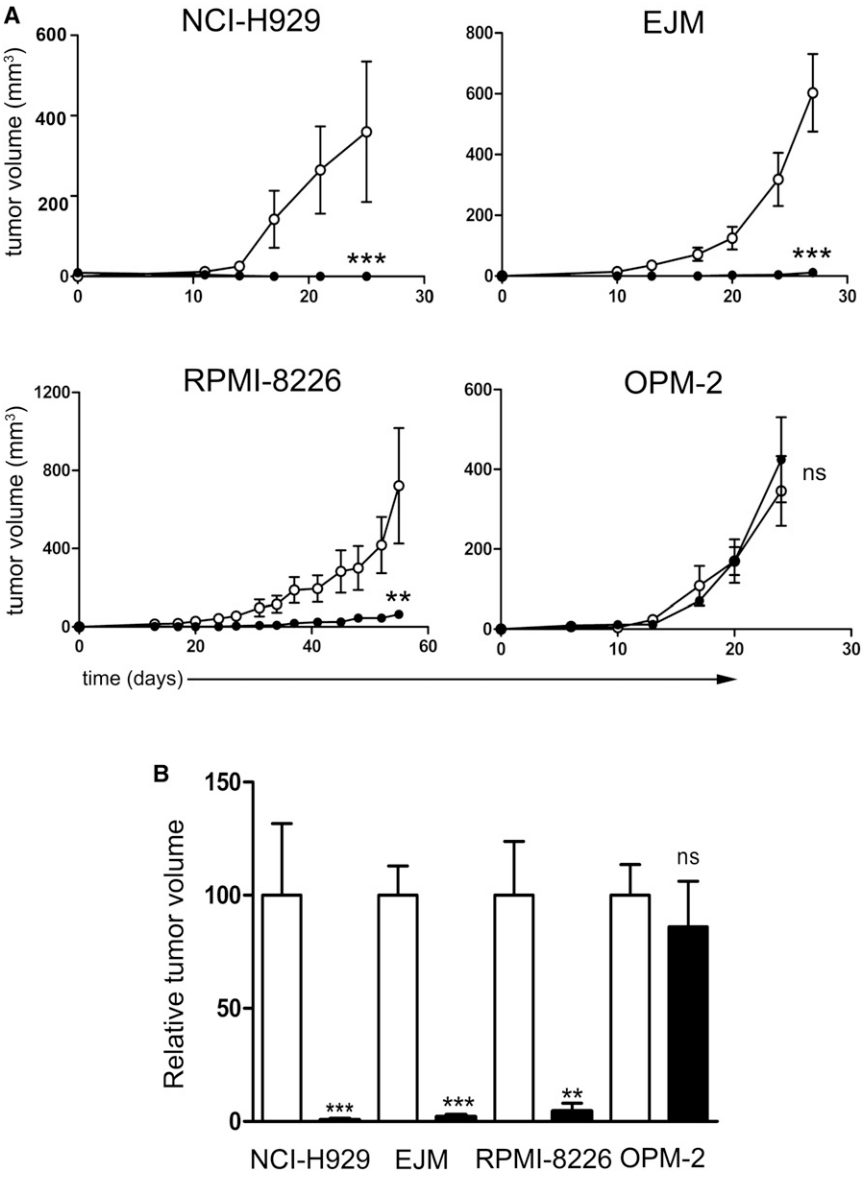

Figure 4. BI-505 Has Broad and ICAM-1-Dependent Anti-MM Activity In Vivo

(A) Tumor volume (mean ± SD) of NCI-H929 (ICAM-1$^+$), EJM (ICAM-1$^+$), RPMI-8226 (ICAM-1$^+$), and OPM-2 (ICAM-1$^-$) MM models after treatment with 2 mg/kg BI-505 (filled circles) or control (open circles) antibody.

(B) Relative tumor volumes following treatment with 2 mg/kg BI-505 (filled bars) or control (open bars) antibody in NCI-H929, EJM, RPMI-8226, and OPM-2 MM models. Graph shows tumor volumes (mean ± SD) relative to the mean tumor volume of control IgG-treated animals. There were eight animals per treatment group.

**p < 0.01, ***p < 0.001; ns, not statistically different.

conferred ADCP of both RPMI-8226 and primary patient's MM cells (Figures 6H and 6I) in the presence of human macrophages. In contrast, FcγR-binding-deficient BI-505 IgG1$_{N297Q}$ did not bind to human FcγR (Figure 6C) and did not confer ADCP of targeted MM cells (Figures 6H–6J). Similarly, preincubation with recombinant-soluble Fc gamma receptor diminished BI-505 IgG$_1$-mediated ADCP (Figure 6J). Therefore, analogous to the in vivo setting, BI-505-mediated ADCP in vitro was Fc: Fc gamma receptor dependent.

We also examined the ability of BI-505 to mediate antibody-dependent cell cytotoxicity (ADCC) against human target tumor cells in the presence of human effector NK cells. BI-505 conferred cytotoxicity in an Fc-dependent manner, although ADCC activity by effector NK cells was less pronounced compared with macrophage-mediated ADCP (data not shown).

Besides Fc:FcγR-dependent antitumor mechanisms, cancer mAb Fc-dependent antitumor activity may result from activation of the complement cascade by complement-dependent cytotoxicity (CDC). We therefore examined the ability of BI-505 to induce CDC in a panel of ICAM-1-expressing tumor cell lines. However, BI-505 did not induce CDC in any of the tumor cell lines monitored (data not shown). In contrast, treatment with the positive control rituximab effectively induced CDC, as has previously been reported (Cragg and Glennie, 2004; Cragg et al., 2003; Manches et al., 2003).

In summary, our data provide strong evidence for Fc:FcgR-dependent antitumor mechanisms, e.g., macrophage-mediated ADCP and FcγR cross-linking-induced antibody tumor PCD underlying BI-505's therapeutic activity.

Safety Profile of the BI-505 Antibody

In addition to exerting significant antitumor activity, a therapeutic cancer antibody must be safe and tolerable for patients. Toxicology studies in relevant animal species may provide important information on drug safety. BI-505 does not, however, cross-react with ICAM-1 from animals that are commonly used for toxicological evaluation (data not shown). Our nonclinical safety assessment therefore focused on evaluating its effects on viability and function of human normal (untransformed) cells expressing ICAM-1.

Based on BI-505's documented ability to confer Fc:FcγR-dependent antitumor activity in malignant B cells, and a proposed general negative role for complement activation with regard to antibody tolerability (Lim et al., 2010; van der Kolk et al., 2001), we examined direct cytotoxic effects (PCD, ADCC, and CDC) of BI-505 in ICAM-1-expressing human peripheral blood B cells and endothelial cells. Whereas peripheral blood B cells and naive B cells show low endogenous expression of the BI-505 epitope (Fransson et al., 2006), human umbilical vascular endothelial cells (HUVECs) and human microvascular endothelial cells (HMVECs) cells showed significant ICAM-1

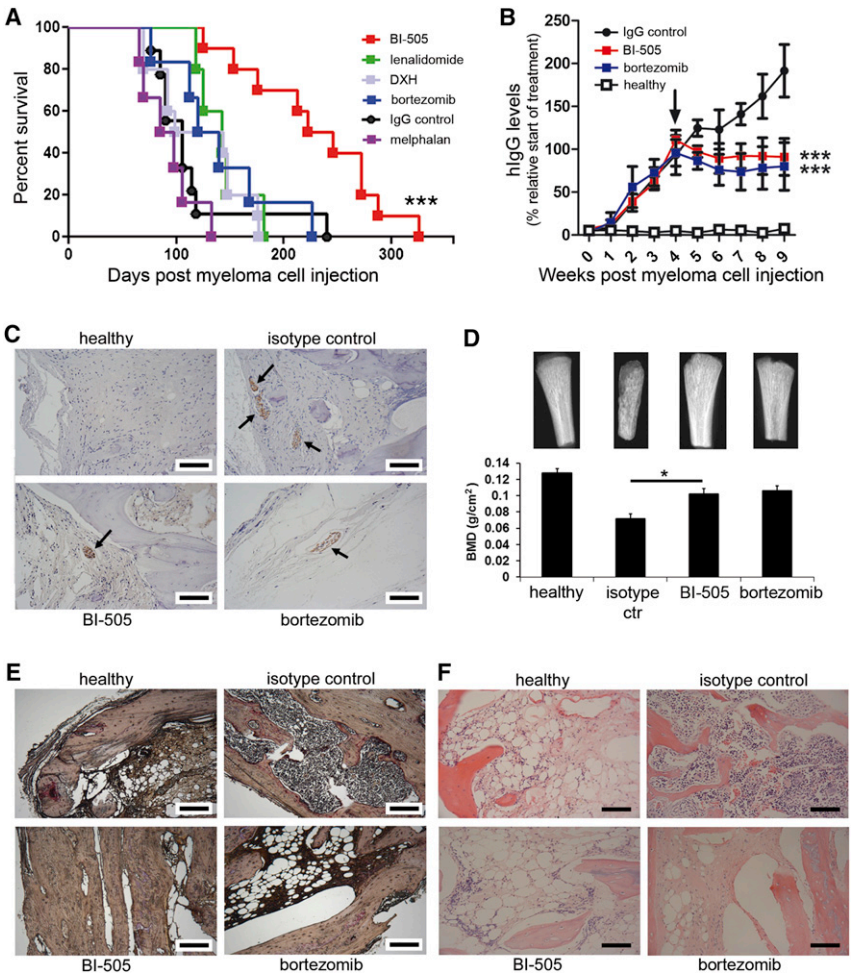

Figure 5. BI-505 Confers Enhanced Survival Compared to Currently Used Treatments in Disseminated Experimental Models of Advanced MM

(A) Animal survival in advanced disseminated RPMI-8226 myeloma model following treatment with control antibody, lenalidomide, bortezomib, dexamethasone (DXH), melphalan, or BI-505. ***$p < 0.001$.

(B) Human immunoglobulin G (hIgG) (mean ± SD) in SCID-hu mice after myeloma cell inoculation and drug treatment. Graph shows pooled data from two independent experiments, each with MM cells obtained from two different patient donors (n = 4). The percentage of hIgG levels compared to start of treatment (arrow) was monitored. ***$p < 0.001$.

(C) Myeloma tumor burden in implanted bones harvested from drug-treated mice. Pictures show representative images of tumor burden as assessed by immunohistochemistry following staining for human CD138-expressing cells. Arrows indicate human CD138-positive myeloma cell regions. Scale bar = 50 μm.

(D) X-radiographic quantification of bone mineral density. Radiographs of implanted human bones receiving drug or control treatment were harvested from mice at end of experimentation (10 weeks postmyeloma cell injection and following 6 weeks of drug treatment). Upper panel shows representative radiographs of bones from healthy mice, control IgG-treated mice, BI-505-treated mice, or bortezomib-treated mice (left to right). Lower panel shows mean ± SD bone mineral density of mice receiving treatment as indicated. *$p < 0.05$.

(E and F) Representative images of trap staining (purple stain) for detection of osteoclasts (E) or hematoxylin and eosin staining for detection of infiltrated nucleated cells (F) performed on healthy and MM cell-injected bones harvested from SCID-hu mice treated as indicated at end of experimentation. Scale bar = 100 μm.

See also Figure S3.

expression, which was further upregulated in response to IFN-γ stimulation as determined by flow cytometric analyses (Figure S5). However, BI-505 did not induce cell death in any of the resting or activated normal ICAM-1-expressing cell types that were examined, regardless of whether or not antibody was crosslinked to mimick Fc:FcγR-crosslinking in vivo (Figures 7A–7C and 7G). In contrast, treatment of endothelial cells with paclitaxel and treatment of B cells with positive control anti-HLA-DR or anti-CD20 antibody induced significant PCD (Figures 7A and 7G).

Cytokine release and T cell proliferation are thought to be common causes of mild and severe adverse reactions to antibody therapy. In order to further investigate any undesirable effects of BI-505 on ICAM-1-expressing immune cells, we therefore assessed putative effects of BI-505 on peripheral blood mononuclear cells (PBMCs) cytokine release and T cell proliferation. In order to maximize the chances of identifying any PBMC-agonistic properties of BI-505, we used two different antibody-coating protocols in which the antibody was hypercrosslinked as previously described (Stebbings et al., 2007). BI-505 immobilized by either protocol induced PCD in Daudi lymphoma cells, demonstrating that biological activity was retained following immobilization (data not shown). BI-505 did not, however, induce PBMC cytokine release and did not induce T cell proliferation by either immobilization protocol or when added in solution in the presence or absence of crosslinking reagent (Figures 7D–7F). In contrast and as expected, incubation of PBMCs with an immobilized positive control anti-CD3 antibody resulted in significant release of IL-1β, IL-2, IL-6, IL-8, TNF-α, and IFN-γ (Figure 7D). Analogous experiments demonstrated that BI-505 added in solution did not induce or enhance cytokine release from resting or lipopolysaccharide prestimulated PBMCs and did not induce T cell proliferation (Figures 7E and 7F).

Taken together therefore, we have found no evidence for undesirable activation or cytotoxicity of BI-505 against ICAM-1-expressing immune cells. Together with limited safety studies in rat, rabbit, and monkey, demonstrating no compound-related off-target toxicity (data not shown), and indicating a long half-life typical of that for a human IgG (i.e., 12–13 days in rat [Table S2], corresponding to 2–3 weeks in man), these observations indicated a therapeutically relevant safety profile and pharmacokinetics of BI-505.

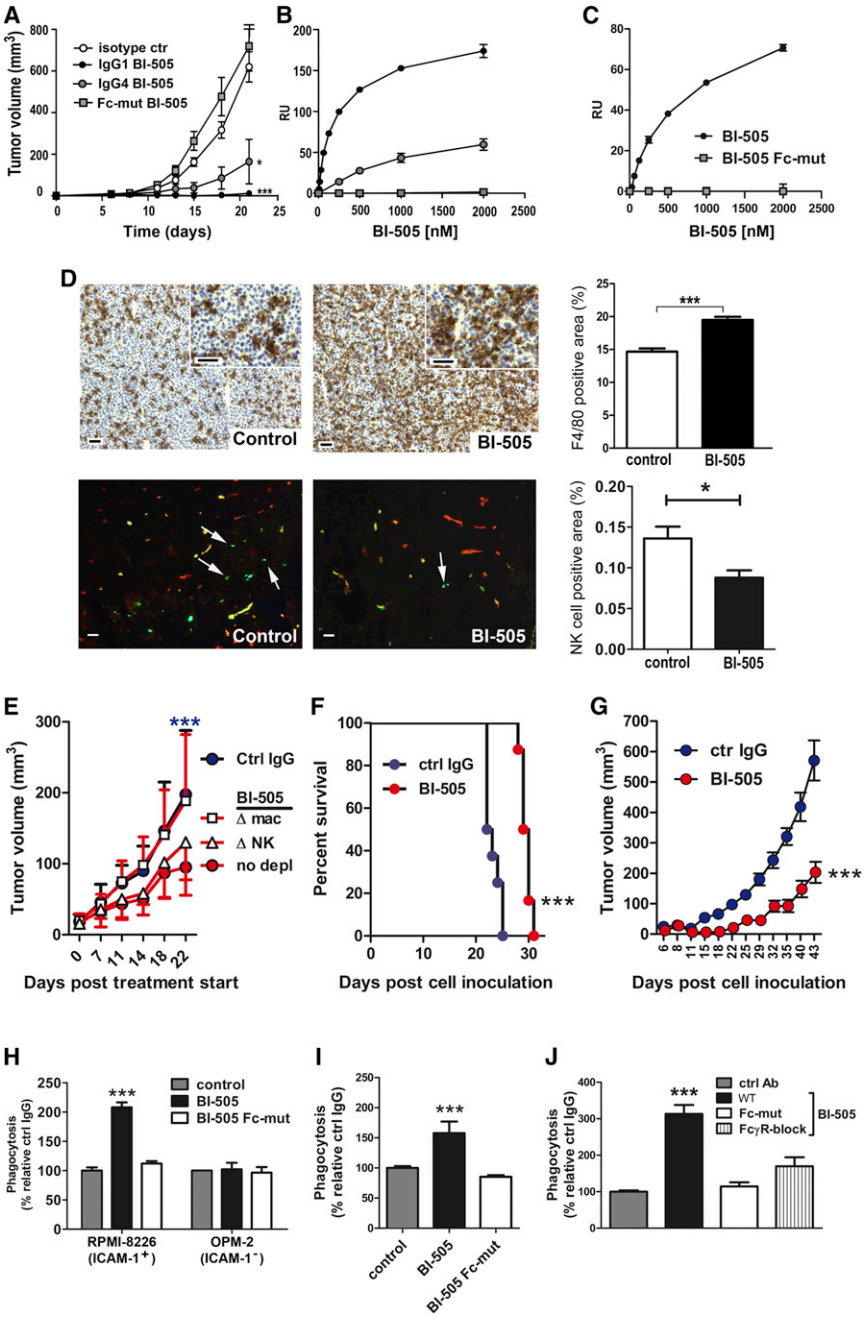

Figure 6. BI-505 Confers Fc-FcγR-Dependent Antitumor Activity through Macrophages

(A) Mean tumor volume of SCID mice bearing established ARH-77 tumors and treated with isotype control antibody or BI-505 IgG_1, BI-505 IgG_4, or BI-505 $IgG_{1\ N297Q}$ (Fc-variant) antibodies. $^*p < 0.05$, $^{**}p < 0.01$.

(B) BiaCore analysis of BI-505 Fc-variant antibodies binding to mouse FcγRIV.

(C) BiaCore analysis of BI-505 Fc-variant antibodies binding to human FcγRIIIa.

(D) Immunohistochemical quantitation of F4/80$^+$ macrophages (top panel) or NK cells (lower panel) in tumor tissue of animals bearing established ARH-77 tumors treated with control antibody or BI-505. Graphs show mean F4/80$^+$ and NK-cell-positive tumor areas, respectively. Bar = 40 μm. $^*p < 0.05$, $^{***}p < 0.001$.

(E) Tumor growth in macrophage or NK-cell-depleted SCID mice bearing established RPMI-8226 myeloma tumors treated with BI-505 or control antibody. $^{***}p < 0.001$.

(F) Animal survival following BI-505 or control antibody treatment in a disseminated NK-cell-deficient NOD/Shi-*scid*/*IL-2Rγ*$^{-/-}$ mouse model comprising i.v. grafted U266 myeloma cells. $^{***}p < 0.001$.

(G) Tumor growth in BI-505 or control antibody-treated NK-cell-deficient NOD/Shi-*scid*/*IL-2Rγ*$^{-/-}$ mice transplanted with RPMI-8226 myeloma cells. $^{***}p < 0.001$.

(H) Macrophage ADCP of RPMI-8226 and OPM-2 myeloma cells. n = 4, $^{***}p < 0.001$.

(I) Macrophage-mediated ADCP of primary multiple myeloma cells. n = 2, $^{***}p < 0.001$.

(J) Macrophage ADCP of ICAM-1$^+$ EJM myeloma cells. n = 2, $^{***}p < 0.001$.

There were eight to ten animals per treatment group. Error bars show ± SD.

See also Figure S4 and Table S1.

DISCUSSION

We report the successful application of a function-first approach to therapeutic antibody discovery, resulting in the isolation of a human ICAM-1 antibody based on its (1) specificity for a surface receptor upregulated on tumor B cells, (2) significant tumor programmed-cell-death-inducing properties, and (3) significant in vivo antitumor activity against human B cell tumors. Thus, our functional screening methodology was successfully applied both to identify a function (induction of PCD in tumor cells) of a well-characterized receptor (ICAM-1) and a human antibody against the same target with significant therapeutic potential.

Our function-first approach to antibody discovery offers several advantages over and differs in several respects from conventional approaches in which antibodies are identified based on specificity for a predefined target structure. By combining powerful differential biopanning of a naive human antibody library with high-throughput tumor cell death screening, our discovery platform enables the simultaneous generation of multiple high-affinity antibodies with therapeutic potential and specificity for different tumor-cell-associated receptors. The value of screening for functionality across different specificities has been indicated by previous studies, which collectively demonstrate that antibodies against different tumor-associated cell surface receptors can have significant antitumor activity against the same cancer cell type (for a review, see Cheson and Leonard [2008]). Thus, in a highly diversified antibody source, such as n-CoDeR, the most therapeutically efficacious, potent, and best-tolerated antibodies with respect to a given type of cancer

could be specific for one of several receptors, and identifying the optimal antibodies requires functional screening of antibodies targeting all such receptors.

The predictive value of tumor PCD as an indicator of an antibody's therapeutic potential was demonstrated by the enhanced in vivo antitumor activity of BI-505 against CD20-expressing tumors, compared to rituximab. Cragg and Glennie (2004) further indicate the importance of using a function-first approach and of screening for tumor PCD. Different antibodies, which bound with similar affinity to CD20 and had identical Fc regions, differed greatly in their therapeutic efficacy in vivo and, intriguingly, conferred antitumor activity by different mechanisms of action. Superior therapeutic activity correlated positively with tumor PCD and inversely with complement-dependent tumor cell cytotoxicity (Beers et al., 2008; Cragg and Glennie, 2004). These and other observations highlight the importance of the function-first approach to identify antibodies with therapeutic activity (Beck et al., 2010; Gan et al., 2009; Ivanov et al., 2009). Our use of cancer cells, which expressly targeted antigens in their true cell surface configuration, should increase the likelihood of identifying antibodies with specificity for functional and disease-associated receptor epitopes compared to conventional techniques using recombinant antigen or transfected cells in the panning process. Finally, it is generally thought that therapeutic targets are limited and that most might already be identified. From this perspective, it is noteworthy that our technology can reveal functions of previously well-characterized receptors, indicating their suitability as targets in previously unrecognized indications and expand the "therapeutic target space." Thus, whereas the well-characterized role of ICAM-1 in inflammation has provided the rationale for anti-ICAM-1 targeted intervention of acute and chronic inflammatory disorders (Kavanaugh et al., 1997; Mileski et al., 2003; Schneider et al., 1998), our findings identify ICAM-1 as a promising target in multiple MM and possibly oncology in a broader sense. Taken together, our function-first approach provides an effective strategy to generate antitumor antibodies, such as BI-505.

Several observations suggest that ICAM-1 may be a suitable target for MM immunotherapy. Strong expression of ICAM-1 is associated with advanced disease, poor survival, and resistance to chemotherapy (Sampaio et al., 2009; Schmidmaier et al., 2006; Zheng et al., 2012), which is the current inevitable end-stage of MM (Kyle and Rajkumar, 2004). Consistent with these observations, we demonstrate that a majority of MM cells express high levels of the epitope targeted by BI-505. High and homogenous expression on the tumor cell surface and upregulated expression in conjunction with disease progression and the development of resistance to chemotherapy are hallmarks of targets suitable for therapy with antibodies that confer direct tumor cell cytotoxicity. The antitumor activity of BI-505 correlated with antibody binding to tumor-cell-expressed ICAM-1 and was shown to be Fc:FcγR dependent. Accumulating evidence suggests that interactions between an antibody's constant domain (Fc) and a host's Fc gamma receptors (FcγR) are instrumental in the therapeutic efficacy of rituximab and other approved anticancer antibodies (Bibeau et al., 2009; Lejeune et al., 2008; Musolino et al., 2008; Weng and Levy, 2003; Zhang et al., 2007) via mechanisms that may involve both innate and adaptive immunity (Alduaij and Illidge, 2011; Park et al., 2010), as well as enhanced tumor PCD following FcγR-dependent crosslinking of tumor bound mAb (Wilson et al., 2011). Consequently, although there is currently no antibody available to treat MM, nonclinical and clinical studies on antibodies approved for treatment of different types of cancer suggest that those—like BI-505—that are capable of triggering MM cell death via Fc:FcγR-dependent immunity hold particular promise of improving MM survival. Our finding that macrophages are principal effector cells conferring BI-505 FcγR-dependent antitumor activity is intriguing. Macrophages are abundantly present in MM bone marrow and accumulating data point to a detrimental role for macrophages and ICAM-1 in MM development of drug resistance (Zheng et al., 2009, 2012). BI-505 harnessing of tumor-associated macrophages to confer antitumor activity thus appears an attractive mechanism of combatting MM.

In addition to exerting significant antitumor activity, a therapeutic cancer antibody must be safe and tolerable for patients. Previous studies by independent investigators demonstrated that treatment with (a murine) anti-ICAM-1 antibody was well tolerated by different patient groups (Kavanaugh et al., 1997; Mileski et al., 2003; Schneider et al., 1998). Herein presented data on BI-505 is consistent with this notion. Owing to its fully human nature, and as indicated from our animal studies, BI-505 should have low immunogenicity.

Collectively, our results demonstrate proof-of-principle for the function-first approach in the search for efficient antitumor antibodies and provide a rationale for further preclinical and clinical evaluation of BI-505 in the treatment of MM. An open-label multicenter phase I dose-escalation study with BI-505 in relapsed/refractory MM patients, approved by the Swedish Medical Product Agency and in accordance with the United States Food and Drug Administration's (FDA) guidance, is ongoing (NCT01025206; http://clinicaltrials.gov/).

EXPERIMENTAL PROCEDURES

Cell Culture and In Vitro Assays

ARH-77, RPMI-8226, and Daudi cell lines were obtained from the American Type Culture Collection (ATCC, Sweden). NCI-H929, EJM, and OPM-2 cell lines were obtained from the Deutsche Sammlung von Mikroorganismen und Zellkulturen (DSMZ, Germany). HUVEC and HMVEC cells were obtained from Cascade Biologics (Portland, OR, USA). Cells were maintained in culture media as recommended by the supplier and maintained at 37°C in a 5% CO_2, 95% humidity incubator. Cell PCD, ADCC, CDC, cytokine release, and T cell proliferation assays were performed as described elsewhere (Fransson et al., 2006; Supplemental Experimental Procedures).

Patient Cell Studies

Plasma cell surface expression of ICAM-1 and the BI-505 epitope was analyzed by fluorescence-activated cell sorting (FACS). Bone marrow aspirates were obtained from 29 patients diagnosed with MM or related diseases at the Department of Hematology, Skånes University Hospital, Lund. All human samples were collected using protocols approved by the Ethics Committee of Skåne University Hospital, and informed consent was obtained from all patients.

Animal Studies

Studies were conducted in accordance with guidelines of the Lund University Hospital, Sweden, or University of Utah, Salt Lake City, USA, following approval from the local ethical committee for animal care and use. BI-505 efficacy and potency was examined in subcutaneous and disseminated, prophylactic and therapeutic, experimental MM models comprising myeloma cell lines RPMI-8226, U266, EJM, and OPM-2. The in vivo efficacy of BI-505 was compared to clinically approved drugs dexamethasone, melphalan,

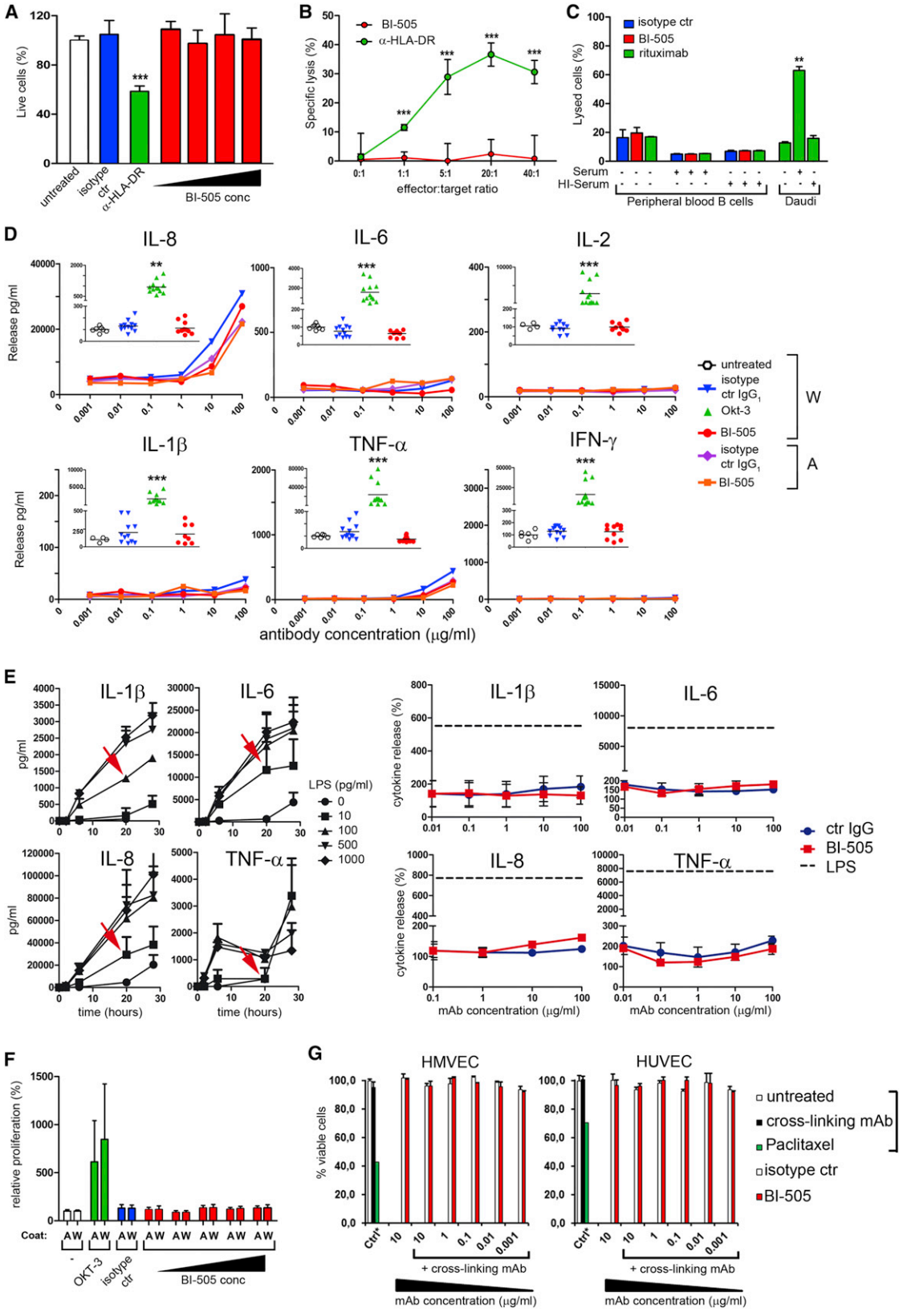

(legend on next page)

bortezomib, and revlimid used at clinically relevant doses in therapeutic disseminated models comprising RPMI-8226 or primary patient myeloma cells, the latter following injection of patient cells in implanted of human fetal bone in SCID mice. For subcutaneous grafting, 1–5 × 10^6 tumor cells (RPMI-8226, NCI-H929, EJM, OPM-2, ARH-77, or Daudi) were subcutaneously injected at a volume of 100 μl into the left flank of anesthetized mice as described in the Supplemental Experimental Procedures. For established xenograft studies, when tumors reached an average size of 80–120 mm^3, animals were sorted to give nearly identical group mean tumor sizes and were treated with isotype control antibody (20 mg/kg/inj), rituximab (20 mg/kg/inj), or BI-505 antibody (0.02 to 20 mg/kg/inj, as indicated in the text) intraperitoneally (i.p.) twice weekly until study termination. For disseminated experimental models of MM, RPMI-8226 (10 × 10^7 tumor cells) were injected intravenously (i.v.) into the caudal vein of anesthetized mice after whole-body irradiation (1.8 Gy, ^{60}Co, INRA, Bretennieres). Treatment with saline, isotype control IgG, bortezomib, lenalidomide, dexamethasone, or BI-505 started on day 5 (RPMI-8226). Treatment with melphalan started on day 10. BI-505 or isotype IgG mAb was administered i.v. at 2 mg/kg/inj twice weekly for 8 weeks; bortezomib at 1 mg/kg/inj once weekly for 8 weeks; lenalidomide orally at 2 mg/kg/inj for two cycles consisting of 5 days of treatment and 2 days of wash out; melphalan i.v. at 3 mg/kg/inj once weekly for 8 weeks; and dexamethasone at 6 mg/kg/inj three times weekly for 2 weeks. In vivo mechanistic studies assessing the role of Fc-FcγR interactions utilized wild-type and engineered FcγR-binding-deficient (N297Q) IgG1 variants of BI-505. The role of macrophages and NK cells for BI-505 in vivo antitumor activity was assessed using anti-asialo antibody treatment, clodronate liposome treatment, or NK-cell-deficient mice. For a detailed description of in vivo studies, see the Supplemental Experimental Procedures.

In Vitro Functional Studies

Peripheral blood-derived monocytes, NK cells, B cells, and T cells were purified from buffy coats from healthy donors obtained from the local blood central at Lund University Hospital and Halmstad Hospital. Briefly, PBMCs were first extracted using Ficoll-Paque PLUS (GE Healthcare Life Sciences, Waukesha, WI, USA), followed by isolation of monocytes with CD14 MicroBeads and MACS Separation (Miltenyi Biotec, Bergisch Gladbach, Germany). Monocyte-derived macrophages were generated by 6–14 days culture in the presence of 25 ng/ml of recombinant human M-CSF (R&D Systems, Minneapolis, MN, USA). For multiple myeloma cells, freshly isolated bone marrow samples were donated by patients at Lund University Hospital and subsequently processed with Ficoll-Paque PLUS. Negative isolation of malignant plasma cells was performed using Plasma Cell Isolation Kit II (Miltenyi Biotec).

ADCP

Cultured macrophages were detached and plated in flat 96-well plates at 50,000 cells/well and placed in 37°C. Carboxyfluorescein succinimidyl ester (CFSE)-stained target cells were incubated with antibodies for up to 1 hr on ice. After washing, the different cell solutions were added to the culture plates containing macrophages at a ratio of 5:1 (target cells:macrophages). Thereafter, the culture plates were incubated at 37°C for 1–2 hr (primary patient MM cells) or 16 hr (RPMI-8226 cells). The percentage of macrophages that had phagocytosed tumor cells ($CFSE^+$, $CD206^+$) per total analyzed macrophages was determined following gating and acquisition of 5,000 $CD206^+$ cells/sample.

ADCC

NK cells were isolated from purified PBMCs using positive or negative NK cell isolation kits (Miltenyi Biotec). Target cells were harvested and incubated in medium with or without the respective antibodies (2 μg/ml) for 60 min on ice before. NK cells were washed, diluted in ADCC medium, and dispensed together with the respective antibody-coated target cells at varying effector/target cell ratios. Experiments were performed in triplicate. After incubation, TO-PRO-3 dye and counting beads (Invitrogen, Carlsbad, CA, USA) were added, and cells were analyzed for membrane permeabilization using flow cytometry.

CDC

Target cells were harvested as described above (under the ADCC heading) and incubated with antibodies at 5 μg/ml for 60 min on ice and then washed. Human serum, normal or heat-inactivated (Sigma, Sweden), was added to tubes, and the samples were incubated for 2 hr at 37°C. After completion of incubation, ToPo-Pro-3 (Invitrogen) was added at a final concentration of 0.3 μM, and cells were analyzed for membrane permeabilization using flow cytometry.

Detailed Experimental Procedures, including protocols for assessment of apoptosis in normal ICAM-1-expressing endothelial cell, T cell proliferation, PBMC cytokine release, and receptor occupancy studies, are described in the Supplemental Experimental Procedures.

SUPPLEMENTAL INFORMATION

Supplemental Information includes five figures, two tables, and Supplemental Experimental Procedures and can be found with this article online at http://dx.doi.org/10.1016/j.ccr.2013.02.026.

ACKNOWLEDGMENTS

We thank Professor Tor Olofsson for help with FACS analyses and Professors Mark Cragg and Christer Betsholtz for critically reviewing our manuscript. M.H. was supported by a grant from The Royal Swedish Academy of Sciences. N.V., A.S., A.L., L.D., Z.C.L., T.M.-N., T.L., M.K., A.L., L.M., and B.F. are or were employees of BioInvent International during their contribution to this paper.

Figure 7. BI-505 Does Not Induce Apoptosis, ADCC, CDC, T Cell Proliferation, or Cytokine Release in Resting or Stimulated Normal Cells Expressing ICAM-1

(A) Apoptosis in peripheral blood B cells. Graph shows percent live (nonapoptotic) B cells following no treatment or treatment with isotype control IgG, anti-HLA-DR (positive control IgG), or BI-505 (0, 1.5, 6, or 24 μg/ml). Values were normalized to untreated cells, where percent living cells was set to 100.

(B) ADCC of peripheral blood B cells. Graph shows specific lysis of target peripheral blood B cells following treatment with BI-505 or anti-HLA-DR IgG_1 (positive control). Values were normalized to treatment with isotype control IgG, where specific lysis was set to 0%.

(C) CDC of peripheral blood B cells and Daudi Burkitt's lymphoma cells. Cells were incubated with BI-505, rituximab, or isotype control IgG and analyzed for CDC.

(D) Antibody-induced PBMC cytokine release. PBMC cytokine release was measured by ELISA of cell culture supernatants for IL-1β, IL-2, IL-6, IL-8, IFN-γ, and TNF-α following incubation of cells in plates coated with hypercrosslinked (air-dried "A" or wet-coated "W") BI-505, isotype control, or positive-control Okt-3 antibody.

(E) Antibody-induced cytokine release in lipopolysaccharide (LPS)-primed PBMCs. PBMCs were incubated with titrated LPS, and concentrations yielding submaximal cellular release of IL-1β (100 pg/ml), IL-6 (10 pg/ml), IL-8 (10 pg/ml), and TNF-α (10 pg/ml) were determined (arrows, left panel) and used in subsequent experiments assessing antibody (BI-505 or control IgG) effects on cytokine release from LPS-primed PBMCs (right panel). Treatment with 100 ng/ml LPS served as positive control for robust cytokine release.

(F) Antibody-induced T cell proliferation. CFSE-labeled T cells were incubated with BI-505, isotype control IgG, or anti-CD3 (okt-3) IgG hyperimmobilized to cell culture plates by air-drying "A" or wet-coating "W." Cells were cultured for 6 days, and T cell proliferation was monitored by flow cytometry as decreased CFSE signals.

(G) Antibody-induced endothelial cell apoptosis. HUVEC or HMVEC endothelial cells were incubated with paclitaxel (positive control), BI-505, or isotype control IgG in the presence or absence of crosslinking mAb. Apoptosis was measured by flow cytometry following staining of cells with annexin V-AF488.

**$p < 0.01$, ***$p < 0.001$. Error bars show ± SD.

See also Figure S5; Table S2.

Received: September 14, 2010
Revised: August 29, 2012
Accepted: February 27, 2013
Published: April 15, 2013

REFERENCES

Aalinkeel, R., Nair, M.P.N., Sufrin, G., Mahajan, S.D., Chadha, K.C., Chawda, R.P., and Schwartz, S.A. (2004). Gene expression of angiogenic factors correlates with metastatic potential of prostate cancer cells. Cancer Res. *64*, 5311–5321.

Alduaij, W., and Illidge, T.M. (2011). The future of anti-CD20 monoclonal antibodies: are we making progress? Blood *117*, 2993–3001.

Beck, A., Wurch, T., Bailly, C., and Corvaia, N. (2010). Strategies and challenges for the next generation of therapeutic antibodies. Nat. Rev. Immunol. *10*, 345–352.

Beers, S.A., Chan, C.H., James, S., French, R.R., Attfield, K.E., Brennan, C.M., Ahuja, A., Shlomchik, M.J., Cragg, M.S., and Glennie, M.J. (2008). Type II (tositumomab) anti-CD20 monoclonal antibody out performs type I (rituximab-like) reagents in B-cell depletion regardless of complement activation. Blood *112*, 4170–4177.

Bibeau, F., Lopez-Crapez, E., Di Fiore, F., Thezenas, S., Ychou, M., Blanchard, F., Lamy, A., Penault-Llorca, F., Frébourg, T., Michel, P., et al. (2009). Impact of FcgammaRIIa-FcgammaRIIIa polymorphisms and KRAS mutations on the clinical outcome of patients with metastatic colorectal cancer treated with cetuximab plus irinotecan. J. Clin. Oncol. *27*, 1122–1129.

Cheson, B.D., and Leonard, J.P. (2008). Monoclonal antibody therapy for B-cell non-Hodgkin's lymphoma. N. Engl. J. Med. *359*, 613–626.

Clynes, R.A., Towers, T.L., Presta, L.G., and Ravetch, J.V. (2000). Inhibitory Fc receptors modulate in vivo cytotoxicity against tumor targets. Nat. Med. *6*, 443–446.

Cragg, M.S., and Glennie, M.J. (2004). Antibody specificity controls in vivo effector mechanisms of anti-CD20 reagents. Blood *103*, 2738–2743.

Cragg, M.S., Morgan, S.M., Chan, H.T., Morgan, B.P., Filatov, A.V., Johnson, P.W., French, R.R., and Glennie, M.J. (2003). Complement-mediated lysis by anti-CD20 mAb correlates with segregation into lipid rafts. Blood *101*, 1045–1052.

Fransson, J., Tornberg, U.C., Borrebaeck, C.A., Carlsson, R., and Frendéus, B. (2006). Rapid induction of apoptosis in B-cell lymphoma by functionally isolated human antibodies. Int. J. Cancer *119*, 349–358.

Gan, H.K., Lappas, M., Cao, D.X., Cvrljevdic, A., Scott, A.M., and Johns, T.G. (2009). Targeting a unique EGFR epitope with monoclonal antibody 806 activates NF-kappaB and initiates tumour vascular normalization. J. Cell. Mol. Med. *13* (9B), 3993–4001.

Hideshima, T., Mitsiades, C., Tonon, G., Richardson, P.G., and Anderson, K.C. (2007). Understanding multiple myeloma pathogenesis in the bone marrow to identify new therapeutic targets. Nat. Rev. Cancer *7*, 585–598.

Huang, Y.W., Richardson, J.A., and Vitetta, E.S. (1995). Anti-CD54 (ICAM-1) has antitumor activity in SCID mice with human myeloma cells. Cancer Res. *55*, 610–616.

Ivanov, A., Beers, S.A., Walshe, C.A., Honeychurch, J., Alduaij, W., Cox, K.L., Potter, K.N., Murray, S., Chan, C.H., Klymenko, T., et al. (2009). Monoclonal antibodies directed to CD20 and HLA-DR can elicit homotypic adhesion followed by lysosome-mediated cell death in human lymphoma and leukemia cells. J. Clin. Invest. *119*, 2143–2159.

Johnson, J.P., Stade, B.G., Hupke, U., Holzmann, B., and Riethmüller, G. (1988). The melanoma progression-associated antigen P3.58 is identical to the intercellular adhesion molecule, ICAM-1. Immunobiology *178*, 275–284.

Kapoor, P., Greipp, P.T., Morice, W.G., Rajkumar, S.V., Witzig, T.E., and Greipp, P.R. (2008). Anti-CD20 monoclonal antibody therapy in multiple myeloma. Br. J. Haematol. *141*, 135–148.

Kavanaugh, A.F., Schulze-Koops, H., Davis, L.S., and Lipsky, P.E. (1997). Repeat treatment of rheumatoid arthritis patients with a murine anti-intercellular adhesion molecule 1 monoclonal antibody. Arthritis Rheum. *40*, 849–853.

Kyle, R.A., and Rajkumar, S.V. (2004). Multiple myeloma. N. Engl. J. Med. *351*, 1860–1873.

Lejeune, J., Thibault, G., Ternant, D., Cartron, G., Watier, H., and Ohresser, M. (2008). Evidence for linkage disequilibrium between Fcgamma RIIIa-V158F and Fcgamma RIIa-H131R polymorphisms in white patients, and for an Fcgamma RIIIa-restricted influence on the response to therapeutic antibodies. J. Clin. Oncol. *26*, 5489–5491, author reply 5491–5492.

Lim, S.H., Beers, S.A., French, R.R., Johnson, P.W., Glennie, M.J., and Cragg, M.S. (2010). Anti-CD20 monoclonal antibodies: historical and future perspectives. Haematologica *95*, 135–143.

Manches, O., Lui, G., Chaperot, L., Gressin, R., Molens, J.P., Jacob, M.C., Sotto, J.J., Leroux, D., Bensa, J.C., and Plumas, J. (2003). In vitro mechanisms of action of rituximab on primary non-Hodgkin lymphomas. Blood *101*, 949–954.

Mileski, W.J., Burkhart, D., Hunt, J.L., Kagan, R.J., Saffle, J.R., Herndon, D.N., Heimbach, D.M., Luterman, A., Yurt, R.W., Goodwin, C.W., and Hansborough, J. (2003). Clinical effects of inhibiting leukocyte adhesion with monoclonal antibody to intercellular adhesion molecule-1 (enlimomab) in the treatment of partial-thickness burn injury. J. Trauma *54*, 950–958.

Mitsiades, C.S., Mitsiades, N.S., Bronson, R.T., Chauhan, D., Munshi, N., Treon, S.P., Maxwell, C.A., Pilarski, L., Hideshima, T., Hoffman, R.M., and Anderson, K.C. (2003). Fluorescence imaging of multiple myeloma cells in a clinically relevant SCID/NOD in vivo model: biologic and clinical implications. Cancer Res. *63*, 6689–6696.

Musolino, A., Naldi, N., Bortesi, B., Pezzuolo, D., Capelletti, M., Missale, G., Laccabue, D., Zerbini, A., Camisa, R., Bisagni, G., et al. (2008). Immunoglobulin G fragment C receptor polymorphisms and clinical efficacy of trastuzumab-based therapy in patients with HER-2/neu-positive metastatic breast cancer. J. Clin. Oncol. *26*, 1789–1796.

Nimmerjahn, F., Bruhns, P., Horiuchi, K., and Ravetch, J.V. (2005). FcgammaRIV: a novel FcR with distinct IgG subclass specificity. Immunity *23*, 41–51.

Park, S., Jiang, Z., Mortenson, E.D., Deng, L., Radkevich-Brown, O., Yang, X., Sattar, H., Wang, Y., Brown, N.K., Greene, M., et al. (2010). The therapeutic effect of anti-HER2/neu antibody depends on both innate and adaptive immunity. Cancer Cell *18*, 160–170.

Rawstron, A.C., Orfao, A., Beksac, M., Bezdickova, L., Brooimans, R.A., Bumbea, H., Dalva, K., Fuhler, G., Gratama, J., Hose, D., et al.; European Myeloma Network. (2008). Report of the European Myeloma Network on multiparametric flow cytometry in multiple myeloma and related disorders. Haematologica *93*, 431–438.

Richardson, P.G., Lonial, S., Jakubowiak, A.J., Harousseau, J.L., and Anderson, K.C. (2011). Monoclonal antibodies in the treatment of multiple myeloma. Br. J. Haematol. Published online July 21, 2011. http://dx.doi.org/10.1111/j.1365-2141.2011.08790.

Sampaio, M.S., Vettore, A.L., Yamamoto, M., Chauffaille, Mde.L., Zago, M.A., and Colleoni, G.W. (2009). Expression of eight genes of nuclear factor-kappa B pathway in multiple myeloma using bone marrow aspirates obtained at diagnosis. Histol. Histopathol. *24*, 991–997.

Schmidmaier, R., Baumann, P., Simsek, M., Dayyani, F., Emmerich, B., and Meinhardt, G. (2004). The HMG-CoA reductase inhibitor simvastatin overcomes cell adhesion-mediated drug resistance in multiple myeloma by geranylgeranylation of Rho protein and activation of Rho kinase. Blood *104*, 1825–1832.

Schmidmaier, R., Mörsdorf, K., Baumann, P., Emmerich, B., and Meinhardt, G. (2006). Evidence for cell adhesion-mediated drug resistance of multiple myeloma cells in vivo. Int. J. Biol. Markers *21*, 218–222.

Schneider, D., Berrouschot, J., Brandt, T., Hacke, W., Ferbert, A., Norris, S.H., Polmar, S.H., and Schäfer, E. (1998). Safety, pharmacokinetics and biological activity of enlimomab (anti-ICAM-1 antibody): an open-label, dose escalation study in patients hospitalized for acute stroke. Eur. Neurol. *40*, 78–83.

Smith, M.R. (2003). Rituximab (monoclonal anti-CD20 antibody): mechanisms of action and resistance. Oncogene *22*, 7359–7368.

Söderlind, E., Strandberg, L., Jirholt, P., Kobayashi, N., Alexeiva, V., Aberg, A.M., Nilsson, A., Jansson, B., Ohlin, M., Wingren, C., et al. (2000). Recombining germline-derived CDR sequences for creating diverse single-framework antibody libraries. Nat. Biotechnol. *18*, 852–856.

Stebbings, R., Findlay, L., Edwards, C., Eastwood, D., Bird, C., North, D., Mistry, Y., Dilger, P., Liefooghe, E., Cludts, I., et al. (2007). "Cytokine storm" in the phase I trial of monoclonal antibody TGN1412: better understanding the causes to improve preclinical testing of immunotherapeutics. J. Immunol. *179*, 3325–3331.

van der Kolk, L.E., Grillo-López, A.J., Baars, J.W., Hack, C.E., and van Oers, M.H. (2001). Complement activation plays a key role in the side-effects of rituximab treatment. Br. J. Haematol. *115*, 807–811.

Weiner, L.M., Surana, R., and Wang, S. (2010). Monoclonal antibodies: versatile platforms for cancer immunotherapy. Nat. Rev. Immunol. *10*, 317–327.

Weng, W.K., and Levy, R. (2003). Two immunoglobulin G fragment C receptor polymorphisms independently predict response to rituximab in patients with follicular lymphoma. J. Clin. Oncol. *21*, 3940–3947.

Wilson, N.S., Yang, B., Yang, A., Loeser, S., Marsters, S., Lawrence, D., Li, Y., Pitti, R., Totpal, K., Yee, S., et al. (2011). An Fcγ receptor-dependent mechanism drives antibody-mediated target-receptor signaling in cancer cells. Cancer Cell *19*, 101–113.

Yaccoby, S., Barlogie, B., and Epstein, J. (1998). Primary myeloma cells growing in SCID-hu mice: a model for studying the biology and treatment of myeloma and its manifestations. Blood *92*, 2908–2913.

Zhang, W., Gordon, M., Schultheis, A.M., Yang, D.Y., Nagashima, F., Azuma, M., Chang, H.M., Borucka, E., Lurje, G., Sherrod, A.E., et al. (2007). FCGR2A and FCGR3A polymorphisms associated with clinical outcome of epidermal growth factor receptor expressing metastatic colorectal cancer patients treated with single-agent cetuximab. J. Clin. Oncol. *25*, 3712–3718.

Zheng, Y., Cai, Z., Wang, S., Zhang, X., Qian, J., Hong, S., Li, H., Wang, M., Yang, J., and Yi, Q. (2009). Macrophages are an abundant component of myeloma microenvironment and protect myeloma cells from chemotherapy drug-induced apoptosis. Blood *114*, 3625–3628.

Zheng, Y., Yang, J., Qian, J., Qiu, P., Hanabuchi, S., Lu, Y., Wang, Z., Liu, Z., Li, H., He, J., et al. (2012). PSGL-1/selectin and ICAM-1/CD18 interactions are involved in macrophage-induced drug resistance in myeloma. Leukemia. Published online September 21, 2012. http://dx.doi.org/10.1038/leu.2012.272.

Cancer Cell
Article

The Pivotal Role of IKKα in the Development of Spontaneous Lung Squamous Cell Carcinomas

Zuoxiang Xiao,[1,6] Qun Jiang,[1,6] Jami Willette-Brown,[1] Sichuan Xi,[2] Feng Zhu,[1] Sandra Burkett,[3] Timothy Back,[1] Na-Young Song,[1] Mahesh Datla,[1] Zhonghe Sun,[4] Romina Goldszmid,[1] Fanching Lin,[1] Travis Cohoon,[5] Kristen Pike,[4] Xiaolin Wu,[4] David S. Schrump,[2] Kwok-Kin Wong,[5] Howard A. Young,[1] Giorgio Trinchieri,[1] Robert H. Wiltrout,[1,*] and Yinling Hu[1,*]

[1]Cancer and Inflammation Program
[2]Thoracic Oncology Section, Surgery Branch
[3]Mouse Cancer Genetics Program
Center for Cancer Research, National Cancer Institute, Frederick, MD 21701, USA
[4]Laboratory of Molecular Technology, Frederick National Laboratory for Cancer Research, SAIC-Frederick, Inc., Frederick, MD 21702, USA
[5]Department of Medical Oncology, Dana-Farber Cancer Institute, 44 Binney Street, Boston, MA 02115, USA
[6]These authors contributed equally to this work
*Correspondence: wiltrour@mail.nih.gov (R.H.W.), huy2@mail.nih.gov (Y.H.)
http://dx.doi.org/10.1016/j.ccr.2013.03.009

SUMMARY

Here, we report that kinase-dead IKKα knockin mice develop spontaneous lung squamous cell carcinomas (SCCs) associated with IKKα downregulation and marked pulmonary inflammation. IKKα reduction upregulated the expression of p63, Trim29, and keratin 5 (K5), which serve as diagnostic markers for human lung SCCs. IKKα^{low}K5^{+}p63^{hi} cell expansion and SCC formation were accompanied by inflammation-associated deregulation of oncogenes, tumor suppressors, and stem cell regulators. Reintroducing transgenic K5.IKKα, depleting macrophages, and reconstituting irradiated mutant animals with wild-type bone marrow (BM) prevented SCC development, suggesting that BM-derived IKKα mutant macrophages promote the transition of IKKα^{low}K5^{+}p63^{hi} cells to tumor cells. This mouse model resembles human lung SCCs, sheds light on the mechanisms underlying lung malignancy development, and identifies targets for therapy of lung SCCs.

INTRODUCTION

Lung cancer is the leading cause of cancer mortality worldwide, and the 5 year survival rate of patients with non-small cell lung carcinomas (NSCLCs) remains as low as 15% (Larsen and Minna, 2011). Therefore, new approaches to detect, cure, and prevent this devastating disease represent an urgent medical need. NSCLCs include adenocarcinomas (ADCs), squamous cell carcinomas (SCCs), and large cell carcinomas. Activating *K-ras* mutations have been identified in 10%–30% of human lung ADCs but in less than 5% of human lung SCCs (DuPage et al., 2009; Larsen and Minna, 2011). An oncogenic mutation in *K-ras* that changes a glycine at codon 12 to aspartic acid (*K-ras*^{G12D}) induces spontaneous lung ADCs in mice (Johnson et al., 2001). This mouse model has greatly enhanced our understanding of the pathogenesis, treatment, and prevention of lung cancer. Lung SCCs are strongly associated with smoking, suggesting that smoking-induced gene damage and inflammation are crucial for the development of this malignancy (Hecht, 2003; Larsen and Minna, 2011). Although many molecular alterations, such as deregulated epidermal growth factor receptor (*EGFR*), *PIK3CA*, *p53*, and *c-Myc*, have been identified in human lung SCCs (Hammerman et al., 2012; Hecht, 2003), lung SCCs have not been well recapitulated in animals.

Although *K-ras*^{G12D} fails to induce spontaneous lung SCCs in mice, Ji et al. (2007) have shown that 56% of *K-ras*^{G12D} mice lacking serine/threonine kinase 11 (also called LKB1) in the lungs develop mixed SCCs and ADCs. The *Lkb1* deletion alone does

Significance

Lung cancer is the leading cause of cancer mortality worldwide. Lung squamous cell carcinoma (SCC), a major type of human lung cancer, is strongly associated with smoking. Although many oncogenes, tumor suppressors, and stem cell regulators have been found in human lung SCCs, mice overexpressing or lacking these genes do not well recapitulate the development of lung SCCs. A robust mouse lung SCC model is an urgent need for human health. Here, we established a robust lung SCC model in kinase-dead IKKα knockin mice and identified shared molecular alterations in human and mouse lung SCCs. Thus, this mouse model provides a suitable tool to study early diagnosis, treatment, and prevention of human lung SCCs.

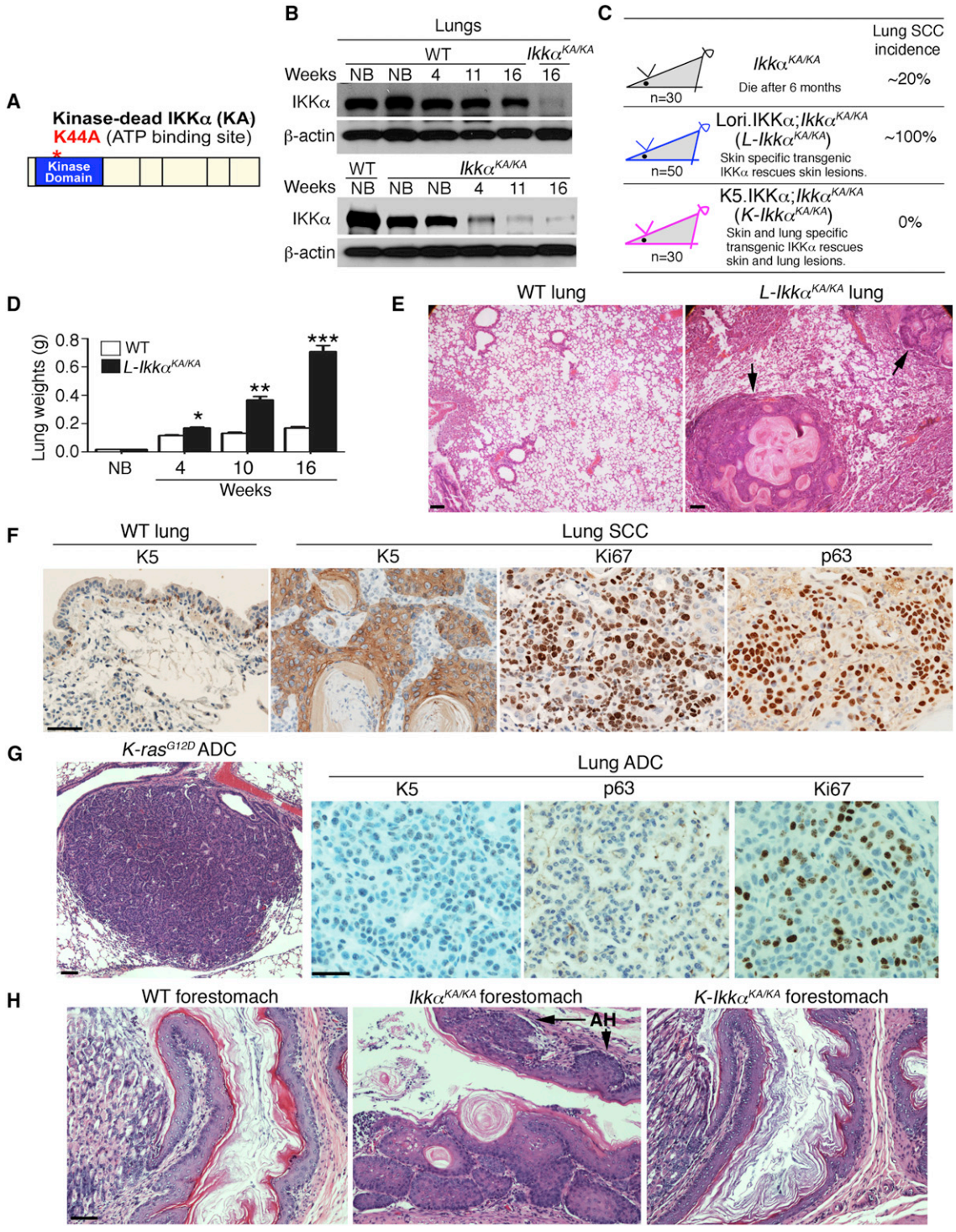

Figure 1. Identification of Lung SCCs in *Ikkα*$^{KA/KA}$ Mice

(A) The K at 44 is replaced by A within the IKKα kinase domain in *Ikkα*$^{KA/KA}$ mice.

(B) Western blot shows IKKα levels in WT and *Ikkα*$^{KA/KA}$ lungs. NB, newborn; β-actin, protein-loading control.

(C) Lung SCC incidence in *Ikkα*$^{KA/KA}$, *L-Ikkα*$^{KA/KA}$, and *K-Ikkα*$^{KA/KA}$ mice with FVB background. n, mouse numbers.

(D) WT and *L-Ikkα*$^{KA/KA}$ lung weights (mean ± SD of three mice per group). NB, newborn; g, gram. Statistical analysis: *p < 0.05; **p < 0.01; ***p < 0.001 (Student's test).

(E) The histology of hematoxylin and eosin (H&E)-stained WT lungs and SCCs derived from *L-Ikkα*$^{KA/KA}$ lungs. Arrows indicate SCC foci. Scale bar, 50 μm.

(F) IHC-stained K5, p63, and Ki67 in paraffin sections of WT lungs and *L-Ikkα*$^{KA/KA}$ lung SCCs. Brown, positive staining; blue, nuclear countering staining. Scale bar, 50 μm.

(legend continued on next page)

not induce lung tumors, suggesting that K-ras activation and LKB1 loss provide complementary pathways, which lead to lung SCC development. In human, germ-line mutations in *Lkb1* are associated with Peutz-Jeghers syndrome, and the *Lkb1* mutations have been also identified in a variety of human epithelial cancers, including lung SCCs (Hearle et al., 2006; Ji et al., 2007). Interestingly, *Lkb1*$^{-/-}$ mouse embryonic fibroblasts (MEFs) are resistant to oncogenic Ras-mediated cell proliferation and transformation (Bardeesy et al., 2002), indicating that LKB1 and Ras cooperate in promoting tumor development in a cell type-specific manner.

Lung SCCs are derived from keratin 5-positive (K5$^+$) basal cells of the pseudostratified bronchial epithelium, while ADCs are derived from the epithelial cells of alveoli (Hackett et al., 2011; Woodworth et al., 1983). Antibodies against transcription factor p63, tripartite motif-containing 29 (Trim29) proteins, and K5 have been used to diagnose human lung SCCs and distinguish poorly differentiated lung SCCs from ADCs in the clinic (Ring et al., 2009). p63, a member of the tumor suppressor p53 family, is required for the formation of the epidermis, other stratified epithelia, and epithelial appendages (Vanbokhoven et al., 2011). The N-terminal-truncated form of p63 (ΔNp63) is predominately expressed in the epidermis and is overexpressed in various epithelial cancers, where it exerts oncogenic activities (Koster et al., 2007; Melino, 2011). In addition, induced bright-p63/K5$^+$ lung epithelial cells can give rise to alveoli, suggesting that the bright-p63/K5$^+$ cells are adult stem cells in the lungs (Kumar et al., 2011). Overexpressed Trim29 has been reported in human lung, bladder, colon, ovarian, endometrial, and gastric cancers. In these cell types, Trim29 promotes cell proliferation and inhibits p53 activity (Hatakeyama, 2011). These findings highlight that increased epithelial cell-specific p63 and Trim29 may also contribute to lung SCC development.

IKKα, one of subunits in the IKK complex (Ghosh and Karin, 2002), is required for the formation of the epidermis during mouse embryonic development and serves as an innate surveillant that prevents skin tumor development through suppressing the EGFR- and c-Myc-related pathways in adult mice (Descargues et al., 2008; Hu et al., 1999; Liu et al., 2008). It is known that K5$^+$ keratinocytes markedly expand in the skin of *Ikkα*$^{-/-}$ mice compared to wild-type (WT) mice, *Ikkα*$^{+/-}$ mice have enhanced susceptibility to chemical carcinogen-induced K5$^+$ SCCs associated with dedifferentiation in the skin, and inducible K5.CreER-mediated *Ikkα* deletion in keratinocytes causes spontaneous skin papillomas and SCCs in *Ikkα*-floxed mice (Hu et al., 1999, 2001; Liu et al., 2008; Park et al., 2007). These data suggest that K5$^+$ epithelial cells lacking IKKα may be the targets for SCC development. IKKα downregulation has been reported in human lung and skin SCCs (Kwak et al., 2011; Marinari et al., 2008); however, the role that IKKα plays in lung cancer has not been investigated. In eukaryotic cells, chromatin consists of packaged chromosomal DNA wound around nucleosome cores formed from histones (H). Modifications at these histone proteins can alter chromatin structure, which facilitates or blocks transcription factor access to DNA, thereby regulating gene transcription without changing gene codes. Epigenetics plays a major role in embryonic development. Notably, the bivalent modifications of H3 lysine 4 trimethylation (H3K4me3), a positive transcription mark, and H3K27me3, a negative transcription mark, on the loci of genes regulate stem cell proliferation and differentiation (Bernstein et al., 2006). Nuclear IKKα has been shown to regulate the cell cycle checkpoint in keratinocytes in an epigenetic manner (Liu et al., 2008; Zhu et al., 2007). Whether altering the normal epigenetic control of the nuclear IKKα affects the establishment of tumor cells during carcinogenesis remains unknown.

Inflammatory cells are mobile, plastic, and able to produce many factors (Hanahan and Coussens, 2012). Thus, they orchestrate complex communications among different types of cells at pathological sites, regulating the development of various diseases. Chronic inflammation plays a crucial role in tumor development.

To understand the pathogenesis of lung SCCs, in this study, we attempt to establish a mouse lung SCC model, which may recapitulate human lung SCC development, and to identify crucial events, which may be used to prevent and treat this lung disease.

RESULTS

IKKα Reduction Is Associated with the Development of Spontaneous Lung SCCs in Kinase-Dead IKKα Knockin Mice

We generated kinase-dead IKKα knockin (*Ikkα*$^{K44A/K44A}$, *Ikkα*$^{KA/KA}$) mice, in which the lysine (K) at amino acid 44, an ATP-binding site, was replaced with alanine (A) (Figure 1A; Zhu et al., 2007). *Ikkα*$^{KA/KA}$ newborn mice did not display any obvious abnormalities, indicating that IKKα kinase inactivation does not affect mouse embryonic development. However, after 3 months of age, mutant mice with an FVB background displayed severe skin lesions and developed systemic inflammation (these phenotypes are not discussed in this study) and the mice began to die after 6–10 months. Unexpectedly, spontaneous lung tumors appeared in FVB *Ikkα*$^{KA/KA}$ mice from 4 to 10 months of age. Despite the fact that *Ikkα*$^{KA/KA}$ mice with severe skin phenotypes have to be euthanized at early age, tumors were detected in 20% of the mutant mice. To determine the relationship between IKKα and lung tumor development, we examined IKKα levels in mouse lungs. Western blotting showed a strong expression of IKKα in WT mouse lungs and that IKKα expression was slightly reduced in elder mice (Figure 1B, top panel). IKKα levels were lower in the lungs of *Ikkα*$^{KA/KA}$ newborns and markedly decreased in the lungs of 4-month-old *Ikkα*$^{KA/KA}$ mice (Figure 1B, bottom panel), indicating that IKKα reduction is associated with lung tumor development. To determine whether the K44A mutation may contribute to the reduction of the IKKα protein, we used

(G) H&E-stained and K5-, p63-, and Ki67 IHC-stained mouse lung ADC induced by *K-ras*^{G12D}. Brown, positive staining; blue, nuclear countering staining. Scale bar, 50 μm.
(H) H&E-stained forestomach paraffin sections of WT, *K-Ikkα*$^{KA/KA}$, and *Ikkα*$^{KA/KA}$ (with SCC in situ; see also Figure S1F) mice at 1.2 years of age. AH, atypical hyperplasia. Scale bar, 50 μm.
See also Figure S1.

pulse-chase analysis to show that this K44A mutation promoted IKKα protein degradation compared to WT IKKα (Figure S1A available online). We previously reported that IKKα RNA levels were decreased in $Ikk\alpha^{KA/KA}$ mice (Balkhi et al., 2012). Thus, IKKα is downregulated both at the level of messenger RNA (mRNA) expression and posttranslationally in $Ikk\alpha^{KA/KA}$ mice. In order to keep the $Ikk\alpha^{KA/KA}$ mice alive long enough to study lung cancer development, the skin phenotype of $Ikk\alpha^{KA/KA}$ mice was corrected by expression of WT IKKα complementary DNA (cDNA) in the epidermis under the control of a truncated loricrin promoter (Lori.IKKα) (Liu et al., 2006; Figure 1C). Although Lori.IKKα;$Ikk\alpha^{KA/KA}$ (*L-*$Ikk\alpha^{KA/KA}$) mice displayed almost no skin phenotype, all of 50 *L-*$Ikk\alpha^{KA/KA}$ mice developed spontaneous lung tumors. Next, we introduced the WT IKKα transgene under the control of the K5 promoter (Liu et al., 2008), which is expressed in the basal epidermal keratinocytes and the basal lung epithelial cells of bronchia, into $Ikk\alpha^{KA/KA}$ mice (Figure 1C). Although K5.IKKα; $Ikk\alpha^{KA/KA}$ (*K-*$Ikk\alpha^{KA/KA}$) mice survived longer than *L-*$Ikk\alpha^{KA/KA}$ mice, we did not observe lung tumors in all of 30 *K-*$Ikk\alpha^{KA/KA}$ mice at more than 1 year of age. Analysis by RT-PCR confirmed that Lori.IKKα was expressed in the skin and that K5.IKKα was expressed in the skin and lungs (Figure S1B). These results demonstrate that epithelial cell-derived IKKα prevents lung tumor development.

The weight of *L-*$Ikk\alpha^{KA/KA}$ lungs compared to WT lungs gradually increased with age (Figure 1D), indicating that lung tumor development is associated with increased lung size. Most FVB *L-*$Ikk\alpha^{KA/KA}$ mice were not able to live longer than 7 or 8 months, because their lung weights continued to increase with age, and most lung SCCs were observed in *L-*$Ikk\alpha^{KA/KA}$ mice at 4–6 months of age. Lung tumor foci with the typical SCC features of keratin pearls and squamous cellular morphology were observed on the mutant lung surface and interior (Figures 1E and S1C). Similar to human lung SCCs (Hackett et al., 2011), lung tumors in *L-*$Ikk\alpha^{KA/KA}$ mice expressed K5, p63, and Ki67 (Figures 1F and S1D), indicating that the spontaneous tumors in *L-*$Ikk\alpha^{KA/KA}$ ($Ikk\alpha^{KA/KA}$) mice are SCCs. *K-*ras^{G12D}-induced lung ADCs were negative for K5 and p63 immunostaining but showed increased Ki67-positive cells (Figures 1G, S1D, and S1E). We did not observe lung SCC metastases in *L-*$Ikk\alpha^{KA/KA}$ mice. It was also reported that metastases from lung ADCs but not from SCCs were seen in *K-*ras^{G12D};$Lkb1^{-/-}$ mice (Ji et al., 2007). In addition, $Ikk\alpha^{KA/KA}$ mice lack lymph nodes (Balkhi et al., 2012). Whether these conditions affect lung SCC metastases remains to be investigated in the future.

To determine whether IKKα reduction is associated with squamous cell hyperproliferation and malignant development in the stratified epithelium of $Ikk\alpha^{KA/KA}$ mice, we histologically examined the forestomach, esophagus, and skin in BL6 *L-*$Ikk\alpha^{KA/KA}$ mice. All of the 16 $Ikk\alpha^{KA/KA}$ mice at 5 months–1.2 years of age developed atypical squamous hyperplasia in the forestomach, and two of three $Ikk\alpha^{KA/KA}$ mice at 1.2 years of age developed forestomach SCCs in situ (Figures 1H and S1F). Reintroduced K5.IKKα rescued the forestomach phenotype in *K-*$Ikk\alpha^{KA/KA}$ mice. We observed esophageal hyperplasia in all three BL6 $Ikk\alpha^{KA/KA}$ mice at 1.2 years of age, but we observed no esophageal phenotypes in all four $Ikk\alpha^{KA/KA}$ mice at 5–7 months of age (Figure S1G). Furthermore, approximately 24% of 25 BL6 $Ikk\alpha^{KA/KA}$ mice at 5–10 months of age developed skin SCCs and all $Ikk\alpha^{KA/KA}$ mice at more than 3 months of age developed epidermal keratinocyte hyperproliferation (Figure S1H; data not shown). Collectively, these results showed a good correlation between the development of SCC and squamous hyperplasia and increased $Ikk\alpha^{KA/KA}$ mouse age. Thus, the squamous cell hyperproliferation and malignancies are associated with IKKα reduction.

Specific Molecular Alterations in the Lungs and Lung SCCs of *L-*$Ikk\alpha^{KA/KA}$ Mice and Similar Molecular Changes in Human and Mouse Lung SCCs

Because *K-*ras^{G12D} induces lung ADCs in mice (DuPage et al., 2009), we sequenced K-, H-, and N-ras cDNA isolated from mouse lung SCCs and found only a low number of random mutations and insertions and no activating mutations in K-, H-, and N-ras (Figure S2A). Using western blot and quantitative real-time PCR (qPCR), we found increases in the stem cell regulators Nanog, Oct3/4, and c-Myc, and small G protein Rhov/Chp (Cdc42 homologous protein) (Aspenström et al., 2007) and decreases in the tumor suppressors p53 and Rb in lung SCCs but not in adjacent lung tissues (Figures 2A and 2B). Similarly to human (Ji et al., 2007; Ring et al., 2009), the levels of insulin growth factor 1, cyclin-dependent kinase 1 (CDK1), Trim29, and p63, and the activities of EGFR, extracellular signal-regulated kinase (ERK), and p38 were elevated in *L-*$Ikk\alpha^{KA/KA}$ lungs and were dramatically increased in lung SCCs compared to WT lungs, while LKB1 levels were significantly decreased in *L-*$Ikk\alpha^{KA/KA}$ lung SCCs compared to WT lungs. In addition, IκBα, an inhibitor of nuclear factor κB (NF-κB) (Ghosh and Karin, 2002), and IKKα levels were reduced, and c-ros-1 receptor tyrosine kinase (ROS1), a pro-oncogene receptor tyrosine kinase (Rikova et al., 2007; Takeuchi et al., 2012), was increased to a similar extent in both *L-*$Ikk\alpha^{KA/KA}$ lungs and SCCs compared to WT lungs, suggesting that the alterations in IKKα, IκBα, and ROS1 levels are ubiquitous rather than epithelial cell-specific in *L-*$Ikk\alpha^{KA/KA}$ mice (Figures 2A and 2B). Because both Trim29 and p63 are specifically expressed in human lung SCCs, we examined their protein levels and found that Trim29 and ΔNp63 levels were increased in *L-*$Ikk\alpha^{KA/KA}$ lungs and further increased in lung SCCs compared to WT lungs (Figure 2C). To determine NF-κB activity, we examined the nuclear p65 levels in the lungs of WT and *L-*$Ikk\alpha^{KA/KA}$ at 4, 16, and 20 weeks of age after depleting $CD45^+$ cells and found elevated nuclear p65 levels in *L-*$Ikk\alpha^{KA/KA}$ lungs with increasing age compared to WT lungs (Figure 2D). We also observed increased p65 levels in the lungs of 16- and 20-week-old *L-*$Ikk\alpha^{KA/KA}$ mice compared to WT using immunohistochemistry (data not shown). Increased nuclear p65 and p50 were detected in a *L-*$Ikk\alpha^{KA/KA}$ lung SCC cell line (KAL^{LU}) compared to a WT lung epithelial cell line M2C (Padilla-Nash et al., 2012) following tumor necrosis factor (TNF) stimulation, and the IKKα level was lower in KAL^{LU} than in M2C cells (Figures 2E and 2F), suggesting that the canonical NF-κB activity was increased in IKKα-deficient lung SCC cells. Collectively, we identified multiple molecular alterations that can be classified into three groups: (1) specifically deregulated in SCCs; (2) deregulated prior to tumor formation; and (3) ubiquitously deregulated in *L-*$Ikk\alpha^{KA/KA}$ mice.

To compare the similarity of molecular alterations between mouse and human lung SCCs, we examined alterations in

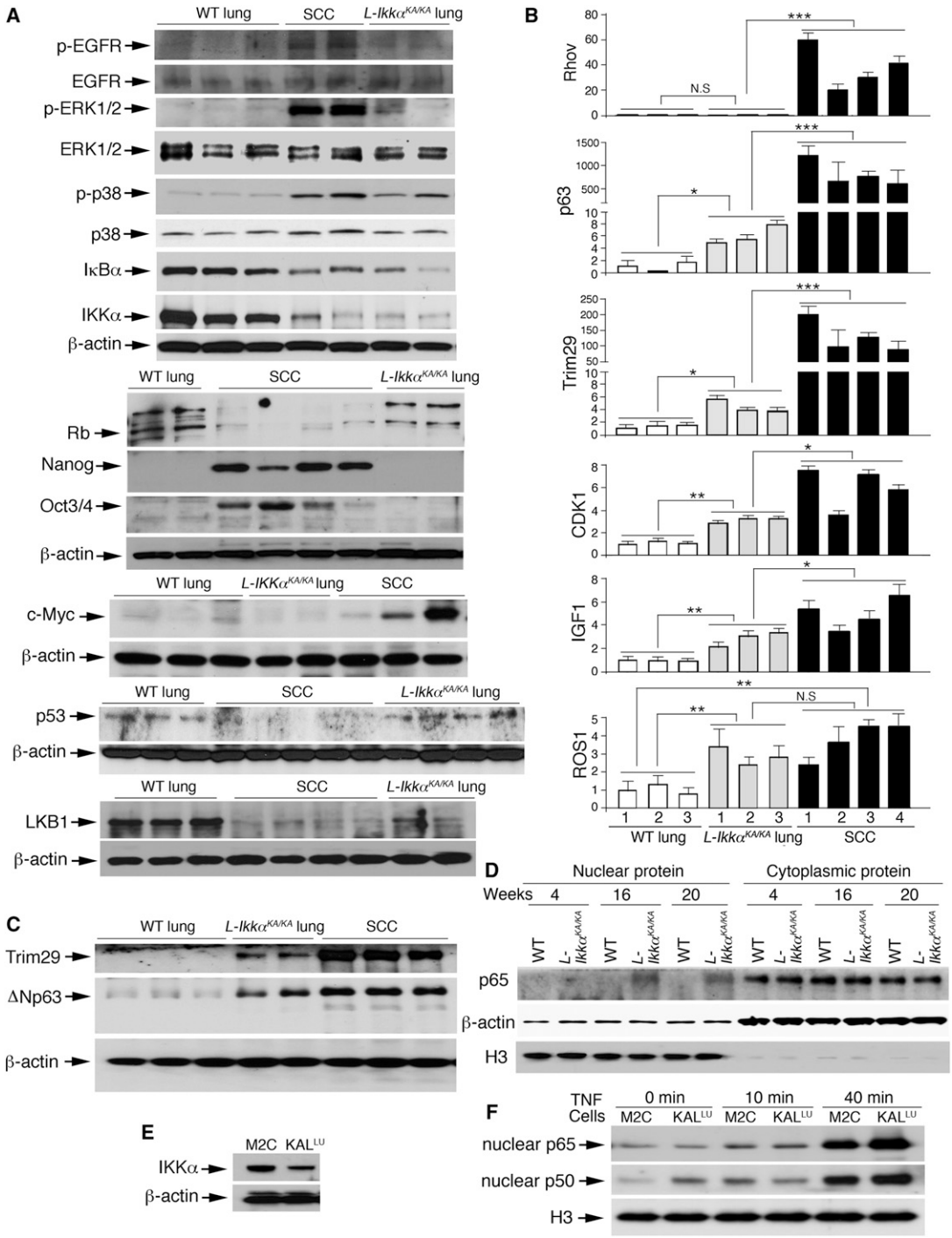

Figure 2. Molecular Alterations in *L-Ikkα*$^{KA/KA}$ Lungs and Lung SCCs

(A) Western blot shows indicated protein levels in WT lungs, *L-Ikkα*$^{KA/KA}$ lung SCCs, and SCC-adjacent lung tissues (*L-Ikkα*$^{KA/KA}$ lungs). β-actin, protein-loading control.

(B) qPCR shows the expression levels (fold) of indicated genes (mean ± SD of three or four mice per group). Each column represents an individual sample that was tested three times. WT and *L-Ikkα*$^{KA/KA}$ lungs were obtained from 9- to 10-week-old mice. *$p < 0.05$; **$p < 0.01$; ***$p < 0.001$ (Student's test). N.S., not statistically significant.

(C) Western blot shows Trim29 and ΔNp63 levels in WT and *L-Ikkα*$^{KA/KA}$ lungs and lung SCCs. β-actin, protein-loading control.

(D) Western blot shows nuclear and cytoplasmic p65 levels in lung cells (CD45$^-$) isolated from WT and *L-Ikkα*$^{KA/KA}$ mice at 4, 16, and 20 weeks of age.

(E) Western blot shows IKKα levels in a WT mouse lung epithelial cell line M2C and an *L-Ikkα*$^{KA/KA}$ lung SCC cell line KAL^{LU}. β-actin, protein-loading control.

(F) Western blot shows nuclear p65 and p50 levels in M2C and KAL^{LU} cells following TNF stimulation (10 ng/ml). H3, histone H3 as nuclear protein loading control; nuclear, nuclear proteins.

See also Figure S2 and Tables S1 and S2.

IKKα, *c-Myc*, and Trim29 in human lung SCCs. Several studies have shown that IKKα is downregulated in a large proportion of human lung SCCs (Kwak et al., 2011; Marinari et al., 2008). We confirmed these findings by showing that IKKα levels as analyzed by western blot were significantly higher in normal human lungs than in all of the eight human lung SCCs and their adjacent lung tissues (Figure S2B). Comparative genomic hybridization revealed *c-Myc* amplification in three (37%) of the eight human lung SCCs (Figure S2C). Moreover, we examined the expression of Trim29 in human lung SCCs compared to cancer-adjacent lung tissues in human tissue array using immunohistochemical (IHC) staining (Figure S2D). Twenty-four (49%) of forty-nine human SCCs strongly expressed Trim29 versus 0 (0%) of 50 in cancer-adjacent lung tissues. Four (8%) of forty-nine human SCCs weakly expressed Trim29 versus 25 (50%) of 50 cancer-adjacent lung tissues. A moderate level of Trim29 immunostaining was detected in 21 (43%) of 49 human SCCs and 25 (50%) of 50 cancer-adjacent lung tissues. In addition to high levels of Trim29 in human and mouse lung SCCs, the localization of Trim29 expression in the cells of human and mouse SCCs was similar (Figures S2E and S2F). These results demonstrate that human and mouse lung SCCs share similar molecular changes.

In addition, we sequenced the genes of *Sox2*, *PIK3CA* (exons 9 and 20), and *DDR2* (exons 4, 7, 12, 13, 14, and 16) in ten lung SCCs derived from *L-Ikkα*$^{KA/KA}$ mice, because the mutations in these genes have been reported in human lung SCCs (Hammerman et al., 2012). We detected several silent mutations in *DDR2* and *Sox2* and some small insertions and deletions in the introns and UTRs of *DDR2* and *Sox2* but no mutations in *PIK3CA* (Tables S1 and S2). Whether these genetic alterations affect the function of these genes remains to be elucidated in the future.

IKKα Suppresses the Expression of ΔNp63 and Trim29 in an Epigenetic Manner

Although ΔNp63 levels were increased in *L-Ikkα*$^{KA/KA}$ lungs compared to WT, the levels were still lower compared to SCCs (Figure 2C). The tumor cells represent the majority of cells in SCCs, whereas the cells in WT and *L-Ikkα*$^{KA/KA}$ lungs are a mixture of epithelial and other cells. Thus, it is possible that the p63 level was already elevated in the K5^{+} epithelial cells in *L-Ikkα*$^{KA/KA}$ lungs. To test this hypothesis, we compared the intensity of ΔNp63 and K5 in WT and *L-Ikkα*$^{KA/KA}$ lungs and lung SCCs using immunofluorescent (IF) staining with anti-ΔNp63 and anti-K5 antibodies. ΔNp63 levels were specifically elevated in the K5^{+} cells of *L-Ikkα*$^{KA/KA}$ lungs compared to WT, and the K5^{+}p63^{hi} cells expanded with the formation of lung SCCs (Figure 3A). The IF-stained ΔNp63 levels were very weak in WT lungs, which is consistent with the results shown in Figures 2B and 2C. Also, Kumar et al. (2011) reported that p63 was undetectable in the lungs of WT mice using IF staining. The intensity of K5 was also elevated in the epithelial cells of *L-Ikkα*$^{KA/KA}$ lungs compared to WT (Figure 3A).

We further investigated whether IKKα regulates the expression of Trim29 and ΔNp63 at the transcriptional level, because mRNA levels of Trim29 and p63 were increased in *L-Ikkα*$^{KA/KA}$ lungs and SCCs compared to WT lungs (Figure 2B). Using the chromatin immunoprecipitation (ChIP) assay with an anti-IKKα antibody, we detected IKKα binding to the promoter regions of *Trim29* and *p63* genes, which was associated with high levels of H3K27me3, a negative transcription modifier, and low levels of H3K4me3, a positive transcription modifier, in WT MEFs; conversely, in *Ikkα*$^{KA/KA}$ and *Ikkα*$^{-/-}$ MEFs and KAL^{LU} lung SCC cells, increased H3K4me3 levels and reduced H3K27me3 levels were associated with the *Trim29* and *p63* loci (Figure 3B). The mRNA levels of Trim29 and ΔNp63 were higher in *Ikkα*$^{KA/KA}$, *Ikkα*$^{-/-}$, and KAL^{LU} cells than in WT cells (Figure 3C). Reintroducing IKKα decreased H3K4me3 levels and increased H3K27me3 levels on *Trim29* and *p63* loci and repressed the expression of Trim29 and p63 in *Ikkα*$^{KA/KA}$, *Ikkα*$^{-/-}$, and KAL^{LU} cells (Figures 3B and 3C). Although *Ikkα*$^{KA/KA}$ MEFs maintained a low level of IKKα, we found that the nuclear kinase-dead IKKα (KA) level was reduced compared to WT IKKα when WT IKKα and IKKα-KA were transfected into cells (data not shown). Thus, the expression levels of Trim29 and ΔNp63 were comparable in *Ikkα*$^{KA/KA}$ and *Ikkα*$^{-/-}$ MEFs. These results suggest that IKKα regulates the expression of both Trim29 and ΔNp63 at the transcription level by modifying the chromatin structure of *Trim29* and *p63* in an epigenetic manner. Furthermore, re-expressed IKKα was found to repress KAL^{LU} cell proliferation compared to the control vector (Figure 3D). Thus, IKKα also inhibited lung epithelial cell proliferation. IHC staining further showed strongly stained nuclear IKKα in the bronchial epithelial cells of WT mice (Figure 3E), which supports the result that IKKα suppressed the expression of ΔNp63 and Trim29 in the nucleus.

Moreover, we examined the relationship between IKKα and the expression of p63 and Trim29 in a WT human bronchial epithelial cell line HBEC (Xi et al., 2010) and a human lung SCC cell line SW-900. Western blot showed a higher IKKα level in HBEC cells than in SW-900 cells (Figure 3F). The expression levels of ΔNp63 and Trim29 were higher in SW-900 cells than in HBEC cells, and reintroducing IKKα repressed the expression of ΔNp63 and Trim29 in SW-900 cells (Figure 3G). ChIP analysis showed higher H3K4me3 levels and lower H3K27me3 levels on *p63* and *Trim29* loci in SW-900 SCC cells compared to HBEC cells (Figure 3H). Reintroducing IKKα reversed H3K4me3 and H3K27me3 levels on *p63* and *Trim29* genes and decreased the expression levels of p63 and Trim29 in SW-900 SCC cells (Figures 3G and 3H). Together, these results indicated a similar regulatory mechanism by which IKKα regulates p63 and Trim29 expression in human and mouse lung epithelial cells.

Excessive Inflammatory Cells, Cytokines, and Chemokines Are Present in the Lungs of *L-Ikkα*$^{KA/KA}$ Mice

To evaluate the effect of the inflammatory microenvironment on lung tumorigenesis, we examined leukocyte infiltration and expression of cytokines and chemokines. We found significantly increased absolute numbers of CD4^{+} cells and macrophages (F4/80^{+}) and moderately increased CD8^{+} cells and neutrophils (Ly6G^{+}/CD11b^{+}) in the lungs of *L-Ikkα*$^{KA/KA}$ mice compared to WT mice at 4 and 16 weeks of age (Figure 4A). B cells did not significantly increase (data not shown), which is consistent with previous results (Balkhi et al., 2012). Significantly increased expression (qPCR analysis) of tumor necrosis factor-α, interleukin (IL)-1β, IL-6, IL-4, IL-13, IL-10, chemokine (C-C motif) ligand 2 (CCL2), chemokine (C-X-C motif) ligand 5, CCL11, and CCL8 was observed in *L-Ikkα*$^{KA/KA}$ lungs compared to WT

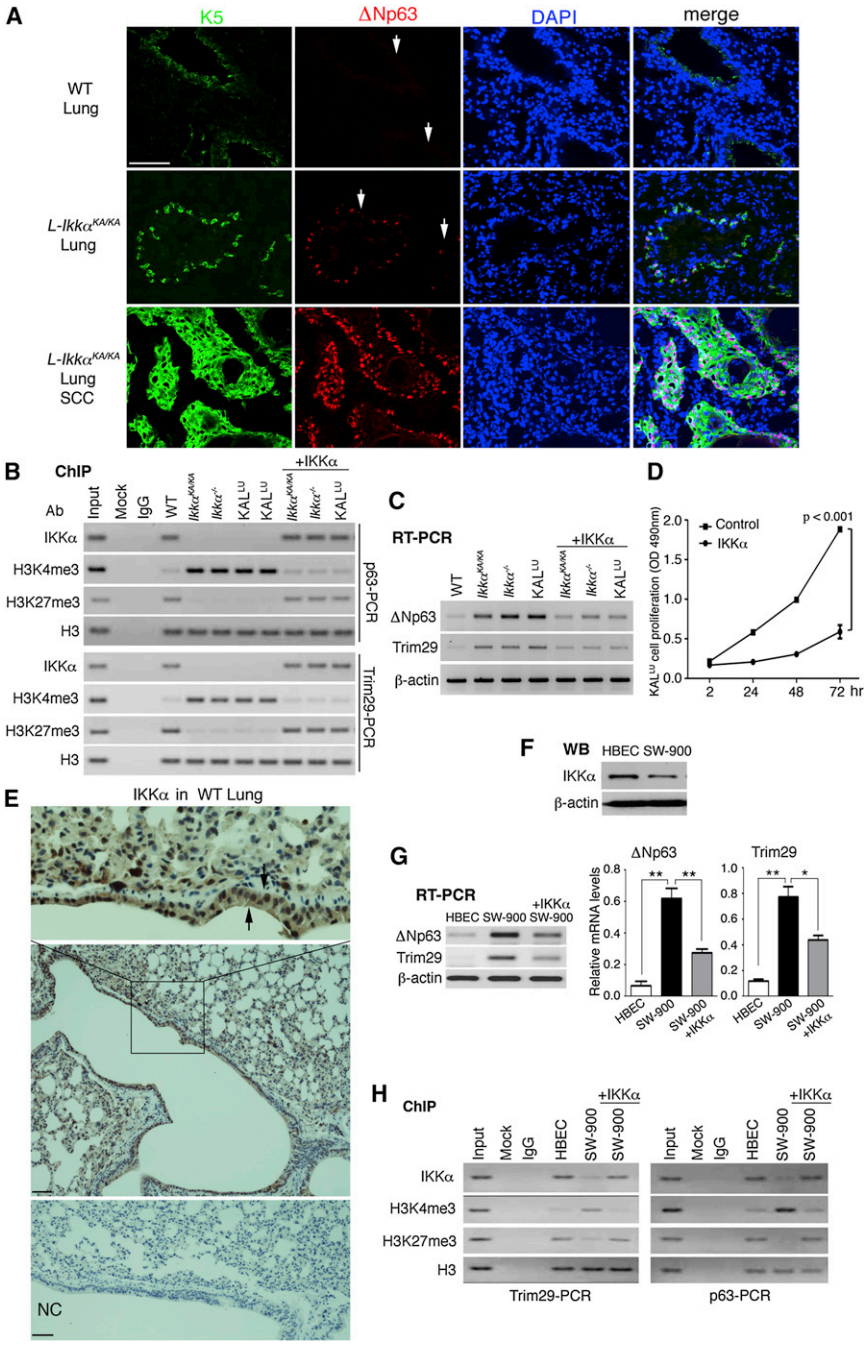

Figure 3. IKKα Regulates Trim29 and p63 Expression in an Epigenetic Manner

(A) Immunofluorescent staining shows K5 (green) and ΔNp63 (red) in WT lungs, *L-Ikkα*$^{KA/KA}$ lungs, and *L-Ikkα*$^{KA/KA}$ lung SCCs. Blue color, DAPI for nuclear staining; arrows indicate ΔNp63 staining. Scale bar, 50 μm.

(B) ChIP assay was performed with indicated antibodies (Abs) and PCR with Trim29 and p63 primers in WT, *Ikkα*$^{KA/KA}$, *Ikkα*$^{-/-}$ MEFs, and a cell line KAL^{LU} from *L-Ikkα*$^{KA/KA}$ lung SCCs. Mock, immunoglobulin G (IgG) as negative controls; +IKKα, reintroducing IKKα into cells; H3, control for ChIP assay.

(C) RT-PCR with ΔNp63 and Trim29 primers from indicated cells. +IKKα, reintroducing IKKα into cells.

(D) The proliferation of KAL^{LU} cells was examined at 2, 24, 48, and 72 hr following transfection with IKKα vector or control vector, using the kit of CellTiter 96 AQ$_{ueous}$ One Solution Cell Proliferation Assay (Promega) and mean ± SD of four samples per group.

(E) IHC staining with an anti-IKKα antibody shows strong nuclear IKKα in the cells of bronchial epithelium of adult WT mice. The area in the box of the middle panel was amplified at the top panel. Brown, positive staining; arrows, bronchial epithelium; blue, nuclear counterstaining; NC, negative control. Scale bar, 50 μm.

(F) Western blotting shows IKKα levels in a WT human lung cell line HBEC and a human lung SCC cell line SW-900. β-actin, protein-loading control.

(G) Left panel: RT-PCR with ΔNp63 and Trim29 primers from indicated cells. +IKKα, reintroducing IKKα into cells. Right panel: the comparison of mRNA levels of ΔNp63 and Trim29 in HBEC and SW-900 cells (mean ± SD of three samples per group). *p < 0.05; **p < 0.01; ***p < 0.01 (Student's test).

(H) ChIP assay was performed with indicated Abs and PCR with Trim29 and p63 primers in a normal human lung cell line and two human lung SCC cell lines. Mock, IgG as negative controls; +IKKα, reintroducing IKKα into cells; H3, control for ChIP assay.

(Figure 4B; Table S3). IF staining showed extensive macrophage infiltration into SCCs and elevated expression of inducible nitric oxide synthase (iNOS) (Lechner et al., 2005) in *L-Ikkα*$^{KA/KA}$ macrophages (Figures 4C and 4D). These results showed that marked inflammation and oxidants were present in *L-Ikkα*$^{KA/KA}$ lungs.

To determine whether increased numbers of macrophages are present in human lung SCCs, we used IHC staining with an anti-CD68 antibody to examine macrophages in a human array containing 32 human lung SCCs with their proximal adjacent lung tissues and distal adjacent lung tissues and found increased macrophages in lung SCCs and proximal adjacent lung tissues compared to distal adjacent lungs, indicating a good correlation between increased macrophages and lung SCC development (Figures 4E and 4F), which is consistent with the observation in the lungs and lung SCCs of *L-Ikkα*$^{KA/KA}$ mice.

Depleting Macrophages Reduces Inflammation and Epithelial Proliferation and Prevents Lung SCC Development

To determine whether inflammation regulates lung SCC development, we depleted macrophages in 7-week-old *L-Ikkα*$^{KA/KA}$ mice by injection of clodronate-loaded liposomes, which induce macrophage apoptosis (Jenkins et al., 2011). A single treatment significantly reduced macrophages in treated *L-Ikkα*$^{KA/KA}$ lungs

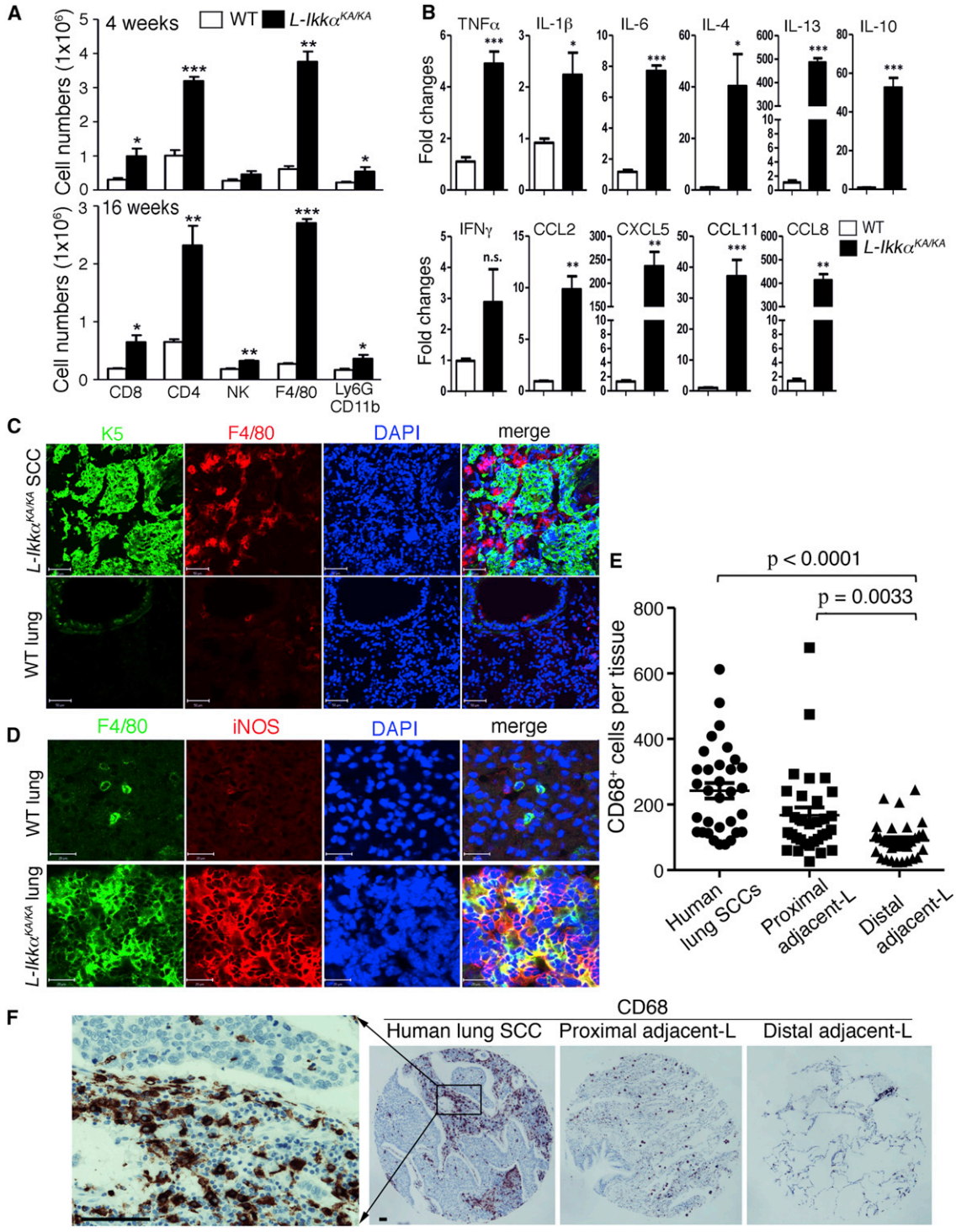

Figure 4. Marked Inflammation in the Lungs of *L-Ikkα*$^{KA/KA}$ Mice

(A) The comparison of indicated leukocytes in the lungs of WT and *L-Ikkα*$^{KA/KA}$ mice at 4 and 16 weeks of age examined with flow cytometry analysis (mean ± SD of four samples per group). *p < 0.05; **p < 0.01; ***p < 0.001.

(B) The expression levels (fold changes) of various cytokines and chemokines in the lungs of *L-Ikkα*$^{KA/KA}$ mice at 4 weeks of age were compared to WT lungs using qPCR. The fold changes were calculated with delta-delta cycle threshold methods (mean ± SD of four samples per group). n.s., not statistically significant.

(C) Macrophages, lung SCCs, and WT lungs were immunofluorescently stained with anti-F4/80 (red for macrophages) and anti-K5 (green for epithelial cells) antibodies. Blue, DAPI for nuclear staining. Scale bar, 50 μm.

(D) The expression of iNOS (red) in macrophages (green) in the lungs of WT and *L-Ikkα*$^{KA/KA}$ mice at 16 weeks of age detected using immunofluorescent staining. Blue, DAPI for nuclear staining. Scale bar, 50 μm.

(legend continued on next page)

compared to untreated *L-Ikkα*$^{KA/KA}$ lungs (Figure 5A). After 3 months of liposome treatment, the weights of *L-Ikkα*$^{KA/KA}$ lungs were significantly reduced in comparison to untreated *L-Ikkα*$^{KA/KA}$ lungs (Figure 5B, right and left panels). The macrophage deletion also decreased Trim29 and ΔNp63 levels, p38 activity, and DNA damage that was indicated by 8-hydroxydeoxyguanosine (Yang et al., 2009) in treated *L-Ikkα*$^{KA/KA}$ lungs (Figures 5C and 5D). Using histological examination, we did not detect lung SCCs in any of the six liposome-treated *L-Ikkα*$^{KA/KA}$ mice.

We analyzed the effect of macrophage depletion on global gene expression by comparing gene expression profiles of *L-Ikkα*$^{KA/KA}$ versus WT lungs and liposome-treated *L-Ikkα*$^{KA/KA}$ versus WT lungs (Figures 5E and S3A); the full gene names are reported in Table S4. K6 and K16, which are highly expressed in hyperproliferative squamous epithelial cells and SCCs (Hackett et al., 2011), as well as K14, K5, and other keratins, were highly expressed in *L-Ikkα*$^{KA/KA}$ lungs compared to WT. Macrophage depletion dramatically reduced the expression of these keratins (Figure 5E, left panel). Macrophage depletion also repressed the expression of cell cycle regulators, metalloproteinases, a disintegrin and metalloproteinases, growth factors, early growth response genes, cytokines, and chemokines, and altered the expression of oxidases in *L-Ikkα*$^{KA/KA}$ lungs (Figures 5E, middle and right panels, and S3A). Although the clodronate-loaded liposome treatment reduced macrophages and prevented lung SCCs, we observed infiltrating lymphocytes in treated *L-Ikkα*$^{KA/KA}$ lungs (Figure S3B). These results indicate that the excessive macrophages increased inflammation, epithelial cell proliferation, DNA damage, and activities of many pathways that may contribute to lung carcinogenesis in *L-Ikkα*$^{KA/KA}$ mice; in contrast, macrophage reduction reverses these abnormal responses.

Because *K-ras*^{G12D};*Lkb1*$^{-/-}$ mice developed mixed lung SCCs and ADCs (Ji et al., 2007) and LKB1 downregulation was found in *L-Ikkα*$^{KA/KA}$ lung SCCs, we examined whether increased numbers of macrophages were present in the lungs of *K-ras*^{G12D};*Lkb1*$^{-/-}$ mice. The IHC staining showed significantly more macrophages in *K-ras*^{G12D};*Lkb1*$^{-/-}$ lungs than in WT lungs but more macrophages in *L-Ikkα*$^{KA/KA}$ lungs than in *K-ras*^{G12D};*Lkb1*$^{-/-}$ lungs (Figures 5F and S3C). These results demonstrated the presence of increased macrophages in the lung SCCs derived from *L-Ikkα*$^{KA/KA}$ mice and *K-ras*^{G12D};*Lkb1*$^{-/-}$ mice, as well as in human lung SCCs.

L-Ikkα$^{KA/KA}$ Bone Marrow Reconstitutes Lung SCCs in Irradiated *L-Ikkα*$^{KA/KA}$ Mice

To investigate the effects of bone marrow (BM)-derived macrophages from WT and *L-Ikkα*$^{KA/KA}$ mice on lung SCC development, we performed BM transplant experiments by intravenously injecting either *L-Ikkα*$^{KA/KA}$ BM into irradiated *L-Ikkα*$^{KA/KA}$ and WT mice or WT BM into irradiated *L-Ikkα*$^{KA/KA}$ mice (Figure S4A). The irradiated WT mice receiving WT BM were similar to WT mice (data not shown). At 3 months after the BM injection, all of the ten irradiated *L-Ikkα*$^{KA/KA}$ mice receiving *L-Ikkα*$^{KA/KA}$ BM had enlarged lungs infiltrated with many macrophages and lymphocytes and developed lung SCCs; all of the seven irradiated WT mice receiving *L-Ikkα*$^{KA/KA}$ BM were SCC-free, and their lungs were infiltrated with a few macrophages and lymphocytes (Figures 6A–6C and S4B). Six out of seven irradiated *L-Ikkα*$^{KA/KA}$ mice receiving WT BM were SCC-free; their lungs, which were infiltrated with many lymphocytes but reduced macrophages, were smaller than the lungs of *L-Ikkα*$^{KA/KA}$ mice receiving *L-Ikkα*$^{KA/KA}$ BM but larger than the lungs of WT mice receiving *L-Ikkα*$^{KA/KA}$ BM (Figures 6A–6C and S4B). However, one out of seven irradiated *L-Ikkα*$^{KA/KA}$ mice receiving WT BM developed a very large lung SCC (Figure S4B). Because we performed BM transplant experiments in mice at 4 or 5 weeks of age and increased pulmonary inflammation was already observed in the lungs of 4-week-old *L-Ikkα*$^{KA/KA}$ mice (Figure 4A), it is possible that the development of this tumor began prior to BM transfer. These results further showed that *L-Ikkα*$^{KA/KA}$-derived macrophages are associated with lung SCC development.

DISCUSSION

IKKα Downregulation Is Associated with Lung Enlargement and Lung SCC Development

In this study, we showed that the lungs of *L-Ikkα*$^{KA/KA}$ newborn mice were relatively normal. The K44A mutation in IKKα destabilized the protein. With increasing age and decreasing IKKα levels, the lungs became enlarged and lung SCCs occurred in *L-Ikkα*$^{KA/KA}$ mice. Reintroducing transgenic K5.IKKα prevented lung enlargement and tumorigenesis, and re-expressing WT IKKα repressed the proliferation of KAL^{LU} lung SCC cells, suggesting that IKKα is important for the tumor initiation and maintenance. The elevated activities of EGFR/ERK, cell cycle regulators, and growth factors may largely contribute to cell proliferation in the lungs of *L-Ikkα*$^{KA/KA}$ mice. We previously reported that IKKα loss promotes keratinocyte proliferation and induces spontaneous skin SCCs (Liu et al., 2008). In the current study of *Ikkα*$^{KA/KA}$ mice, we found squamous cell hyperproliferation and SCCs in the forestomach, esophagus, and skin, which were associated with IKKα reduction. Again, reintroducing K5.IKKα rescued these phenotypes. These findings demonstrate that IKKα is required for maintaining the normal function of squamous cells in multiple epithelial organs.

Furthermore, we found significant downregulation of LKB1, a tumor suppressor, in *L-Ikkα*$^{KA/KA}$ lung SCCs and adjacent lung tissues compared to WT lungs. It is known that *Lkb1* deletion promotes SCC development in both the lungs and skin (Gurumurthy et al., 2008; Ji et al., 2007). *Lkb1*$^{-/-}$ knockout mice died at midgestation with vascular and neural tube defects (Ylikorkala et al., 2001). Thus, the role of LKB1 in the formation of stratified epithelial organs is unclear. K14.Cre-mediated *Lkb1*

(E) Comparison of IHC-stained CD68^{+} cell counts in each tissue of the human array slide (LC991) among three groups (mean ± SD of 32 tissues per group). The p value was examined by Student's test.
(F) One representative case [see (E)] was shown, and the region in the box was amplified in the left panel, indicated by lines. Brown, CD68 positive staining; blue, nuclear counterstaining; -L, lung tissue. Scale bar, 50 μm.
See also Table S3.

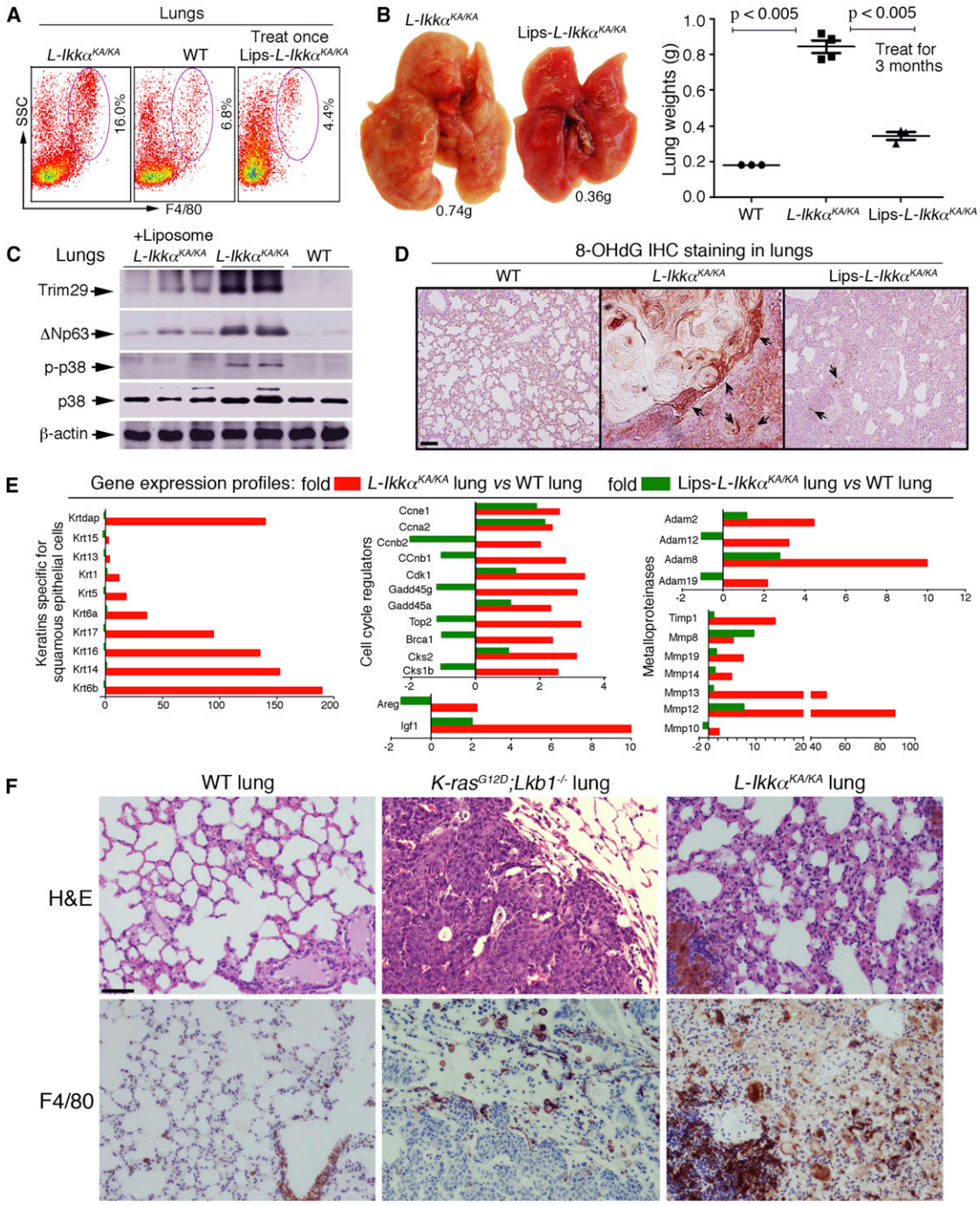

Figure 5. Depletion of Macrophages Prevents Lung SCC Development

(A) Flow cytometry analysis shows the number of macrophages (F4/80) in the lungs of WT, *L-Ikkα*$^{KA/KA}$, and liposome-treated (Lips-, one treatment) *L-Ikkα*$^{KA/KA}$ mice.

(B) Left panel: the lungs (g, gram) of *L-Ikkα*$^{KA/KA}$ mice after 3 months of treatment and untreated *L-Ikkα*$^{KA/KA}$ mice. Right panel: the comparison of the lung weights of treated *L-Ikkα*$^{KA/KA}$, untreated *L-Ikkα*$^{KA/KA}$, and WT mice (mean ± SD of three or four mice per group).

(C) Trim29, ΔNp63, p38, and p-p38 levels in WT, *L-Ikkα*$^{KA/KA}$, and Lips-*L-Ikkα*$^{KA/KA}$ lungs detected using western blotting. β-actin, protein-loading control.

(D) The IHC-stained 8-hydroxydeoxyguanosine in WT, *L-Ikkα*$^{KA/KA}$, and Lips-*L-Ikkα*$^{KA/KA}$ lungs. Brown, positive staining. Scale bar, 50 μm.

(E) The comparison of the gene expression profiles (fold) of *L-Ikkα*$^{KA/KA}$ versus WT (red bars) and Lips-*L-Ikkα*$^{KA/KA}$ versus WT lungs (green bars) using microarray.

(F) H&E- or F4/80-IHC-stained lungs of WT, *K-ras*^{G12D};*Lkb1*$^{-/-}$, and *L-Ikkα*$^{KA/KA}$ mice. Blue, nuclear-countering staining; brown, positive staining. Scale bar, 50 μm.

See also Figure S3 and Table S4.

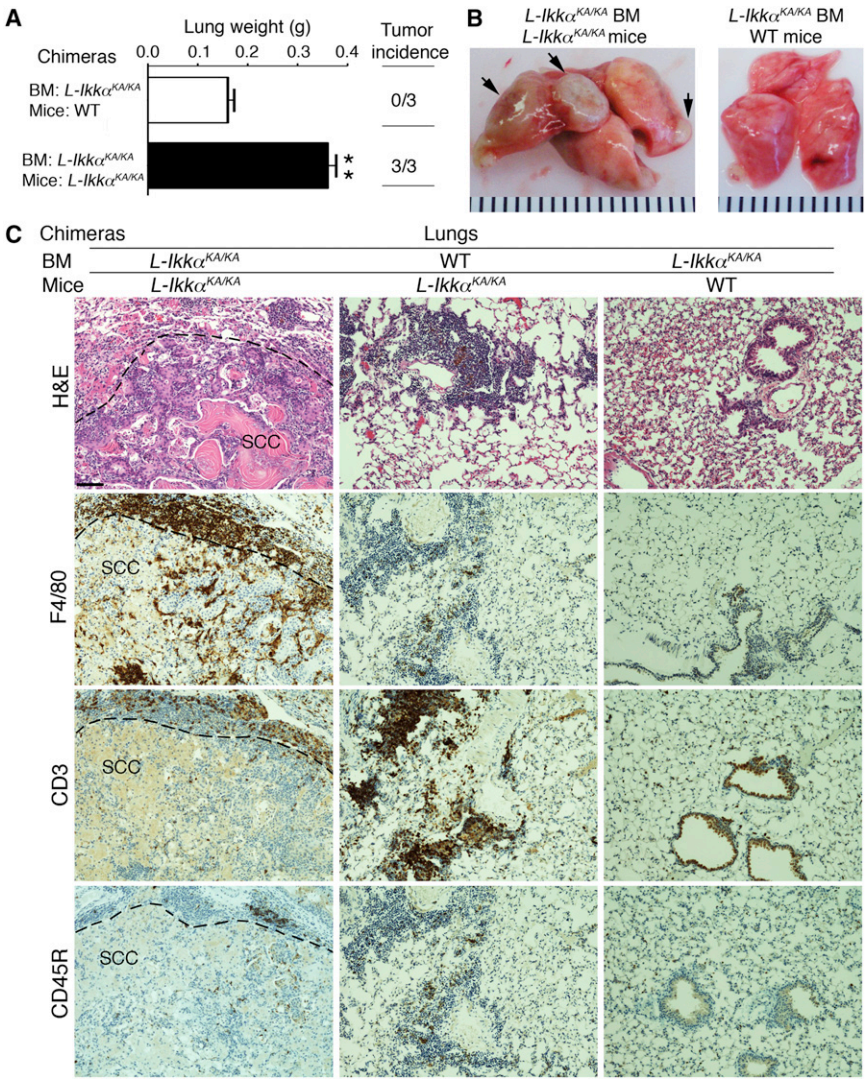

Figure 6. The Effect of BM Cells on Inflammation and SCC Development in the Lungs of Mice

(A) Left panel: the lung weights (g, gram) of irradiated WT and *L-Ikkα*$^{KA/KA}$ chimeras at 16 weeks of age (mean ± SD of three mice per group). Right panel: tumor incidence in indicated irradiated chimeras. **$p < 0.01$.

(B) The appearance of indicated mice at 4 months of age.

(C) H&E staining and IHC-CD3, -F4/80, and -CD45R staining in the lungs of indicated irradiated chimera. Brown, positive staining; blue, nuclear counterstaining. Scale bar, 50 μm.

See also Figure S4.

deletion does not cause epidermal hyperplasia and does not promote the development of chemical carcinogen-induced benign papillomas, but it does enhance malignant skin SCC development (Gurumurthy et al., 2008), suggesting that LKB1 loss does not provide a selective growth advantage. Interestingly, however, LKB1 loss-associated SCCs showed increased EGFR and ERK activities; thus, an indirect mechanism may activate EGFR/ERK pathways, which cooperate with LKB1 deficiency to promote carcinogenesis. Although the mechanism of how IKKα regulates LKB1 expression in different cell types remains to be elucidated, the phenotypic similarities and differences between IKKα and LKB1 suggest that LKB1 reduction provides an important pathway to promote IKKα deficiency-associated tumorigenesis.

In this study, IHC staining showed that the majority of IKKα was located in the nuclei of lung epithelial cells, underscoring the importance of nuclear IKKα in maintaining the normality of lung epithelial cells. We found that IKKα deficiency increased the transcription levels of Trim29 and ΔNp63 and that reintroduced WT IKKα repressed the expression of Trim29 and ΔNp63 by modifying H3K4me3 and H3K27me3 levels on the *Trim29* and *p63* loci, indicating that Trim29 and ΔNp63 are IKKα targets in the lung epithelial cells. Human lung SCC cells are K5$^+$ and overexpress p63 and Trim29 (Ring et al., 2009). In mice, *Ikkα* loss promotes K5$^+$ keratinocyte proliferation (Hu et al., 1999, 2001; Liu et al., 2008). Here, we observed K5$^+$p63^{hi} cells in the lungs of *L-Ikkα*$^{KA/KA}$ mice as well as in lung SCCs but not in WT mice, and re-expression of IKKα under the K5 promoter prevented lung SCC development in *Ikkα*$^{KA/KA}$ mice. We will further investigate whether IKKα^{low}K5$^+$p63^{hi} cells have stem cell features and whether IKKα^{low}K5$^+$p63^{hi} cells serve as tumor-initiating cells.

In addition to the further changes in EGFR/ERK activity and Trim29, ΔNp63, IGF, CDK1, and LKB1 levels in SCCs, only lung SCCs, not precancerous lungs, from *L-Ikkα*$^{KA/KA}$ mice showed decreased p53 and Rb and increased Nanog, Oct3/4, c-Myc, and Rhov traits, which have also been reported in human lung SCCs (Larsen and Minna, 2011; Yuan et al., 2010). It is known that p53 loss can promote tumorigenesis by accelerating pluripotent cell generation induced by stem cell regulators (Utikal et al., 2009). Elevated small G proteins can regulate the cytoskeleton and cellular polarity and promote mitogen-activated protein kinase and EGFR activities, tumor cell proliferation, and abnormal polarity, resulting in tumor genomic heterogeneity (Iden and Collard, 2008). These combined abnormal properties may be critical for maintaining the specific oncogenic cell lineage during lung SCC development in *L-Ikkα*$^{KA/KA}$ mice. Although *p53* genetic alterations are most frequently detected in human lung SCCs (Hammerman et al., 2012), most human lung SCCs bear multiple genetic alterations. Mice lacking p53 and Rb or overexpressing the oncogenes and stem-like genes do not develop spontaneous lung SCCs. Therefore, these specific molecular alterations in *L-Ikkα*$^{KA/KA}$ lungs and lung SCCs may be important for lung SCC development.

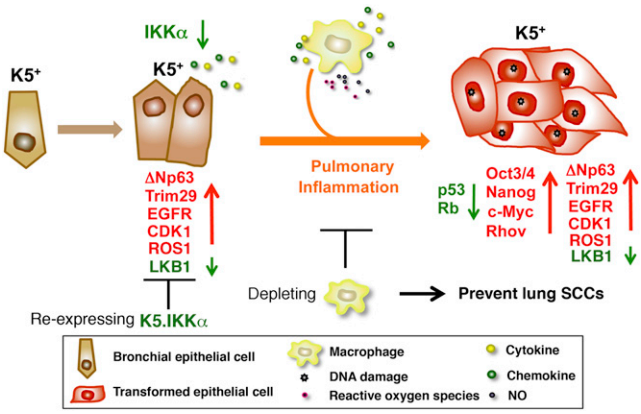

Figure 7. A Working Model of Lung SCC Development in *L-Ikkα*$^{KA/KA}$ Mice

IKKα downregulation dysregulates the expression of multiple oncogenes and tumor suppressors in K5$^+$ lung epithelial cells. The mutant macrophages increase inflammatory responses and oxidative stress to promote DNA damage in IKKα mutant K5$^+$ lung epithelial cells, which further dysregulate the levels of multiple oncogenes, tumor suppressors, and stem cell genes, thereby promoting the IKKα^{low}K5$^+$p63^{hi} cell transition to tumor cells in *L-Ikkα*$^{KA/KA}$ lungs. Arrow down (green), downregulation; arrow up (red), upregulation; crossing two lines, inhibition.

Inflammation Is Required for Lung SCC Development in *L-Ikkα*$^{KA/KA}$ Mice

Notably, adult *L-Ikkα*$^{KA/KA}$ mice retain a low level of IKKα. Previously, we showed that *Ikkα*$^{+/-}$ mice were relatively normal but were haploid insufficient in chemical carcinogen-induced skin carcinogenesis (Park et al., 2007), suggesting that reduced IKKα fails to protect skin cells from environmental inducers. Thus, it is possible that microenvironmental signals may trigger and accelerate the development of lung malignancy in *L-Ikkα*$^{KA/KA}$ mice. Most human lung SCC patients have a long history of smoking, which is known to induce DNA damage and inflammation and to affect immune functions (Hecht, 2003). Defining these inflammatory inducers may facilitate the development of immunotherapy for human lung SCCs.

In this study, we found markedly higher infiltration of macrophages and lymphocytes and expression of cytokines and chemokines in *L-Ikkα*$^{KA/KA}$ lungs compared to WT lungs. The pulmonary inflammation and lung enlargement occurred prior to SCC formation. Macrophage depletion using liposome treatment significantly reduced lung weights and prevented SCC formation in *L-Ikkα*$^{KA/KA}$ mice, indicating that increased macrophages promote lung SCC development. Although macrophages were reduced, infiltrating lymphocytes were still present in the lungs of treated *L-Ikkα*$^{KA/KA}$ mice, suggesting that the lymphocytes alone were not sufficient to promote lung tumorigenesis. The precise functions of lymphocytes in the lung SCC development in *L-Ikkα*$^{KA/KA}$ mice remain to be further investigated.

Previously, we demonstrated that kinase-dead IKKα downregulates the expression of Pax5, a B cell regulator, thereby impairing early B cell development and promoting myeloid-cell differentiation in *Ikkα*$^{KA/KA}$ BM (Balkhi et al., 2012). It is possible that increased mutant macrophages may be one of the inducers for lung SCC development. The BM transfer experiments showed that six of seven irradiated *L-Ikkα*$^{KA/KA}$ mice receiving WT BM were SCC-free; all irradiated *L-Ikkα*$^{KA/KA}$ mice receiving *L-Ikkα*$^{KA/KA}$ BM developed lung SCCs. Although we observed markedly increased lymphocytes in the lungs of both irradiated *L-Ikkα*$^{KA/KA}$ mice, there were more macrophages in the lungs of irradiated *L-Ikkα*$^{KA/KA}$ mice receiving *L-Ikkα*$^{KA/KA}$ BM than in the lungs of irradiated *L-Ikkα*$^{KA/KA}$ mice receiving WT BM. Together, these results suggest that *L-Ikkα*$^{KA/KA}$ BM, not WT BM, strongly promotes lung SCC development. In addition, we observed a good correlation between increased macrophages and human lung SCCs or/and lungs bearing SCCs and ADCs in *K-ras*^{G12D};*Lkb1*$^{-/-}$ mice, although the effect of increased macrophages on lung tumorigenesis in different systems remains to be determined in the future.

It is well known that macrophages generate oxidative stresses that can induce DNA damage (Hanahan and Coussens, 2012). We observed increased iNOS, a source of oxidative stress, in *L-Ikkα*$^{KA/KA}$ macrophages and increased DNA damage in *L-Ikkα*$^{KA/KA}$ lungs compared to WT. These IKKα mutant macrophages were surrounding the SCCs as well as infiltrating into SCCs. Depleting macrophages not only repressed ΔNp63 and Trim29 expression, K5$^+$ epithelial cell expansion, and oxidative stress-associated DNA damage, but also prevented SCCs in the *L-Ikkα*$^{KA/KA}$ lungs. Thus, the inflammation-mediated DNA damage may facilitate to select and promote the IKKα^{low}K5$^+$p63^{hi} cell transition to SCC cells by deregulating tumor suppressors, oncogenic proteins, and stem cell regulators (Figure 7). In the future, it will be important to precisely define the critical molecular events in *L-Ikkα*$^{KA/KA}$ macrophages that promote lung SCC development and the specific signature of the inflammation-mediated DNA damage in lung SCCs, and whether IKKα kinase inactivation plays a role in promoting gene instability in the lung epithelial cells surrounded by an inflamed microenvironment. In addition, we found IKKα downregulation in SCC adjacent lung tissues. Thus, further investigation is needed to determine whether reduced IKKα contributes to the inflammatory microenvironment.

The results obtained in BM transfer experiments and in those in which IKKα was re-expressed in K5-expressing cells showed that the IKKα mutant lung epithelium contributed to the development of inflammation and SCCs in *L-Ikkα*$^{KA/KA}$ mice. Many overexpressed factors, such as IL-13 and IL-4, may educate macrophages in inflamed *L-Ikkα*$^{KA/KA}$ lungs (Biswas and Mantovani, 2010). Thus, identifying crucial inflammatory mediators may help to develop immunotherapy for lung SCCs. IKKα regulates canonical and noncanonical NF-κB signaling pathways (Sun, 2011), and its activity is different for these NF-κB pathways in different types of cells, due to specific cell receptors (Balkhi et al., 2012). Previously, we showed that IKKα loss reduces IκBα levels and elevates TNF-mediated NF-κB activity in keratinocytes, because the stronger IKKβ kinase may replace IKKα in the IKK complex (Hu et al., 2001; Park et al., 2007). On the other hand, canonical and noncanonical NF-κB activities are decreased in the BM B cells of *Ikkα*$^{KA/KA}$ mice (Balkhi et al., 2012). In this study, we found that the levels of IκBα were reduced in *L-Ikkα*$^{KA/KA}$ lungs compared to WT. The canonical NF-κB activity was higher in *L-Ikkα*$^{KA/KA}$ lungs (CD45$^-$ cells), lung SCCs, and *L-Ikkα*$^{KA/KA}$ lung SCC cell line than in WT lungs and a WT lung epithelial cell line. Some cytokines and

chemokines overexpressed in *L-Ikkα*$^{KA/KA}$ lungs are NF-κB targets and may help with recruiting leukocytes to the lungs. Also, increased NF-κB activity can reduce cell apoptosis (Ghosh and Karin, 2002). Therefore, we will further determine whether the increased canonical NF-κB pathway contributes to lung SCC development in *L-Ikkα*$^{KA/KA}$ mice and whether the NF-κB pathway can be used as a therapeutic target to prevent and treat lung SCCs.

EXPERIMENTAL PROCEDURES

Animal Experiments, Human Samples, and Microarray Data

All mice used in this study were cared for in accordance with the guidelines of the Institutional Animal Care and Use Committee (IACUC) of the National Institutes of Health, and all animal experiments were approved by IACUC (protocols 08-074, 08-075, 11-051, and 11-052). *Ikkα*$^{KA/KA}$ (Zhu et al., 2007), Lori.IKKα (Liu et al., 2006), and K5.IKKα (Liu et al., 2011) mice with FVB or BL6 background were used in this study. Human lung tumors were obtained from Dr. David Schrump at the Surgery Branch, National Cancer Institute. All human samples used in this study were approved by National Institutes of Health Internal Review Board (protocol 06-C-0014), and informed consent has been obtained from patients. Human normal lung tissue lysates were obtained from abcam (ab43320, ab42178, and ab42527, Cambridge, MA). The tissue array (LC991) containing 32 human SCCs with their proximal and distal adjacent lung tissues was purchased from US Biomax. The human lung squamous cell carcinoma cell line SW-900 (HTB-59) was purchased from American Type Culture Collection. Dr. Kwok-Kin Wong provided the paraffin lung sections of five *K-ras*^{G12D};*Lkb1*$^{-/-}$ mice, and this animal experiment was approved by IACUC of Harvard Medical School (protocol 04-094) (Ji et al., 2007).

ACCESSION NUMBERS

Microarray results (accession number: GSE37655) have been deposited at the NCBI Gene Expression Omnibus (http://www.ncbi.nlm.nih.gov/geo/).

SUPPLEMENTAL INFORMATION

Supplemental Information includes four figures, four tables, and Supplemental Experimental Procedures and can be found with this article online at http://dx.doi.org/10.1016/j.ccr.2013.03.009.

ACKNOWLEDGMENTS

We thank Teri Plona, Scott Coccodrilli, Arati Raziuddin, Hue Vuong, Vika Grinberg, and Robin Stewart from Laboratory of Molecular Technology, SAIC-Frederick, Inc., Frederick National Laboratory for Cancer Research for sequencing *DDR2*, *Sox2*, and *PIK3CA* genes in mouse lung SCCs and Dr. Hesed Padilla-Nash and Dr. Thomas Ried from National Institutes of Health for kindly providing a spontaneously transformed lung murine epithelial cell line M2C. This work was supported by the National Cancer Institute (ZIA BC 011212 and ZIA BC 011391 to Y.H.).

Received: October 27, 2012
Revised: January 21, 2013
Accepted: March 12, 2013
Published: April 15, 2013

REFERENCES

Aspenström, P., Ruusala, A., and Pacholsky, D. (2007). Taking Rho GTPases to the next level: the cellular functions of atypical Rho GTPases. Exp. Cell Res. *313*, 3673–3679.

Balkhi, M.Y., Willette-Brown, J., Zhu, F., Chen, Z., Liu, S., Guttridge, D.C., Karin, M., and Hu, Y. (2012). IKKα-mediated signaling circuitry regulates early B lymphopoiesis during hematopoiesis. Blood *119*, 5467–5477.

Bardeesy, N., Sinha, M., Hezel, A.F., Signoretti, S., Hathaway, N.A., Sharpless, N.E., Loda, M., Carrasco, D.R., and DePinho, R.A. (2002). Loss of the Lkb1 tumour suppressor provokes intestinal polyposis but resistance to transformation. Nature *419*, 162–167.

Bernstein, B.E., Mikkelsen, T.S., Xie, X., Kamal, M., Huebert, D.J., Cuff, J., Fry, B., Meissner, A., Wernig, M., Plath, K., et al. (2006). A bivalent chromatin structure marks key developmental genes in embryonic stem cells. Cell *125*, 315–326.

Biswas, S.K., and Mantovani, A. (2010). Macrophage plasticity and interaction with lymphocyte subsets: cancer as a paradigm. Nat. Immunol. *11*, 889–896.

Descargues, P., Sil, A.K., Sano, Y., Korchynskyi, O., Han, G., Owens, P., Wang, X.J., and Karin, M. (2008). IKKalpha is a critical coregulator of a Smad4-independent TGFbeta-Smad2/3 signaling pathway that controls keratinocyte differentiation. Proc. Natl. Acad. Sci. USA *105*, 2487–2492.

DuPage, M., Dooley, A.L., and Jacks, T. (2009). Conditional mouse lung cancer models using adenoviral or lentiviral delivery of Cre recombinase. Nat. Protoc. *4*, 1064–1072.

Ghosh, S., and Karin, M. (2002). Missing pieces in the NF-kappaB puzzle. Cell Suppl. *109*, S81–S96.

Gurumurthy, S., Hezel, A.F., Sahin, E., Berger, J.H., Bosenberg, M.W., and Bardeesy, N. (2008). LKB1 deficiency sensitizes mice to carcinogen-induced tumorigenesis. Cancer Res. *68*, 55–63.

Hackett, N.R., Shaykhiev, R., Walters, M.S., Wang, R., Zwick, R.K., Ferris, B., Witover, B., Salit, J., and Crystal, R.G. (2011). The human airway epithelial basal cell transcriptome. PLoS ONE *6*, e18378.

Hammerman, P.S., Hayes, D.N., Wilkerson, M.D., Schultz, N., Bose, R., Chu, A., Collisson, E.A., Cope, L., Creighton, C.J., Getz, G., et al.; Cancer Genome Atlas Research Network. (2012). Comprehensive genomic characterization of squamous cell lung cancers. Nature *489*, 519–525.

Hanahan, D., and Coussens, L.M. (2012). Accessories to the crime: functions of cells recruited to the tumor microenvironment. Cancer Cell *21*, 309–322.

Hatakeyama, S. (2011). TRIM proteins and cancer. Nat. Rev. Cancer *11*, 792–804.

Hearle, N., Schumacher, V., Menko, F.H., Olschwang, S., Boardman, L.A., Gille, J.J., Keller, J.J., Westerman, A.M., Scott, R.J., Lim, W., et al. (2006). Frequency and spectrum of cancers in the Peutz-Jeghers syndrome. Clin. Cancer Res. *12*, 3209–3215.

Hecht, S.S. (2003). Tobacco carcinogens, their biomarkers and tobacco-induced cancer. Nat. Rev. Cancer *3*, 733–744.

Hu, Y., Baud, V., Delhase, M., Zhang, P., Deerinck, T., Ellisman, M., Johnson, R., and Karin, M. (1999). Abnormal morphogenesis but intact IKK activation in mice lacking the IKKalpha subunit of IkappaB kinase. Science *284*, 316–320.

Hu, Y., Baud, V., Oga, T., Kim, K.I., Yoshida, K., and Karin, M. (2001). IKKalpha controls formation of the epidermis independently of NF-kappaB. Nature *410*, 710–714.

Iden, S., and Collard, J.G. (2008). Crosstalk between small GTPases and polarity proteins in cell polarization. Nat. Rev. Mol. Cell Biol. *9*, 846–859.

Jenkins, S.J., Ruckerl, D., Cook, P.C., Jones, L.H., Finkelman, F.D., van Rooijen, N., MacDonald, A.S., and Allen, J.E. (2011). Local macrophage proliferation, rather than recruitment from the blood, is a signature of TH2 inflammation. Science *332*, 1284–1288.

Ji, H., Ramsey, M.R., Hayes, D.N., Fan, C., McNamara, K., Kozlowski, P., Torrice, C., Wu, M.C., Shimamura, T., Perera, S.A., et al. (2007). LKB1 modulates lung cancer differentiation and metastasis. Nature *448*, 807–810.

Johnson, L., Mercer, K., Greenbaum, D., Bronson, R.T., Crowley, D., Tuveson, D.A., and Jacks, T. (2001). Somatic activation of the K-ras oncogene causes early onset lung cancer in mice. Nature *410*, 1111–1116.

Koster, M.I., Dai, D., Marinari, B., Sano, Y., Costanzo, A., Karin, M., and Roop, D.R. (2007). p63 induces key target genes required for epidermal morphogenesis. Proc. Natl. Acad. Sci. USA *104*, 3255–3260.

Kumar, P.A., Hu, Y., Yamamoto, Y., Hoe, N.B., Wei, T.S., Mu, D., Sun, Y., Joo, L.S., Dagher, R., Zielonka, E.M., et al. (2011). Distal airway stem cells yield alveoli in vitro and during lung regeneration following H1N1 influenza infection. Cell *147*, 525–538.

Kwak, Y.T., Radaideh, S.M., Ding, L., Li, R., Frenkel, E., Story, M.D., Girard, L., Minna, J., and Verma, U.N. (2011). Cells lacking IKKα show nuclear cyclin D1 overexpression and a neoplastic phenotype: role of IKKα as a tumor suppressor. Mol. Cancer Res. *9*, 341–349.

Larsen, J.E., and Minna, J.D. (2011). Molecular biology of lung cancer: clinical implications. Clin. Chest Med. *32*, 703–740.

Lechner, M., Lirk, P., and Rieder, J. (2005). Inducible nitric oxide synthase (iNOS) in tumor biology: the two sides of the same coin. Semin. Cancer Biol. *15*, 277–289.

Liu, B., Park, E., Zhu, F., Bustos, T., Liu, J., Shen, J., Fischer, S.M., and Hu, Y. (2006). A critical role for I kappaB kinase alpha in the development of human and mouse squamous cell carcinomas. Proc. Natl. Acad. Sci. USA *103*, 17202–17207.

Liu, B., Xia, X., Zhu, F., Park, E., Carbajal, S., Kiguchi, K., DiGiovanni, J., Fischer, S.M., and Hu, Y. (2008). IKKalpha is required to maintain skin homeostasis and prevent skin cancer. Cancer Cell *14*, 212–225.

Liu, B., Willette-Brown, J., Liu, S., Chen, X., Fischer, S.M., and Hu, Y. (2011). IKKα represses a network of inflammation and proliferation pathways and elevates c-Myc antagonists and differentiation in a dose-dependent manner in the skin. Cell Death Differ. *18*, 1854–1864.

Marinari, B., Moretti, F., Botti, E., Giustizieri, M.L., Descargues, P., Giunta, A., Stolfi, C., Ballaro, C., Papoutsaki, M., Alemà, S., et al. (2008). The tumor suppressor activity of IKKalpha in stratified epithelia is exerted in part via the TGF-beta antiproliferative pathway. Proc. Natl. Acad. Sci. USA *105*, 17091–17096.

Melino, G. (2011). p63 is a suppressor of tumorigenesis and metastasis interacting with mutant p53. Cell Death Differ. *18*, 1487–1499.

Padilla-Nash, H.M., Hathcock, K., McNeil, N.E., Mack, D., Hoeppner, D., Ravin, R., Knutsen, T., Yonescu, R., Wangsa, D., Dorritie, K., et al. (2012). Spontaneous transformation of murine epithelial cells requires the early acquisition of specific chromosomal aneuploidies and genomic imbalances. Genes Chromosomes Cancer *51*, 353–374.

Park, E., Zhu, F., Liu, B., Xia, X., Shen, J., Bustos, T., Fischer, S.M., and Hu, Y. (2007). Reduction in IkappaB kinase alpha expression promotes the development of skin papillomas and carcinomas. Cancer Res. *67*, 9158–9168.

Rikova, K., Guo, A., Zeng, Q., Possemato, A., Yu, J., Haack, H., Nardone, J., Lee, K., Reeves, C., Li, Y., et al. (2007). Global survey of phosphotyrosine signaling identifies oncogenic kinases in lung cancer. Cell *131*, 1190–1203.

Ring, B.Z., Seitz, R.S., Beck, R.A., Shasteen, W.J., Soltermann, A., Arbogast, S., Robert, F., Schreeder, M.T., and Ross, D.T. (2009). A novel five-antibody immunohistochemical test for subclassification of lung carcinoma. Mod. Pathol. *22*, 1032–1043.

Sun, S.C. (2011). Non-canonical NF-κB signaling pathway. Cell Res. *21*, 71–85.

Takeuchi, K., Soda, M., Togashi, Y., Suzuki, R., Sakata, S., Hatano, S., Asaka, R., Hamanaka, W., Ninomiya, H., Uehara, H., et al. (2012). RET, ROS1 and ALK fusions in lung cancer. Nat. Med. *18*, 378–381.

Utikal, J., Polo, J.M., Stadtfeld, M., Maherali, N., Kulalert, W., Walsh, R.M., Khalil, A., Rheinwald, J.G., and Hochedlinger, K. (2009). Immortalization eliminates a roadblock during cellular reprogramming into iPS cells. Nature *460*, 1145–1148.

Vanbokhoven, H., Melino, G., Candi, E., and Declercq, W. (2011). p63, a story of mice and men. J. Invest. Dermatol. *131*, 1196–1207.

Woodworth, C.D., Mossman, B.T., and Craighead, J.E. (1983). Induction of squamous metaplasia in organ cultures of hamster trachea by naturally occurring and synthetic fibers. Cancer Res. *43*, 4906–4912.

Xi, S., Yang, M., Tao, Y., Xu, H., Shan, J., Inchauste, S., Zhang, M., Mercedes, L., Hong, J.A., Rao, M., and Schrump, D.S. (2010). Cigarette smoke induces C/EBP-β-mediated activation of miR-31 in normal human respiratory epithelia and lung cancer cells. PLoS ONE *5*, e13764.

Yang, G.Y., Taboada, S., and Liao, J. (2009). Induced nitric oxide synthase as a major player in the oncogenic transformation of inflamed tissue. Methods Mol. Biol. *512*, 119–156.

Ylikorkala, A., Rossi, D.J., Korsisaari, N., Luukko, K., Alitalo, K., Henkemeyer, M., and Mäkelä, T.P. (2001). Vascular abnormalities and deregulation of VEGF in Lkb1-deficient mice. Science *293*, 1323–1326.

Yuan, P., Kadara, H., Behrens, C., Tang, X., Woods, D., Solis, L.M., Huang, J., Spinola, M., Dong, W., Yin, G., et al. (2010). Sex determining region Y-Box 2 (SOX2) is a potential cell-lineage gene highly expressed in the pathogenesis of squamous cell carcinomas of the lung. PLoS ONE *5*, e9112.

Zhu, F., Xia, X., Liu, B., Shen, J., Hu, Y., Person, M., and Hu, Y. (2007). IKKalpha shields 14-3-3sigma, a G(2)/M cell cycle checkpoint gene, from hypermethylation, preventing its silencing. Mol. Cell *27*, 214–227.

Cancer Cell
Article

Relapse or Eradication of Cancer Is Predicted by Peptide-Major Histocompatibility Complex Affinity

Boris Engels,[1,*] Victor H. Engelhard,[2] John Sidney,[3] Alessandro Sette,[3] David C. Binder,[1] Rebecca B. Liu,[1] David M. Kranz,[4] Stephen C. Meredith,[1] Donald A. Rowley,[1] and Hans Schreiber[1]
[1]Department of Pathology, Committee on Immunology and Committee on Cancer Biology, The University of Chicago, Chicago, IL 60637, USA
[2]Department of Microbiology and Carter Immunology Center, University of Virginia Health System, Charlottesville, VA 22908, USA
[3]Division of Vaccine Discovery, La Jolla Institute for Allergy and Immunology, La Jolla, CA 92037, USA
[4]Department of Biochemistry, University of Illinois Urbana-Champaign, Urbana, IL 61801, USA
*Correspondence: bengels@bsd.uchicago.edu
http://dx.doi.org/10.1016/j.ccr.2013.03.018

SUMMARY

Cancers often relapse after adoptive therapy, even though specific T cells kill cells from the same cancer efficiently in vitro. We found that tumor eradication by T cells required high affinities of the targeted peptides for major histocompatibility complex (MHC) class I. Affinities of at least 10 nM were required for relapse-free regression. Only high-affinity peptide-MHC interactions led to efficient cross-presentation of antigen, thereby stimulating cognate T cells to secrete cytokines. These findings highlight the importance of targeting peptides with high affinity for MHC class I when designing T cell-based immunotherapy.

INTRODUCTION

Relapse of cancers is very common, even following combinatorial therapy of surgery, chemotherapy, radiation, and/or immunotherapy. For maximal efficacy, drugs depend on reaching the necessary concentration in the tumor microenvironment (Skipper, 1986). This critical concentration concept also applies to cellular effectors, such as neutrophils and T cells (Budhu et al., 2010; Li et al., 2002, 2004). While cellular effectors or drugs at optimal concentrations can eradicate all sensitive cancer cells, relapse may still occur because of the outgrowth of variants. Cancer cells show extremely high genetic instability, and cancers always contain variants that are resistant to destruction by a particular drug or T cell (Anders et al., 2011; Hanson et al., 2000), very similar to what is found for viruses (Hensley et al., 2009).

For complete eradication, it is important to eliminate every residual cancer cell, including heritable variants (Singh et al., 1992; Spiotto et al., 2004; Zhang et al., 2007). However, factors responsible for T cell elimination of variants have not been determined. In experiments designed to explore the reason for failed T cell treatment, we took a reductionist approach, ultimately directing our focus to the target peptides and, in particular, to their affinities for major histocompatibility complex (MHC) class I. We selected several peptides that, when targeted, caused tumor eradication and others that caused relapse. To reduce the influence of differences between cancers, we used two cancer cell lines that were both transduced to express the different peptides. To reduce differences due to expression levels, we used the same design of triple peptides fused to fluorescent proteins. Proteasomal cleavage of proteins may not generate (Chapiro et al., 2006; Popovic et al., 2011) or destroy immunogenic peptides (Schultz et al., 2002). To minimize differences in proteasomal cleavage of the fusion proteins, we designed peptide triplets separated by ''Ala-Ala-Tyr'' cleavage sites. We targeted antigens with no known oncogenic activity to reduce the possibility that the nature of a particular targeted antigen prevented the cancer from escaping. To exclude the influence of other T cells helping or regulating the relevant $CD8^+$ T cells, T cell receptor (TCR)-transgenic T cells with a single specificity were adoptively transferred into hosts, which were TCR-transgenic for an irrelevant target. Finally, a single adoptive T cell transfer regimen was used without providing any additional stimulation, such as vaccination or administration of cytokine.

RESULTS

Cancer Cells Expressing Different Peptides Are Killed by T Cells with Similar Efficacy In Vitro

EGFP was fused to minigenes encoding the peptides hen egg ovalbumin$_{257–264}$ (OVA_{257}), model peptide SIYRYYGL

Significance

Cancer relapse remains the greatest obstacle to virtually any cancer therapy. Our data show that high affinity of the targeted peptides for MHC is required for strong stimulation of T cells to secrete cytokines and cause relapse-free tumor eradication. Adoptive T cell transfer therapies should, therefore, target peptides that have high affinities for the presenting MHC class I.

Table 1. Abbreviations, Conditions, and Summary of Results for Key Experiments

Target Peptide on Cancer Cells				Hosts		T Cells		
Designation	Sequence	MHC	Affinity of Peptide for MHC (IC_{50} [nM])[a]	Designation	Relationship of Antigen to Recipient	Designation	Relationship of Antigen to Donor	Tumor Rejection
SIY	SIYRYYGL	K^b	1.1	OT-I	nonself	2C	nonself	5/5[b,c,d,e]
						none		0/6[b]
$OVA_{257–264}$	SIINFEKL		0.9	2C	nonself	OT-I	nonself	4/4[f]
						none		0/4[f]
$Tyr_{369–377}$	FMDGTMSQV	A2	4.2[g]	OTA	self	FH	self	6/7[h]
						none		0/5[h]
$hgp100_{25–33}$	KVPRNQDWL[i]	D^b	186	OT-I	nonself	pmel	nonself	1/8[c]
						none		0/2
EGP	EGPRNQDWL		454	OT-I	nonself	pmel	nonself	1/6[d]
						none		0/5
$mgp100_{25–33}$	EGSRNQDWL		22,975	OT-I	self	pmel	self	1/12[e]
						none		0/6

See Table S1 for details.
[a]IC_{50} values represent the geometric mean of five or more experiments.
[b]$p = 0.002$.
[c]$p < 0.005$.
[d]$p = 0.015$.
[e]$p < 0.001$.
[f]$p < 0.029$.
[g]A higher IC_{50} value of 65 nM was published for this peptide earlier (Colella et al., 2000). The differences in affinity measurements likely arose as a result of small differences in reagents, methodology, and procedures.
[h]$p = 0.015$.
[i]Only the underlined amino acids differ between the three gp100 peptide variants.

(SIY), mouse $Tyrosinase_{369–377}$ (Tyr_{369}), mouse or human $gp100_{25–33}$ ($mgp100_{25}$ and $hgp100_{25}$, respectively), and a heteroclitic $gp100_{25–33}$ (EGP); EGP differs from $mgp100_{25}$ only in the third amino acid (EGPRNQDWL versus EGSRNQDWL), while it shares the proline at position 3 with $hgp100_{25}$ (KVPRNQDWL) (Table 1). A Cerulean fusion gene was generated only for SIY (Figures 1A and 1C, top). The fibrosarcoma line MC57 of C57BL/6 origin was used to generate lines that expressed the fusion genes at high levels (Figure 1B). Furthermore, the chimeric human leukocyte antigen (HLA)-A2.1/H-$2D^b$ molecule HHD was cotransduced with the Tyr_{369}-EGFP fusion protein to generate MC57-TyrHHD (Figure 1C, bottom).

Assays in vitro demonstrated similar killing of the cancer lines by cognate peptide-activated T cells (Figure 1D). 2C T cells, whose TCR binds SIY, killed the MC57-SIY line, and pmel T cells killed MC57 cells expressing mouse $gp100_{25}$, human $gp100_{25}$ or EGP. Interestingly, Tyr_{369}-specific T cells derived from the *FH* TCR-transgenic, tyrosinase (*Tyr*)-deficient albino mouse (AFH) or *Tyr*-positive black mouse (FH) killed MC57-TyrHHD target cells similarly well. Together, the results imply there is sufficient direct presentation of all processed peptides and sufficient avidity of the T cells for efficient killing in vitro.

T Cells Targeting SIY, OVA_{257}, or Tyr_{369} Eradicate Large Tumors

SIY-expressing MC57-SIY cells were injected in TCR-transgenic mice of irrelevant specificity (OT-I). OVA_{257}-transfected cancer cells were injected in *2C* TCR-transgenic mice; MC57-TyrHHD cancer cells were grown in *OT-I* TCR- and *AAD*-transgenic mice, which did (OTA) or did not express tyrosinase (albino; AOTA). In all cases, cancer cells produced progressively growing tumors within 1 week (Figure 2A). At least 2 weeks after cancer cell injection, when tumors reached about 500 mm^3, mice were treated with T cells. As published by our laboratory, tumors expressing SIY and treated with 2C T cells were eradicated (Figure 2B, upper left; Table 1; Table S1 available online; Spiotto et al., 2004). Here, we also show that OVA_{257}-expressing tumors treated with OT-I T cells were rejected (Figure 2B, middle left) and FH T cells eradicated Tyr-positive tumors (Figure 2B, lower left). In this last experiment, FH T cells derived from a *Tyr*-positive donor were transferred into a *Tyr*-positive host and eradicated a Tyr-expressing tumor. Together, this and other experiments using *FH* TCR-transgenic T cells from *Tyr*-negative donors (AFH) and *Tyr*-negative (AOTA) or *Tyr*-positive (OTA) hosts showed that tumors could be rejected (1) whether the targeted peptide was self or nonself for the tumor-bearing host and (2) whether the targeted peptide was self or nonself for the donor T cells (Figure S2A). This may be unique to our model, since a different model showed that low ubiquitous expression of a transgene prevented the rejection of antigen-expressing tumors through the induction of tolerance (Buschow et al., 2010). Levels of antigen expression in the host and/or tumor, type of cells that express the self-antigen, and the source of T cells may likely influence the outcome. Taken together, targeting any of the three peptides, SIY, OVA_{257}, or Tyr_{369}, caused eradication of established large and solid tumors.

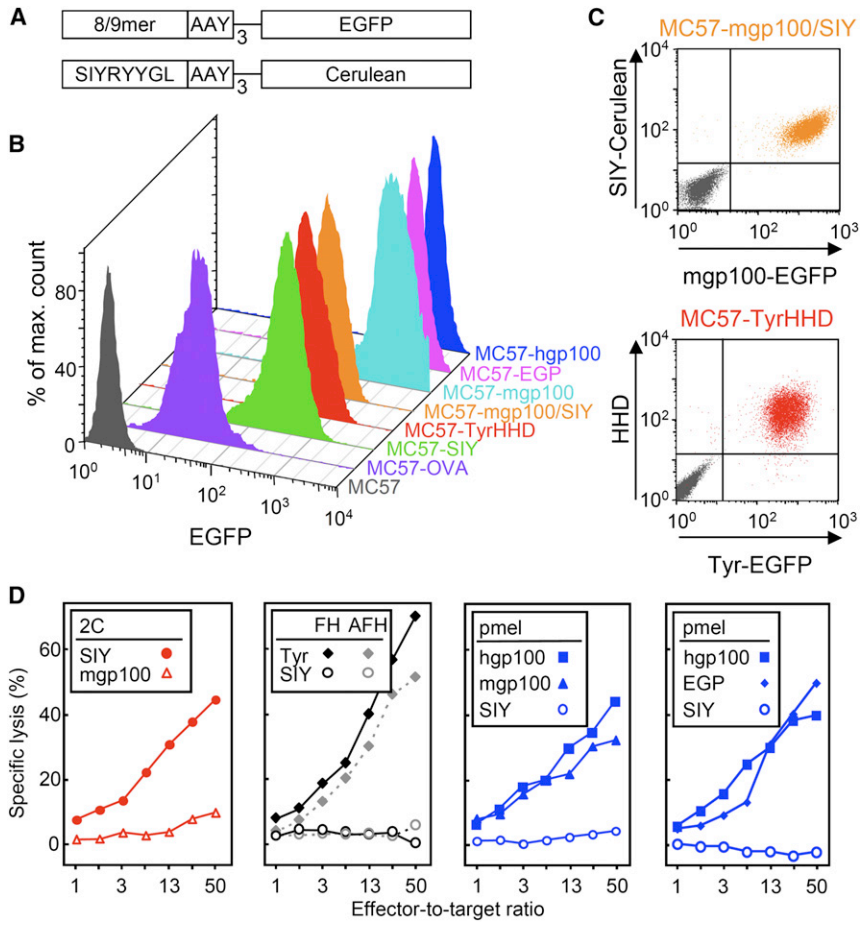

Figure 1. All Transduced Cancer Cell Lines that Express Antigens at High Levels Were Effectively Killed In Vitro

(A) Diagram of fusion proteins constructed to express antigen in MC57 cancer cells. Triple repeats of peptide and alanine-alanine-tyrosine (AAY) proteasomal cleavage sites were fused to fluorescent proteins: OVA_{257}, SIY, mouse $tyrosinase_{369-377}$ (Tyr_{369}), mouse or human $gp100_{25-33}$ ($mgp100_{25}$ and $hgp100_{25}$, respectively), and EGP; a Cerulean fusion gene was generated only for SIY.

(B) Flow cytometric analysis of peptide-EGFP fusion proteins expressed by the transduced MC57 fibrosarcoma lines.

(C) MC57-mgp100/SIY expressed $mgp100_{25}$ and SIY antigens as EGFP and Cerulean fusion proteins, respectively. The HLA-A2/D^b chimeric protein HHD was cotransduced with the Tyr_{369}-EGFP fusion protein to generate MC57-TyrHHD. Parental MC57 (gray) was analyzed for comparison.

(D) Cytolysis of MC57 target cells overexpressing SIY, $mgp100_{25}$, $hgp100_{25}$, EGP, or Tyr_{369} and HHD (Tyr) by 2C, pmel, AFH (*Tyr*-negative), or FH (*Tyr*-positive) T cells in a 4.5 hr ^{51}Cr release assay. Cancer cells expressing noncognate peptide were used as negative controls. These data are compiled of three experiments and are representative for seven independent experiments.

See Figure S1 for induction of vitiligo by FH and pmel T cells.

Large $mgp100_{25}$, $hgp100_{25}$, or EGP-Expressing Tumors Relapse after Initial Regression Caused by Transferred T Cells

In contrast, T cells targeting the self-peptide $mgp100_{25}$ and the nonself heteroclitic peptides $hgp100_{25}$ or EGP did not result in tumor eradication. MC57 lines overexpressing $mgp100_{25}$, $hgp100_{25}$, or EGP were injected into *OT-I* TCR-transgenic mice and produced progressively growing tumors within 1 week (Figure 2A). At least 2 weeks after cancer cell injection, when the tumors reached about 500 mm^3, the mice were treated with pmel T cells. The tumors regressed initially, but eventually almost all tumors relapsed (Figure 2B, right panels; Tables 1 and S1).

To exclude any nonantigenic differences in the cancer lines (caused by transduction and sorting), we used a cell line that expressed both SIY and $mgp100_{25}$ antigens (MC57-mgp100/SIY; Figure 1C). When mice bearing these tumors were treated with 2C or pmel T cells, the outcome was the same as when tumors from single antigen lines were treated (Figure 2B, upper panels, red curves). In conclusion, neither human nor mouse $gp100_{25}$ or EGP expressed by the cancer cells supported rejection by pmel T cells.

These findings were not limited to the methylcholanthrene-induced cancer line MC57 but were confirmed using the UV-induced cancer line 8101 (Figures S2B and S2D). The line was transduced to overexpress SIY, human, or mouse $gp100_{25}$. Again, we observed eradication of established tumors by adoptive T cell transfer only when SIY was targeted. Interestingly, in this model, targeting $hgp100_{25}$ was more effective than targeting $mgp100_{25}$; tumors expressing $hgp100_{25}$ regressed after pmel transfer, while tumors expressing $mgp100_{25}$ continued to grow uninhibitedly.

Treatment of Tumors Expressing Human $gp100_{25}$ but Not Murine $gp100_{25}$ or EGP Results in Outgrowth of Antigen-Loss Variants

We isolated cancer cells from tumors expressing $mgp100_{25}$, $hgp100_{25}$, or EGP that had relapsed following treatment with pmel T cells (Figure 2B) and analyzed these for antigen-loss variants (ALV). All MC57-hgp100 tumors had lost EGFP expression, which indicated loss of $hgp100_{25}$, as both were expressed as a single fusion protein (one representative tumor is shown in Figure 3). Importantly, the tumor isolated from a nontreated mouse retained EGFP expression. MC57-mgp100 and MC57-EGP tumors treated with pmel had also not lost EGFP expression. All lines expressed mgp100-EGFP or EGP-EGFP at levels similar to the isolate from a nontreated mouse (Figure 3). These data suggest that pmel T cells were capable of killing all $hgp100_{25}$-expressing MC57 cancer cells but were not capable of killing all $mgp100_{25}$- or EGP-expressing cancer cells in the respective tumors. These findings seem to be influenced also by the targeted cell, as relapsed tumors formed by 8101-hgp100 cells mostly retained expression of the antigen (only

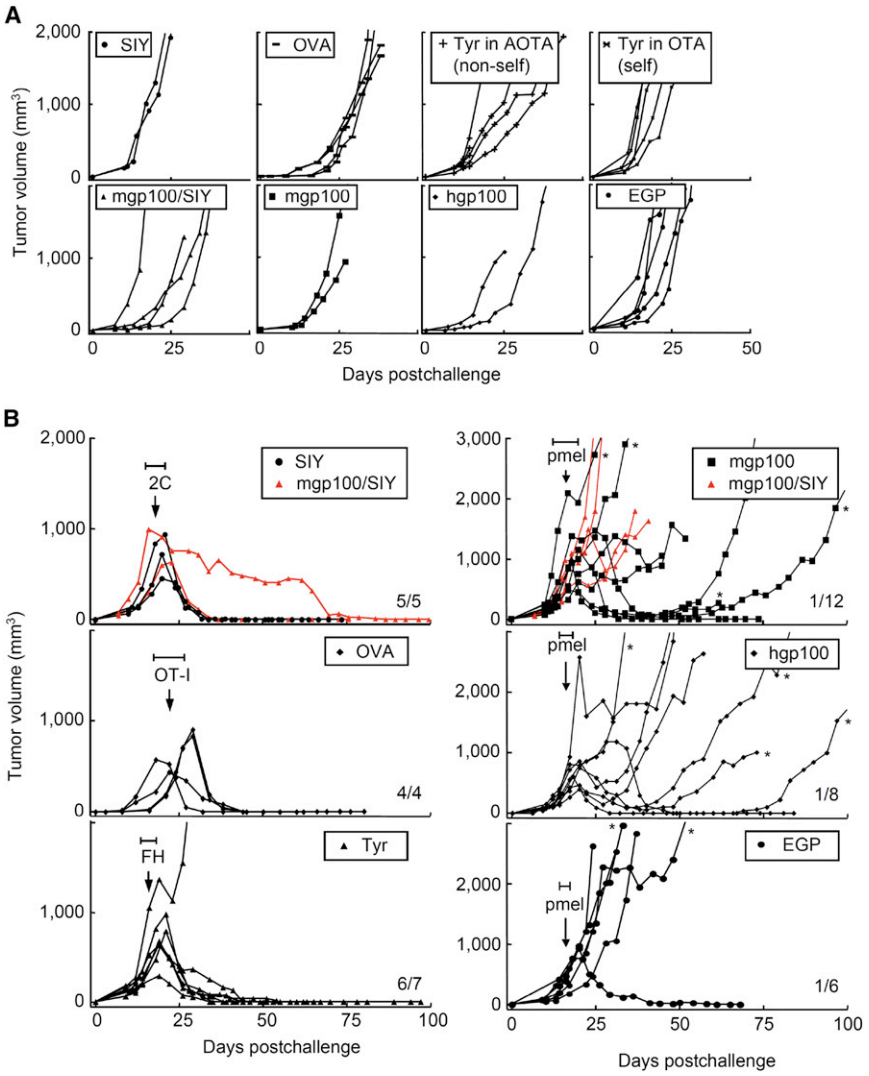

Figure 2. Targeting SIY, OVA_{257}, or Tyr_{369} Eradicated Large Tumors while Targeting $mgp100_{25}$, $hgp100_{25}$, or EGP Caused Initial Tumor Regression but Was Followed by Relapse

(A) Cancer cell lines formed progressively growing tumors within 1 week. TCR-transgenic mice with irrelevant specificity were challenged subcutaneously with 2×10^6 cancer cells. MC57-SIY, MC57-mgp100, MC57-mgp100/SIY, MC57-hgp100, and MC57-EGP were injected into OT-I mice; MC57-OVA grew in 2C mice and MC57-TyrHHD grew in AOTA (*Tyr*-deficient, nonself) and OTA (*Tyr*-positive, self). Graphs represent single mice in 11 experiments, listed as nontreated controls in Tables 1 and S1 and Figure S3C.

(B) At least 2 weeks after cancer cell injection, when tumors reached about 500 mm^3, each mouse was treated once with cognate T cells (treatment between days 13 and 26, depending on tumor size, as indicated by the horizontal bars [H]). Average size of tumors at day of treatment: 2C: 720 mm^3, ranging from 448 to 995 mm^3; OT-I: 608 mm^3, ranging from 440 to 715 mm^3; FH: 517 mm^3, ranging from 250 to 848 mm^3; pmel, targeting $mgp100_{25}$: 601 mm^3, ranging from 325 to 980 mm^3; targeting $hgp100_{25}$: 470 mm^3, ranging from 264 to 936 mm^3; and targeting EGP: 337 mm^3, ranging from 180 to 600 mm^3. MC57-TyrHHD was grown in OTA (self) and treated with FH T cells (self). The number of rejected tumors per number of tumors treated is indicated. Data are derived from 15 independent experiments, compiled in Tables 1 and S1. *Tumors were isolated and analyzed for antigen expression (see Figure 3).

See also Figure S2.

one of the isolated relapsed tumors was an ALV; data not shown).

While we did not observe significant differences when targeting either human or mouse $gp100_{25}$ in treatments of established MC57 tumors, we did see differences in protection against cancer cell inoculations. Pmel T cells prevented the outgrowth of MC57-hgp100 but not of MC57-mgp100 tumors (Figures S3A and S3C). MC57-mgp100 cells formed tumors in which a large fraction of cells still expressed the antigen (Figure S3B). Taken together, pmel T cells showed a stronger effect when targeting $hgp100_{25}$ compared to $mgp100_{25}$ and EGP.

Tumor Eradication Correlates with High Affinity of Targeted Peptides for MHC

In an effort to understand why targeting some peptides led to eradication while targeting others resulted in relapse, we first analyzed the activation status of the T cells transferred to treat the different tumors. Upon transfer, after peptide stimulation in vitro, all T cells showed the same $CD44^{hi}$ and $CD62L^{hi}$ phenotype of activated T cells (Figure 4) and demonstrated very similar killing capabilities in vitro (Figure 1). It is worth mentioning that before stimulation, splenocytes from self-reactive TCR-transgenic mice (pmel and AFH) showed an antigen-experienced phenotype ($CD44^{hi}$), while T cells from the nonself, reactive TCR-transgenic 2C mice showed a truly naive phenotype. However, this difference was overcome after peptide stimulation in vitro. Interestingly, when isolated from tumors 4 days after adoptive transfer, the T cells that led to eradication of tumors (2C and AFH) showed a more effector-like phenotype ($CD62L^{lo}$ and $CD44^{hi}$) compared to the more central memory-like phenotype ($CD62L^{hi}$ and $CD44^{hi}$) found for pmel T cells. Together, these data suggest that the differences in tumor rejection were not due to differing activation statuses of the T cells at the time of transfer.

As another variable that could influence the efficacy of tumor rejection, we analyzed the affinities of the peptides for the presenting MHC molecules. In a cell-free competition-binding assay, the concentration of inhibitor peptides needed to displace half of the probe peptide (half maximal peptide displacing concentration [IC_{50}] in nM) was determined. IC_{50} values are reasonable approximations of real K_D values (see Experimental Procedures). A wide range in binding affinities was measured (Table 1). There was a strong correlation between affinity of the

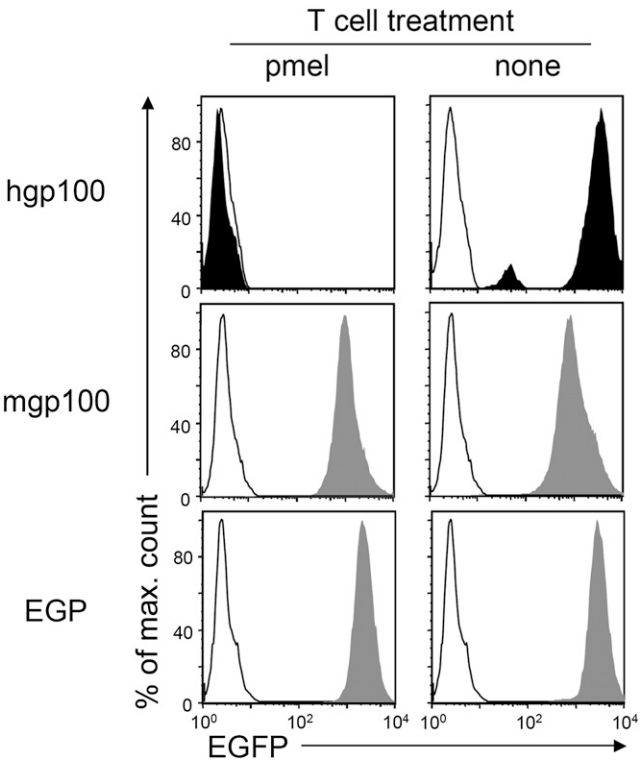

Figure 3. Outgrowth of Antigen-Loss Variants after pmel T Cell Treatment of Cancer Cells Expressing hgp100$_{25}$ but Not of Cancers Expressing mgp100$_{25}$ or EGP

Cancer cells of relapsed tumors expressing mgp100$_{25}$, EGP (both gray), or hgp100$_{25}$ (black) were isolated after pmel T cell treatment, adapted to culture, and analyzed for peptide-EGFP fusion gene expression (left panels). MC57 cells (white histogram) cultured in vitro and MC57-mgp100, MC57-EGP (both gray), or MC57-hgp100 (black) cells isolated from nontreated mice (right panels) were analyzed as controls. Isolated lines from mgp100- or hgp100-expressing tumors are representative for four lines each and the isolate from the EGP-expressing tumor is representative for two lines; all lines were isolated after relapse (respective tumors were marked with an asterisk in Figure 2B). The repeatability in independent experiments strongly suggests that loss of antigen expression from the hgp100$_{25}$ cancer cells was not an artifact caused by adaptation or postisolation culturing.

See also Figure S3.

peptide for MHC and tumor eradication. The three target peptides supporting tumor eradication, OVA$_{257}$, SIY, and Tyr$_{369}$ displayed strong binding to their cognate MHC (0.9, 1.1, and 4.2 nM, respectively). These high affinities stood in stark contrast to the affinities we measured for mgp100$_{25}$, EGP, and hgp100$_{25}$ (22,975, 454, and 186 nM, respectively). These three peptides bound the MHC poorly and, when targeted, resulted in relapse rather than tumor eradication.

Stromal Cells Isolated from Tumors Formed by Cancer Cells Expressing Peptides with High Affinity to MHC Stimulate Cognate T Cells Effectively

To analyze why high peptide-MHC affinities were required for tumor eradication, we performed assays to evaluate the level of cross-presentation in growing tumors. MC57 and 8101 lines expressing SIY, mgp100$_{25}$, or hgp100$_{25}$ were grown in *OT-I* TCR-transgenic or *Rag1*$^{-/-}$ mice, respectively; MC57-TyrHHD was grown in AOTA (nonself) mice. SIY was used as a representative peptide for the two highest binding peptides OVA$_{257}$ and SIY. Enriched populations of CD11b$^+$ stromal cells were obtained from at least 2-week-old untreated tumors and were compared in their ability to stimulate T cells in vitro to analyze the level of cross-presentation of the different peptides expressed by the tumors. For comparison, we used the transduced MC57 and 8101 cancer lines grown in vitro. As seen for the similar killing of MC57 cells presenting the different peptides in Figure 1D, direct presentation also led to comparable amounts of interferon (IFN)-γ and tumor necrosis factor (TNF)-α secretion by cognate T cells (Figure 5). However, in the 8101 model, more IFN-γ was found when targeting SIY versus hgp100$_{25}$ and mgp100$_{25}$ (Figure S2C). Even bigger differences occurred in both cancer models when T cells were stimulated with stromal cells. CD11b$^+$ stromal cells cross-presenting SIY and Tyr$_{369}$ stimulated cognate T cells even more strongly than directly presenting cancer cells (Figure 5). In contrast, both gp100$_{25}$ peptides were very poorly cross-presented. While stromal cells from hgp100$_{25}$-expressing tumors stimulated T cells to secrete low levels of both cytokines, stromal cells from mgp100$_{25}$ tumors did not stimulate T cells at all (Figures 5 and S2C). The heteroclitic peptide EGP behaved similarly to hgp100$_{25}$ when cross-presented; it stimulated pmel T cells to secrete low amounts of IFN-γ (Figure S4). Thus, the peptides with high affinities for MHC (SIY and Tyr$_{369}$) were well cross-presented, while peptides with low affinities (all three gp100$_{25}$ peptides) were so poorly cross-presented that the respective stromal cells could not efficiently stimulate cognate T cells.

Destruction of Tumor Stroma Is Stronger when Targeted Peptides Have High Affinity for MHC

We analyzed regressing MC57 tumors to help us understand how tumor eradication correlated to peptide-MHC affinities. Tumors were dissected on day 5 after adoptive T cell transfer, and we analyzed the viability of CD11b$^+$ stromal cells. Stroma from tumors expressing SIY or Tyr$_{369}$ showed a high percentage of dead cells (Figure 6), a 6- and 5.8-fold increase over background, respectively. In accordance with the relapse of tumors from gp100$_{25}$ peptide-expressing cells, death of tumor stroma was low, with only 1.9- and 2.2-fold increases over background for hgp100$_{25}$ and mgp100$_{25}$, respectively. In conclusion, tumors that were eradicated by cognate T cell therapy showed a high rate of stromal death, while relapsing tumors contained less dead CD11b$^+$ stromal cells.

DISCUSSION

Our results have a direct impact on the design of adoptive immunotherapy. First, and most importantly, the affinity of the targeted peptide for the presenting MHC was highly predictable of success or failure of T cell therapy, indicating that this is a key variable. Only high-affinity peptides that were efficiently presented by cancer cells and/or stroma induced cytokine secretion by T cells, stromal death, and relapse-free regression of tumors. Second, targeting self-antigens on tumors did not preclude eradication of large cancers, even though the treated mice developed vitiligo (data not shown). Such autoimmunity was

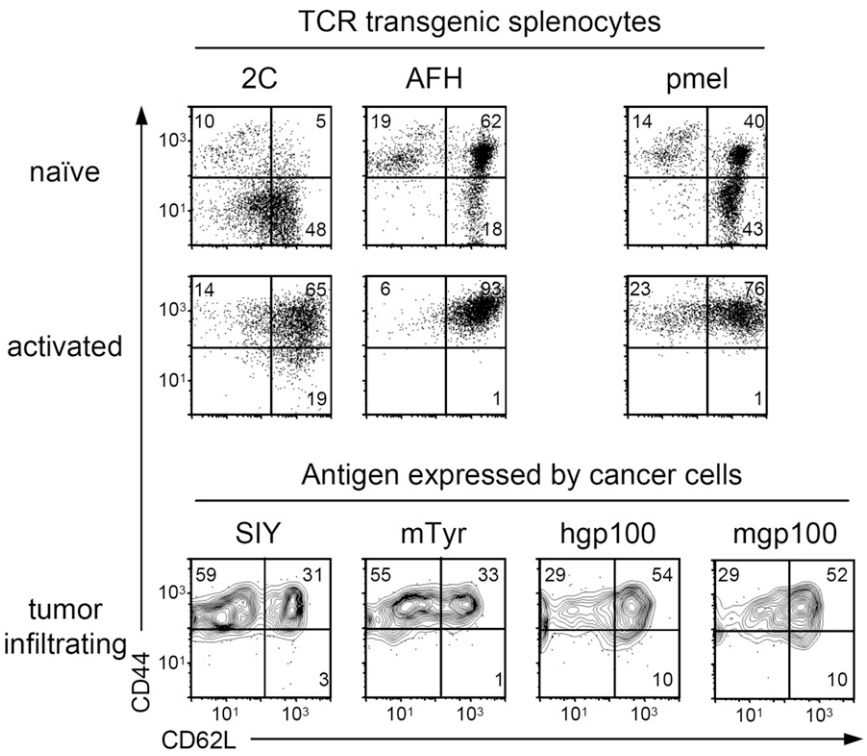

Figure 4. T Cells Transferred to Treat the Tumors Expressing the Different Peptides Showed the Same Phenotype of Activated T Cells

T cells of *2C*, *AFH*, and *pmel* TCR-transgenic mice were tested for their activation status in "naive," untreated mice (splenocytes) at day 3 after peptide activation in vitro and on day 4 after adoptive transfer (tumor infiltrating cells). Cells were analyzed by flow cytometry for expression of CD44 and CD62L and gated on $CD8^+$ T cells expressing the cognate Vβ-chain: Vβ8 for 2C, Vβ11 for AFH, and Vβ13 for pmel. Data are representative for two or three independent experiments for the data in vivo and in vitro, respectively.

also observed in patients treated with antiself T cells (Morgan et al., 2010; Palmer et al., 2008; Parkhurst et al., 2011; Yee et al., 2000). As might be expected, we found that the self-peptide with the higher affinity for the presenting MHC molecule was associated with stronger autoimmunity ($mTyr_{369}$ as opposed to $mgp100_{25}$). Vitiligo was also detected earlier in mice transgenic for the FH TCR compared to pmel (Figure S1; Gregg et al., 2010).

We have analyzed the potential of the different peptides to be cross-presented by tumor stroma. This is an effective readout to evaluate different affinities of peptides for MHC and more sensitive than direct presentation by cancer cells. All peptides were overexpressed by the cancer lines; therefore, no differences in direct presentation were detected in killing and cytokine secretion assays, but cross-presentation reflected the results obtained from the cell-free affinity measurements. Death of stroma correlated with the amount of cross-presentation and tumor relapse. Though stromal death seems to be required for tumor eradication, we do not know whether cross-presentation is essential. For example, direct T cell stimulation provided by cancer cells expressing peptides with high affinity for MHC can lead to strong cytokine production, Fas ligand upregulation, and bystander killing (Wang et al., 1996), which could destroy stroma. Stromal cross-presentation may also not be needed when an essential oncogene on the cancer is targeted (Anders et al., 2011; Listopad et al., 2013).

Targeted peptides that led to tumor eradication fell into a category of high-affinity MHC binders (IC_{50} < 10 nM), whereas affinities of peptides that led to relapse fell into a category of intermediate (IC_{50} between 50 and 500 nM) or low binders (IC_{50} > 500 nM). These data are consistent with the low nanomolar affinities needed to provide full protection against lethal *Vaccinia* virus infection (Moutaftsi et al., 2009). Low affinity peptides may allow perforin-mediated killing, which requires only two to three peptide/MHC complexes and brief T cell-target cell interactions (Purbhoo et al., 2004). However, the efficacy of adoptively transferred T cells to eradicate tumors does not depend on perforin (Garcia-Hernandez et al., 2010; Listopad et al., 2013). The high affinity of peptides for MHC is probably needed for tumor eradication, because this allows the formation of stable synapses between T cells and antigen-positive cancer cells and/or stromal cells cross-presenting the antigen. At least ten peptide/MHC complexes need to be engaged for the prolonged interactions required to stimulate T cells to secrete cytokines (Purbhoo et al., 2004), which are essential for tumor eradication (Garcia-Hernandez et al., 2010; Listopad et al., 2013; Zhang et al., 2008). It appears that targeting peptides with affinities below a certain threshold will result in a level of stimulation of effector T cells that is insufficient to eradicate the cancer, resulting in relapse of antigen-positive or negative cancer cells.

Several studies have tried to overcome relapse after adoptive T cell therapy. They show that the antitumor effects of adoptively transferred T cells can be enhanced by selecting for more effective T cell populations, multiple transfers of T cells, high-dose interleukin-2, vaccinations, and/or total body irradiation (Cheever et al., 1980; Cho et al., 2012; Dummer et al., 2002; Ho et al., 2003; Ly et al., 2010; Matsui et al., 2003; North, 1982; Overwijk et al., 2003). But even under these conditions, relapse was often observed when peptides with low affinities for MHC were targeted (Antony et al., 2005; Gattinoni et al., 2005, 2009; Overwijk et al., 2003).

TCR affinity can undoubtedly be an important factor (Gottschalk et al., 2012). However, in the study presented here, the affinity of the peptides for MHC seemed to determine if T cells could eradicate tumors or not. As reasons for this, we propose that the affinities (K_D) of the majority of natural TCRs, measured by surface plasmon resonance, are 1–100 μM (Davis et al., 1998; Williams et al., 1999). This is a very narrow range, considering the affinity range from under 1 to more than 20,000 nM measured for the different peptides binding MHC.

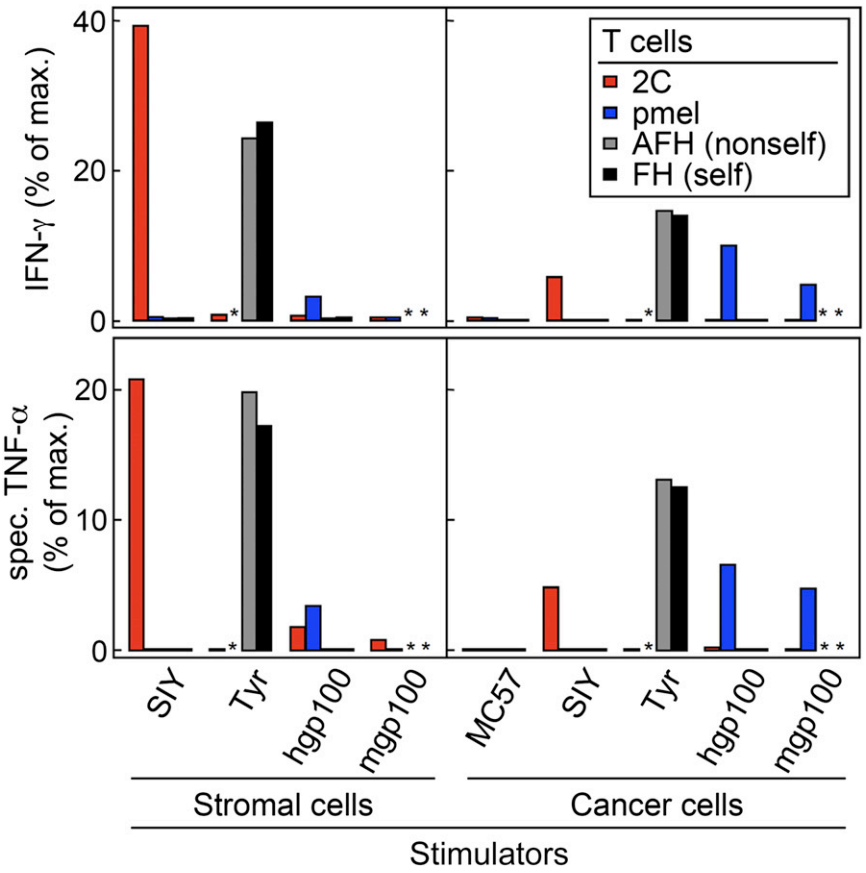

Figure 5. Only SIY and Tyr_{369} Are Cross-Presented, as Detected by Cytokine Secretion by T Cells Stimulated by Stromal Cells Isolated from Untreated Tumors

$CD11b^+$ stromal cells were isolated from established untreated tumors and were cocultured with peptide-activated T cells. Enriched stromal cells from tumors grown from MC57-SIY, MC57-hgp100, and MC57-mgp100 cells (all grown in OT-I mice) and MC57-TyrHHD (grown in AOTA mice [nonself]) were cocultured with *2C*, *pmel*, *AFH* (nonself), or *FH* (self) TCR-transgenic T cells. Stromal cells from the various tumors were compared to cultured cancer cells expressing the same antigen. Supernatants were harvested after 24 hr of coculture and amounts of IFN-γ and TNF-α measured by ELISA. Data are shown as percent of maximal cytokine secretion (anti-CD3 and anti-CD28 antibody stimulation, defined as 100%). For TNF-α, cytokine secretion by stromal cells without T cells was subtracted to obtain specific TNF-α secretion by T cells (443–975 pg/ml by 1×10^5 cells cultured in 200 μl for 24 hr, depending on experiment). Unstimulated T cells served as negative control (below 0.7% for all responders, not shown). Data shown are combined from two experiments and are representative for four independent experiments.
See also Figure S4.
The asterisk indicates experiments were not done.

In the same line of argument, a study by Bowerman and colleagues demonstrated in vitro that the magnitude of T cell activity against peptide/MHC was influenced more by peptide binding to MHC than by binding of TCR to peptide/MHC, especially for higher affinity TCRs (Bowerman et al., 2009). Finally, T cells expressing the 2C TCR, even when targeting a peptide/MHC complex with a 30-fold higher affinity, could not prevent relapse in the absence of cross-presentation. Using 2C T cells to treat MC57-SIY and MC57-L^d tumors, SIY-expressing tumors were rejected (Figure 2B; Spiotto et al., 2004; affinity of 2C TCR for SIY-K^b [K_D = 30 μM]), while MC57-L^d cancer cells grew out as ALV (Spiotto et al., 2004; affinity of 2C for QL9- and p2Ca-L^d [$K_D \approx 1$ μM]; Corr et al., 1994; Garcia et al., 1997; Holler and Kranz, 2003). In contrast to SIY, QL9- and p2Ca-L^d, recognized by 2C as alloantigens, cannot be cross-presented, as the entire peptide/MHC complex would need to be taken up by the stromal cells and then be re-presented on their surface.

While we did not study the influence of several TCRs with different affinities to one (same) peptide MHC complex, the influence of one TCR (pmel) on tumors expressing three peptides with different affinities for MHC was studied here. The affinities of the pmel TCR for the three peptide/MHC complexes studied, $mgp100_{25}$, EGP, and $hgp100_{25}$ binding D^b, are not known; however, alanine scans of murine and human $gp100_{25}$ suggest similar affinities, since the first three amino acids, which harbor the only differences between the three peptides, do not contribute to the binding of the peptide/MHC complex to the TCR (but are important for the binding of the peptides to MHC; Overwijk et al., 1998). Also, structural studies of these peptides (van Stipdonk et al., 2009) in complexes with D^b indicate that the two positions that influenced binding to D^b (p2 and p3) are both pointing down into the MHC pocket. In fact, the authors did not see significant differences in any of the exposed regions of the peptides, which would be in contact with the TCR. Nevertheless, only cancer cells expressing the peptide with the highest affinity for D^b ($hgp100_{25}$) were effectively killed in vivo, tumors expressing the other peptides relapsed being antigen positive. As none of the three peptides supported complete tumor eradication, we further analyzed their affinity for MHC in detail, which has given us insight into the importance of the stability of peptide-MHC interactions. In the original description of EGP (van Stipdonk et al., 2009), two different RMA-S cell-based assays were employed to determine the relative affinity of EGP for D^b compared to the murine gp100 peptide (murine gp100 peptide [25–33] EGSRNQDWL ["EGS"]) and human gp100 peptide "KVP"). These assays were: first, a binding assay that measured cell surface D^b levels as a function of peptide concentration; in this assay, EGP was almost 100-fold better than $hgp100_{25}$ (KVP) and 1,000-fold better than $mgp100_{25}$ (EGS). Second, a stabilization assay measured the cell surface lifetimes of the peptide/D^b complexes. In this stabilization assay, EGP and $hgp100_{25}$ (KVP) showed similar lifetimes, whereas $mgp100_{25}$ (EGS) had a considerable shorter lifetime (i.e., the complex was less stable). Consistent with their results, we observed a 50-fold increased affinity of EGP over $mgp100_{25}$, and this affinity

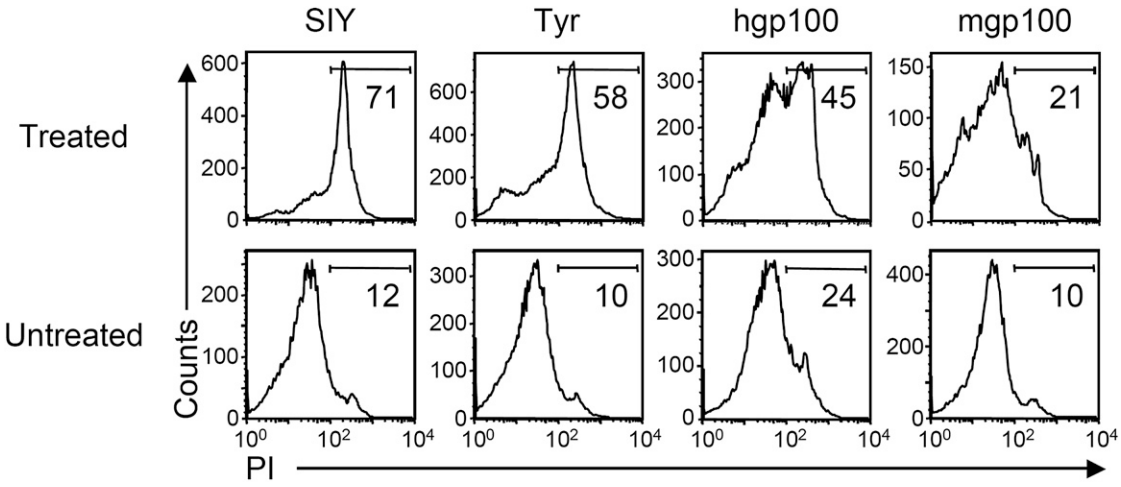

Figure 6. Death of Stromal Cells in T Cell-Treated SIY- and Tyr_{369}-Expressing Tumors

MC57-SIY, MC57-TyrHHD, MC57-hgp100, and MC57-mgp100 tumors were treated with 2C, AFH (nonself) or pmel T cells, respectively. Five days after adoptive transfer, single cell suspensions were generated from treated and untreated tumors and analyzed by flow cytometry. Histograms show $CD11b^+$ T cells stained with propidium iodide (PI) to identify cell death. Numbers indicate the percentage of dead cells among $CD11b^+$ cells. Data are representative for four independent experiments, with single mice per group.

of EGP was similar to that of $hgp100_{25}$ (454 nM and 186 nM, respectively). We used a cell-free competition-binding assay, which is influenced by on- and off-rates (giving an approximation of the dissociation constant [K_D]). Taken together, EGP demonstrated similar MHC stabilization compared to $hgp100_{25}$ (van Stipdonk et al., 2009). Indeed, like $hgp100_{25}$, the affinity of EGP for D^b was insufficient to allow for tumor eradication.

Heteroclitic peptides can induce strong T cell responses that include TCRs with high affinities (Gold et al., 2003; van Stipdonk et al., 2009). However, these T cells will not be able to eradicate tumors if the targeted tumor antigen has low affinity for its presenting MHC. An example is a recent clinical trial that showed no improvement of antimelanoma effects by addition of vaccinations with heteroclitic gp100 peptides to the immune stimulating anti-cytotoxic T-lymphocyte antigen (CTLA) 4 antibody (Hodi et al., 2010). The affinities of the corresponding natural peptides are $gp100_{209}$: 83–172 nM and $gp100_{280}$: 94–455 nM (Kawakami et al., 1995; Parkhurst et al., 1996; Tsai et al., 1997).

Since our data show that high affinity of peptide for MHC results in tumor eradication along with strong stimulation of T cells to secrete cytokines, future studies should concentrate on targeting peptides that have high affinities for presenting MHC class I. There are several algorithms that are constantly being improved to give a fairly reliable prediction of peptide affinities for MHC (e.g., Immune Epitope Database Analysis Resource). Nevertheless, the predicted affinities of the peptides show 2- to 20-fold differences when compared to the measured affinities (as analyzed here for SIY and OVA_{257}, respectively). While the affinities of peptides for MHC can be accurately measured in standardized cell-free assays, natural processing and presentation of these putative peptides needs also to be confirmed before selecting a peptide as a therapeutic target (Popovic et al., 2011). Together, it should be possible to identify optimal targets for T cell therapies when analysis of peptide-MHC affinity is included.

EXPERIMENTAL PROCEDURES

Cell Lines

Phoenix-ampho (Fujita et al., 1992) cells were cultured in Dulbecco's modified Eagle's medium (DMEM) (Mediatech, Manassas, VA), 10% nonheat inactivated fetal calf serum (FCS) (Sigma-Aldrich, St. Louis, MO) at 37°C in a 5% CO_2 humidified incubator. Cancer cells lines were cultured in DMEM, 5% FCS (Gemini Bio-Products, West Sacramento, CA) at 37°C in a 10% CO_2 dry incubator. 8101 originated in a UV-treated C57BL/6 and has been described (Dubey et al., 1997; Schreiber et al., 2001). P. Ohashi (University of Toronto, Toronto, Ontario, Canada), with permission of H. Hengartner (University Hospital Zurich, Zurich, Switzerland), provided the MC57G methylcholanthrene-induced, C57BL/6-derived fibrosarcoma (MC57). Its transfectant MC57-SIY-1 (MC57-SIY) has been described previously (Spiotto et al., 2002). The new cell lines 8101- and MC57-hgp100, 8101- and MC57-mgp100, 8101-SIY, MC57-EGP, and MC57-OVA were generated by transductions of 8101 or MC57 with the Moloney murine leukemia virus-derived retroviral vector MFG expressing peptide-EGFP fusion genes (see Supplemental Experimental Procedures for details on retroviral vectors and transductions). MC57-mgp100/SIY was derived from MC57 by subsequent transduction with MFG-$(SIY)_3$-Cerulean and MFG-mgp100-EGFP. MC57-TyrHHD was obtained by sequential transductions with MFG-Tyr-EGFP and MP71-HHD, encoding a fusion protein of a HLA-A2/D^d chimera and human β2m (Pascolo et al., 1997).

Mice

A list of the pairs of mice used as hosts of tumors and donors of T cells can be found in Table 1. OVA_{257}-K^b-specific TCR-transgenic OT-I mice were provided by M. Mescher (University of Minnesota, Twin Cities, MN), the SIY-K^b-specific TCR-transgenic 2C mice were provided by J. Chen (Massachusetts Institute of Technology, Cambridge, MA), and the human and murine $gp100_{25}$-D^b-specific pmel-1 (referred to as pmel) were provided by N. Restifo (National Cancer Institute, Bethesda, MD) (Overwijk et al., 2003). Other TCR-transgenic mice used in this study are the murine Tyr_{369}-A2-specific AFH mouse (Nichols et al., 2007), which is also *AAD*-transgenic (HLA-A2 and D^b chimera; Newberg et al., 1996) and albino (*Tyr*-deficient; Colella et al., 2000). It is important to note that the FH TCR used for targeting the self-peptide $mTyr_{369}$ has been derived in a nonself setting. The TCR was obtained from a *Tyr*-deficient albino mouse (Nichols et al., 2007), while the mouse from which pmel was obtained expressed $mgp100_{25}$ (Overwijk et al., 2003). This does not imply that the pmel TCR specific for $mgp100_{25}$ is of lower affinity but rather that TCRs with a certain

affinity for peptide/MHC can only be found naturally, if the target peptide is not expressed (FH) or of low affinity for MHC (pmel). The *Tyr*-positive, Tyr_{369}-A2-specific, *AAD*-transgenic FH mice were generated by crossing AFH to C57BL/6J (The Jackson Laboratory, Bar Harbor, ME) and selecting black (Tyr^{+}) mice. The *OT-I*-, *Thy1.1*-, and *AAD*-transgenic strains AOTA (albino, Tyr^{-}) and OTA (Tyr^{+}) were obtained by crossing ATA (Nichols et al., 2007) to OT-I/Thy1.1 ($Thy1^{a}$; provided by T. Gajewski, The University of Chicago, Chicago, IL) and selecting for mice with white or black fur color, respectively. All colonies, including $Rag1^{-/-}$ (B6.129S7-$Rag1^{tm1Mom}$/J, The Jackson Laboratory), were maintained at the University of Chicago facilities. The Institutional Animal Care and Use Committee at the University of Chicago approved all animal experiments, and all experiments were performed to conform to the relevant regulatory standards.

Peptides

The peptides EGP (EGPRNQDWL), $hgp100_{25}$ (KVPRNQDWL), $mgp100_{25}$ (EGSRNQDWL), OVA_{257} (SIINFEKL), SIY (SIYRYYGL), and Tyr_{369} (FMDGTMSQV) were made by solid-phase peptide synthesis using standard 9-fluorenylmethoxycarbonyl chemistry (see Supplemental Experimental Procedures for details).

T Cell Cultures

NH_4Cl^{-}treated splenocytes were cultured at 4 × 10^6 cells/ml, 3 ml per well of a 6-well plate in Roswell Park Memorial Institute medium (RPMI), 10% FCS (Sigma-Aldrich), 2 mM glutamine, 50 μM β-mercaptoethanol, 1 mM 4-(2-hydroxyethyl)-1-piperazineethanesulfonic acid (Hepes), 1 mM sodium pyruvate, 1X nonessential amino acids, 100 U/ml penicillin, 100 μg/ml streptomycin, and 50 μg/ml gentamicin (all GIBCO/Invitrogen, Carlsbad, CA). T cells were activated with 1 μg/ml anti-CD3 (145-2C11) and anti-CD28 (37.51, both eBioscience, San Diego, CA) for killing assays in vitro or 1 μM cognate peptide: SIY for 2C, Tyr_{369} for AFH and FH, OVA_{257} for OT-I, and $hgp100_{25}$ for pmel. Activated T cells were used for adoptive transfer after 3 days and for assays in vitro after 4 days of culture.

Cytotoxicity Assay

Cell-mediated lysis of target cells by activated T cells was determined by standard 4.5 hr ^{51}Cr-release assay. Briefly, target cells were labeled for 1 hr with 100 μCi ^{51}Cr (Perkin Elmer, Waltham, MA) and incubated with T cells using E:T ratios from 50:1 to 1.3:1 using 5 × 10^3 target cells. The ^{51}Cr-released was measured using a gamma counter (Titertek, Huntsville, AL). The percentage of specific lysis was calculated as: % specific lysis = ([experimental release − spontaneous release]/[maximum release − spontaneous release]) × 100.

Tumor Challenge and Treatment

Cultured cancer cells were trypsinized and washed with PBS. Cancer cells in suspension (MC57: 2 × 10^6/200 μl, 8101: 5–10 × 10^6/200 μl) were injected subcutaneously onto the shaved back of mice. Tumor volumes were measured along three orthogonal axes (*a*, *b*, and *c*) every 3 to 4 days and tumor volume calculated as *abc*/2. MC57 tumors were treated after at least 14 days, when tumors reached approximately 500 mm^3; 8101 tumors were treated after at least 5 weeks, when tumors reached approximately 300 mm^3. Mice were treated with 3 day activated T cells, one spleen per recipient. We injected 5.5 ± 1.3 × 10^7 activated 2C T cells, 5.3 ± 2.4 × 10^7 activated FH T cells, and 6.9 ± 2.2 × 10^7 activated pmel T cells (numbers were derived from six independent experiments). 8101 tumors were treated with cells from half a spleen only and with naive T cells in some of the experiments (see Table S2). T cell suspensions were injected into the recipient via the retro orbital plexus in two doses of 150 μl. For tumor protection, T cells were injected on the day of tumor challenge or 3 days later, as indicated.

Isolation of Stromal and Cancer Cells from Tumors

Two-week-old, untreated tumors were used for functional analysis; tumors of mice treated with T cells 4 or 5 days prior were used for flow cytometric analysis of T cells and stromal death, respectively. Tumors were surgically excised and single cell suspensions generated by enzymatic digestion (see Supplemental Experimental Procedures). For stromal cross-presentation, $CD11b^{+}$ cells were enriched using magnetic beads (Dynabeads FlowComp Flexi [Invitrogen Dynal, Oslo, Norway] and anti-CD11b antibody [M1/70, BD Bioscience, Franklin Lakes, NJ]).

To analyze antigen loss, relapsed tumors were surgically excised under sterile conditions and placed in DMEM on ice. Tumors were minced to 1 to 2 mm pieces and seeded in DMEM, 10% FCS, 100 U/ml penicillin, 100 μg/ml streptomycin, 50 μg/ml gentamicin, and 50 μg/ml nystatin. Cells and fragments in the flask were not moved for the initial three days and then cultured normally.

Cytokine Release Assay

T cells activated in vitro for 4 days were incubated with cancer cells cultured in vitro or tumor stromal cells obtained ex vivo. For 24 hr, 1 × 10^5 responders were cultured with 1 × 10^5 stimulators per well of a 96-well U-bottom plate. Wells coated with 1 μg/ml of anti-CD3 (145-2C11) and anti-CD28 (37.51, eBioscience) served as positive controls and maximal stimulation. All supernatants were removed and tested for IFN-γ and TNF-α using ELISA Kits ("Femto-HS" High Sensitivity, eBioscience), according to the manufacturer's protocol.

Flow Cytometry

Cells were stained using directly labeled antibodies (see Supplemental Experimental Procedures). Flow cytometry data were acquired on FACSCalibur or FACSCanto machines (BD), and data were analyzed using FlowJo (Tree Star, Ashland, OR) software. Cell sorting was performed using FACSAria (BD) or MoFlo-HTS (Beckman Coulter, Brea, CA) at the Flow Cytometry Facility of The University of Chicago.

MHC Peptide-Binding Assays

MHC purification and quantitative assays to measure the binding affinity of peptides to purified H2-K^b, H2-D^b, and HLA-A*0201 molecules were performed as previously described (Assarsson et al., 2007; Sidney et al., 2001; see Supplemental Experimental Procedures for details). Under the conditions used, where [label] < [MHC] and $IC_{50} \geq$ (MHC), the measured IC_{50} values are reasonable approximations of the true K_D values.

Statistical Analysis

Results of treatment of small groups of mice were analyzed using the two-tailed probability calculated by the Fisher's exact probability test ($p \leq 0.05$ is considered significant, $p \leq 0.01$ highly significant).

SUPPLEMENTAL INFORMATION

Supplemental Information includes four figures, one table, and Supplemental Experimental Procedures and can be found with this article online at http://dx.doi.org/10.1016/j.ccr.2013.03.018.

ACKNOWLEDGMENTS

We thank Dr. Theodore Karrison (The University of Chicago) for help with statistical analysis, Zhang Yi for generating the cancer lines MC57-hgp100 and MC57-mgp100, Andrea Schietinger for the pMFG-$(SIY)_3$-Cerulean vector, Andrew Hawk for peptide synthesis, and the University of Chicago Flow Cytometry Core Facility. We also thank Ainhoa Arina and Christian Idel for critical review of the manuscript. This work was supported by a Research Fellowship of the DFG EN 703/3-1 (to B.E.); NIH grants P01-CA97296 (to D.M.K. and H.S.), R01-CA22677, and R01-CA37156 (to H.S.); a grant from the Melanoma Research Alliance (to D.M.K.), and the Cancer Center at the University of Chicago.

Received: March 28, 2012
Revised: February 21, 2013
Accepted: March 19, 2013
Published: April 15, 2013

REFERENCES

Anders, K., Buschow, C., Herrmann, A., Milojkovic, A., Loddenkemper, C., Kammertoens, T., Daniel, P., Yu, H., Charo, J., and Blankenstein, T. (2011). Oncogene-targeting T cells reject large tumors while oncogene inactivation selects escape variants in mouse models of cancer. Cancer Cell *20*, 755–767.

Antony, P.A., Piccirillo, C.A., Akpinarli, A., Finkelstein, S.E., Speiss, P.J., Surman, D.R., Palmer, D.C., Chan, C.C., Klebanoff, C.A., Overwijk, W.W., et al. (2005). CD8+ T cell immunity against a tumor/self-antigen is augmented by CD4+ T helper cells and hindered by naturally occurring T regulatory cells. J. Immunol. *174*, 2591–2601.

Assarsson, E., Sidney, J., Oseroff, C., Pasquetto, V., Bui, H.H., Frahm, N., Brander, C., Peters, B., Grey, H., and Sette, A. (2007). A quantitative analysis of the variables affecting the repertoire of T cell specificities recognized after vaccinia virus infection. J. Immunol. *178*, 7890–7901.

Bowerman, N.A., Colf, L.A., Garcia, K.C., and Kranz, D.M. (2009). Different strategies adopted by K(b) and L(d) to generate T cell specificity directed against their respective bound peptides. J. Biol. Chem. *284*, 32551–32561.

Budhu, S., Loike, J.D., Pandolfi, A., Han, S., Catalano, G., Constantinescu, A., Clynes, R., and Silverstein, S.C. (2010). CD8+ T cell concentration determines their efficiency in killing cognate antigen-expressing syngeneic mammalian cells in vitro and in mouse tissues. J. Exp. Med. *207*, 223–235.

Buschow, C., Charo, J., Anders, K., Loddenkemper, C., Jukica, A., Alsamah, W., Perez, C., Willimsky, G., and Blankenstein, T. (2010). In vivo imaging of an inducible oncogenic tumor antigen visualizes tumor progression and predicts CTL tolerance. J. Immunol. *184*, 2930–2938.

Chapiro, J., Claverol, S., Piette, F., Ma, W., Stroobant, V., Guillaume, B., Gairin, J.E., Morel, S., Burlet-Schiltz, O., Monsarrat, B., et al. (2006). Destructive cleavage of antigenic peptides either by the immunoproteasome or by the standard proteasome results in differential antigen presentation. J. Immunol. *176*, 1053–1061.

Cheever, M.A., Greenberg, P.D., and Fefer, A. (1980). Specificity of adoptive chemoimmunotherapy of established syngeneic tumors. J. Immunol. *125*, 711–714.

Cho, H.I., Reyes-Vargas, E., Delgado, J.C., and Celis, E. (2012). A potent vaccination strategy that circumvents lymphodepletion for effective antitumor adoptive T-cell therapy. Cancer Res. *72*, 1986–1995.

Colella, T.A., Bullock, T.N., Russell, L.B., Mullins, D.W., Overwijk, W.W., Luckey, C.J., Pierce, R.A., Restifo, N.P., and Engelhard, V.H. (2000). Self-tolerance to the murine homologue of a tyrosinase-derived melanoma antigen: implications for tumor immunotherapy. J. Exp. Med. *191*, 1221–1232.

Corr, M., Slanetz, A.E., Boyd, L.F., Jelonek, M.T., Khilko, S., al-Ramadi, B.K., Kim, Y.S., Maher, S.E., Bothwell, A.L., and Margulies, D.H. (1994). T cell receptor-MHC class I peptide interactions: affinity, kinetics, and specificity. Science *265*, 946–949.

Davis, M.M., Boniface, J.J., Reich, Z., Lyons, D., Hampl, J., Arden, B., and Chien, Y. (1998). Ligand recognition by alpha beta T cell receptors. Annu. Rev. Immunol. *16*, 523–544.

Dubey, P., Hendrickson, R.C., Meredith, S.C., Siegel, C.T., Shabanowitz, J., Skipper, J.C., Engelhard, V.H., Hunt, D.F., and Schreiber, H. (1997). The immunodominant antigen of an ultraviolet-induced regressor tumor is generated by a somatic point mutation in the DEAD box helicase p68. J. Exp. Med. *185*, 695–705.

Dummer, W., Niethammer, A.G., Baccala, R., Lawson, B.R., Wagner, N., Reisfeld, R.A., and Theofilopoulos, A.N. (2002). T cell homeostatic proliferation elicits effective antitumor autoimmunity. J. Clin. Invest. *110*, 185–192.

Fujita, T., Nolan, G.P., Ghosh, S., and Baltimore, D. (1992). Independent modes of transcriptional activation by the p50 and p65 subunits of NF-kappa B. Genes Dev. *6*, 775–787.

Garcia, K.C., Tallquist, M.D., Pease, L.R., Brunmark, A., Scott, C.A., Degano, M., Stura, E.A., Peterson, P.A., Wilson, I.A., and Teyton, L. (1997). Alphabeta T cell receptor interactions with syngeneic and allogeneic ligands: affinity measurements and crystallization. Proc. Natl. Acad. Sci. USA *94*, 13838–13843.

Garcia-Hernandez, Mde.L., Hamada, H., Reome, J.B., Misra, S.K., Tighe, M.P., and Dutton, R.W. (2010). Adoptive transfer of tumor-specific Tc17 effector T cells controls the growth of B16 melanoma in mice. J. Immunol. *184*, 4215–4227.

Gattinoni, L., Finkelstein, S.E., Klebanoff, C.A., Antony, P.A., Palmer, D.C., Spiess, P.J., Hwang, L.N., Yu, Z., Wrzesinski, C., Heimann, D.M., et al. (2005). Removal of homeostatic cytokine sinks by lymphodepletion enhances the efficacy of adoptively transferred tumor-specific CD8+ T cells. J. Exp. Med. *202*, 907–912.

Gattinoni, L., Zhong, X.S., Palmer, D.C., Ji, Y., Hinrichs, C.S., Yu, Z., Wrzesinski, C., Boni, A., Cassard, L., Garvin, L.M., et al. (2009). Wnt signaling arrests effector T cell differentiation and generates CD8+ memory stem cells. Nat. Med. *15*, 808–813.

Gold, J.S., Ferrone, C.R., Guevara-Patiño, J.A., Hawkins, W.G., Dyall, R., Engelhorn, M.E., Wolchok, J.D., Lewis, J.J., and Houghton, A.N. (2003). A single heteroclitic epitope determines cancer immunity after xenogeneic DNA immunization against a tumor differentiation antigen. J. Immunol. *170*, 5188–5194.

Gottschalk, R.A., Hathorn, M.M., Beuneu, H., Corse, E., Dustin, M.L., Altan-Bonnet, G., and Allison, J.P. (2012). Distinct influences of peptide-MHC quality and quantity on in vivo T-cell responses. Proc. Natl. Acad. Sci. USA *109*, 881–886.

Gregg, R.K., Nichols, L., Chen, Y., Lu, B., and Engelhard, V.H. (2010). Mechanisms of spatial and temporal development of autoimmune vitiligo in tyrosinase-specific TCR transgenic mice. J. Immunol. *184*, 1909–1917.

Hanson, H.L., Donermeyer, D.L., Ikeda, H., White, J.M., Shankaran, V., Old, L.J., Shiku, H., Schreiber, R.D., and Allen, P.M. (2000). Eradication of established tumors by CD8+ T cell adoptive immunotherapy. Immunity *13*, 265–276.

Hensley, S.E., Das, S.R., Bailey, A.L., Schmidt, L.M., Hickman, H.D., Jayaraman, A., Viswanathan, K., Raman, R., Sasisekharan, R., Bennink, J.R., and Yewdell, J.W. (2009). Hemagglutinin receptor binding avidity drives influenza A virus antigenic drift. Science *326*, 734–736.

Ho, W.Y., Blattman, J.N., Dossett, M.L., Yee, C., and Greenberg, P.D. (2003). Adoptive immunotherapy: engineering T cell responses as biologic weapons for tumor mass destruction. Cancer Cell *3*, 431–437.

Hodi, F.S., O'Day, S.J., McDermott, D.F., Weber, R.W., Sosman, J.A., Haanen, J.B., Gonzalez, R., Robert, C., Schadendorf, D., Hassel, J.C., et al. (2010). Improved survival with ipilimumab in patients with metastatic melanoma. N. Engl. J. Med. *363*, 711–723.

Holler, P.D., and Kranz, D.M. (2003). Quantitative analysis of the contribution of TCR/pepMHC affinity and CD8 to T cell activation. Immunity *18*, 255–264.

Kawakami, Y., Eliyahu, S., Jennings, C., Sakaguchi, K., Kang, X., Southwood, S., Robbins, P.F., Sette, A., Appella, E., and Rosenberg, S.A. (1995). Recognition of multiple epitopes in the human melanoma antigen gp100 by tumor-infiltrating T lymphocytes associated with in vivo tumor regression. J. Immunol. *154*, 3961–3968.

Li, Y., Karlin, A., Loike, J.D., and Silverstein, S.C. (2002). A critical concentration of neutrophils is required for effective bacterial killing in suspension. Proc. Natl. Acad. Sci. USA *99*, 8289–8294.

Li, Y., Karlin, A., Loike, J.D., and Silverstein, S.C. (2004). Determination of the critical concentration of neutrophils required to block bacterial growth in tissues. J. Exp. Med. *200*, 613–622.

Listopad, J.J., Kammertoens, T., Anders, K., Silkenstedt, B., Willimsky, G., Schmidt, K., Kuehl, A.A., Loddenkemper, C., and Blankenstein, T. (2013). Fas expression by tumor stroma is required for cancer eradication. Proc. Natl. Acad. Sci. USA *110*, 2276–2281.

Ly, L.V., Sluijter, M., Versluis, M., Luyten, G.P., van Stipdonk, M.J., van der Burg, S.H., Melief, C.J., Jager, M.J., and van Hall, T. (2010). Peptide vaccination after T-cell transfer causes massive clonal expansion, tumor eradication, and manageable cytokine storm. Cancer Res. *70*, 8339–8346.

Matsui, K., O'Mara, L.A., and Allen, P.M. (2003). Successful elimination of large established tumors and avoidance of antigen-loss variants by aggressive adoptive T cell immunotherapy. Int. Immunol. *15*, 797–805.

Morgan, R.A., Yang, J.C., Kitano, M., Dudley, M.E., Laurencot, C.M., and Rosenberg, S.A. (2010). Case report of a serious adverse event following the administration of T cells transduced with a chimeric antigen receptor recognizing ERBB2. Mol. Ther. *18*, 843–851.

Moutaftsi, M., Salek-Ardakani, S., Croft, M., Peters, B., Sidney, J., Grey, H., and Sette, A. (2009). Correlates of protection efficacy induced by vaccinia virus-specific CD8+ T-cell epitopes in the murine intranasal challenge model. Eur. J. Immunol. *39*, 717–722.

Newberg, M.H., Smith, D.H., Haertel, S.B., Vining, D.R., Lacy, E., and Engelhard, V.H. (1996). Importance of MHC class 1 alpha2 and alpha3 domains in the recognition of self and non-self MHC molecules. J. Immunol. *156*, 2473–2480.

Nichols, L.A., Chen, Y., Colella, T.A., Bennett, C.L., Clausen, B.E., and Engelhard, V.H. (2007). Deletional self-tolerance to a melanocyte/melanoma antigen derived from tyrosinase is mediated by a radio-resistant cell in peripheral and mesenteric lymph nodes. J. Immunol. *179*, 993–1003.

North, R.J. (1982). Cyclophosphamide-facilitated adoptive immunotherapy of an established tumor depends on elimination of tumor-induced suppressor T cells. J. Exp. Med. *155*, 1063–1074.

Overwijk, W.W., Tsung, A., Irvine, K.R., Parkhurst, M.R., Goletz, T.J., Tsung, K., Carroll, M.W., Liu, C., Moss, B., Rosenberg, S.A., and Restifo, N.P. (1998). gp100/pmel 17 is a murine tumor rejection antigen: induction of "self"-reactive, tumoricidal T cells using high-affinity, altered peptide ligand. J. Exp. Med. *188*, 277–286.

Overwijk, W.W., Theoret, M.R., Finkelstein, S.E., Surman, D.R., de Jong, L.A., Vyth-Dreese, F.A., Dellemijn, T.A., Antony, P.A., Spiess, P.J., Palmer, D.C., et al. (2003). Tumor regression and autoimmunity after reversal of a functionally tolerant state of self-reactive CD8+ T cells. J. Exp. Med. *198*, 569–580.

Palmer, D.C., Chan, C.C., Gattinoni, L., Wrzesinski, C., Paulos, C.M., Hinrichs, C.S., Powell, D.J., Jr., Klebanoff, C.A., Finkelstein, S.E., Fariss, R.N., et al. (2008). Effective tumor treatment targeting a melanoma/melanocyte-associated antigen triggers severe ocular autoimmunity. Proc. Natl. Acad. Sci. USA *105*, 8061–8066.

Parkhurst, M.R., Salgaller, M.L., Southwood, S., Robbins, P.F., Sette, A., Rosenberg, S.A., and Kawakami, Y. (1996). Improved induction of melanoma-reactive CTL with peptides from the melanoma antigen gp100 modified at HLA-A*0201-binding residues. J. Immunol. *157*, 2539–2548.

Parkhurst, M.R., Yang, J.C., Langan, R.C., Dudley, M.E., Nathan, D.A., Feldman, S.A., Davis, J.L., Morgan, R.A., Merino, M.J., Sherry, R.M., et al. (2011). T cells targeting carcinoembryonic antigen can mediate regression of metastatic colorectal cancer but induce severe transient colitis. Mol. Ther. *19*, 620–626.

Pascolo, S., Bervas, N., Ure, J.M., Smith, A.G., Lemonnier, F.A., and Pérarnau, B. (1997). HLA-A2.1-restricted education and cytolytic activity of CD8(+) T lymphocytes from beta2 microglobulin (beta2m) HLA-A2.1 monochain transgenic H-2Db beta2m double knockout mice. J. Exp. Med. *185*, 2043–2051.

Popovic, J., Li, L.P., Kloetzel, P.M., Leisegang, M., Uckert, W., and Blankenstein, T. (2011). The only proposed T-cell epitope derived from the TEL-AML1 translocation is not naturally processed. Blood *118*, 946–954.

Purbhoo, M.A., Irvine, D.J., Huppa, J.B., and Davis, M.M. (2004). T cell killing does not require the formation of a stable mature immunological synapse. Nat. Immunol. *5*, 524–530.

Schreiber, K., Wu, T.H., Kast, W.M., and Schreiber, H. (2001). Tracking the common ancestry of antigenically distinct cancer variants. Clin. Cancer Res. *7*(3, Suppl), 871s–875s.

Schultz, E.S., Chapiro, J., Lurquin, C., Claverol, S., Burlet-Schiltz, O., Warnier, G., Russo, V., Morel, S., Lévy, F., Boon, T., et al. (2002). The production of a new MAGE-3 peptide presented to cytolytic T lymphocytes by HLA-B40 requires the immunoproteasome. J. Exp. Med. *195*, 391–399.

Sidney, J., Southwood, S., Oseroff, C., del Guercio, M.F., Sette, A., and Grey, H.M. (2001). Measurement of MHC/peptide interactions by gel filtration. Curr. Protoc. Immunol. *31*, 18.3.1–18.3.19.

Singh, S., Ross, S.R., Acena, M., Rowley, D.A., and Schreiber, H. (1992). Stroma is critical for preventing or permitting immunological destruction of antigenic cancer cells. J. Exp. Med. *175*, 139–146.

Skipper, H.E. (1986). On mathematical modeling of critical variables in cancer treatment (goals: better understanding of the past and better planning in the future). Bull. Math. Biol. *48*, 253–278.

Spiotto, M.T., Yu, P., Rowley, D.A., Nishimura, M.I., Meredith, S.C., Gajewski, T.F., Fu, Y.X., and Schreiber, H. (2002). Increasing tumor antigen expression overcomes "ignorance" to solid tumors via crosspresentation by bone marrow-derived stromal cells. Immunity *17*, 737–747.

Spiotto, M.T., Rowley, D.A., and Schreiber, H. (2004). Bystander elimination of antigen loss variants in established tumors. Nat. Med. *10*, 294–298.

Tsai, V., Southwood, S., Sidney, J., Sakaguchi, K., Kawakami, Y., Appella, E., Sette, A., and Celis, E. (1997). Identification of subdominant CTL epitopes of the GP100 melanoma-associated tumor antigen by primary in vitro immunization with peptide-pulsed dendritic cells. J. Immunol. *158*, 1796–1802.

van Stipdonk, M.J., Badia-Martinez, D., Sluijter, M., Offringa, R., van Hall, T., and Achour, A. (2009). Design of agonistic altered peptides for the robust induction of CTL directed towards H-2Db in complex with the melanoma-associated epitope gp100. Cancer Res. *69*, 7784–7792.

Wang, R., Rogers, A.M., Ratliff, T.L., and Russell, J.H. (1996). CD95-dependent bystander lysis caused by CD4+ T helper 1 effectors. J. Immunol. *157*, 2961–2968.

Williams, C.B., Engle, D.L., Kersh, G.J., Michael White, J., and Allen, P.M. (1999). A kinetic threshold between negative and positive selection based on the longevity of the T cell receptor-ligand complex. J. Exp. Med. *189*, 1531–1544.

Yee, C., Thompson, J.A., Roche, P., Byrd, D.R., Lee, P.P., Piepkorn, M., Kenyon, K., Davis, M.M., Riddell, S.R., and Greenberg, P.D. (2000). Melanocyte destruction after antigen-specific immunotherapy of melanoma: direct evidence of t cell-mediated vitiligo. J. Exp. Med. *192*, 1637–1644.

Zhang, B., Bowerman, N.A., Salama, J.K., Schmidt, H., Spiotto, M.T., Schietinger, A., Yu, P., Fu, Y.X., Weichselbaum, R.R., Rowley, D.A., et al. (2007). Induced sensitization of tumor stroma leads to eradication of established cancer by T cells. J. Exp. Med. *204*, 49–55.

Zhang, B., Karrison, T., Rowley, D.A., and Schreiber, H. (2008). IFN-gamma- and TNF-dependent bystander eradication of antigen-loss variants in established mouse cancers. J. Clin. Invest. *118*, 1398–1404.

Engels, B., Engelhard, V.H., Sidney, J., Sette, A., Binder, D.C., Liu, R.B., Kranz, D.M., Meredith, S.C., Rowley, D.A., and Schreiber, H. (2013). Cancer Cell *23*, this issue, 516–526.

Johnson, L.A., Morgan, R.A., Dudley, M.E., Cassard, L., Yang, J.C., Hughes, M.S., Kammula, U.S., Royal, R.E., Sherry, R.M., Wunderlich, J.R., et al. (2009). Blood *114*, 535–546.

Schreiber, H. (2013). Cancer Immunology. In Fundamental Immunology, Seventh Edition, W.E. Paul, ed. (Philadelphia, PA, USA: Lippincott Williams and Wilkins, a Wolters Kluwer business), pp. 1200–1234.

Schreiber, H., and Rowley, D.A. (2008). Science *319*, 164–165.

Schumacher, T.N. (2002). Nat. Rev. Immunol. *2*, 512–519.

Stone, J.D., Chervin, A.S., and Kranz, D.M. (2009). Immunology *126*, 165–176.

Standing Out from the Crowd: Cancer Stem Cells in Hepatocellular Carcinoma

Bruno Sainz, Jr.[1] **and Christopher Heeschen**[1,*]
[1]Stem Cells and Cancer Group, Molecular Pathology Programme, Spanish National Cancer Research Centre (CNIO), Madrid 28029, Spain
*Correspondence: cheeschen@cnio.es
http://dx.doi.org/10.1016/j.ccr.2013.03.023

Cancer stem cells (CSCs) drive solid tumor formation. In this issue of *Cancer Cell*, Zhao and colleagues identify the calcium channel α2δ1 subunit as a new functional hepatocellular carcinoma (HCC) CSC biomarker, which is vital for CSC biology as blocking α2δ1 in combination with doxorubicin treatment hinders HCC tumor formation.

Hepatocellular carcinoma (HCC) accounts for 90% of primary liver cancers and is the third most common cause of cancer-related deaths worldwide (Edwards et al., 2010). Unlike most other carcinomas, where mutations in specific oncogenes or tumor suppressors drive tumor initiation and progression, the majority of HCCs are multifactorial and primarily due to infections with hepatitis B virus (HBV) or hepatitis C virus (HCV). However, worldwide cases of nonviral HCC are on the rise due to growing numbers of patients with metabolic liver diseases (Alberti et al., 2005; Van Thiel and Ramadori, 2011). This multi-causality makes identification and subsequent targeting of a common HCC-specific alteration or even a cell-of-origin virtually impossible. Fortunately, where consensus does exist is in the concept that the majority of HCC arise from a subpopulation of cancer cells referred to as tumor-initiating cells (TICs) or cancer stem cells (CSCs) (Majumdar et al., 2012). Thus, identifying and therapeutically targeting these cells represents a more feasible approach for treating HCC regardless of the underlying cause.

CSCs are believed to possess stem cell-like properties such as unlimited self-renewal, exclusive in vivo tumorigenicity, and subsequent generation of differentiated progeny recapitulating the parental tumor phenotype (Figure 1). Evidence for their existence in several solid tumors has been experimentally demonstrated (reviewed in Hermann et al., 2010). For HCC, cells expressing diverse markers such as CD133, CD13, CD24, CD90, and EpCAM as well as cells defined as the side population have all been demonstrated to bear CSC characteristics. Apparently, the utility of these different markers across established cell lines and primary tumors varies significantly, and their suitability for therapeutic targeting has not been extensively evaluated. Therefore, the identification of markers, preferably a single marker, for efficient isolation of CSCs from the complex tumor cellular environment across different HCC tissues is still critically needed.

In this issue of *Cancer Cell*, Zhao et al. (2013) report that HCC CSCs can be specifically isolated with a new antibody (1B50-1) identified using a whole-cell subtractive immunization approach that recognizes the isoform 5 of the cell surface calcium channel α2δ1 subunit. 1B50-1 binds a subpopulation of HCC cells, hereafter termed $\alpha2\delta1^+$ cells, exhibiting stem cell-like properties, such as increased invasiveness, expression of stem cell-associated genes (*OCT4*, *SOX2*, *NANOG*, and *BMI1*), increased self-renewal, and the ability to give rise to both $\alpha2\delta1^+$ and $\alpha2\delta1^-$ cells. More importantly, the authors showed that subcutaneously injected $\alpha2\delta1^+$ cells from cell lines and primary HCC tumors were more tumorigenic in NOD/SCID mice compared to their $\alpha2\delta1^-$ counterparts. Although the increased tumorigenic potential of $\alpha2\delta1^+$ cells was evident with as little as 10^3 cells, limiting dilution assays (injection with less than 100 cells were not performed) revealed that not all $\alpha2\delta1^+$ cells were tumorigenic (TIC frequency in primary cases: 1 in 458 [748-281]), and higher numbers of $\alpha2\delta1^-$ cells were also capable of forming tumors (TIC frequency: 1 in 1,957 [3,785-1,012]) (calculated from Table 1 in Zhao et al., 2013). Therefore, $\alpha2\delta1^+$ cells from primary tumors were enriched for CSCs 4-fold.

Unlike many normal tissues where a stringent unidirectional hierarchy and strict balanced asymmetric division preserve tissue integrity (Jan and Jan, 1998), data in solid tumors are generally not as clear cut. On the one hand, this might be related to our still limited ability

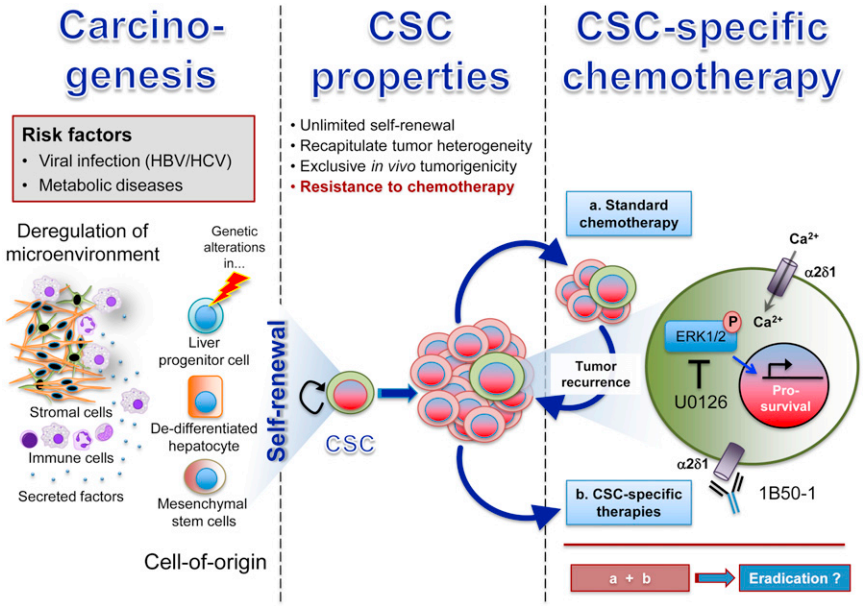

Figure 1. The CSC Concept

HCC, like many other solid tumors, is composed of a heterogeneous population of cells that contain CSCs. Although the process of hepatocarcinogenesis is multi-causal and multi-factorial, HBV and HCV infection, as well as metabolic liver diseases are the primary mediators of HCC. During tumor initiation, liver progenitor cells, hepatocytes, or circulating bone marrow-derived cells are believed to suffer genetic and epigenetic changes, which, together with a deregulation of the microenvironment (e.g., chronic inflammation and cirrhosis), eventually give rise to a distinct subpopulation of CSCs that have stem-like properties. CSCs can survive current standard therapies, resulting in tumor recurrence and disease relapse. The work by Zhao et al. (2013) suggests that HCC CSCs overexpress the calcium channel α2δ1 subunit, and thus targeting α2δ1 (e.g., using 1B50-1), or its downstream mediators (e.g., inhibition of ERK1/2), and in combination with standard chemotherapy may eradicate HCC.

for thoroughly dissecting the hierarchical organization of solid tumors. Indeed, Zhao et al. (2013) also showed a clear hierarchical organization within the $\alpha2\delta1^+$ sub-population for HCC, demonstrating that $\alpha2\delta1^+$ cells additionally expressing CD133, CD13, or EpCAM were even more tumorigenic in vivo. However, these marker combinations remain challenging, because $\alpha2\delta1^+$ cells that are negative for the second marker and vice versa also result in a moderate enrichment for CSC, and double negative populations are still not void of CSC activity (Figure 1H in Zhao et al., 2013). On the other hand, the border between tumorigenic CSCs and their nontumorigenic progenies might be more dynamic than in normal tissue, and intermediate progenitors in cancer tissue might be capable of replenishing tumorigenic CSCs. The latter should be more stringently tested in vitro and in vivo at the single cell level in order to identify the specific subset of $\alpha2\delta1^+$ cells with exclusive tumorigenic potential as well as to thoroughly evaluate the possibility that a subset of $\alpha2\delta1^-$ cells is capable of replenishing $\alpha2\delta1^+$ CSCs. Furthermore, we also should not underestimate the important role of the tumor microenvironment that could dramatically alter a cell's in vivo tumorigenic potential (Lonardo et al., 2012; Quintana et al., 2008).

While these studies remain pending, Zhao et al. (2013) further showed that in 86 paired HCC and paracancerous tissue samples, $\alpha2\delta1^+$ cells could be found not only in the majority of primary HCC samples but also in many of the corresponding paracancerous tissues. Moreover, when sorted, only $\alpha2\delta1^+$ cells from both the primary tumor and paracancerous tissues were tumorigenic in vivo (even though the number of tested samples was very small) and could recapitulate the parental tumor phenotype. Interestingly, although $\alpha2\delta1^+$ staining in the primary tumor did not correlate with any clinicopathological factor, $\alpha2\delta1^+$ staining in the paracancerous tissue strongly correlated with cirrhosis, quicker recurrence, and shorter survival, supporting the potential use of $\alpha2\delta1^+$ staining in paracancerous tissue as a prognostic HCC biomarker. Although the present study was not really powered to model the multifactorial panorama of HCC and therefore more extensive studies are still warranted, this study clearly supports the hypothesis that $\alpha2\delta1^+$ cells in paracancerous tissue represent a putative cell-of-origin for HCC recurrence.

Next, the authors determined the function of α2δ1 in HCC CSC biology. α2δ1 is a protein component of the voltage-dependent calcium channel complex, of which there exist several types. Calcium influx is an essential cellular process mediating a plethora of intracellular signaling cascades such as MAPK signaling. Not only was α2δ1 over-expressed in $\alpha2\delta1^+$ cells, but also intracellular calcium concentrations and calcium oscillations were higher in $\alpha2\delta1^+$ cells and could be modulated by 1B50-1 treatment or α2δ1 silencing. In addition, ERK1/2 phosphorylation was suppressed by α2δ1 inhibition, suggesting that α2δ1 may potentiate HCC CSC by activating pro-survival pathways mediated by MAPKs via a calcium-dependent mechanism. Indeed, the authors show that $\alpha2\delta1^+$ cells were also susceptible to the ERK1/2 inhibitor U0126. Therefore, these findings highlight not only α2δ1 as a marker amenable for HCC CSC isolation but also a previously unappreciated role for Ca^{2+} influx in CSC biology.

Finally, one of the most interesting aspects of the present study centered on the therapeutic potential of targeting α2δ1. Zhao et al. (2013) convincingly demonstrate that treatment of HCC cells with 1B50-1 or silencing of α2δ1 decreases CSC activity via induction of cellular apoptosis by downregulation of BCL2 and upregulation of BAX and BAD. Importantly, 1B50-1 not only reduced tumor size and induced cell apoptosis but also affected the CSC content, as determined by loss of $\alpha2\delta1^+$ cells and loss of serial transplantation capacity in NOD/SCID mice. Importantly, the effects could be further augmented by the addition of doxorubicin, supporting a bimodal treatment approach in which CSCs and their progenies are simultaneously targeted. This kind of combinatorial approach has also been proposed for other solid tumors, such as pancreatic ductal adenocarcinoma (Lonardo et al., 2011), and may also reflect the need for blocking replenishment of CSCs from their more

differentiated $\alpha2\delta1^-$ progenies. Based on these promising results, studies focusing on the use of 1B50-1 or other agents that target $\alpha2\delta1$ in HCC and potentially in other solid tumors should be extensively pursued.

REFERENCES

Alberti, K.G., Zimmet, P., and Shaw, J. (2005). Lancet *366*, 1059–1062.

Edwards, B.K., Ward, E., Kohler, B.A., Eheman, C., Zauber, A.G., Anderson, R.N., Jemal, A., Schymura, M.J., Lansdorp-Vogelaar, I., Seeff, L.C., et al. (2010). Cancer *116*, 544–573.

Hermann, P.C., Bhaskar, S., Cioffi, M., and Heeschen, C. (2010). Semin. Cancer Biol. *20*, 77–84.

Jan, Y.N., and Jan, L.Y. (1998). Nature *392*, 775–778.

Lonardo, E., Hermann, P.C., Mueller, M.T., Huber, S., Balic, A., Miranda-Lorenzo, I., Zagorac, S., Alcala, S., Rodriguez-Arabaolaza, I., Ramirez, J.C., et al. (2011). Cell Stem Cell *9*, 433–446.

Lonardo, E., Frias-Aldeguer, J., Hermann, P.C., and Heeschen, C. (2012). Cell Cycle *11*, 1282–1290.

Majumdar, A., Curley, S.A., Wu, X., Brown, P., Hwang, J.P., Shetty, K., Yao, Z.X., He, A.R., Li, S., Katz, L., et al. (2012). Nat Rev Gastroenterol Hepatol *9*, 530–538.

Quintana, E., Shackleton, M., Sabel, M.S., Fullen, D.R., Johnson, T.M., and Morrison, S.J. (2008). Nature *456*, 593–598.

Van Thiel, D.H., and Ramadori, G. (2011). J Gastrointest Cancer *42*, 191–194.

Zhao, W., Wang, L., Han, H., Jin, K., Lin, N., Guo, T., Chen, Y., Cheng, H., Lu, F., Fang, W., et al. (2013). Cancer Cell *23*, this issue, 541–556.

Autophagy in Multiple Myeloma: What Makes You Stronger Can Also Kill You

Richard G. Carroll[1] and Seamus J. Martin[1,*]
[1]Molecular Cell Biology Laboratory, Department of Genetics, The Smurfit Institute, Trinity College, Dublin 2, Ireland
*Correspondence: martinsj@tcd.ie
http://dx.doi.org/10.1016/j.ccr.2013.04.001

Autophagy, a process for recycling cellular constituents, is normally associated with cell survival and is thought to be beneficial for tumor maintenance. However, in this issue of *Cancer Cell*, Lamy and colleagues report that multiple myeloma utilizes caspase-10 to restrain autophagy and undergoes autophagic cell death upon its removal or inhibition.

Autophagy is a stress-induced catabolic process that is used to capture and eliminate defective organelles, protein aggregates, and intracellular microbes by targeting these to lysosomes for destruction (reviewed in Choi et al., 2013). Autophagy can also be deployed to recycle bulk cytoplasmic constituents in response to starvation, thereby sustaining cell survival. The role of autophagy in tumorigenesis has been debated. There is evidence supporting the view that autophagy is ramped up in transformed cells and is beneficial for tumor maintenance and progression (reviewed in White, 2012). On the other hand, there is also evidence to argue that excessive autophagy can act as a tumor-suppressive mechanism (Elgendy et al., 2011; Choi et al., 2013), possibly through initiation of cell death or senescence. Autophagic cell death typically displays none of the features of apoptosis and can be attenuated through ablation of key autophagy regulators such as Atg proteins or Beclin-1. There has been skepticism that cells can die through excessive autophagy (Kroemer and Levine, 2008), however, a significant body of evidence is emerging to argue that autophagic cell death occurs in several important contexts (Das et al., 2012). In this issue of *Cancer Cell*, Lamy et al. (2013) provide support for the idea that deregulated autophagy can result in cellular autodestruction in multiple myeloma.

Multiple myeloma is a clonal B cell malignancy arising from plasma cells, which are specialized antibody-producing cells critical for antibody-based immunity. Upon activation by the appropriate antigen, B cells differentiate into long-lived plasma cells that are equipped with an extensive endoplasmic reticulum (ER) and serve as antibody factories, synthesizing prodigious quantities of immunoglobulin. However, the latter capability is a source of proteotoxic stress due to misfolding of a proportion of newly synthesized immunoglobulin, the accumulation of which can lead to ER stress and cell death if not properly dealt with. Plasma cells solve this problem by ramping up several protein handling systems, including the ubiquitin-proteasome pathway, the unfolded protein response (UPR) pathway, and the autophagy machinery. Autophagy facilitates the removal of protein aggregates by encapsulating these in autophagosomes, followed by their degradation through fusion with lysosomes. Indeed, a recent study has shown that mice deficient in a critical component of the autophagy machinery, Atg5, preferentially lose Atg5-deficient plasma cells and are compromised in making long-term antibody responses as a result (Pengo et al., 2013). Thus, plasma cells rely heavily on autophagy, as well as other protein degradation systems, to keep the factory floor free of debris that would otherwise choke up the antibody production line. Because of this, multiple myeloma displays particular sensitivity to proteasome inhibitors, such as bortezomib, and the possibility of combining such treatments with inhibitors of autophagy is under investigation (Aronson and Davies, 2012).

Using an RNA interference library screening approach, Lamy et al. (2013) searched for molecules critical for the survival of multiple myeloma cells. Somewhat counter-intuitively, caspase-10, a protease normally associated with induction of apoptosis in response to TNF family members, emerged as a survival factor for all myeloma cell lines tested (Lamy et al., 2013). This observation was confirmed using a variety of approaches. Further investigation revealed that inhibition of caspase-10 or knockdown of a molecule involved in facilitating its activation, $cFLIP_L$, led to a dramatic increase in autophagic flux followed by cell death lacking features of apoptosis. More compellingly, knockdown of two constituents of the autophagy machinery, Atg5 or Beclin-1, led to protection from cell death caused by caspase-10 inhibition (Lamy et al., 2013). Taken together, these data suggest that caspase-10 sets a threshold for autophagy in multiple myeloma that, if breached, can lead to autophagic cell death (Figure 1).

So how does caspase-10 put the brakes on autophagy? Lamy et al. (2013) found that BCLAF1, a protein of uncertain function that was originally identified as a binding partner of pro-survival Bcl-2 family members, might be the key target of caspase-10 in this context (Figure 1A). Although members of the Bcl-2 family are well known for their role as inhibitors of apoptosis, several members of this family also directly interact with and inhibit Beclin-1, thereby suppressing autophagy (Elgendy et al., 2011; Choi et al., 2013). Silencing of BCLAF1 expression in myeloma abrogated cell death caused by caspase-10 inhibition, whereas overexpression of BCLAF1 promoted cell death with features of autophagy. Thus, upon inhibition of caspase-10, BCLAF1 is stabilized and displaces Bcl-2 from Beclin-,1 thereby ramping up autophagy and leading to cell death (Figure 1B). Several questions remain to be resolved, however. The precise nature

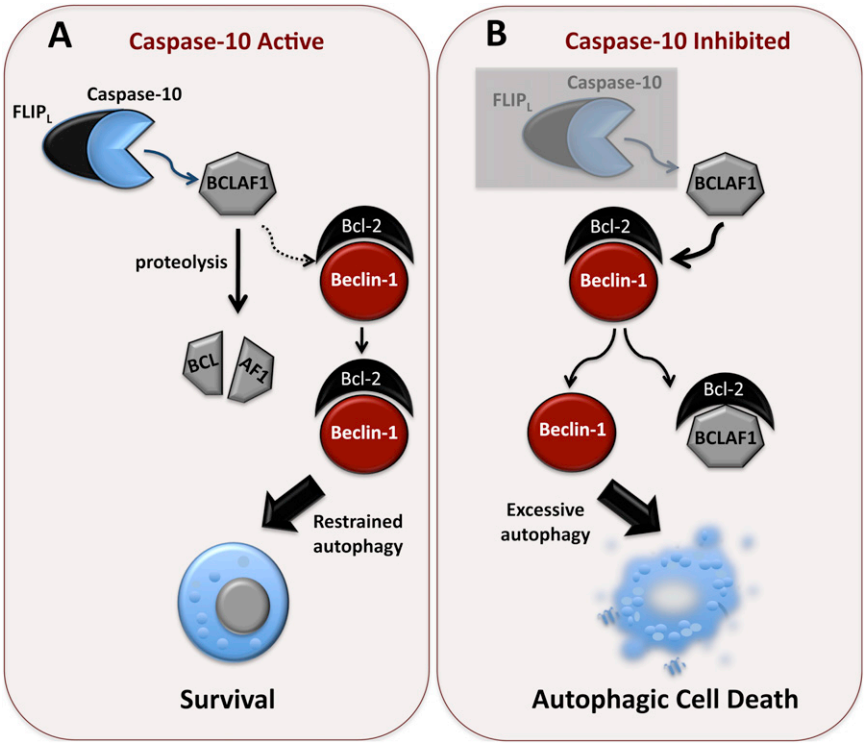

Figure 1. Caspase-10 Puts a Brake on Autophagy in Multiple Myeloma
(A) Under steady-state conditions in multiple myeloma, a FLIP$_L$/caspase-10 complex cleaves and inactivates BCLAF1 preventing its participation in autophagy.
(B) Upon inhibition or knockdown of caspase-10, BCLAF1 becomes stabilized, displacing Bcl-2 from Beclin-1, leading to excessive autophagy followed by autophagic cell death.

of the FLIP$_L$/caspase-10-activating complex remains to be clarified, as does the issue of whether assembly of this complex is spontaneous or driven by autocrine or paracrine death receptor signals. The role of BCLAF1 as a driver of autophagy and how deregulated autophagy leads to cell death also require significant clarification.

Interestingly, previous studies have also implicated autophagy as a component of the cell death response of multiple myeloma to inhibitors of the protein handling machinery. Inhibition of autophagy partly antagonized the cytotoxic effects of bortezomib, suggesting that autophagic cell death may be partly responsible for the cytotoxic effects of proteasome inhibitors in myeloma (Hoang et al., 2009). Silencing of the UPR sensors PERK, IRE1, or ATF6 also led to the death of myeloma cells via excessive induction of autophagy (Michallet et al., 2011). Thus, due to the pressures resulting from the accumulation of misfolded immunoglobulin, multiple myeloma may be uniquely predisposed toward autophagic cell death if protein handling pathways are tampered with.

One implication of the current study is that the process leading to the transformation of plasma cells places their malignant counterparts in a precarious state of "autophagic stress" that needs to be reined in for such cells to survive. Indeed, this may be a general property of many tumors, as several oncogenes such as H-Ras, B-Raf, and Myc have been found to ramp up autophagy by different mechanisms. Thus, excessive autophagy may represent a tumor suppressor mechanism that needs to be counteracted during tumorigenesis to constrain this tendency toward self-immolation. Varying solutions to this problem are likely to be found among different tumors, with some losing one allele of the Beclin-1 gene, as is frequently seen in breast, prostate, and ovarian tumors, while others upregulate the expression of Bcl-2 family proteins that can inhibit the actions of Beclin-1 (Choi et al., 2013). Multiple alternative strategies may also be employed to constrain autophagy within acceptable limits, such as the caspase-10-dependent mechanism described by Lamy et al. (2013).

Thus, autophagy appears to be a double-edged sword that can be beneficial as well as detrimental to tumor development. Tumors need to get the autophagy balance right to avail its advantages, which help to cope with the demands of limited nutrient and oxygen supply, while avoiding the disadvantages of untrammelled autophagy, which can lead to excessive self-consumption of cellular resources.

An obvious therapeutic implication of the finding that caspase-10 acts as a survival factor in multiple myeloma is that inhibitors of caspase-10 might have therapeutic utility in this malignancy. However, such inhibitors would have to be sufficiently specific to avoid disruption of caspases in critical processes such as apoptosis and inflammation. One of the key lessons from the current study is that, in cancer, too much autophagy may be as bad as too little. Thus, encouraging the self-cannibalistic tendencies of multiple myeloma may be a viable therapeutic strategy.

REFERENCES

Aronson, L.I., and Davies, F.E. (2012). Haematologica *97*, 1119–1130.

Choi, A.M., Ryter, S.W., and Levine, B. (2013). N. Engl. J. Med. *368*, 651–662.

Das, G., Shravage, B.V., and Baehrecke, E.H. (2012). Cold Spring Harb. Perspect. Biol. *4*, pii: a008813.10.1101/cshperspect.a008813.

Elgendy, M., Sheridan, C., Brumatti, G., and Martin, S.J. (2011). Mol. Cell *42*, 23–35.

Hoang, B., Benavides, A., Shi, Y., Frost, P., and Lichtenstein, A. (2009). Mol. Cancer Ther. *8*, 1974–1984.

Kroemer, G., and Levine, B. (2008). Nat. Rev. Mol. Cell Biol. *9*, 1004–1010.

Lamy, L., Ngo, V.N., Emre, N.C., Shaffer, A.L., 3rd, Yang, Y., Tian, E., Nair, V., Kruhlak, M.J., Zingone, A., Landgren, O., and Staudt, L.M. (2013). Cancer Cell *23*, this issue, 435–449.

Michallet, A.S., Mondiere, P., Taillardet, M., Leverrier, Y., Genestier, L., and Defrance, T. (2011). PLoS ONE *6*, e25820.

Pengo, N., Scolari, M., Oliva, L., Milan, E., Mainoldi, F., Raimondi, A., Fagioli, C., Merlini, A., Mariani, E., Pasqualetto, E., et al. (2013). Nat. Immunol. *14*, 298–305.

White, E. (2012). Nat. Rev. Cancer *12*, 401–410.

Sirt4: The Glutamine Gatekeeper

Pablo J. Fernandez-Marcos[1] and Manuel Serrano[1,*]
[1]Tumor Suppression Group, Spanish National Cancer Research Centre (CNIO), Madrid 28029, Spain
*Correspondence: mserrano@cnio.es
http://dx.doi.org/10.1016/j.ccr.2013.04.003

Little is known about how DNA damage and metabolism are interconnected. In this issue of *Cancer Cell*, Jeong and colleagues report that an important component of the DNA damage response is the SIRT4-mediated blockade of glutamine catabolism. Failure to shut down glutamine consumption results in unscheduled proliferation, genomic instability, and cancer.

DNA damage is a natural process that occurs in all cells under normal physiological conditions. Multiple cellular mechanisms sense the presence of DNA damage and trigger adaptive responses (collectively known as DNA damage response or DDR), which culminate in a proliferative arrest that allows for DNA repair. Defects in the DDR can lead to unrepaired DNA damage, including oncogenic DNA alterations, and eventually to cancer. In recent years, it has become evident that cell proliferation and metabolism are intimately connected (DeBerardinis et al., 2008), therefore implying that DDR-induced proliferative arrest must be accompanied by metabolic changes. However, although much is known about the molecular biology of the DDR, the metabolic consequences of DNA damage have remained largely unexplored until very recently. The DDR has been shown to increase the cellular antioxidant defenses through the production of NADPH by the pentose phosphate pathway (Bensaad et al., 2006; Cosentino et al., 2011). In other settings, the DDR downregulates glucose uptake and glycolysis (Zhou et al., 2002). These precedents support the concept that metabolic changes constitute an intrinsic aspect of the DDR.

A new study by Jeong et al. (2013) in this issue of *Cancer Cell* uncovers a new connection between the DDR and metabolism. By performing metabolic analyses of cells in the presence or absence of DNA damage, the authors confirmed previous reports indicating that DNA damage increases the flux through the pentose phosphate pathway (Bensaad et al., 2006; Cosentino et al., 2011). In addition, they found an unexpected decrease in glutamine uptake and in intermediates of the tricarboxylic acid (TCA) cycle. These initial observations set the focus on the connection between DNA damage, glutamine, and the TCA cycle.

Quiescent cells use the TCA cycle to produce energy from glucose. In contrast, proliferating cells mostly use it for a completely different purpose: as a carbon source for lipogenesis through the mitochondrial efflux of citric acid. This efflux must be compensated by an influx of TCA cycle intermediates, a process known as anaplerosis. Of relevance, glutamine is the main source for TCA anaplerosis in proliferating cells (DeBerardinis et al., 2008). In a first reaction, glutamine is converted into glutamate by glutaminase (GLS) and then into α-ketoglutarate (αKG) by either glutamate dehydrogenase (GDH) or, less prominently, by transamination-coupled reactions. Jeong et al. (2013) characterize how several types of DNA damage block glutamine anaplerosis in proliferating cells. They had previously shown that SIRT4 ADP-ribosylates and inhibits GDH (Haigis et al., 2006), and based on this, they reasoned that SIRT4 might be involved in the inhibition of glutamine uptake and anaplerosis triggered by DNA damage. SIRT4 is a member of the sirtuin family (SIRT1–7) of protein deacetylases and ADP-ribosylases involved in multiple cellular processes, including the maintenance of genomic stability and regulation of metabolism (Sebastián et al., 2012). Interestingly, *SIRT4* mRNA levels were highly induced upon different types of DNA damage, even higher than other sirtuin members previously related to the DDR, such as SIRT1 or SIRT3. Importantly, the authors demonstrate that SIRT4-mediated inhibition of glutamine anaplerosis is necessary for efficient cell cycle arrest upon DNA damage (Figure 1). In the absence of SIRT4, failure to arrest the cell cycle in response to DNA damage results in delayed DNA repair and increased chromosomal aneuploidies. Even more, SIRT4-deficient primary fibroblasts already show aberrant levels of polyploidy, suggesting that SIRT4 is important not only in response to exogenously inflicted DNA damage, but also to protect cells from spontaneous damage.

The above findings suggest that the SIRT4-mediated blockade of glutamine anaplerosis could be a tumor suppressor mechanism. Indeed, Jeong et al. (2013) present multiple lines of evidence. First, they show that SIRT4-deficient fibroblasts grow faster than their wild-type counterparts. Also, neoplastic SIRT4-deficient fibroblasts are less dependent on glucose and form larger allograft tumors than SIRT4-proficient cells. These pro-tumorigenic phenotypes were reversed when cells were treated with GLS1 or GDH inhibitors or upon ectopic expression of catalytically active, but not catalytically dead, SIRT4. Moreover, several human malignancies present reduced *SIRT4* mRNA levels, and this is associated with a poorer outcome in the case of lung adenocarcinomas.

The authors recapitulate their main findings in genetically modified mice lacking SIRT4 (Jeong et al., 2013). Importantly, two independently generated strains of SIRT4-deficient mice present a significant incidence of spontaneous lung tumors compared to their wild-type littermates. In support of a direct inhibitory effect of SIRT4 on GDH (Haigis et al., 2006), lung extracts from SIRT4-deficient mice presented higher constitutive levels of GDH activity. Moreover, ionizing irradiation decreased GDH activity in wild-type but not SIRT4-deficient lungs. Together, these observations compellingly demonstrate that SIRT4 is a tumor suppressor contributing to the DDR by

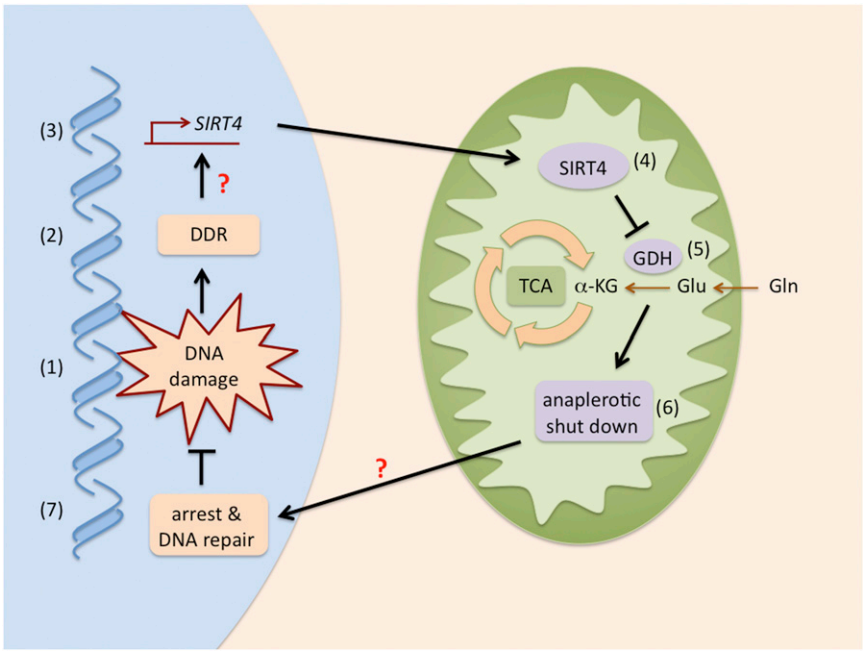

Figure 1. SIRT4: The Glutamine Gatekeeper
DNA damage (1) elicits the DDR (2) that, through undefined mechanisms (indicated with a question mark), results in enhanced *SIRT4* transcription (3) and higher SIRT4 activity in the mitochondria (4). In turn, SIRT4 inhibits glutamine conversion into αKG by inhibiting glutamate dehydrogenase (GDH) (5). Decreased αKG shuts down the anaplerotic replenishment of the tricarboxylic acid cycle (TCA) (6), which, through mechanisms that remain to be clarified (question mark), result in arrest and DNA repair (7).

shutting down glutamine metabolism (Figure 1).

The new findings by Jeong et al. (2013) strongly reinforce previous evidences pointing to glutamine-dependent anaplerosis as an attractive Achilles' heel of cancer cells. For example, GLS1 inhibition impairs neoplastic transformation (Wang et al., 2010). Also, estrogen receptor-negative breast cancers present a particular type of glutamine-dependent anaplerosis characterized by elevated levels of the gene encoding phosphoglycerate dehydrogenase (PHGDH) (Possemato et al., 2011). This enzyme diverts phosphoglycerate (a glycolytic intermediate) into the so-called serine pathway. The relevance of this pathway for cancer does not reside in the synthesis of serine but on the fact that its transamination step is coupled to the conversion of glutamate into αKG, thereby directly contributing to TCA anaplerosis independently of GDH (Possemato et al., 2011). Importantly, inhibition of PHGDH in breast cancer cell lines induces a metabolic collapse in TCA cycle intermediates that is highly reminiscent to the one observed upon DDR-induced SIRT4 upregulation and the ensuing GDH inhibition (Jeong et al., 2013; Possemato et al., 2011).

A few aspects in the DDR-mediated block in glutamine anaplerosis still remain to be elucidated. Not much is known about the mechanisms that upregulate *SIRT4* mRNA by DNA damage, apart from the lack of involvement of p53 (Jeong et al., 2013). Finding the exact components of the DDR pathway responsible for *SIRT4* induction could point to new strategies to shut down glutamine-dependent anaplerosis. It is also unclear yet how the glutamine-dependent anaplerotic blockade contributes to the implementation of DDR-induced cell cycle arrest.

Intriguingly, with the current report, essentially all members of the sirtuin family have been involved in cancer protection and metabolism (Sebastián et al., 2012). The fact that sirtuin activity depends on the intracellular levels of the co-substrate NAD^+ opens the possibility that enhancing NAD^+ biosynthetic pathways could result in a general activation of sirtuins and a concurrent enhancement of tumor suppression. As a proof of principle, treating mice with an NAD^+ precursor, nicotinamide riboside, activates at least SIRT1 and SIRT3, improves energy expenditure and fatty acid oxidation, and protects mice from diet-induced obesity and metabolic syndrome (Cantó et al., 2012). How these metabolic effects will apply to a cancer scenario is not clear yet, but the increasing body of evidence suggests that global sirtuin activation will protect against cancer.

In summary, the current paper together with previous evidences reinforces two parallel strategies for treating cancer: (1) SIRT4 activation either through specific approaches or through a general activation of sirtuins, and (2) inhibition of glutamine-dependent anaplerosis through inhibition of GLS, GDH, or even PHGDH.

REFERENCES

Bensaad, K., Tsuruta, A., Selak, M.A., Vidal, M.N., Nakano, K., Bartrons, R., Gottlieb, E., and Vousden, K.H. (2006). Cell *126*, 107–120.

Cantó, C., Houtkooper, R.H., Pirinen, E., Youn, D.Y., Oosterveer, M.H., Cen, Y., Fernandez-Marcos, P.J., Yamamoto, H., Andreux, P.A., Cettour-Rose, P., et al. (2012). Cell Metab. *15*, 838–847.

Cosentino, C., Grieco, D., and Costanzo, V. (2011). EMBO J. *30*, 546–555.

DeBerardinis, R.J., Lum, J.J., Hatzivassiliou, G., and Thompson, C.B. (2008). Cell Metab. *7*, 11–20.

Haigis, M.C., Mostoslavsky, R., Haigis, K.M., Fahie, K., Christodoulou, D.C., Murphy, A.J., Valenzuela, D.M., Yancopoulos, G.D., Karow, M., Blander, G., et al. (2006). Cell *126*, 941–954.

Jeong, S.M., Xiao, C., Finley, L.W.S., Lahusen, T., Souza, A.L., Pierce, K., Li, Y.-H., Wang, X., Laurent, G., German, N.J., et al. (2013). Cancer Cell *23*, this issue, 450–463.

Possemato, R., Marks, K.M., Shaul, Y.D., Pacold, M.E., Kim, D., Birsoy, K., Sethumadhavan, S., Woo, H.K., Jang, H.G., Jha, A.K., et al. (2011). Nature *476*, 346–350.

Sebastián, C., Satterstrom, F.K., Haigis, M.C., and Mostoslavsky, R. (2012). J. Biol. Chem. *287*, 42444–42452.

Wang, J.B., Erickson, J.W., Fuji, R., Ramachandran, S., Gao, P., Dinavahi, R., Wilson, K.F., Ambrosio, A.L., Dias, S.M., Dang, C.V., et al. (2010). Cancer Cell *18*, 207–219.

Zhou, R., Vander Heiden, M.G., and Rudin, C.M. (2002). Cancer Res. *62*, 3515–3520.

It's the Peptide-MHC Affinity, Stupid

Thomas Kammertoens[1,2] and Thomas Blankenstein[1,2,*]
[1]Max-Delbrück-Center for Molecular Medicine, 13125 Berlin, Germany
[2]Institute of Immunology, Charité, Campus Buch, 13125 Berlin, Germany
*Correspondence: tblanke@mdc-berlin.de
http://dx.doi.org/10.1016/j.ccr.2013.04.004

Adoptively transferred T cells can reject large established tumors, but recurrence due to escape variants frequently occurs. In this issue of Cancer Cell, Engels et al. demonstrate that the affinity of the target peptide to the MHC molecule determines whether large tumors will relapse following adoptive T cell therapy.

Tumor rejection usually requires $CD8^+$ effector T (T_E) cells, which recognize complexes of peptide bound to major histocompatibility complex (MHC) I molecules (pMHC) on tumor cells using their T cell receptor (TCR). The peptide is the proteasomal degradation product of the tumor antigen (TA). Upon recognition of pMHC, T_E cells produce effector molecules such as perforin, IFN-γ, and TNF. Although it has long been believed that direct killing of cancer cells by T_E cells alone is responsible for tumor rejection, recent studies show that destruction of the tumor stroma by T_E cells is critical for tumor eradication, with different mechanisms being discussed (Anders and Blankenstein, 2013; Schreiber, 2013 and references therein). While adoptively transferred T_E cells can reject large established tumors in experimental models and in humans, tumor recurrence after initial regression is a major obstacle. To overcome this problem, research has focused on improving T cell function by in vitro TCR affinity maturation, which can result in the loss of T cell fitness or specificity (Engels et al., 2012; Stone et al., 2009). Little attention has been paid to another variable in the three-molecule interaction: the affinity of the peptide to the MHC (pMHC affinity). This is surprising, given that the affinity of the TCR for pMHC usually lies within a narrow range (1–100 μM) due to the complex T cell selection process, while pMHC affinity ranges between <1 nM to >20,000 nM due to the partly stochastic nature of peptide sampling (Figure 1).

In this issue of *Cancer Cell*, Engels et al. (2013) addressed the impact of pMHC affinity on tumor eradication versus relapse. In a reductionist approach, they expressed the same amount of different peptide antigens in the same cancer cells. The peptide antigens were derived from mouse and human TA, presented by H-2 or HLA molecules, respectively, and all known as T cell epitopes. Mice with large tumors containing abundant stroma were then treated with TCR-transgenic T_E cells specific for the respective pMHC complex so that the peptide was the only variable. Therapy outcome correlated perfectly with pMHC affinity (Engels et al., 2013; Figure 1). pMHC affinities <10 nM (IC_{50} as measured by cell-free assays) elicited tumor rejection, and those with >100 nM caused relapse. Only high-affinity peptides were cross-presented by tumor stroma cells, causing stroma destruction and thereby preventing antigen loss variants. Peptides with very low affinity to MHC (IC_{50} ~22,900 nM) could not even induce the selection of escape variants, and antigen-positive tumors progressed. In vitro T cell kill assays did not predict rejection epitopes. In the clinic, the reasons for tumor relapse often remain unknown. Based on this study, experiments in HLA-transgenic mice with established HLA^+ syngeneic mouse tumors expressing human TA may allow prediction of epitopes that should or should not be targeted clinically. These mice can be treated with mouse T_E cells specific for the human TA to ask whether tumors will be rejected or recur. The human TA-specific mouse T_E cells can be generated by the transfer of TCR genes, which can be isolated against virtually any human TA from the nontolerant repertoire, termed TCR gene therapy (Anders and Blankenstein, 2013; Schumacher, 2002).

Another important question addressed by Engels et al. (2013) is: how useful are many of the TA epitopes currently employed clinically as therapeutic targets? T cell epitopes of human TAs are usually defined by autologous systems. Most TAs are self-proteins (self-TA), and only low-avidity T cells that survived tolerance mechanisms are in the normal repertoire. Typically, one or few TA epitopes for a given MHC restriction molecule are described. Algorithms quite accurately predict pMHC affinity, and the IC_{50} values determined by cell-free assays in Engels et al. (2013) did not differ greatly from the predicted values. Many of the described T cell epitopes of human self-TA have low affinity, e.g., IC_{50} for NY-$ESO_{157–165}$ (HLA-A*02:01): 1,262 nM, Melan-A/MART-$1_{26–35}$ (HLA-A*02:01): 7,600 nM, or MAGE-$A1_{161–169}$ (HLA-A*01:01): 165 nM, as predicted by Immune Epitope Database Analysis Resource. Peptides predicted with high affinity have rarely been described as T cell epitopes. Although it is possible that some of these peptides are not generated (processed and presented), it is more likely that these T cells have been deleted during negative selection in the thymus, if one assumes that with increasing pMHC affinity the immunogenicity of the epitope and the risk of autoimmunity also increase. Thus, the best, but also the most dangerous, epitopes as targets for T cell therapy may not yet be known. Conversely, cancer vaccines targeting self-TA face the difficulty of not only relying on T cells, which survived central tolerance, but also targeting epitopes of low pMHC affinity.

A critical issue in this study is the source of the TCRs expressed by the transgenic T_E cells and whether the TA is of self or non-self origin. The TCRs specific for high-affinity pMHC (SIY, ovalbumin, and

tyrosinase) were derived from an antigen-free (nontolerant) host, whereas the TCR specific for low affinity pMHC (gp100) was isolated from an antigen-positive (tolerant) host. Even if the human gp100 peptide (sharing six of nine amino acids with mouse gp100) was of non-self origin for the mouse T cells, it is unclear whether the TCR affinity for this pMHC is comparable to those TCRs from the nontolerant repertoire, recognizing pMHC with high affinity. Thus, one cannot exclude that a higher affinity of the TCR for pMHC, isolated from the non-tolerant repertoire and used for TCR gene therapy, can, at least partially, compensate for lower pMHC affinity.

The experiments targeting the self-TA gp100 with low pMHC affinity reflected a clinical TCR gene therapy trial with transient autoimmunity and little efficacy (Johnson et al., 2009), indicating that the experimental cancer model can predict clinical success/failure. The experiments targeting tyrosinase, another melanocyte differentiation antigen with high pMHC affinity, self for the host and non-self for the T_E cells resulted in tumor rejection and autoimmune vitiligo. However, the severity of autoimmunity may be difficult to predict using the mouse model and depends greatly on the respective self-TA. As noted earlier, unforeseen expression of self-TA on rare vital cells is an unresolved problem when using TCRs from the nontolerant repertoire that target TA with assumed restricted tissue expression such as differentiation or cancer-testis antigens (Blankenstein et al., 2012). TCR from the nontolerant repertoire can be biological weapons (Bos et al., 2008). However, we hypothesize that the thymus overshoots in deleting more T cells than necessary. The repertoire is still large enough to cope with most pathogens, and the evolutionary priority was to minimize the risk of autoimmunity. There may be a useful compartment of T cells against self-TA in the nontolerant repertoire that cause little or no damage but are nevertheless deleted. Nonetheless, targeting somatically mutated non-self TA would clearly be advantageous (Anders and Blankenstein, 2013; Schreiber and Rowley, 2008).

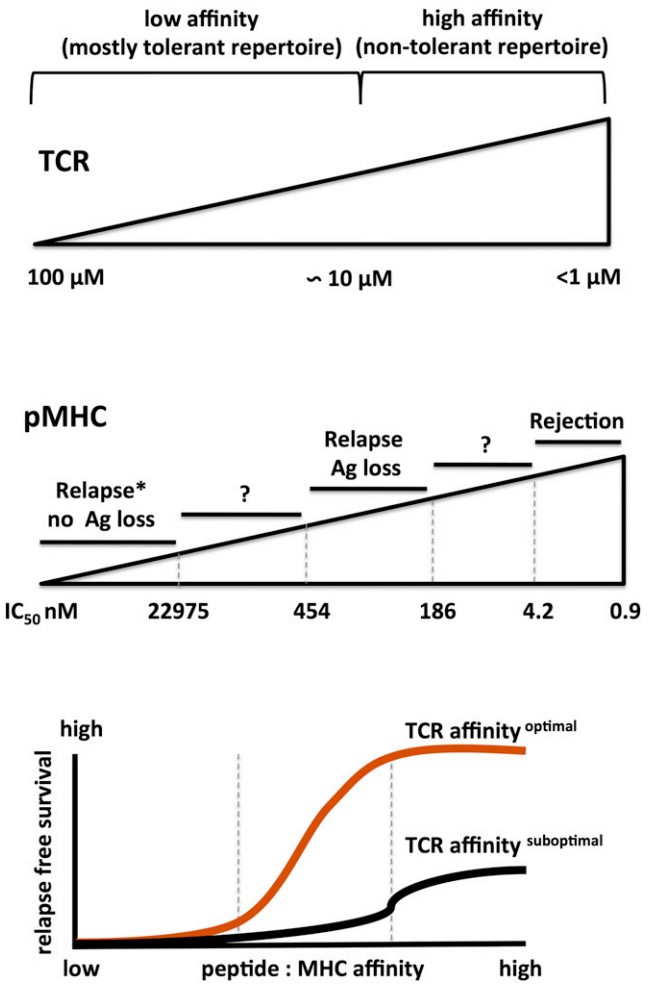

Figure 1. Tripartite Molecular Interaction Influences whether T Cells Reject Large Established Tumors or Select Escape Variants

Top: the range of affinities of the T cell receptor (TCR) to peptide/MHC I complexes (pMHC) is narrow (1–100 μM). TCRs specific for self-antigens (tolerant repertoire) tend to have lower affinity, whereas TCRs specific for non-self antigens (non-tolerant repertoire) tend to have a higher affinity for their cognate pMHC.

Middle: the range of pMHC affinities is broad (<1 nM to >20,000 nM). Indicated are pMHC affinities used in Engels et al. (2013) relative to therapeutic outcome. With decreasing pMHC affinity, adoptive T cell therapy leads from rejection to regression/recurrence of antigen (Ag) loss variants and then to recurrence without antigen loss (*or therapy failure). Note the gap in affinities between the different therapeutic outcomes, e.g., between 4.2 and 186 nM. For a variety of human tumor antigens, T cell epitopes are predicted within this range, raising the question of the cut-off value of "rejection epitopes".

Bottom: the relationship between pMHC affinity and success of T cell therapy is shown. If the TCR to pMHC affinity is optimal (red line), increasing pMHC affinity will (from a certain threshold onward) lead to an increase of success in therapy (relapse free survival) until a plateau (100% success) is attained. Black line, hypothetical graph illustrating that not only pMHC affinity but also TCR affinity decides over rejection versus relapse.

The study by Engels et al. (2013) is important, because it teaches us which epitopes not to target and how relevant experimental cancer models can be. However, a high affinity pMHC is not a good target per se. Too-low TA expression, inefficient processing and peptide presentation or posttranslational modification of the peptide could impede T cell therapy despite targeting a high-affinity pMHC. TAs are not always homogenously expressed within the tumor. In this case, the mechanism of tumor stroma destruction and the extent of bystander elimination of escape variants need to be better understood. Together, suitable TAs and particularly epitopes as targets in adoptive T cell therapy can and should be selected based on rational experimental models before clinical tests are done.

ACKNOWLEDGMENTS

This work was supported by the Deutsche Forschungsgemeinschaft through Sonderforschungsbereich TR36. We thank Maya Schreiber for editorial input.

REFERENCES

Anders, K., and Blankenstein, T. (2013). Clin. Cancer Res. *19*, 320–326.

Blankenstein, T., Coulie, P.G., Gilboa, E., and Jaffee, E.M. (2012). Nat. Rev. Cancer *12*, 307–313.

Bos, R., van Duikeren, S., Morreau, H., Franken, K., Schumacher, T.N., Haanen, J.B., van der Burg, S.H., Melief, C.J., and Offringa, R. (2008). Cancer Res. *68*, 8446–8455.

Engels, B., Chervin, A.S., Sant, A.J., Kranz, D.M., and Schreiber, H. (2012). Mol. Ther. *20*, 652–660.

Engels, B., Engelhard, V.H., Sidney, J., Sette, A., Binder, D.C., Liu, R.B., Kranz, D.M., Meredith, S.C., Rowley, D.A., and Schreiber, H. (2013). Cancer Cell *23*, this issue, 516–526.

Johnson, L.A., Morgan, R.A., Dudley, M.E., Cassard, L., Yang, J.C., Hughes, M.S., Kammula, U.S., Royal, R.E., Sherry, R.M., Wunderlich, J.R., et al. (2009). Blood *114*, 535–546.

Schreiber, H. (2013). Cancer Immunology. In Fundamental Immunology, Seventh Edition, W.E. Paul, ed. (Philadelphia, PA, USA: Lippincott Williams and Wilkins, a Wolters Kluwer business), pp. 1200–1234.

Schreiber, H., and Rowley, D.A. (2008). Science *319*, 164–165.

Schumacher, T.N. (2002). Nat. Rev. Immunol. *2*, 512–519.

Stone, J.D., Chervin, A.S., and Kranz, D.M. (2009). Immunology *126*, 165–176.

Standing Out from the Crowd: Cancer Stem Cells in Hepatocellular Carcinoma

Bruno Sainz, Jr.[1] **and Christopher Heeschen**[1,*]
[1]Stem Cells and Cancer Group, Molecular Pathology Programme, Spanish National Cancer Research Centre (CNIO), Madrid 28029, Spain
*Correspondence: cheeschen@cnio.es
http://dx.doi.org/10.1016/j.ccr.2013.03.023

Cancer stem cells (CSCs) drive solid tumor formation. In this issue of *Cancer Cell*, Zhao and colleagues identify the calcium channel α2δ1 subunit as a new functional hepatocellular carcinoma (HCC) CSC biomarker, which is vital for CSC biology as blocking α2δ1 in combination with doxorubicin treatment hinders HCC tumor formation.

Hepatocellular carcinoma (HCC) accounts for 90% of primary liver cancers and is the third most common cause of cancer-related deaths worldwide (Edwards et al., 2010). Unlike most other carcinomas, where mutations in specific oncogenes or tumor suppressors drive tumor initiation and progression, the majority of HCCs are multifactorial and primarily due to infections with hepatitis B virus (HBV) or hepatitis C virus (HCV). However, worldwide cases of nonviral HCC are on the rise due to growing numbers of patients with metabolic liver diseases (Alberti et al., 2005; Van Thiel and Ramadori, 2011). This multi-causality makes identification and subsequent targeting of a common HCC-specific alteration or even a cell-of-origin virtually impossible. Fortunately, where consensus does exist is in the concept that the majority of HCC arise from a subpopulation of cancer cells referred to as tumor-initiating cells (TICs) or cancer stem cells (CSCs) (Majumdar et al., 2012). Thus, identifying and therapeutically targeting these cells represents a more feasible approach for treating HCC regardless of the underlying cause.

CSCs are believed to possess stem cell-like properties such as unlimited self-renewal, exclusive in vivo tumorigenicity, and subsequent generation of differentiated progeny recapitulating the parental tumor phenotype (Figure 1). Evidence for their existence in several solid tumors has been experimentally demonstrated (reviewed in Hermann et al., 2010). For HCC, cells expressing diverse markers such as CD133, CD13, CD24, CD90, and EpCAM as well as cells defined as the side population have all been demonstrated to bear CSC characteristics. Apparently, the utility of these different markers across established cell lines and primary tumors varies significantly, and their suitability for therapeutic targeting has not been extensively evaluated. Therefore, the identification of markers, preferably a single marker, for efficient isolation of CSCs from the complex tumor cellular environment across different HCC tissues is still critically needed.

In this issue of *Cancer Cell*, Zhao et al. (2013) report that HCC CSCs can be specifically isolated with a new antibody (1B50-1) identified using a whole-cell subtractive immunization approach that recognizes the isoform 5 of the cell surface calcium channel α2δ1 subunit. 1B50-1 binds a subpopulation of HCC cells, hereafter termed $\alpha2\delta1^+$ cells, exhibiting stem cell-like properties, such as increased invasiveness, expression of stem cell-associated genes (*OCT4*, *SOX2*, *NANOG*, and *BMI1*), increased self-renewal, and the ability to give rise to both $\alpha2\delta1^+$ and $\alpha2\delta1^-$ cells. More importantly, the authors showed that subcutaneously injected $\alpha2\delta1^+$ cells from cell lines and primary HCC tumors were more tumorigenic in NOD/SCID mice compared to their $\alpha2\delta1^-$ counterparts. Although the increased tumorigenic potential of $\alpha2\delta1^+$ cells was evident with as little as 10^3 cells, limiting dilution assays (injection with less than 100 cells were not performed) revealed that not all $\alpha2\delta1^+$ cells were tumorigenic (TIC frequency in primary cases: 1 in 458 [748-281]), and higher numbers of $\alpha2\delta1^-$ cells were also capable of forming tumors (TIC frequency: 1 in 1,957 [3,785-1,012]) (calculated from Table 1 in Zhao et al., 2013). Therefore, $\alpha2\delta1^+$ cells from primary tumors were enriched for CSCs 4-fold.

Unlike many normal tissues where a stringent unidirectional hierarchy and strict balanced asymmetric division preserve tissue integrity (Jan and Jan, 1998), data in solid tumors are generally not as clear cut. On the one hand, this might be related to our still limited ability

Cancer Cell
Erratum

Mechanistic Rationale for Inhibition of Poly(ADP-Ribose) Polymerase in ETS Gene Fusion-Positive Prostate Cancer

J. Chad Brenner, Bushra Ateeq, Yong Li, Anastasia K. Yocum, Qi Cao, Irfan A. Asangani, Sonam Patel, Xiaoju Wang, Hallie Liang, Jindan Yu, Nallasivam Palanisamy, Javed Siddiqui, Wei Yan, Xuhong Cao, Rohit Mehra, Aaron Sabolch, Venkatesha Basrur, Robert J. Lonigro, Jun Yang, Scott A. Tomlins, Christopher A. Maher, Kojo S.J. Elenitoba-Johnson, Maha Hussain, Nora M. Navone, Kenneth J. Pienta, Sooryanarayana Varambally, Felix Y. Feng, and Arul M. Chinnaiyan*
*Correspondence: arul@umich.edu
http://dx.doi.org/10.1016/j.ccr.2013.04.005

(Cancer Cell *19*, 664–678; May 17, 2011)
In Figure 3B of this article, the VCAP and the control siRNA images are identical. This was the result of a mistake in constructing the figure. The correction to the figure does not affect the conclusion of the paper and the authors would like to apologize for any confusion the error may have caused. The corrected image is printed below.

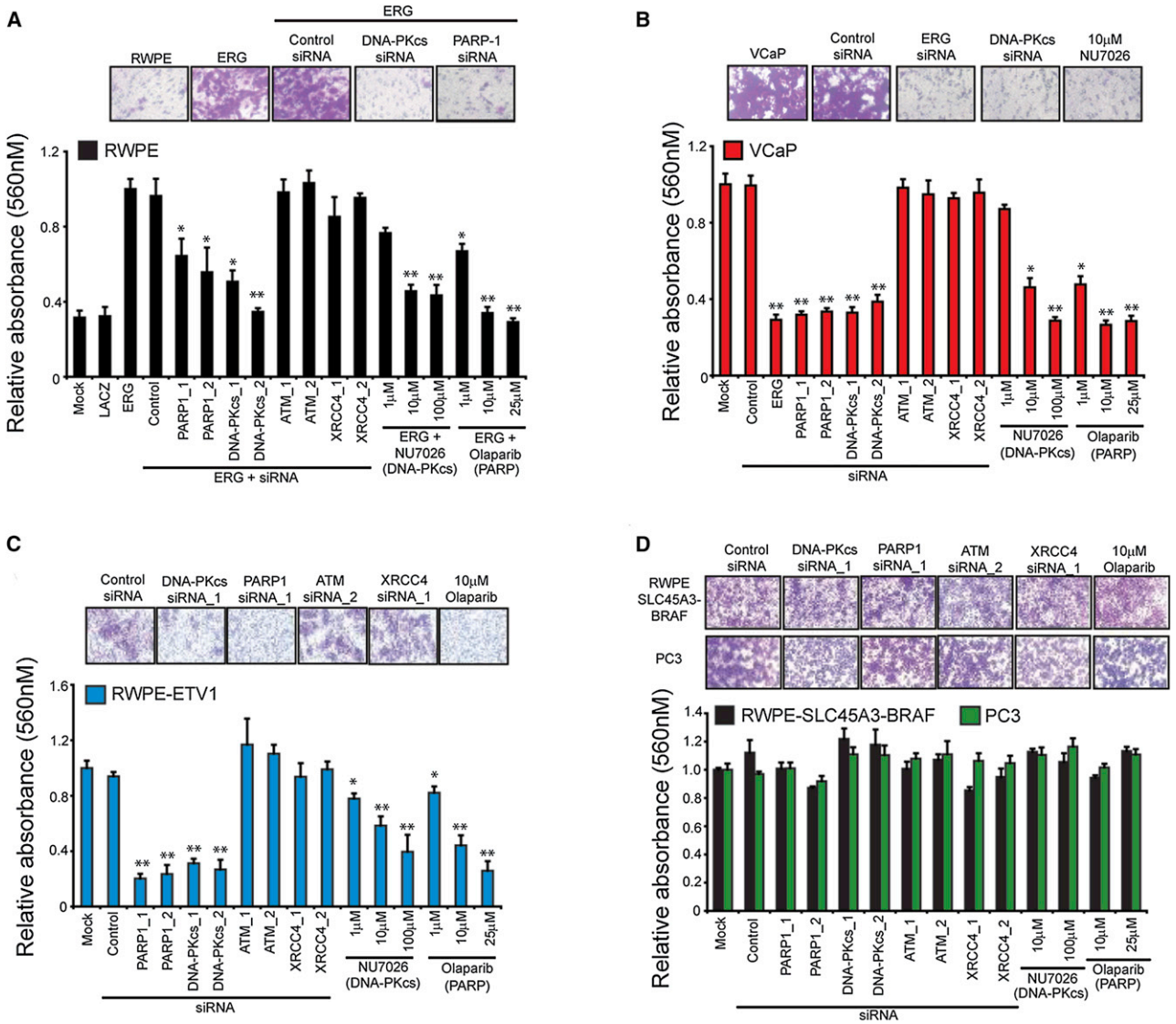

Figure 3. ERG-Mediated Invasion Requires Engagement of PARP1 and DNA-PKcs